

RADC-TR-89-121, Vol I (of two)
In-House Report
June 1989



PROCEEDINGS OF THE 1988 ANTENNA APPLICATIONS SYMPOSIUM (1988).

Paul Mayes, Et al.

DTIC
ELECTE
AUG 15 1989
S B D

Sponsored by
ELECTROMAGNETIC SCIENCES DIVISION
ROME AIR DEVELOPMENT CENTER
HANSCOM AFB, BEDFORD MASS. 01731
AIR FORCE SYSTEMS COMMAND

APPROVED FOR PUBLIC RELEASE; DISTRIBUTION UNLIMITED.

ROME AIR DEVELOPMENT CENTER
Air Force Systems Command
Griffiss Air Force Base, NY 13441-5700

Unclassified

SECURITY CLASSIFICATION OF THIS PAGE

REPORT DOCUMENTATION PAGE

1a. REPORT SECURITY CLASSIFICATION Unclassified			1b. RESTRICTIVE MARKINGS		
2a. SECURITY CLASSIFICATION AUTHORITY			3. DISTRIBUTION/AVAILABILITY OF REPORT Approved for public release; Distribution unlimited		
2b. DECLASSIFICATION/DOWNGRADING SCHEDULE					
4. PERFORMING ORGANIZATION REPORT NUMBER(S) RADC-TR-89-121 Volume I			5. MONITORING ORGANIZATION REPORT NUMBER(S)		
6a. NAME OF PERFORMING ORGANIZATION Rome Air Development Center		6b. OFFICE SYMBOL (If applicable) EEAS	7a. NAME OF MONITORING ORGANIZATION		
6c. ADDRESS (City, State, and ZIP Code) Hanscom AFB Massachusetts 01731-5000			7b. ADDRESS (City, State, and ZIP Code)		
8a. NAME OF FUNDING/SPONSORING ORGANIZATION		8b. OFFICE SYMBOL (If applicable)	9. PROCUREMENT INSTRUMENT IDENTIFICATION NUMBER		
8c. ADDRESS (City, State, and ZIP Code)			10. SOURCE OF FUNDING NUMBERS		
PROGRAM ELEMENT NO.		PROJECT NO.	TASK NO.	WORK UNIT ACCESSION NO.	
62702F		4600	14	01	
11. TITLE (Include Security Classification) Proceedings of the 1988 Antenna Applications Symposium					
12. PERSONAL AUTHOR(S)					
13a. TYPE OF REPORT In-house Final		13b. TIME COVERED FROM 9/21/88 TO 9/23/88		14. DATE OF REPORT (Year, Month, Day) 1989 June	
15. PAGE COUNT 300					
16. SUPPLEMENTARY NOTATION VOLUME I CONSISTS OF PAGES 1 THROUGH 291; VOLUME II CONSISTS OF PAGES 293 THROUGH 590					
17. COSATI CODES			18. SUBJECT TERMS (Continue on reverse if necessary and identify by block number)		
FIELD	GROUP	SUB-GROUP	Antennas, Microstrip, Multibeam Antennas		
			Satellite Antennas, Reflector, Array Antennas,		
			Broadband Antennas, HF, VHF, UHF		
19. ABSTRACT (Continue on reverse if necessary and identify by block number)					
<p>The Proceedings of the 1988 Antenna Applications Symposium is a collection of state-of-the-art papers relating to phased array antennas, multibeam antennas, satellite antennas, microstrip antennas, reflector antennas, HF, VHF, UHF and various other antennas.</p> <p><i>See also, included:</i></p>					
20. DISTRIBUTION/AVAILABILITY OF ABSTRACT <input type="checkbox"/> UNCLASSIFIED/UNLIMITED <input type="checkbox"/> SAME AS RPT. <input type="checkbox"/> DTIC USERS			21. ABSTRACT SECURITY CLASSIFICATION Unclassified		
22a. NAME OF RESPONSIBLE INDIVIDUAL John Antonucci			22b. TELEPHONE (Include Area Code) (617) 377-3549		22c. OFFICE SYMBOL RADC/EEAS

DD FORM 1473, 84 MAR

83 APR edition may be used until exhausted.
All other editions are obsolete.SECURITY CLASSIFICATION OF THIS PAGE
Unclassified

Accession For	
NTIS GRA&I	<input checked="" type="checkbox"/>
DTIC TAB	<input type="checkbox"/>
Unannounced	<input type="checkbox"/>
Justification	
By	
Distribution/	
Availability Codes	
Dist	Avail and/or Special
A-1	



CONTENTS

- * Keynote: "Antennas: Our Eyes and Ears on the World," John Kraus,
Ohio State University, Columbus, OH

WEDNESDAY, 21 SEPTEMBER 1988

SESSION I

RADIATING ELEMENTS

- | | |
|---|----|
| 1. "Semi-Conductor Dipole: Possible Radiating Element for Microwave/Millimeter Wave Monolithic Integrated Circuits (MIMIC)," P. D. Patel | 1 |
| 2. "Experimental Design and Performance of Endfire and Conformal Flared Slot (Notch) Antennas and Applications to Phased Arrays: An Overview of Development," M. J. Povinelli | 27 |
| 3. "Power Handling Printed Sub-Array for Wide Bandwidth Scanning Antenna Array," P. Pons, L. Maury and S. Dutheil | 53 |

* NOT INCLUDED IN THIS VOLUME

- | | | |
|------|--|-----|
| 4. | "Printed Circuit Antenna Designs," D. A. Mullinix and P. M. Proudfoot | 71 |
| * 5. | "Log-Periodic Slot Antenna With Meanderline Feeder," S. C. Kuo and C. G. Roberts | |
| 6. | "A Study of the Propagation and Radiation Characteristics of Tape Helical Structures," A. F. Peterson, B. Greene and R. Mittra | 105 |

SESSION II

ARRAYS

- | | | |
|-------|--|-----|
| 7. | "Advanced Architecture for a Monopulse Active Aperture Array," P. D. Hrycak, A. C. Sullivan and G. E. Evans | 133 |
| 8. | "Broadband MMIC T/R Module/Subarray Performance," D. Brubaker, D. Scott, S. Ludvik, M. Lynch, H. H. Chung, W. Foy and S. Y. Peng | 157 |
| 9. | "Array Trade-Off Study Using Multilayer Parasitic Subarrays," A. Zaman, R. Q. Lee and R. Acosta | 187 |
| 10. | "A K-Band MMIC Active Phased Array Antenna," C. Donn, A. E. Bollesen and S. H. Wong | 199 |
| 11. | "Sidelobe Reduction via Multi-Aperture Microwave Systems," S. M. Watson, J. P. Mills and D. H. Stone | 225 |
| * 12. | "Low Sidelobe, Short, Highly Produciible Microstrip Array," R. Chew | |
| 13. | "Dual-Polarized, Common-Aperture Monopulse Antenna," R. Kliger, R. Mariano, N. Sa and J. Toth | 255 |

THURSDAY, 22 SEPTEMBER 1988

SESSION III

MICROSTRIP ANTENNAS

- | | | |
|-----|---|-----|
| 14. | "Improved Bandwidth Microstrip Antenna Array," S. Sanzgiri, B. Powers, Jr., and J. Hart | 277 |
| 15. | "Broadbanding Techniques for Microstrip Patch Antennas - A Review," K. C. Gupta | 293 |

* NOT INCLUDED IN THIS VOLUME

Contents

16. "Characteristics of Electromagnetically Coupled Rectangular Patch Antennas With Overlaying Parasitic Elements," R. Q. Lee and K. F. Lee	323
17. "The Annular Sector Microstrip Antenna Mounted on Planar and Conical Surfaces," D. C. Thompson and C. A. Balanis	337
18. "Mode Purity of Rectangular Patch Antennas With Post and Aperture Excitations," H. K. Smith and P. E. Mayes	363
19. "Circular Polarization From Stacked Microstrip Patches," A. Adrian and D. H. Schaubert	377
20. "Analysis of the Annular-Ring-Loaded Circular-Disk Microstrip Antenna," Z. Nie, W. C. Chew and Y. T. Lo	391

SESSION IV

SYSTEM ANALYSIS AND MEASUREMENT

21. "Design and Economic Considerations for Broad Band Phased-Array Elements," G. J. Monser	413
22. "A Large Multibeam Lens Antenna for EHF SATCOM," J. P. Montgomery, D. L. Runyon and J. A. Fuller	431
23. "Measured Antenna Performance of an EHF Hybrid Scan Array Antenna for MILSATCOM Applications," J. F. Pedersen	461
24. "Technique to Measure Large Antenna Arrays," P. Franchi and H. Tobin	485
25. "Mathematical Model of a Large Aperture Focusing Antenna," T. B. Smerczynski, N. Marchand and G. Smith	505
26. "Analytical Approximation of a Distorted Reflector Surface Defined by a discrete Set of Points," R. Acosta and A. Zaman	525
27. "The Flexible Adaptive Spatial Signal Processor," R. N. Smith, A. M. Greci, S. A. Carollo, D. Jackson and E. Toughlian	539

* NOT INCLUDED IN THIS VOLUME

Contents

FRIDAY, 23 SEPTEMBER 1988

SESSION V

THEORY AND EXPERIMENT

- * 28. "Asymmetric Ridge Waveguide Radiating Element for a Scanned Array," H. Shnitkin, J. Green and P. Bertalan
- 29. "A Rapid, Accurate Test Method for Measuring Electrical Phase Length," G. J. Monser 557
- 30. "2-D Microwave Imaging of Aircraft," B. D. Steinberg 571
- * 31. "Application of Method of Moments to Dual Polarization Finite Array Antennas," E. Conaty
- * 32. "Broadband, Low Sidelobe, Zero Height, Slotted Circular Disk Antenna," K. Alemu

* NOT INCLUDED IN THIS VOLUME

PREFACE

The Antenna Applications Symposium, held at the University of Illinois, Robert Allerton Park, was cosponsored by Rome Air Development Center's Electromagnetics Directorate (RADC/EEAA), Hanscom AFB, MA and the University of Illinois' Electromagnetics Laboratory under contract F19628-88-M-0015. Professor John Mayes of UI was the symposium chairman. John Antonucci of RADC/EEA was the symposium manager for the Air Force.

SEMI-CONDUCTOR DIPOLE: POSSIBLE RADIATING
ELEMENT FOR MICROWAVE/MILLIMETER WAVE
MONOLITHIC INTEGRATED CIRCUITS (MIMIC)

Parbhu D. Patel
Bell Aerospace Textron
P. O. Box 1
Buffalo, NY 14240

ABSTRACT:

A wideband, semi-conductor compatible dipole, derived from the conventional metallic half wavelength dipole is described. This dipole is resistively loaded along its length, producing a travelling wave current distribution that is insensitive to frequency variations. The resistive loading, however, produces a reduction in efficiency but an increase in bandwidth. Graphs are presented which relate the resistive loading, with efficiency and bandwidth for a given length to diameter ratio of the dipole. These graphs could be useful as design curves in the tradeoff between bandwidth and efficiency.

The resistive loading for a conventional dipole can be achieved by varying the thickness of the resistive material coating along the length of the dipole. For a semi-conductor, however, the resistivity can be varied by changing the doping concentration (N_D) of the impurities. Hence, a wideband resistively loaded dipole can now be realized on a semi-conductor substrate.

1. INTRODUCTION:

Considerable effort is directed towards the realization of microwave/millimeter wave monolithic integrated circuits. Indeed, many of the sub-components of the transmit/receive module have been realized, at least in the hybrid form, and the research is now directed towards a fully integrated monolithic circuit. Even when a fully integrated transmit/receive module is available, there remains the question of coupling of the power, to and from free space.

Microstrip radiating elements or some derivatives of the microstrip^[1,3] element offer partial solution, in the sense that they can be incorporated with the monolithic integrated circuit T/R modules. These types of radiating elements are very attractive due to their low weight, ease of manufacture and low profile. However, the major disadvantage of this type of radiator is the inherently narrow bandwidth (\approx few percent).

What is required with MIMIC modules is a type of radiator which can produce a bandwidth, in excess of 25%. The radiating element should be GaAs or other semi-conductor compatible, so that it can be simultaneously fabricated with the sub-components of the T/R

module. Furthermore, it should provide a low profile, with ease of coupling of power to the MIMICs as well as making the MIMIC module easy to protect. Such a radiating element is the semi-conductor dipole, which is essentially derived from a half wavelength cylindrical dipole.

2. GENERAL THEORY:

It is well known that a conventional cylindrical dipole antenna essentially supports a standing wave distribution of current. Such an antenna is highly frequency sensitive because its antenna characteristics such as current distribution, antenna admittance and radiation patterns are strong functions of frequency.

A travelling wave antenna on the other hand, supports a distribution of current which is essentially an outward travelling wave. Only an infinitely long wire antenna will support such a current distribution, since there will not be reflections from the ends to produce standing waves. Such an antenna is physically unrealizable. The practical solution to the problem requires that the current on the dipole decreases with distance, away from the

input terminals. After a certain point along the antenna the current is reduced to a negligible value and therefore the dipole may be truncated, without seriously affecting the properties of the antenna. The first notable contribution on travelling wave dipole is due to Altshuler^[4], who inserted lumped resistors at a quarter of a wavelength from the ends of the antenna. This cannot be really considered as a travelling wave antenna with broadband characteristics since the value and the location of the loading resistor are functions of frequency. The logical extension of this approach is to resistively load the dipole continuously, along its length. Two cases must be considered:

- (i) Uniform (constant) impedance loading
- (ii) Variable impedance loading.

By resistively loading the dipole along its length, its efficiency is necessarily reduced but its bandwidth is enhanced. Our objective here is to relate the efficiency and bandwidth with the resistive loading.

3. FORMULATION:

The theoretical formulation of a resistively loaded dipole are given by King and Wu^[5] for the constant

internal impedance case, and by Wu and King [6] for the variable internal impedance case and therefore only an outline will be given.

The antenna to be analyzed is a hollow cylinder of length '2h' and radius 'a' aligned along the Z-axis and centered at the origin, as shown in Figure 1. It has an internal impedance of $Z^i(Z)$ due to continuous impedance loading and carries an axial current $I_z(Z)$, which is assumed uniform around the periphery of the cylinder since the radius 'a' is much less than the wavelength λ . When the antenna is driven by a Delta function voltage V_0^e at $Z=0$, the axial component of the vector potential $A_z^s(Z)$, on the surface of the antenna satisfies the one-dimensional wave equation

$$\left(\frac{\partial^2}{\partial Z^2} + k_0^2\right) A_z^s(Z) = \frac{-jk_0^2}{w} [Z^i(Z) I(Z) - V_0^e \delta(Z)] \quad (1)$$

where $Z^i(Z) = r^i(Z) + jX^i(Z)$ is the internal impedance per unit length

$k_0 = \frac{2\pi}{\lambda}$ is the free space propagation constant,
and $e^{j\omega t}$ time dependence is assumed.

The vector potential on the surface of the antenna is given by the potential integral

$$A_z^s(z) = \frac{\mu_0}{4\pi} \int_{-h}^h I_z(z') K(z, z') dz' \quad (2)$$

where $K(z, z') = \frac{e^{-jk_0 r}}{r}$

and $r = [(z-z')^2 + a^2]^{1/2}$ and $\mu_0 = 4\pi \times 10^{-7}$ H/m.

Equation (2) assumes that the antenna is thin; i.e., $K_0 a \ll 1$.

If the thickness of the resistive coating for the tubular dipole is less than the skin depth $d < \delta_s$, then $Z^i(z)$, the internal impedance per unit length becomes

$$Z^i(z) = r^i(z) = \frac{1}{2\pi a \sigma d} \quad (3)$$

where σ = conductivity of the resistive coating

a = radius of the dipole

d = thickness of the resistive coating

Equations (1) and (2) are now solved simultaneously to determine $I_z(z)$ for a given resistive loading distribution of $Z^i(z)$.

Once the current distribution $I_z(z)$ is known, other antenna characteristics such as the radiation pattern, the input admittance and the radiation efficiency can be computed. The input admittance Y and the radiation efficiency η are related to I_z through

$$Y = \frac{I_z(0)}{V_0 e} \quad (4)$$

and for a uniformly loaded antenna, the radiation efficiency

$$\eta = \frac{\text{Power radiated}}{\text{Power radiated} + \text{Power dissipated}}$$

$$= 1 - \frac{r^i}{\text{Re}[|I_z(0)|^2/Y]} \int_{-h}^h |I_z(z)|^2 \cdot dz \quad (5)$$

Two specific cases of uniform and tapered (travelling wave case) loading are now considered in detail.

3.1 Uniform Impedance Loading:

In the case of uniform resistive loading^[5] along the length of the antenna, the conductivity and hence the impedance per unit length $Z^1(z)$ will be constant. The solution of coupled eqn (1) and (2) is then given by:

$$I_z(z) = \frac{j2\pi k_o V_o^e}{\xi_o K \psi_{dR} \cos kh} [\sin k(h - |z|)] \quad (6)$$

$$+ Tu(\cos kz - \cos kh) + T_D (\cos \frac{1}{2} k_o z - \cos \frac{1}{2} k_o h)]$$

and

$$V = \frac{j2\pi k_o}{\xi_o K \psi_{dR} \cos kh} [\sin kh + Tu(1 - \cos kh) + T_D (1 - \cos \frac{1}{2} k_o h)] \quad (7)$$

where Tu and T_D are coefficients defined in King and Wu^[5]

$$\xi_o = 120\pi$$

The complex wave number k is defined by

$$k = \beta - j\alpha = k_o \left[1 - \frac{j4\pi Z^1}{k_o \xi_o \psi_{dR}} \right]^{1/2} \quad (8)$$

$$\text{and } \psi_{dR} = \begin{cases} \psi_{dR}(0) & k_o h \leq \pi/2 \\ \psi_{dR}(h - \lambda/4) & k_o h \geq \pi/2 \end{cases} \quad (9)$$

and $\psi_{dR}(z) = \csc [k(h-|z|)] \int_{-h}^h \sin k(h-|z'|) \cdot$

$$\left[\frac{\cos k_o r}{r} - \frac{\cos k_o r_u}{r_u} \right] dz' \quad (10)$$

where $r = [(z-z')^2 + a^2]^{1/2}$ (11)

$$r_u = [(h-z')^2 + a^2]^{1/2} \quad (12)$$

ψ_{dR} and k are related to each other in a complicated manner through equations (8) - (10) and an iterative scheme is used to compute these parameters.

3.2 Variable Impedance Loading:

When the impedance $Z^i(z)$ along the length of the dipole is tapered we have the practical case of a travelling wave array. In general, solution for equation (1) and (2) for an arbitrary $Z^i(z)$ can be obtained numerically. However, the practically important case of a travelling wave has been solved analytically by Wu and King [6] who show that if

$$Z^i(z) = \frac{\epsilon_o \psi}{2\pi (h - |z|)} \quad (13)$$

then the solution of equation (1) and (2) is

$$I_z(z) = \frac{2\pi V_o^e}{\xi_o \psi (1 - j/k_o h)} \left[1 - \frac{|z|}{h} \right] \exp(jk_o |z|) \quad (14)$$

$$\text{where } \psi = 2 \int_0^h \left(1 - \frac{z'}{h} \right) \exp(-jk_o z') \exp\left(-\frac{jk_o r_o}{r_o}\right) dz' \quad (15)$$

$$\text{and } r_o = (z'^2 + a^2) \quad (16)$$

Again, the other antenna characteristics can now be computed from the current distribution.

4.0 Semiconductor Dipole

The previous section has considered ways of making a basic dipole element into a wideband radiator by means of resistive loading. This section will deal with how the resistively loaded dipole (either variable or constant) can be implemented in the GaAs technology.^[7,8]

We have defined the hollow tube to be of thickness 'd'. If $d \ll \delta_s$, where δ_s is the skin depth, then the internal impedance per unit length $Z^i(z)$ is well approximated by

$$Z^i(z) = \frac{1}{2\pi a \sigma(z) \cdot d} \quad (17)$$

where $\sigma(Z)$ = conductivity along the length of the
dipole

d = thickness of the resistive loading along
the dipole ($d \ll ds$)

From Semi-Conductor Physics Theory, for an n-type semi-conductor dipole having a concentration of ionized donors N_D and an electron mobility μ_n , the conductivity is given by

$$\sigma = q \cdot \mu_n \cdot N_D \quad (18)$$

where q is the electron charge. Substituting (18) into (17) gives the internal impedance per unit length along a hollow tube, covered with n-type of semi-conductor dipole of thickness d , as

$$Z^i(Z) = \frac{1}{2\pi \cdot a \cdot q \cdot \mu_n \cdot N_D \cdot d} \quad (19)$$

The hollow n-type semi-conductor dipole can now be related to a planar dipole through the equivalent radii concept. This technique relates the cross-section of a non-circular wire to a circular wire of equivalent radii, by equating their electrostatic

capacitances. For example, a rectangular conducting strip of cross-sectional dimension 'w' and 't', as shown in Figure 2, can be analyzed in terms of a circular cylinder of radius a, where $a = 1/4 (w + t)$. Thus the resistively loaded cylindrical antenna can now be used to analyze the planar semi-conductor dipole, with enhanced bandwidth.

5. Bandwidth Considerations

The bandwidth^[9] of the dipole is computed from its impedance considerations and is defined here as the half-power width of the equivalent circuit impedance response. For a series type resonance, the bandwidth (BW) is

$$BW = \frac{2R}{w_0 \cdot \left. \frac{dX}{dw} \right|_{w_0}} \quad (20)$$

where $Z = R + jX$ is the input impedance at the resonant frequency w_0 . This definition of bandwidth implies a standing wave ratio of about 2.4 for a transmission line of characteristic impedance R ohms. The derivative in (20) can be evaluated by calculating the input impedance at two frequencies near resonance and using a finite difference approximation.

6. Computations of Efficiency and Bandwidth

Computer programs were written to theoretically evaluate the current distribution and the input admittance for both the uniform resistive loading as well as the variable resistive loading case. The results are summarized below.

6.1 Variable Impedance Case:

A $\lambda/2$ long dipole at 1 GHz with $h/a \approx 59$ ($\Omega=9.54$) with a variable impedance loading as described by equation (13) producing a current distribution described by equation (14), produced a radiation efficiency^[10] of $\approx 9\%$. Clearly, the low radiation efficiency is unacceptable for a possible radiating element in a phased array and hence this type of loading is not considered further. Interesting applications of this type of loading however, are given elsewhere^[11].

6.2 Uniform Impedance Loading:

A computer program was also generated to compute the current distribution for a given uniform impedance loading along the length of the dipole. The radiation efficiency was then computed as a function of loading ($\phi_i = 2\lambda r^i/\eta_0$). Figure 3 shows a graph

of efficiency versus resistive loading (ρ_i) for a varying dipole h/a ratio. The graph shows that there is a very small variation in the efficiency as a function of resistive loading.

The input impedance ($R+jX$) was also computed as a function of the resistive loading (ρ_i) for a given dipole h/a ratio. Figure 4 shows a graph of the input impedance (resistance and reactance) as a function of resistive loading for an $h/a = 35.6$ ($\Omega = 2 \ln(2 h/a) = 8.53$) at 42.09 GHz. The variation of the input impedance over a $\pm 10\%$ bandwidth is also plotted in Figure 4. These curves are used to determine the bandwidth of the dipoles as given in Section 5.

Figure 5 and Figure 6 show similar plots but with an h/a ratio of 142.24 ($\Omega = 11.3$) and 570.7 ($\Omega = 14.07$) respectively.

The bandwidth of the resistively loaded dipoles is computed from the input impedance plots and is shown in Figure 7. The bandwidth is given for a different h/a ratio of the dipole. The results are consistent with the classical antenna theory of achieving wider bandwidth from a thicker dipole.

7. Discussions of the Results:

Figure 3 and Figure 7 form the basis of our design curves. Given that a certain radiation efficiency is required, one could calculate the required resistive loading from Figure 3. Figure 7 can then be used to calculate the approximate bandwidth for a given h/a ratio of the dipole, or vice versa.

For practical MIMIC applications, the resistive loading must then be translated into the concentration of ionized donors (N_D) through Equation (19). As an example, consider a tabular dipole of outer radius of $25\text{ }\mu\text{m}$ with a thickness of $2\text{ }\mu\text{m}$ to be realized in a $n\text{-GaAs}^{[12]}$ substrate. If we assume $N_D \approx 10^{18}\text{ cm}^{-3}$, with $\mu_n \approx 3.5 \times 10^3\text{ cm}^2/\text{volt-sec}$, then at 42.09 GHz , we have $\phi_i \approx 2.1$, which corresponds to $\approx 44\%$ radiation efficiency and the bandwidth in excess of 52% for each of the dipoles with different h/a ratio considered. Other combinations are obviously possible.

8. Conclusion:

We have presented some results of a parametric study of a semi-conductor dipole, which could be a possible candidate as a radiating element in the design of MIMICs. The semi-conductor dipole offers wider bandwidth but at a reduced efficiency. This study has established the relationship between the resistive loading (doping concentration), the efficiency and the bandwidth.

9. Acknowledgements:

This work was supported by Bell Aerospace Textron through its internal R&D project.

The author acknowledges discussions with Mr. Carl E. Klingenschmitt in the initial stage of the project.

10. References

1. Munson, R. E., "Conformal Microstrip Antennas & Microstrip Phased Arrays", IEEE Trans. on A&P, Vol. 22 No. 1, Jan. 1974, pp. 74-78.
2. Derneryd, A., "A Theoretical Investigation of the Rectangular Microstrip Antenna Element", IEEE Trans. on A&P, Vol. 26, July 1978, pp. 532-535.
3. Oltman, H. G., "Electromagnetically Coupled Microstrip Dipole Antenna Element" in Proc. European Microwave Conference, 1977.
4. Altshuler, E. E., "The Travelling-Wave Linear Antenna", IRE Trans. on A&P, July 1961, pp. 324-329.
5. King, R. W. P., and Wu, T. T., "The Imperfectly Conducting Cylindrical Transmitting Antenna", IEEE Trans. on A&P, Vol. 14, No. 5, Sept. 1966, pp. 524-534 and correction in IEEE Trans. on A&P, July 1967, p. 576.

6. Wu, T. T., and King, R. W. P., "The Cylindrical Antenna with Nonreflecting Resistive Loading", IEEE Trans. on A&P, Vol. 13, No. 3, May 1965, pp. 369-373 and correction in IEEE Trans. on A&P, Nov. 65, p. 998.
7. Jain, F. C. and Bansal, R., "Monolithic MM-Wave Antennas", Microwave Journal, July 1984, pp. 123-133.
8. Jain, F. C. and Bansal, R., "Semiconductor Antennas for Millimetre-Wave Integrated Circuits, Infrared and Millimetre Waves, Vol. 15, Chapter 6, Academic Press 1986.
9. Pozar, D. M., "Considerations for Millimetre Wave Printed Antennas", IEEE Trans. on A&P, Vol. 31, Nov. 1983, pp. 740-747.
10. Shen, I. C., and King, R. W. P., "The Cylindrical Antenna with Non-Reflecting Resistive Loading, IEEE Trans. on A&P, Vol. 13, p. 998, 1965.

11. Kanda, M., "A Relatively Short Cylindrical
Broadband Antenna with Tapered Resistive
Loading for Picosecond Pulse Measurements",
IEEE Trans on A&P, Vol. 26, May 1978, pp.
439-447.
12. Sze, S. M., "Physics of Semiconductor Devices",
Wiley, New York 1981, pp. 38-41.

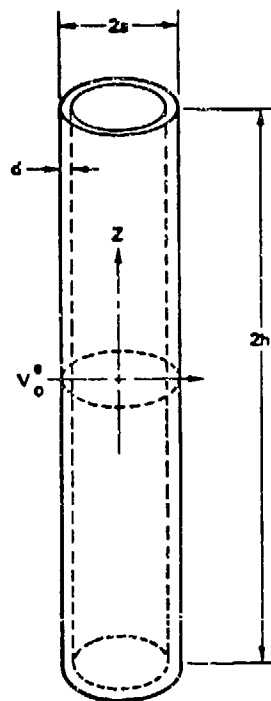


Figure 1. Hollow Cylindrical Dipole

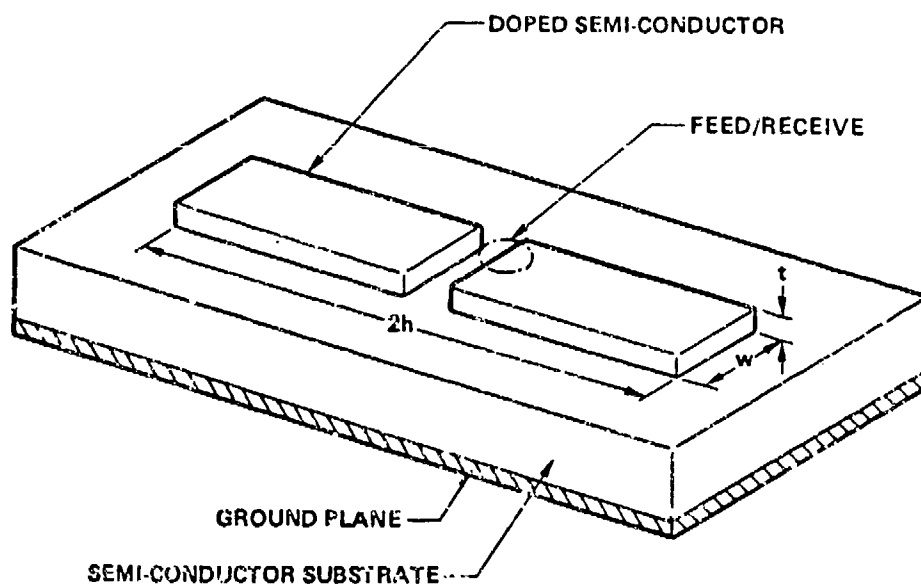


Figure 2. Monolithic Semi-Conductor Dipole Antenna

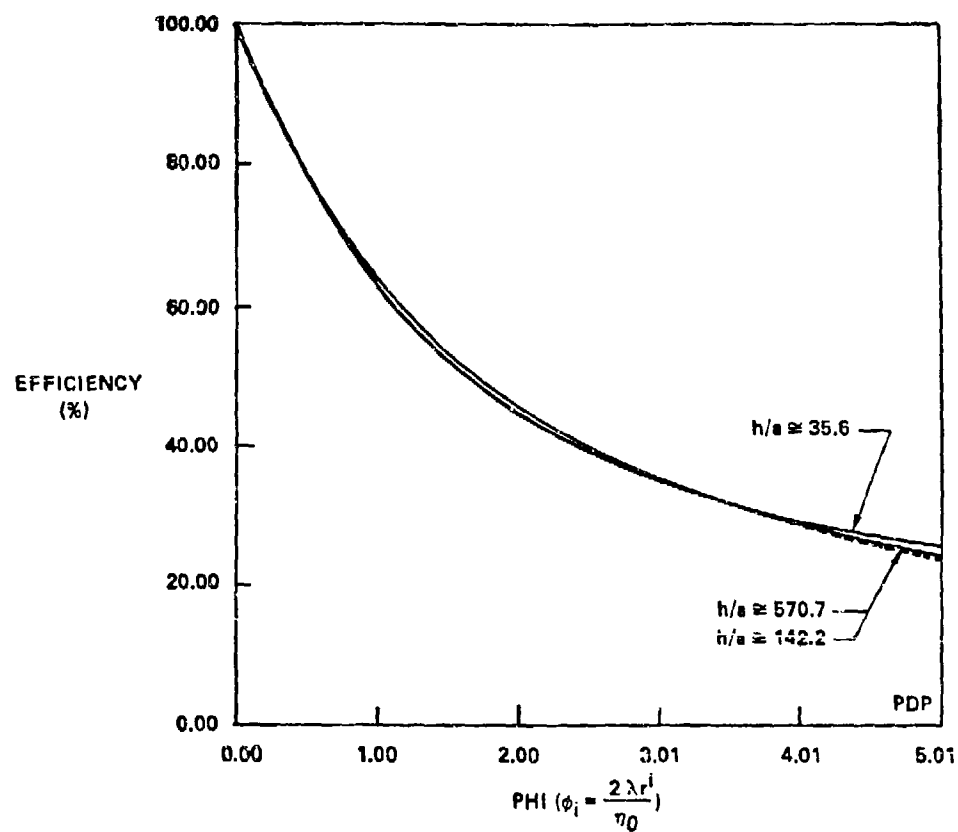


Figure 3. Graph of Efficiency versus Resistive Loading
for Different (h/a) Dipole Thickness

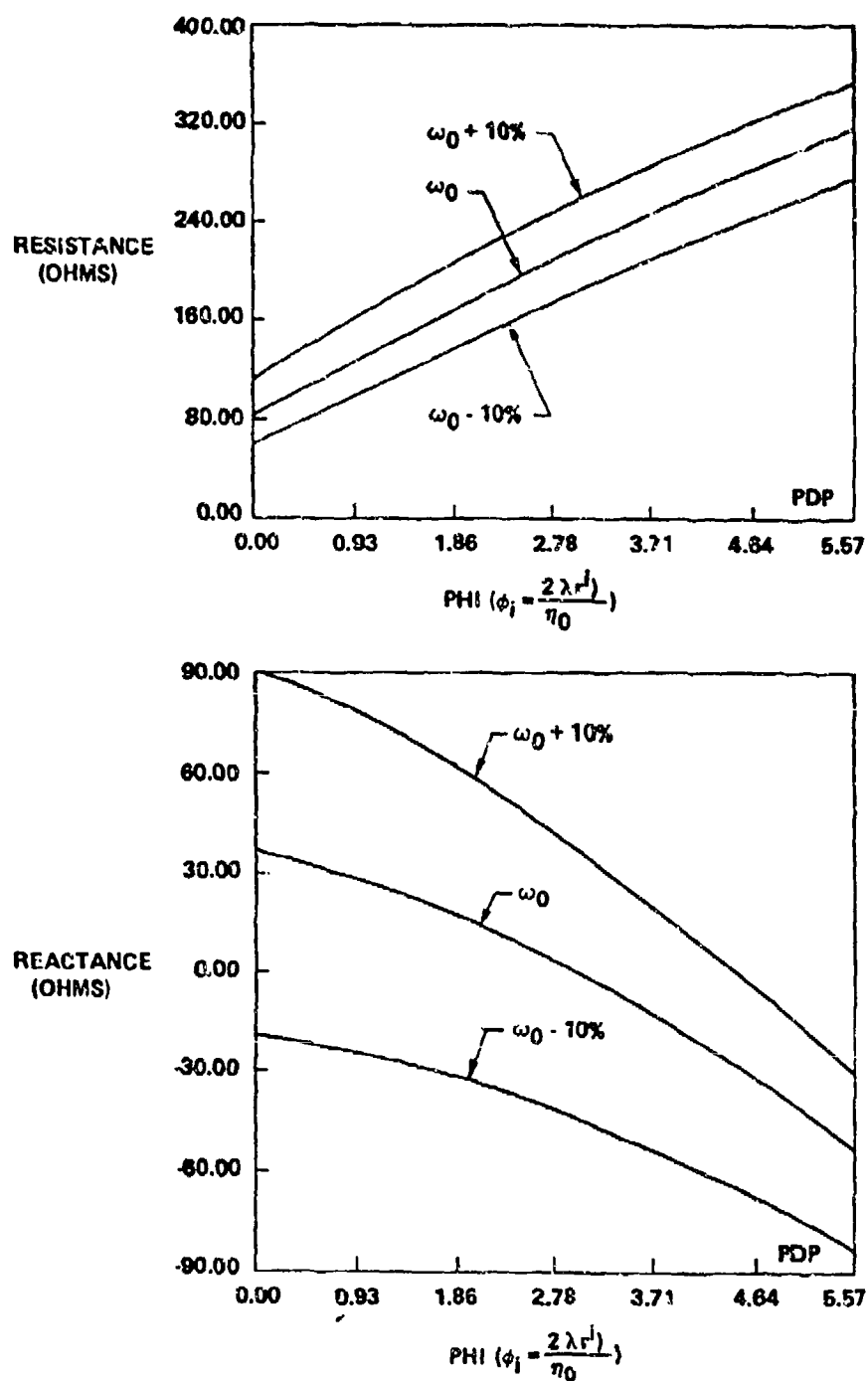


Figure 4. Graph of the Input Impedance ($R + jX$) versus Resistive Loading (ϕ_1) for $h/a = 35.6$ at 42.09 GHz

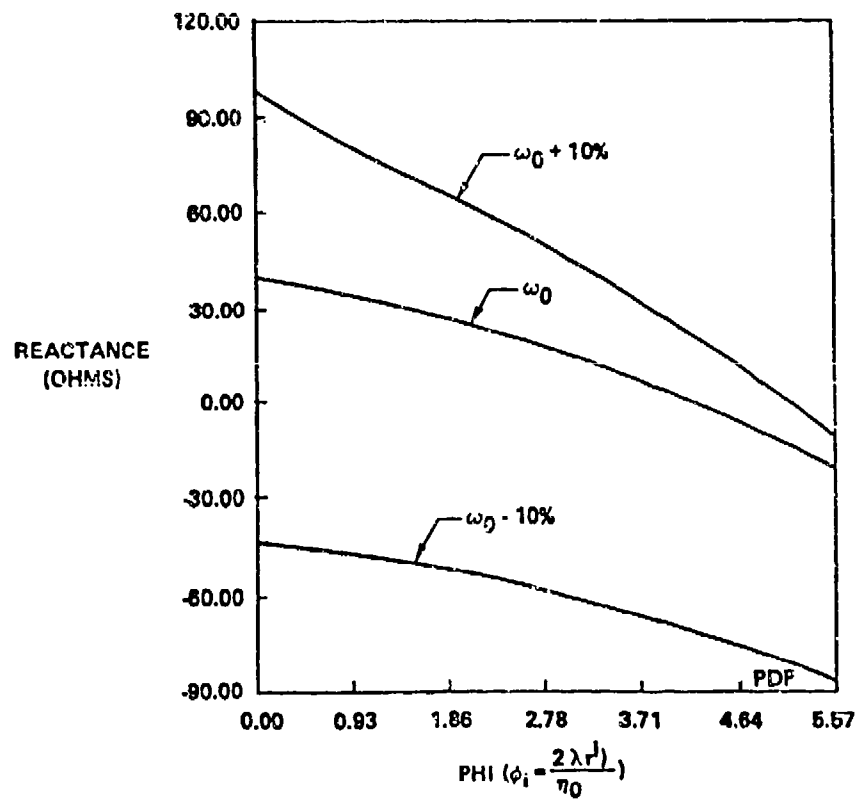
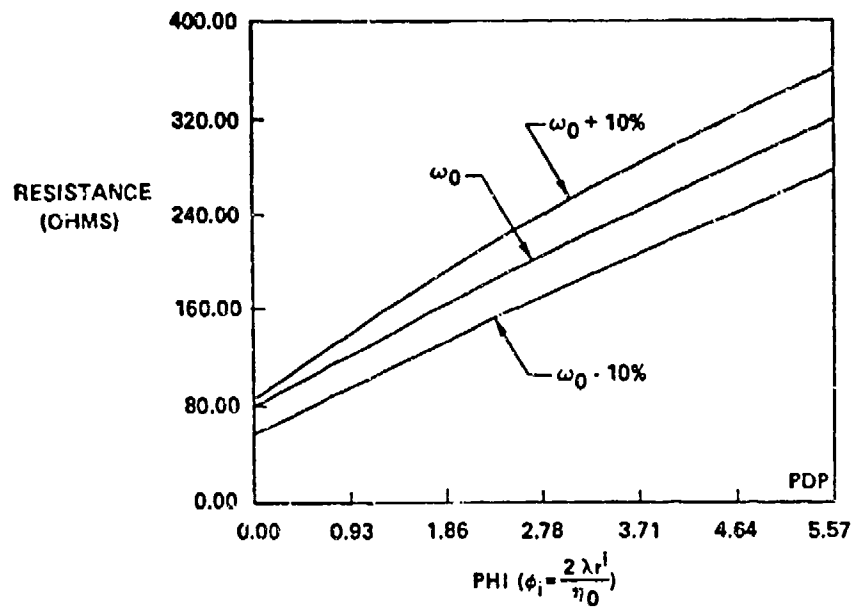


Figure 5. Graph of the Input Impedance ($R + jX$) versus Resistive Loading (ϕ_i) for $h/a = 142.2$ at 42.09 GHz

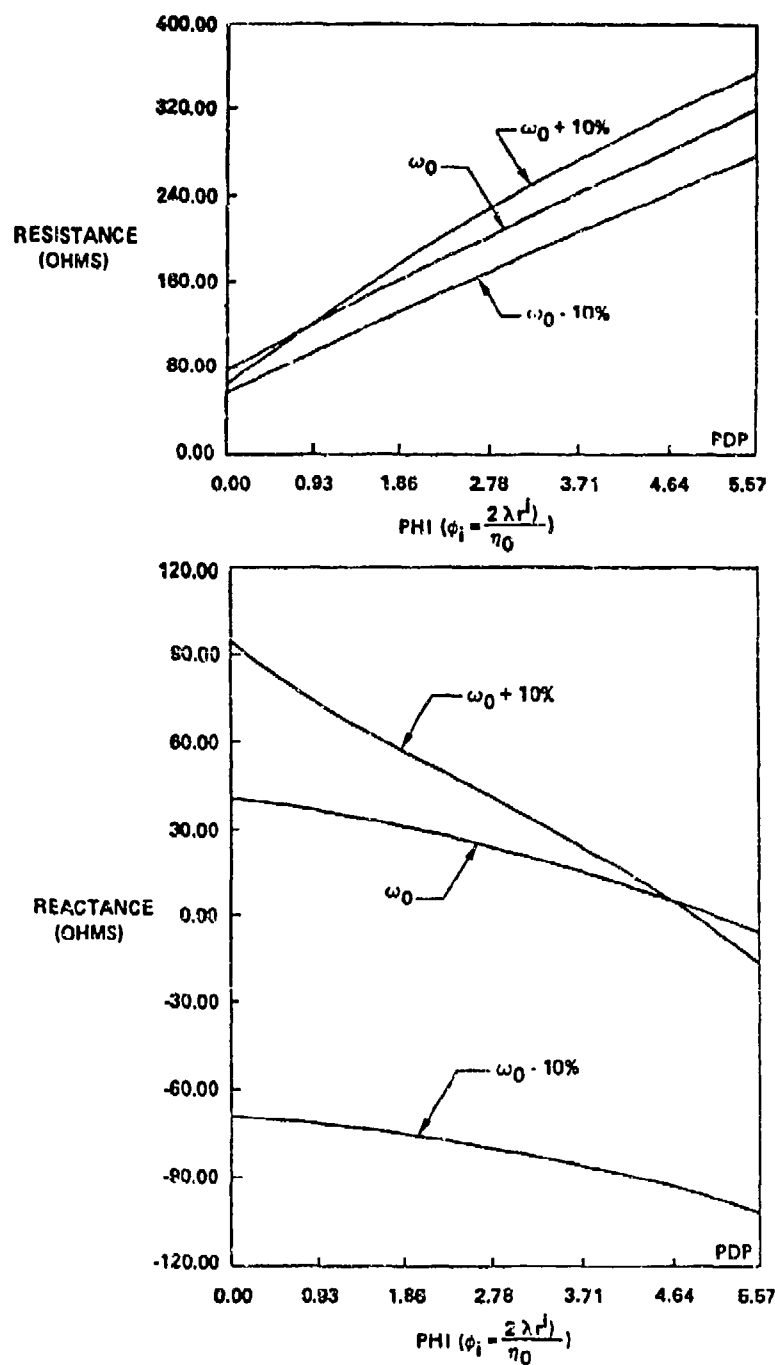


Figure 6. Graph of Input Impedance ($R + jX$) versus Resistive Loading (ϕ_1) for $h/a = 570.7$ at 42.07 GHz

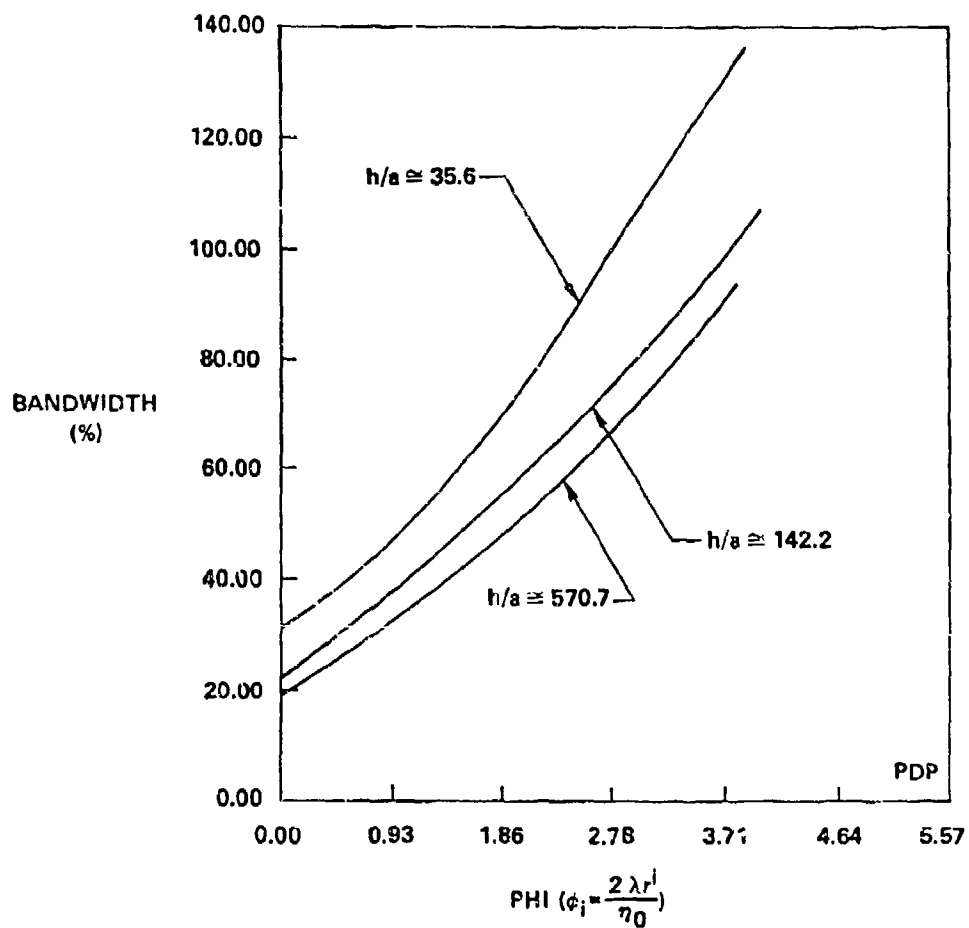


Figure 7. Graph of Bandwidth versus Resistive Loading
for Different (h/a) Dipole Thickness

EXPERIMENTAL DESIGN AND PERFORMANCE OF ENDFIRE AND CONFORMAL FLARED SLOT (NOTCH) ANTENNAS AND APPLICATION TO PHASED ARRAYS: AN OVERVIEW OF DEVELOPMENT

**Mark J. Povinelli
GE Aerospace
Aerospace Electronic Systems
Utica, NY 13503**

ABSTRACT

The empirical development of the flared slot or notch antenna for wide bandwidth operation is discussed along with the endfire and conformal printed circuit designs of this antenna element type. Array-element and active impedance characterization of three dual polarized planar arrays of two densities are presented. A conformal aperture design is also given for a wideband crossed microstrip flared slot.

1.0 INTRODUCTION

Recent research in airborne antenna systems has focused on including multifunction (radar, Electronic Warfare (EW), Electronic Countermeasure (ECM)) capability into phased arrays which operate over multioctave frequency bands. Both planar and conformal (smart skin) applications of airborne phased array systems are being pursued with the requirement that they possess horizontal, vertical, and circular polarization capabilities. Reduced grating lobe requirements at the upper frequencies have driven the array-element spacings closer, which in turn has reduced the array-element width. Given the wide frequency range (several octaves) that planar arrays are required to cover, only endfire antenna elements such as the flared slot (notch) or the log-periodic antenna can be considered potential candidates. However, log-periodic antennas have inherent limitations which make them less useful for planar phased arrays. First, because the individual element arms occupy a large portion of the total element height coupling interaction between adjacent elements is problematic. Second, the necessity of a closely confined element spacing (area) restricts the low frequency arm lengths beyond the point of their optimal performance (half-wavelength). Fortunately, the printed circuit stripline fed flared slot antenna offers a viable alternative. While the nominal low frequency

limitation of a free space half-wavelength in element width still exists, the reduction in performance at the low end of the frequency band is not as severe. For conformal arrays, a microstrip flared slot antenna element with dual polarization capability when crossed can also be used over a multioctave frequency bandwidth [1].

The printed circuit flared slot antenna with a microstrip or stripline feed is a complex three-dimensional structure which does not lend itself in full to available analysis methods. This paper will focus on experimental designs and results while pointing out available design techniques in the literature. In particular, an endfire stripline fed version of the printed circuit flared slot or notch antenna has become popular and is extremely useful as a planar multioctave phased array-element. This general flare design is being used for both endfire and conformal printed circuit antenna elements. The historical development of the flare design is traced in several antenna and transmission line structures and the factors that have resulted in the parallel evolution of this design are considered. The design and performance characterization of three planar multioctave (6.0 to 18.0 GHz) dual polarized phased array apertures (using endfire stripline fed flared slot elements) and a conformal microstrip flared slot antenna element will be discussed.

2.0 OVERVIEW OF DEVELOPMENT

The development of the endfire flared slot or notch antenna (in particular the flare) can be derived from using the results of a transverse slot in an aircraft leading edge, slotline field containment, rudimentary horn, fin line, and V-dipole designs. While the esthetic value of the flare is not central to the functional empirical design, examples of similar manifestations can be found in art and nature (i.e., "Vivaldi" horn, corolla of *Ipomea purpurea*).

The notch antenna was developed out of the applications of conformal half-wavelength slot antennas to aircraft leading edges. The relationship of the standing wave slot antenna in an infinite ground plane as the complementary of a dipole antenna was given by Booker in 1946 [2]. The two most common coaxial excitation schemes for this type of half-wavelength slot are the center fed and edge fed versions. The edge fed slot provides

better impedance match at resonance [3]. Conformal slot antennas suited for the curved structure of aircraft and for drag reduction were given by Carry in 1952 [4]. In this paper, he describes experimental results of axial and transverse slots in fin and wing edges (leading edges). The transverse slot gave good forward radiation with minimal back radiation which appeared to increase with smaller lengths and thicknesses of the streamlined cylinder. As the leading edge angle is reduced, the edge fed element behaves quite differently from that of a half-wavelength standing wave slot. As the angle goes to zero, the half-wavelength slot is transformed into a quarter-wavelength opened slot element with unique characteristics. In a 1955 paper, Johnson [5] describes this opened slot endfire element as a notch antenna. In his paper, the antenna performance is described for several notch antennas cut in the top of finite ground plane edges. It was found that a quarter-wavelength notch yielded broad bandwidth behavior in an edge fed configuration.

The flared slot antenna can be derived from transmission line structures. Slot line on a dielectric substrate as a form of printed circuit transmission line was given by Cohn in 1969 [6]. Examining the electric field distribution in a slot transmission line, Reuss, in a 1974 report [7], described a broadband slotline antenna obtained by flaring the transmission line.

Another development of this type of antenna is derived from the horn antenna design. The silhouette of the horn given by Carr [8] can be used to derive a low profile printed circuit version of flared slot. Kerr describes a very broadband low profile antenna which is also determined from a horn [9]. A rudimentary horn antenna was presented by Sengupta and Ferris which was developed from the broadband ridged horn [10].

A printed microstrip version of the notch antenna having the form of a flared slot was given by Monser, Hardle, and Ehrhardt [11]. A stripline fed version of a flared notch antenna for multiple polarization broadband arrays was discussed by Lewis, Fassett, and Hunt [12]. Gibson used the name Vivaldi after the composer Antonio Vivaldi to describe a printed circuit wideband flared antenna [13]. A flared slot antenna was also constructed in a fin line by extending and flaring the printed circuit beyond the housing [14]. This type of flare design can also be expressed as a V-dipole or (flared dipole) design as shown in Figure 1.



Figure 1. V-Dipole Flare Designs

3.0 ENDFIRE FLARED SLOT (NOTCH) DESIGN

The notch antenna proposed by Carry and Johnson can be realized as a printed circuit structure as described. The element notch can be etched on the metallized side of a dielectric substrate, and the transmission line which feeds the antenna can be realized as a microstrip or a stripline feed. A stripline fed double-sided board can be constructed where the notch is etched on both sides of the ground plane and the open circuited stripline feeds at a right angle across the slots. In general, the transmission line can be directly shorted to the ground plane at the end, or left open circuited.

The three principle components which make up the printed circuit stripline or microstrip flared slot (Notch) antenna are the 50-ohm stripline or microstrip feed, a stripline- (or microstrip) to-slotline coupling transition, and a flared slot or notch tapered to provide a wideband impedance match to free space. The first component, the stripline or microstrip feed, can be determined from standard design equations like those given by Wheeler [15], and Cohn [16].

The microstrip or stripline-to-slotline transition is used to couple energy from the stripline to the slotline. Cohn describes the design of a microstrip-to-slotline transition, where the short-circuited slotline and open-circuited microstrip line end a quarter-wavelength beyond the crossover point; a 30 percent bandwidth is possible [6]. This type of transition was essential to simplifying the feed design from coaxial to that of a simple printed circuit design. In this design, the low impedance line acts as a quarter-wavelength short at the slot and the high impedance slot acts as a quarter-wavelength open at the line, thereby maximizing the coupling. If the guide wavelength is made less than 40 percent of the free space wavelength, the quasi-TEM fields will be adequately contained and will not radiate giving propagation down the

slotline guide. Increases in bandwidth of an octave can be produced by terminating the microstrip line in a radial stub and the slot in a short. This design was proposed by Robinson [17] in his 1969 paper. Further increases in bandwidths (multioctave) have been obtained by terminating the slotline in an open circuit and the stripline or microstripline in a d.c. short to the ground plane [18] or in a radial stub. So far, this overview has not discussed the characteristic impedances or losses of slotline and its relationship with microstrip or stripline feed impedances. Rigorous three-dimensional analysis of this microstrip-to-slotline design has not been done in the literature. More recent work of Janaswamy and Schaubert [19] have formulated the problem in the spectral domain and have given characteristic impedance curves for single-sided slotline on low dielectric substrates.

A characteristically traveling wave antenna is realized by flaring a notch or transmission line out to provide a smooth impedance transformation from the line impedance to the characteristic impedance of free space. The term flared slot is used to describe this element on a printed circuit substrate. The launched quasi-TEM fields of the slotline radiate when the guide wavelength is greater than approximately 40 percent of the freespace wavelength. Therefore, the phase center of the point of radiation moves up the flare with decrease in frequency. This results in a low frequency limit based on element width. This low frequency limitation in width occurs at a freespace half-wavelength where a moderate roll-off can be obtained down to a tenth of a freespace wavelength. For shorter length flares ($\lambda_0/4 \leftrightarrow \lambda_{\epsilon_r}/4$, and widths $< \lambda_0/2$), the possibility of a more resonant antenna exists. A first-order approximation to the gain is given by the directivity of the element width squared where the gain increases as roughly the square of the frequency. Modification of the flare shape can result in beam broadening, pattern shaping, and impedance matching. More discussion on flare design and analysis can be found in the literature [13,20-23].

With the design evolution of these three components, a stripline fed design with a printed circuit flare on both sides of the dielectric substrates can be realized, as shown in Figure 2. This printed circuit endfire element which has a multioctave bandwidth can be realized into a number of array and phased array applications [12,24-26].

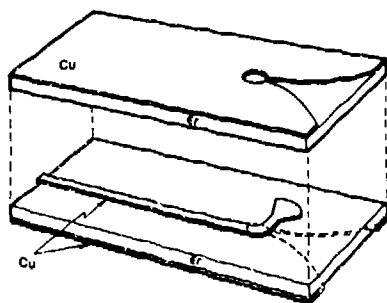


Figure 2. Stripline Fed Flare Slot (Notch) Antenna Element

4.0 PLANAR ARRAY DESIGN AND PERFORMANCE

The design and performance of three dual-polarized planar arrays, an 8×8 half-populated square lattice (HPS), an 8×8 fully-populated square lattice (FPS), and a half-populated equilateral triangular lattice (HPT) with close element spacings to reduce grating lobes at higher frequencies will be discussed. The population refers to the module density behind the aperture. For half-population there are half the number of active T/R modules needed behind the array-elements because the elements are driven in pairs. Full-population refers to each array-element being driven by an active T/R module. These arrays are used to characterize the stripline fed flared slot as a phased array-element. This performance is determined in part by the mutual coupling between elements in the array environment. A short flare length (at low frequencies) was used to reduce array mutual coupling interactions and to optimize array-element patterns. The central array-element performance (gain, patterns, and mutual coupling) and active VSWR with scan are given for all three arrays.

Both square lattice arrays have a rotated square grid with 0.375-inch like polarization spacings and 0.265-inch spacings between unlike polarizations. Both arrays consist of eight rows by eight columns of dual polarized elements for a total of 256 radiating elements. The triangle lattice is layed out on a 0.433-inch equilateral phase center grid spacing. The like polarized elements have a 0.306-inch spacing and an adjacent overlapping separation of 0.112 inch. These lattice spacings determine the allowable element width for a given element thickness in the array design.

The array-element used in both half-populated arrays is etched on a 0.04-inch ground plane spacing (GPS) low loss durcoid substrate ($\epsilon_r = 2.2$). Half-population is achieved by

combining, with a Wilkinson power divider, every two like polarized elements into a two-element subarray as shown in Figure 3. Two orthogonal polarizations (with common phase centers) are realized by joining (co-locating at 90 degrees) a pair of subarrays through a mechanical slot cut in the top of one subarray and the bottom of the other subarray. An absorber load is used to mask the ground plane reflection and optimize the array-element gain and impedance match. This electrically unique orthogonal subarray-element pair, shown in Figure 4, is then used in the square lattices described above, yielding 0.53-inch in phase center spacing with 128 subarrays in the 8 x 8 array shown in Figure 5. The central subarray-element (passive) return loss is shown in Figure 6 from 2.0 to 20.0 GHz. This same design with the element width foreshortened is used in the denser HPT array, yielding 0.433-inch equilateral triangular phase center spacings with 128 subarrays in the array shown in Figure 7. The fully populated aperture, shown in Figure 8, uses a stripline notch element etched on 0.062 GPS high loss G10 substrate ($\epsilon_r = 4.5$). The element was designed to fit in the prescribed lattice spacing, yielding one unique element with a width of 0.3 inch. This results in an electrically small element at the lower frequencies, which reduces the radiation efficiency.

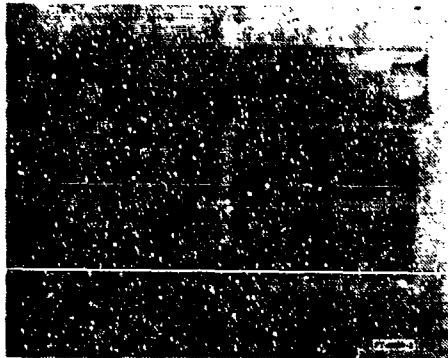


Figure 3. Wilkinson Stripline Fed Flared Slot HP Subarray Element Pairs

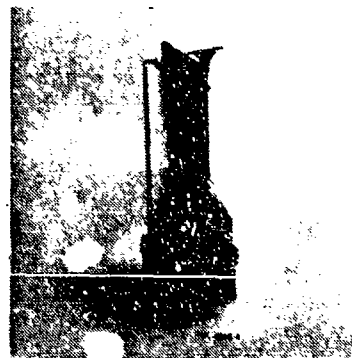


Figure 4. Orthogonal Subarray Element Pair

In the HPS and HPT arrays, the central subarray-elements number 71 and 74 and the orthogonal subarray-elements number 72 and 73 were measured, respectively, along with the central array-element number 120 in the FPS array for gain and E- and H-plane patterns. The gains of elements 71, 72, 73, 74, and 120 are shown in Figure 9. The gain of element 72 with a slot cut in the bottom is approximately 2 dB below that of the allowable directivity. Triangular subarray-element number 74 and 73 gain has a 4 dB

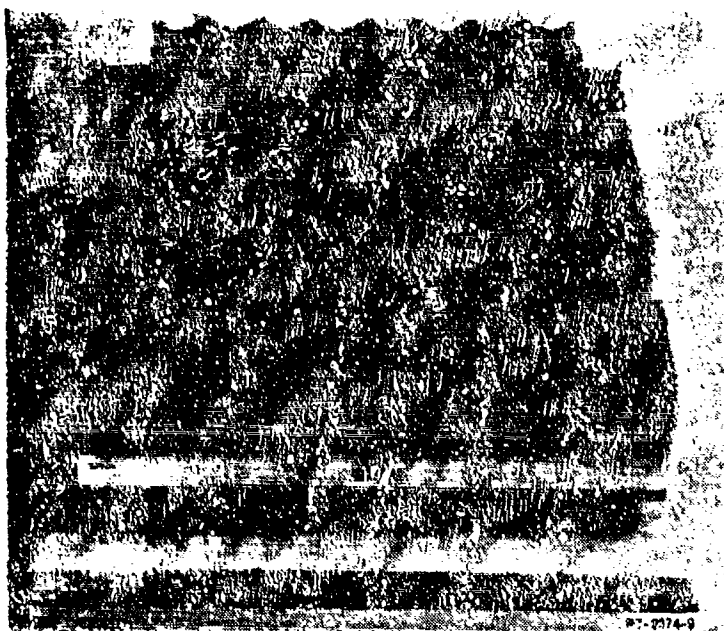


Figure 5. 8 x 8
HPS Array

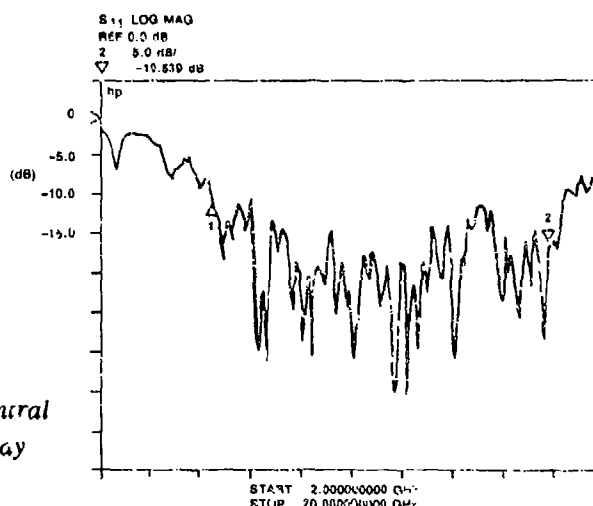


Figure 6. Self-Impedance of Central
Subarray Element 72 HPS Array

ripple without the absorber loads in between subarray-element pairs. A close-up view of the central subarray-elements 73, 74, 57, and 58 in the HPT array is shown in Figure 10 detailing the overlapping elements. The gain of array-element 120 in the FPS array is, on the average, 5 dB below that of its directivity. The majority of this gain difference is a result of power losses in the element substrate. The embedded E- and H-plane patterns of the arrays are shown in Figures 11, 12, and 13 for subarray-element 71 at 6.0, 12.0, and 18.0 GHz, array-element 120 at 7.0, 12.0, and 17.0 GHz, and subarray-element 74

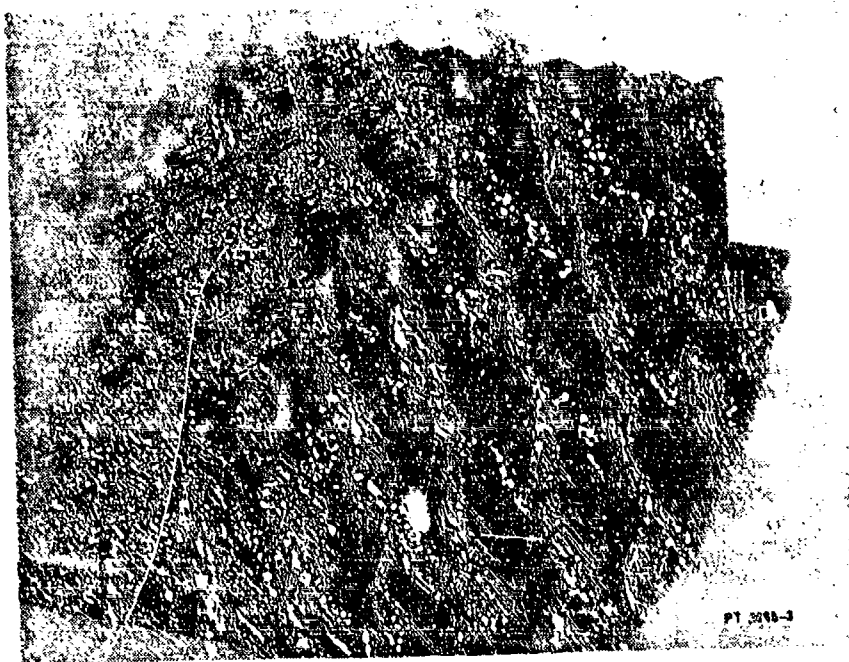


Figure 7. HPT Array

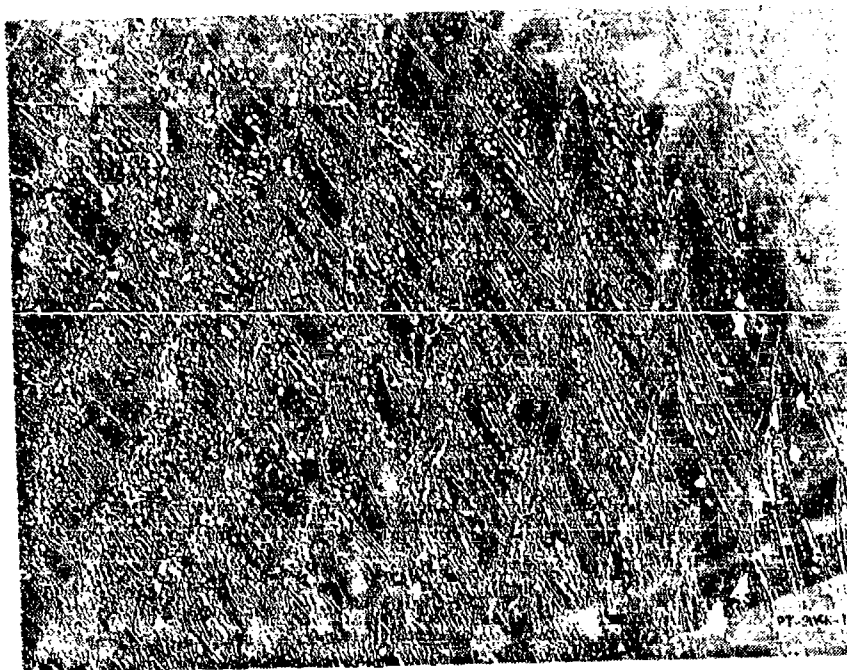


Figure 8. 8 x 8 FPS Array

at 12 GHz. Figure 14 shows the E-plane half-power beamwidths for elements 71, 72, 73, 74 and 120. The H-plane half-power beamwidths are shown in Figure 15. The E- and H-plane beamwidths of the HPT subarray-element patterns vary more widely than the HPS subarray-element beamwidths due to interaction between the overlapping elements.

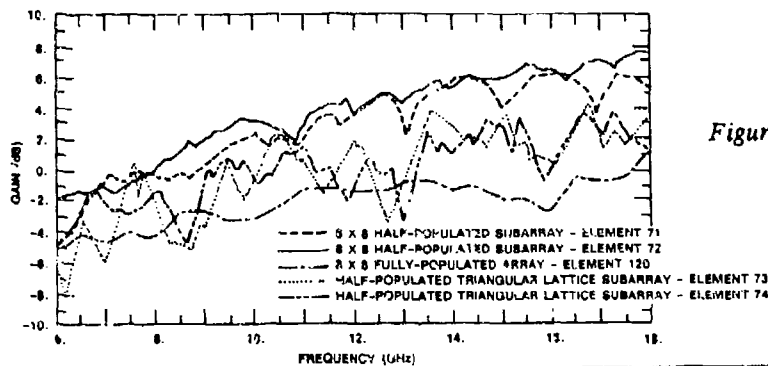
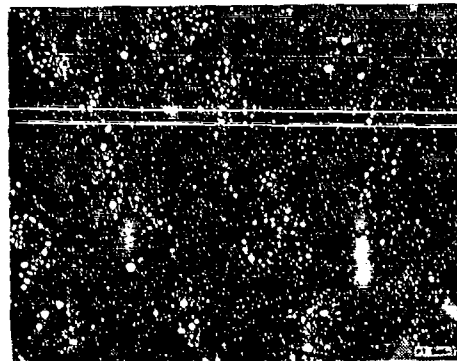


Figure 9. Array-Element Gain

Figure 10. Close-Up View of Overlapping Orthogonal Subarray-Element Pairs in the HPT Array



The active VSWR with scan was calculated for central array-elements 71, 72, 57, 58, 121, and 120 using mutual coupling data measured from the respective arrays. The mutual coupling measurements are made from element to element while all other array-elements are terminated in 50 ohms. This corresponds to free excitation (method) of the radiating elements [27]. The mutual coupling from three element orientations in the three arrays is shown in Figures 16, 17, and 18. These transmission plots show coupling in the adjacent E-Plane and H-Plane of a central array-element. Figure 16 shows the E-Plane coupling of element 71 to element 57, 58 to 76, and 121 to 106. Figure 17 shows the H-Plane coupling of elements 71 to 53, 58 to 44, and 121 to 104. The coupling in the HPT array is higher in both the E-Plane and H-Plane. The coupling in the H-Plane is higher than the coupling in the E-Plane similar to that of two half-wavelength dipoles. The orthogonal array-element coupling data is shown in Figure 18 for

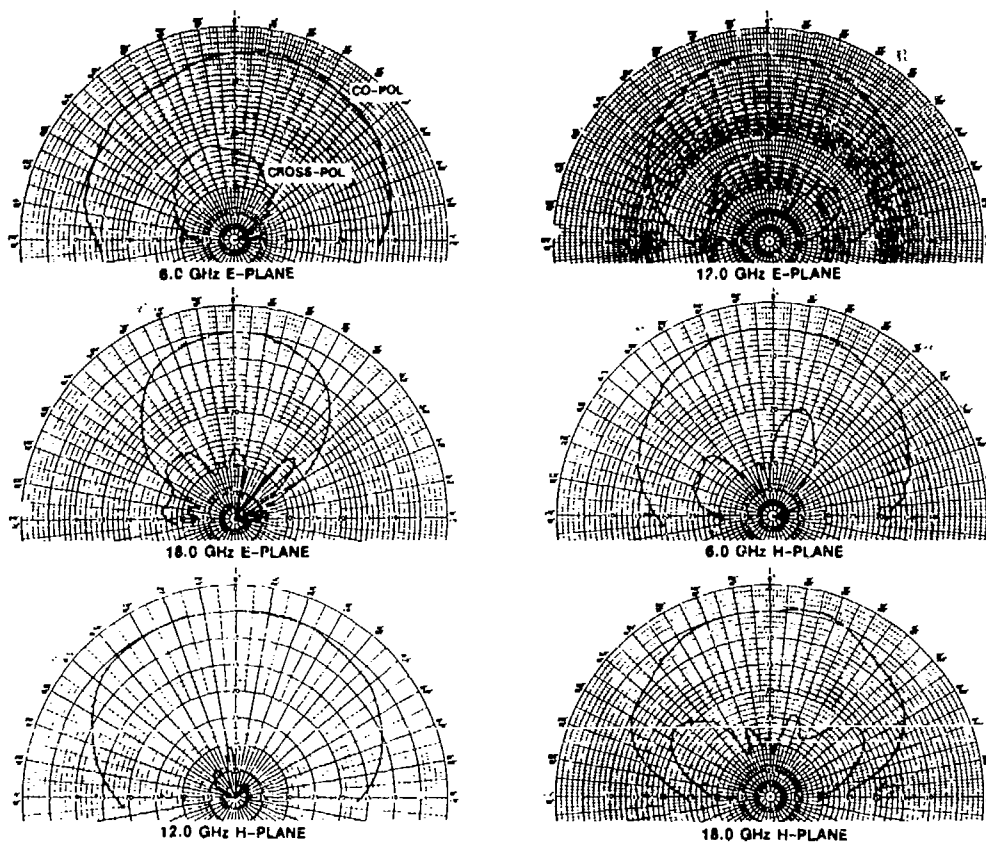


Figure 11. 8 x 8 HPS Subarray-Element 71 Patterns

elements 71 to 72, 58 to 57, and 121 to 120. The orthogonal coupling in the HPT array is greater at the lower frequencies than the HPS array. Active VSWR is the VSWR of the element in the active array environment. For an infinite array this would be the active VSWR presented to the T/R modules by all the array-elements. The transmission data, along with the return loss of central array-element, was used to calculate the active VSWR as the aperture is mathematically activated and scanned over all radiating half-space. The active VSWR with scan is plotted in sine theta space from 6 to 18 GHz in 0.125-GHz steps over all radiating half-space. The data points are taken in approximately 3-degree increments for a total of 1961 points per plot. The active VSWR with scan for array-elements 72, 57, and 120 at 7, 12, and 18 GHz is shown in color density plots in Figures 19, 20, and 21 with 30-, 45-, 60-, and 70-degree scan volume rings superimposed. The active VSWR at boresight is shown in Figure 22. The average active VSWR at boresight in all arrays from 6 to 18 GHz is below 2.0. The maximum

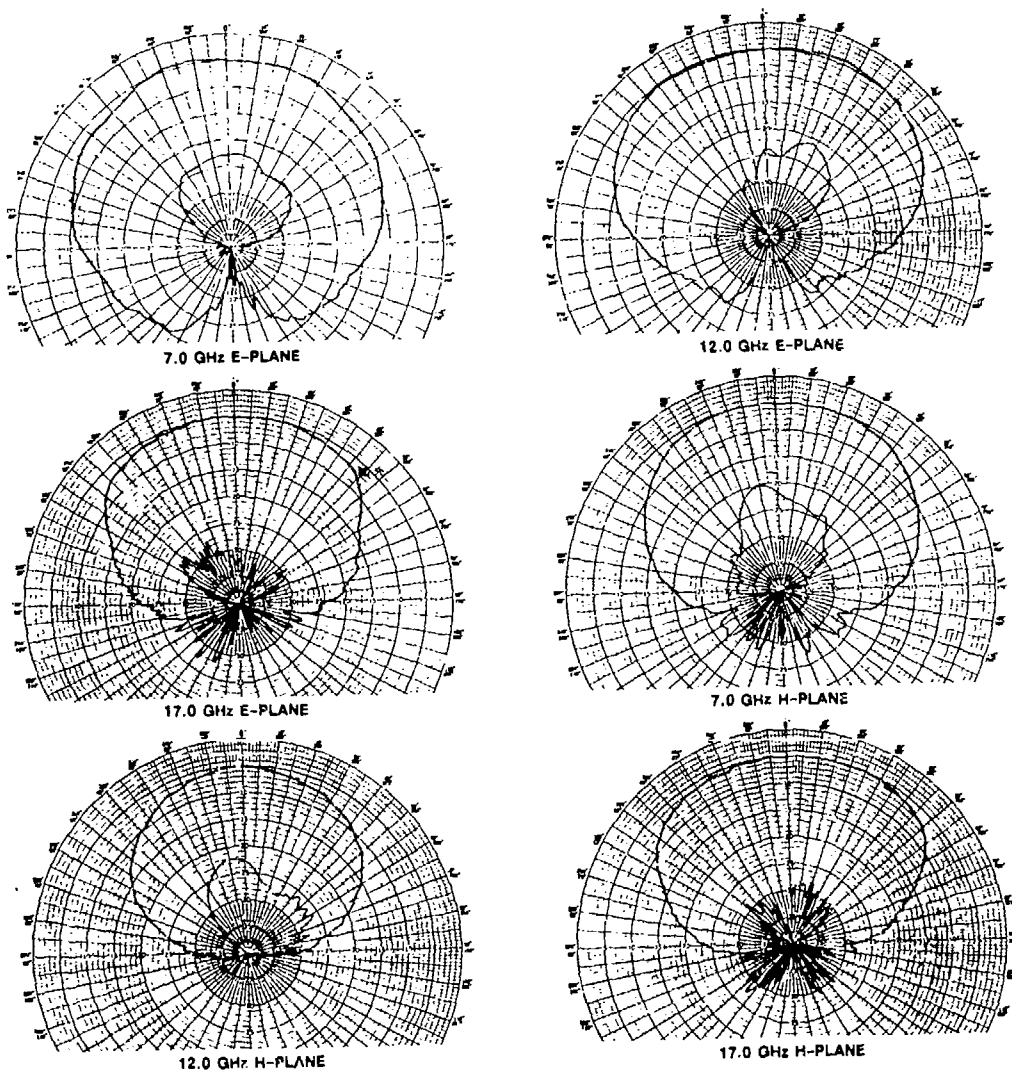


Figure 12. 8 x 8 FPS Array-Element 120 Patterns

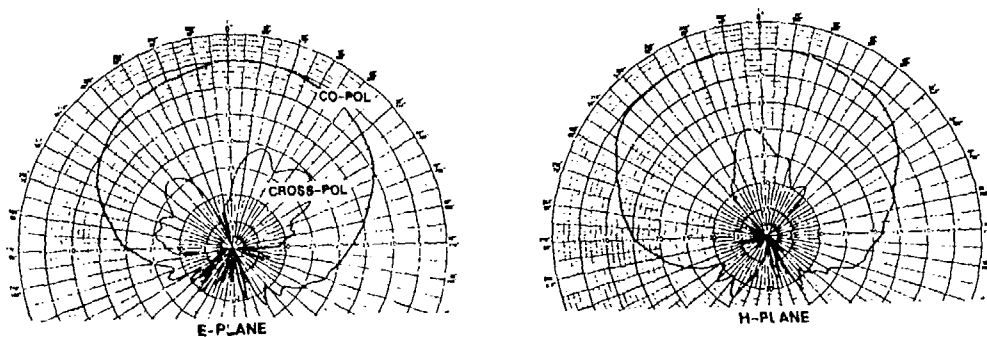


Figure 13. HPT Subarray-Element Patterns at 12 GHz

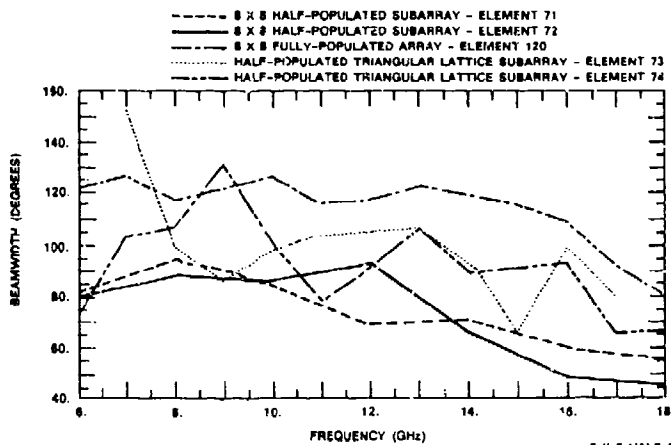


Figure 14. Array-Element
E-Plane Beamwidths

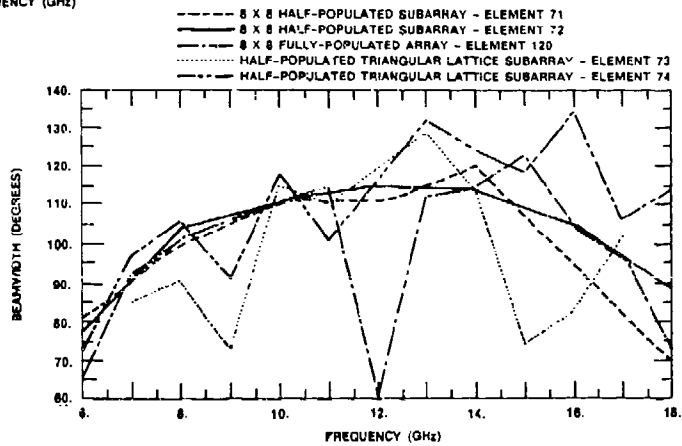


Figure 15. Array-Element
H-Plane Beamwidths

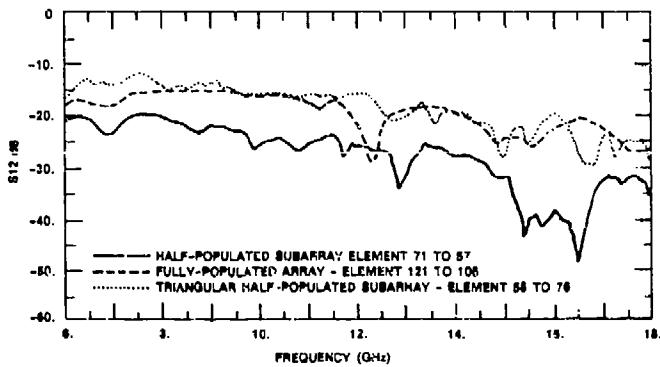


Figure 16. E-Plane Adjacent
Array-Element Coupling

number of occurrences for any value of active VSWR from 6 to 18 GHz for a 70 scan volume is shown in Figure 23. The mean, medium, and standard deviation for 71 are 1.94, 1.74, 0.91; for 57 are 2.27, 1.91, 1.27; and for 120 are 2.05, 1.82, 0.87. The HPT array has a larger occurrence of high active VSWR than the other two arrays.

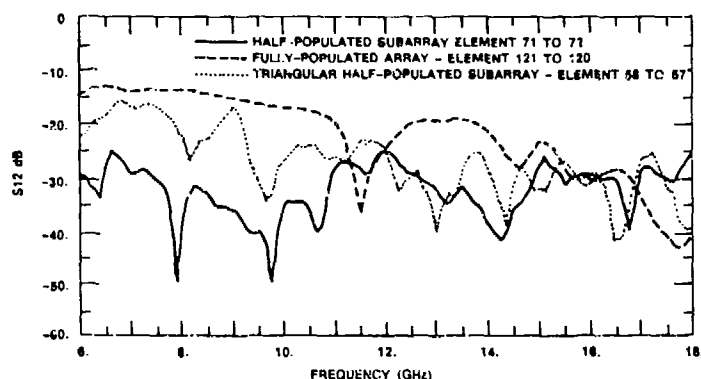


Figure 17. H-Plane Adjacent Array-Element Coupling

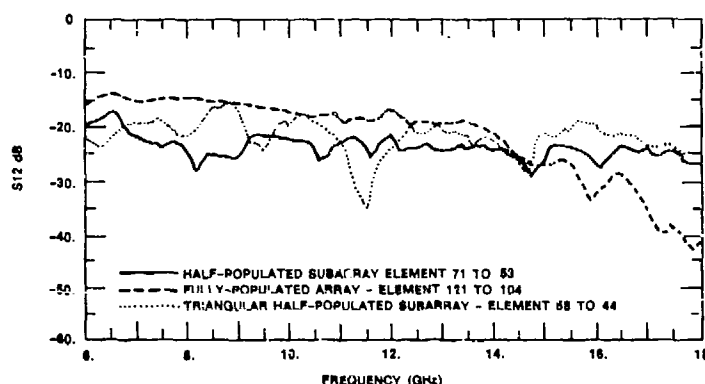


Figure 18. Orthogonal Array-Element Coupling

The stripline flared slot has been shown to be useful as an array element when increased bandwidth is a requirement. The 8 x 8 HPS and FPS arrays are applicable to multifunction multioctave phased array, with reduced grating lobe restrictions and dual polarization requirements. For the dual polarized arrays, the 8 x 8 HPS array yields better array-element performance. The 8 x 8 FPS aperture has tighter coupling and lower active VSWR with scan. Interelement absorber loads provide for array-element optimization of performance.

5.0 CONFORMAL MICROSTRIP FLARED SLOT DESIGN AND PERFORMANCE

A flare design can be used along with a microstrip-to-slotline transition design to construct a conformal printed circuit flared slot antenna element [1,28]. Microstrip and crossed slot antennas with limited bandwidth have been extensively discussed in the literature [29,30]. A new conformal wideband crossed microstrip flared slot, shown in Figure 24, having a greater than three-to-one bandwidth, will be discussed. The origins

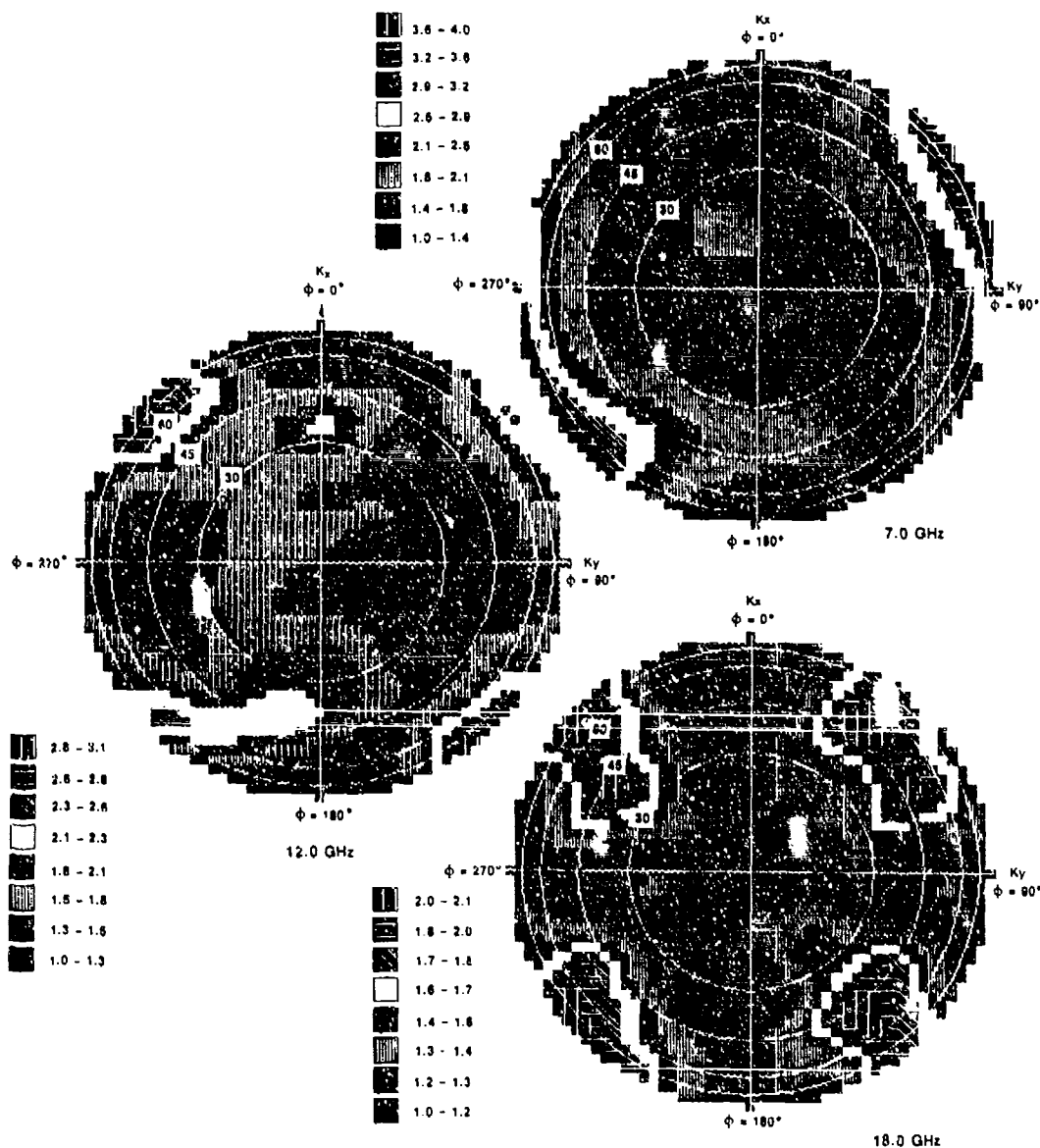


Figure 19. Active VSWR with Scan Subarray-Element 72 in HPS Array

of a conformal traveling wave flared slot antenna can be found in the literature for flush mounted broadband antennas [31,32]. In this design the standard half-wavelength resonant slot is flared at both ends towards the center where they meet (dual flared slot), or it can be foreshortened to half of this slot. This type of conformal flared slot evolved from a half-wavelength resonant slot design (or stepped slot design) and the general flared slotline approach to impedance matching.

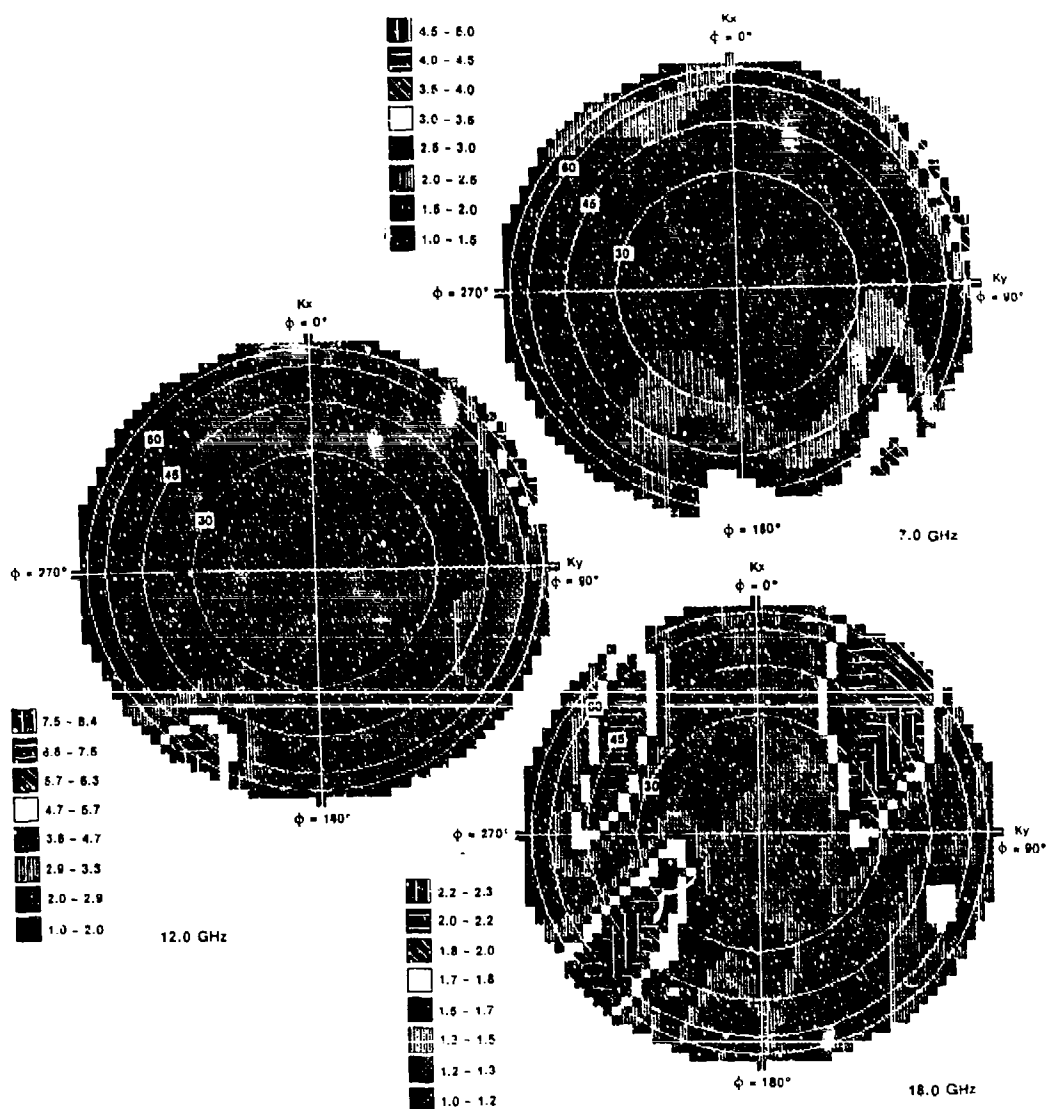


Figure 20. Active VSWR with Scan Array-Element 120 in FPS Array

The aperture element was built on high loss copper clad G10 glass substrate. A crossed flared slot is etched on one side of the copper clad dielectric, and two or four 50-ohm microstrip lines are etched on the opposite side of the printed circuit board. The two orthogonal flared slots can be driven 0 degrees and 90 degrees, or two more 50-ohm lines can be added to create a four-point feed (0, 90, 0, and 90 degrees) for maximizing the radiation efficiency as shown in Figure 24 [33]. The two orthogonal slots, both being a resonant freespace half-wavelength long at 8.85 GHz, are combined at their centers

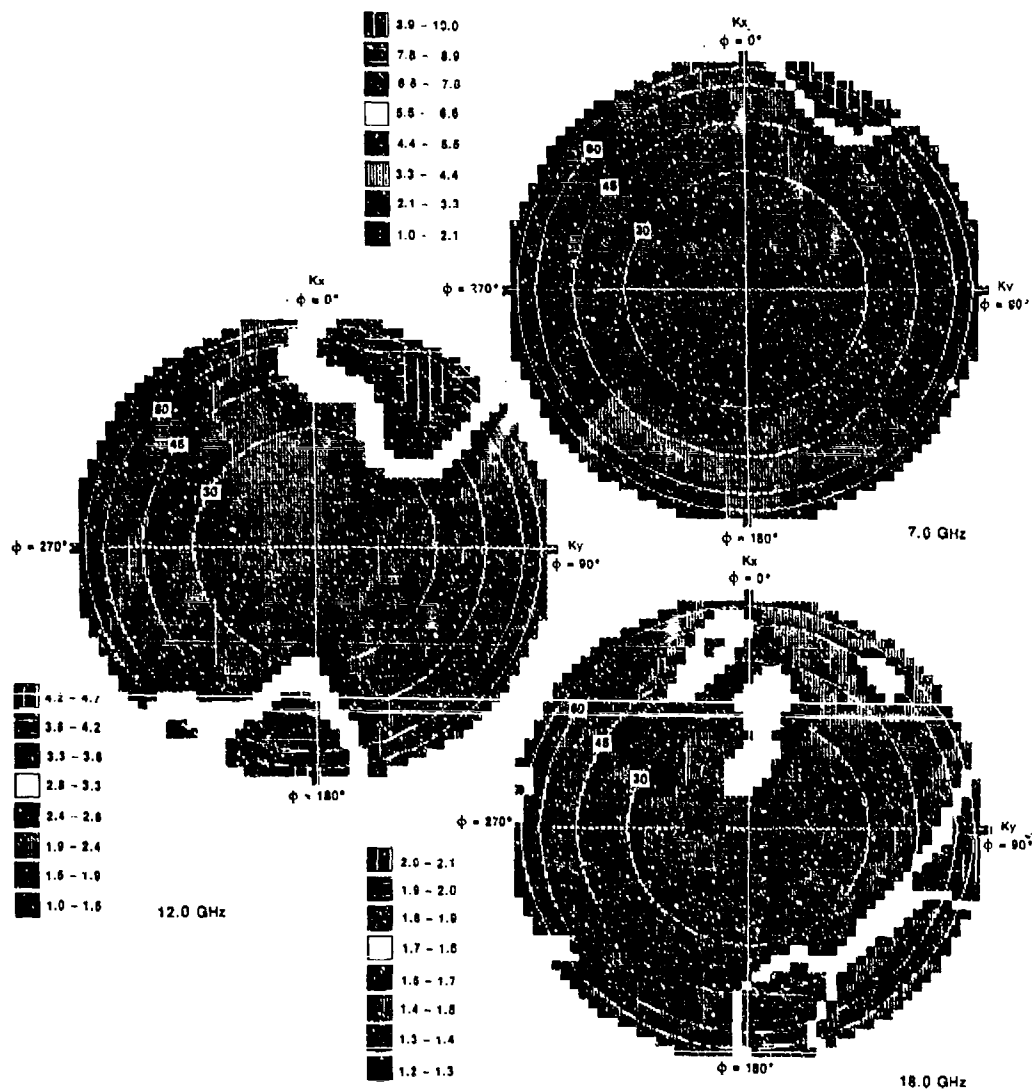


Figure 21. Active VSWR with Scan Subarray-Element 57 in HPT Array

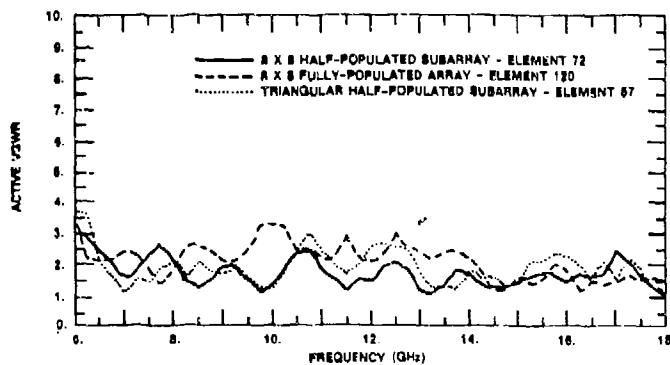


Figure 22. Active VSWR at Boresight

where a current null exists. The two flared slots are also a freespace wavelength long at 17.7 GHz. A two-octave-plus bandwidth in the slotline coupling response is achieved by use of a microstrip line terminated in a radial stub fed across a slotline open circuit. In order to obtain unidirectional radiation, a reflecting ground plane is placed on the side of the dielectric substrate parallel to the flared slot surface. To cover a broader range of frequencies, the element was formed into a cavity type resonator by use of standard design techniques [34] (Figure 25).

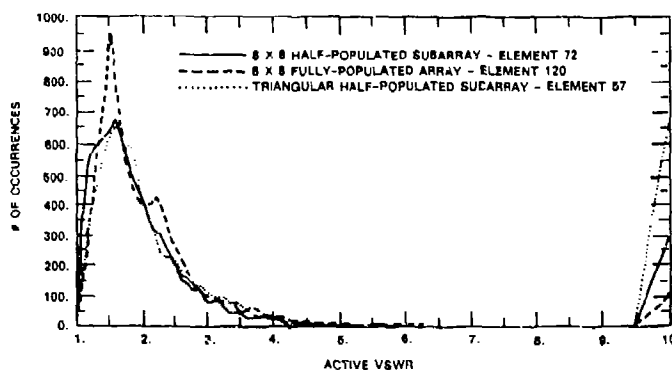


Figure 23. Number of VSWR Occurrences in a 70° Scan Volume

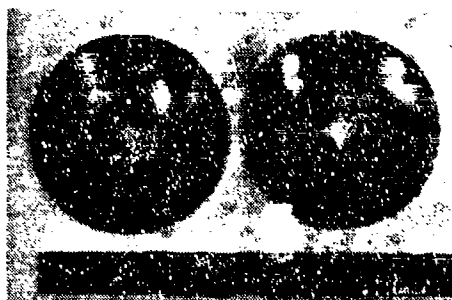


Figure 24. Conformal Crossed Microstrip Flared Slot with Four-Point Feed

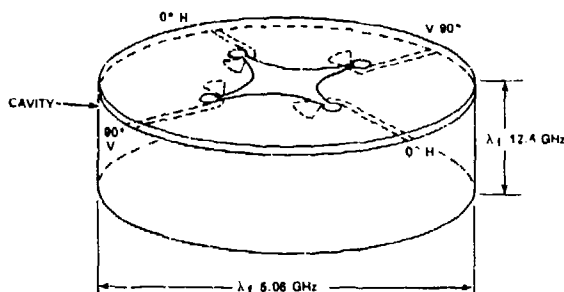


Figure 25. Geometry of Conformal Dual Polarized Microstrip Flared Slot and Cavity

The measured impedance of this element in both its unidirectional and bidirectional configurations has a well-matched wideband response. Figure 26 shows the return loss of the cavity backed element from 4.5 to 18.0 GHz. The low frequency limit in element match has been found to be the point at which the flared slot's maximum width is equal to a half-wavelength in the dielectric. In this element design, the horizontal or vertical slot flare opens into the bisecting slot. This gives the slot a flare width equal to the bisected slot's length. The width and length of both crossed slots shown in Figure 25 is 0.667 inch, corresponding to a low frequency limit of 4.17 GHz.

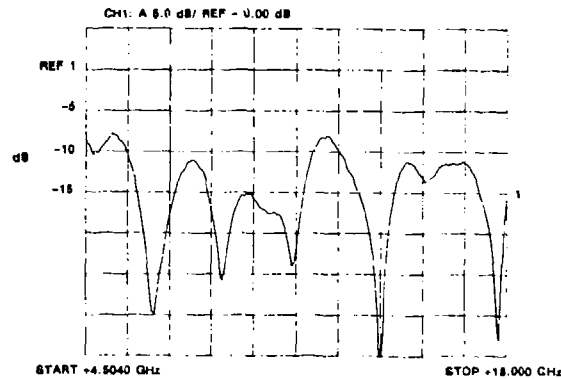


Figure 26. Return Loss of Cavity-Backed Crossed Microstrip Flared Slot

The measured results of the vertical and horizontal radiation patterns show a fairly well-behaved response for the cavity-backed element from 2.0 to 18.0 GHz. Radiation patterns were measured feeding one element port and driving two element ports in the four-point feed element shown in Figure 25. The H-plane radiation patterns are shown in Figure 27 at 2.1, 3.5, 4.0, 6.0, 14.0, and 18.0 GHz feeding one port. These patterns are approximately symmetric, but as frequency is increased to 14.0 GHz, the slot becomes longer than a half-wavelength and a skew in the pattern becomes visible. Observing the patterns as the frequency is increased to 18.0 GHz, the skew becomes less noticeable. This imbalance was believed to be caused by the traveling wave characteristics of the slot. When the H-plane pattern at 14.0 GHz was remeasured feeding the element at two points (H:0, 0), the skew in the previous pattern was reduced as shown in Figure 28. The E-plane patterns at 2.0, 3.5, 4.0, 6.0, 12.0, and 18.0 GHz are shown in Figure 29. The E-plane response from 14.0 to 18.0 GHz exhibits a ripple that is caused by the interaction between the slot and the finite ground plane [3].

This microstrip planar crossed flared slot shows promise of being extremely useful as a conformal dual polarized wideband antenna element for use in conformal array concepts. There appears to be a compromise between impedance match (as the slot is flared to its length) and cross polarization level. The skew in the H-plane at upper frequencies is caused by a traveling wave due to a slot width greater than $0.4 \lambda_f$ and a length greater than λ_f . This skew was reduced by using a four-point feed design. The flare can be optimized to provide maximum match with minimum cross polarization levels.

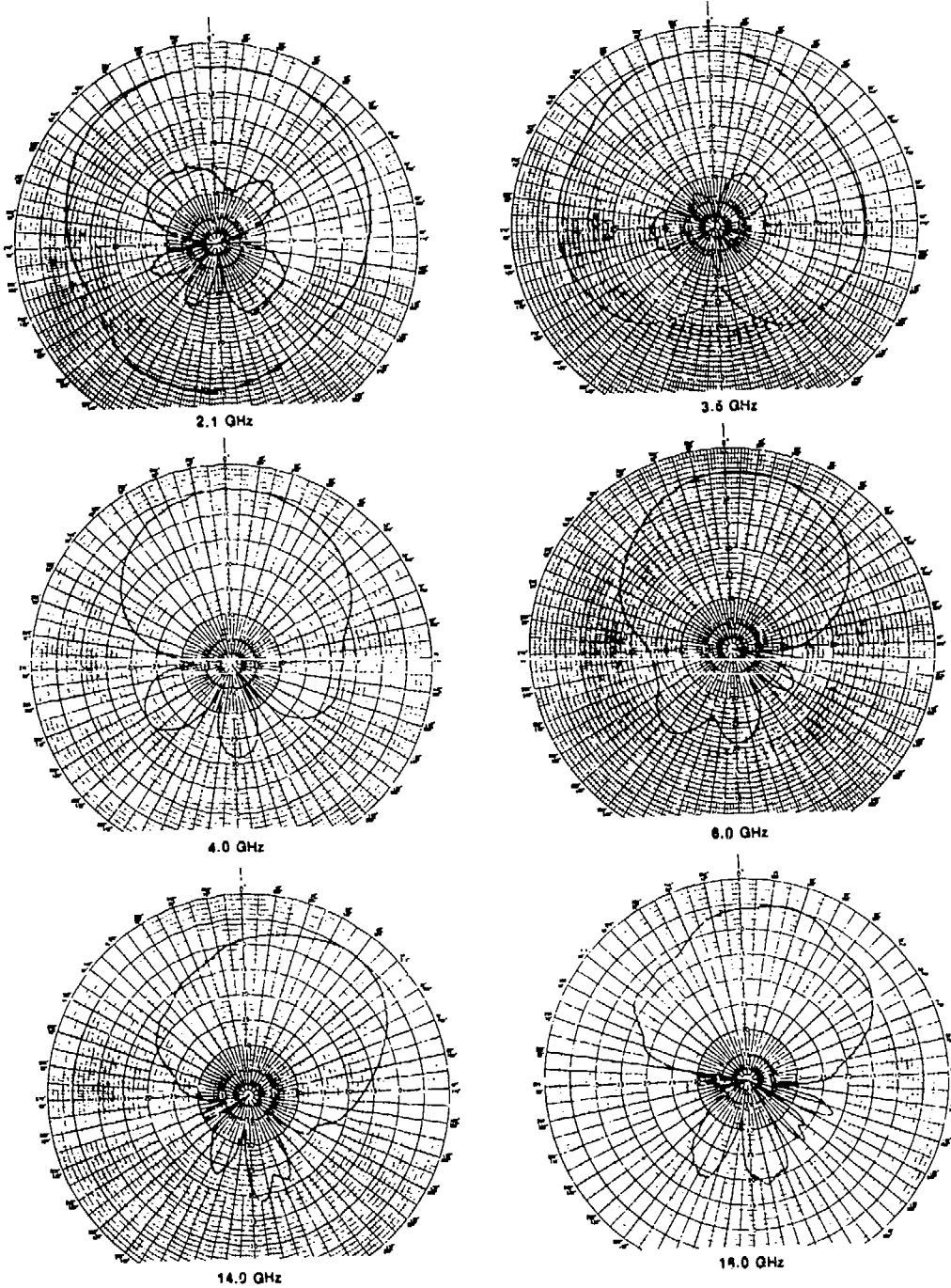


Figure 27. H-Plane Patterns of Cavity-Backed Crossed Flared Slot

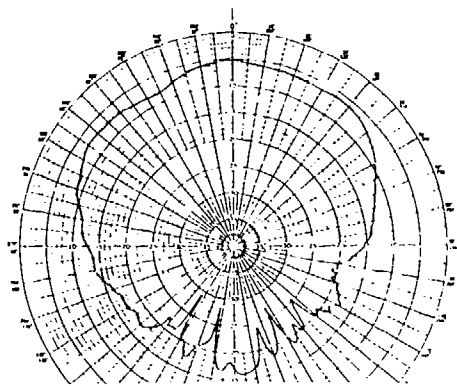


Figure 28. Cavity-Backed Crossed Flared Slot H-Plane Pattern at 14 GHz (Both Ends of Linearly-Polarized Slot Fed $0^\circ, 0^\circ$)

6.0 FINAL CONCLUSION

Printed circuit flared slots, both conformal and endfire, are becoming more useful for phased arrays requiring reduced grating lobes and multioctave frequency coverage with dual polarization capability. The design history has involved experimental insight and evolving analysis techniques. Future three-dimensional analysis methods are needed to model these complex printed circuit antenna geometries.

REFERENCES

1. Povinelli, M.J. (1987) A Planar Broadband Flared Microstrip Slot Antenna. *IEEE Transactions on Antennas and Propagation*, Vol. AP-35, No. 8, pp. 968-972.
2. Booker, H.G. (1946) "Slot Aerials and Their Relation to Complementary Wire Aerials (Babinet's Principle)". *Journal I.E.E.*, 93, Part IIIA p. 620.
3. Kraus, J.D. *Antennas*, McGraw-Hill, New York, pp. 760-762.
4. Cary, R.H. Jr. (1952) The Slot Aerial and Its Application to Aircraft. *Proceedings IEE (London)*, Part. III, Vol. 99, pp. 187-196.
5. Johnson, W.A. (1955) The Notch Aerial and Some Applications to Aircraft Radio Installations. *Proc. IEE (London)*, Part B, Vol. 102, pp. 211-218.

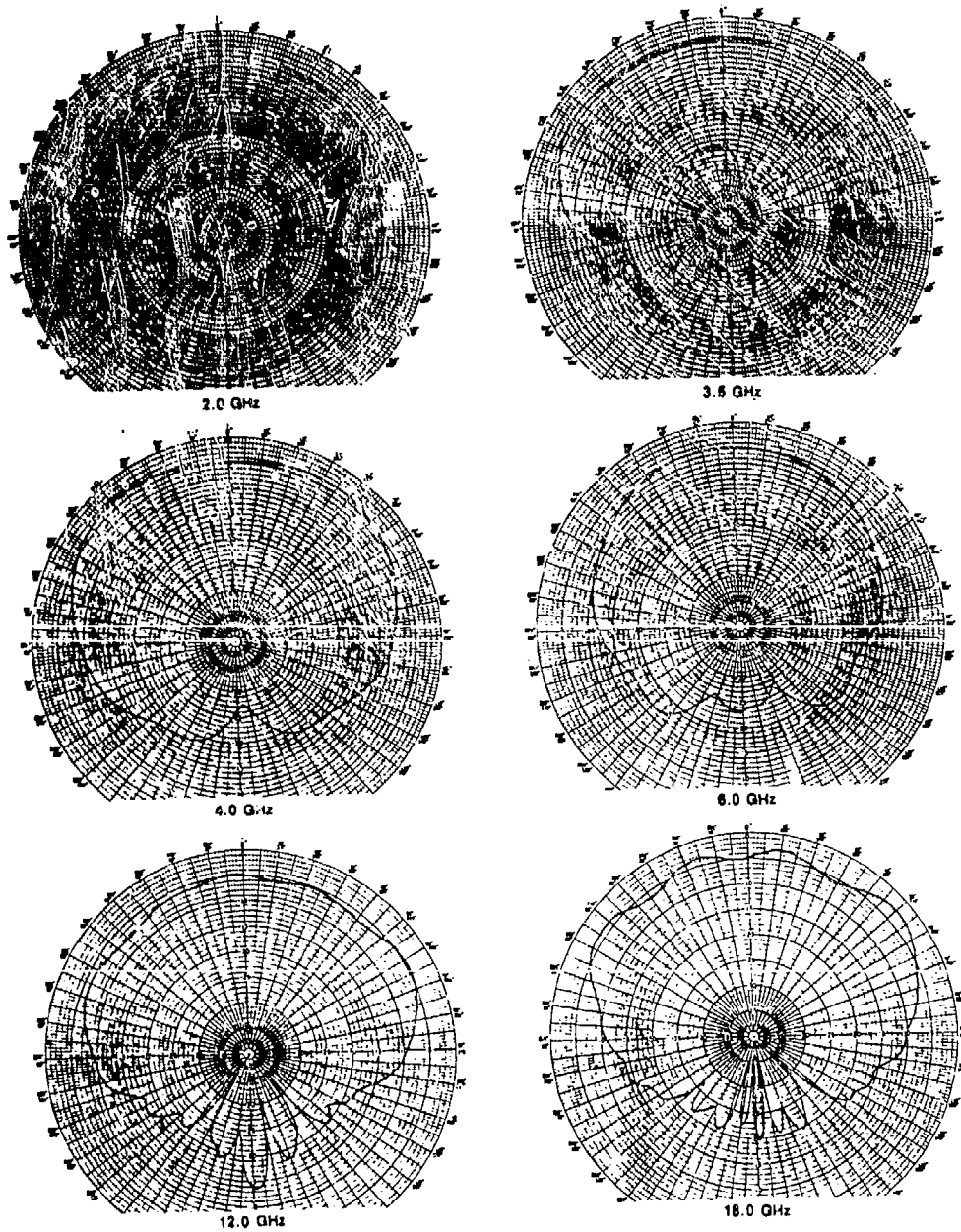


Figure 29. E-Plane Patterns of Cavity-Backed Crossed Flared Slot

6. Cohn, S.B. (1969) Slot Line On A Dielectric Substrate. *IEEE Transactions on Microwave Theory and Techniques*, Vol. MMT-17, pp. 768-778.
7. Reuss, M.L. Jr. (1974) A Cursory Investigation of a Slotline Radiator. *NRL Memorandum Rept. 2796*.
8. Carr, J.W. (1963) V-strip antenna with artificial dielectric lens. U.S. Patent 3609836.
9. Kerr, J.L. (1969) A very broadband low silhouette antenna. *Tech. Rep. ECOM-3087*, AD 684915.
10. Sengupta, D.L. and Ferris, J.E. (1971) Rudimentary Horn Antenna. *IEEE Transactions on Antennas and Propagation*, Vol. AP-19, pp. 124-126.
11. Monser, G. J., Hardle, G. S., Ehrhardt, J. R. (1974) Closely Spaced Orthogonal Dipole Array. U.S. patent 3,836,976, September 17, 1974.
12. Lewis, L.R., Fasset M., and Hunt J. (1974) A Broadband Stripline Array Element. *IEEE/AP-S Symposium Program and Digest*, pp. 335-337.
13. Gibson, P.J. (1979) The Vivaldi Aerial in *Proceedings of the 9th European Microwave Conference*, pp. 101-105.
14. Meier, Paul J. (1978) Millimeter Integrated Circuits Suspended in the E-Plane of Rectangular Waveguide. *IEEE*, Vol. MTT-26, No. 10, pp 726-733.
15. Wheeler, Harold A. (1965) Transmission-line properties of parallel strips separated by a dielectric sheet. *T-MTT v13 n2*, pp. 172-185.
16. Cohn, Seymour B. (1954) Characteristic impedance of the shielded-strip transmission line. *T-MTT f2 n2*, pp. 52-57.
17. Robinson, G.H. and Allen, J.L. (1969) Slotline Application to Miniature Ferite Devices. *IEEE Transactions on Microwave Theory and Techniques*, Vol. MTT-17, pp. 1097-1101.

18. de Ronde, F.C. (1970) A new class of microstrip directional couplers. *Digest Tech. Papers*, 6-MTT Symp., pp. 184-189.
19. Janaswamy, R. and Schaubert, D.H. (1986) Characteristic Impedance of a Wide Slot Line on Low Permittivity Substrates. *IEEE Transactions on Microwave Theory and Techniques*, Vol. MTT-34, pp. 900-902.
20. Yngvesson, K.S., Schaubert, D.H., Korzeniowski, T.L., Kollberg, E.L., Thungren, T., and Johansson, J.F. (1985) Endfire Tapered Slot Antennas on Dielectric Substrates. *IEEE Transactions on Antennas and Propagation*, Vol. AP-33, pp. 1392-1400.
21. Lewis, L.R., Pozgay, J.H., Hessel, A. (1975) Design and Analysis of Broadband Notch Antennas and Arrays. *IEEE/AP-S Symposium Program Digest*, pp. 44-47.
22. Janaswamy, R. and Schaubert, D.H. (1986) Analysis of the Tapered Slot Antenna. *IEEE AP-S Symposium Digest*, Vol. 2, Philadelphia, PA, pp. 689-692.
23. D'Angelo, J., Povinelli, M. J., Palmo, M. (1988) Hybrid Finite Element/Boundary Element Analysis of a Stripline Notch Array. *IEEE AP-S, Symposium Digest*, Vol. 3, pp. 1126-1129.
24. Pepe, C.D., Povinelli M.J., and Komiak, J.J. (1987) Wideband Active Phased Array. *1987 Antenna Applications Symposium*, Allerton Park, University of Illinois, pp. 1-24.
25. Prasad, S.N. and Mahapatra, S. (1979) A Novel MIC Slot Line Aerial. *Proceedings of the 9th European Microwave Conference*, Brighton, UK, pp. 120-124.
26. Povinelli, M.J. and Johnson, J. (1988) Design and Performance of Wideband Dual Polarized Stripline Notch Arrays. *1988 IEEE AP-S International Symposium Digest*, Vol. 1, pp. 200-203.
27. Debskin, T. R. and Hannan, P. W. (1965) Complex Mutual Coupling Measured in a Large Phased Array Antenna. *The Microwave Journal*, pp. 93-96.

28. Povinelli, M.J. (1988) Further Characteristics of a Planar Wideband Microstrip Flared Slot Antenna. *1988 IEEE AP-S International Symposium Digest*, Vol. 2, pp. 712-715.
29. Oliver, A.A. (1954) The Radiation Conductance of a Series Slot in Strip Transmission Line. *IRE Nat. Conv. Rec.*, Vol 2, Part 8, pp. 89-90.
30. C. A. Lindberg (1969) A shallow-cavity UHF crossed-slot antenna. *IEEE Transactions on Antennas and Propagation*, Vol. AP-17, pp. 558-563.
31. Stevenson, B.T., and Walter, C.H. (1955) Endfire slot antennas. *IEEE Transactions on Antennas and Propagation*, Vol. AP-3, pp. 81-86.
32. Eberle, J.W., Levis, C.A., and McCoy, D. (1960) The flared slot: A moderately directive flush-mounted broadband antenna. *IEEE Transactions on Antennas and Propagation*, Vol. AP, pp. 461-468.
33. H. H. Chung, Wong Foy, S.Y. Peng (1987) MSAT-X Phased Array Crossed-Slot Element Design. *IEEE AP-S Digest* Vol. 1, pp. 356-358.
34. Jasik, J., (1984) *Antenna Engineering Handbook*, 2nd ed.. McGraw-Hill, New York, pp. 14-17.

POWER HANDLING PRINTED SUB-ARRAY
FOR WIDE BANDWIDTH SCANNING
ANTENNA ARRAY

Patrick PONS -- Laurent MAURY -- Serge DUTHEIL
MICROWAVE DEPARTMENT
ELECTRONIQUE SERGE DASSAULT
SAINT-CLOUD (FRANCE)

NE.334.319

July, 20th, 1988

A B S T R A C T

POWER HANDLING PRINTED SUB-ARRAY FOR WIDE BANDWIDTH SCANNING ANTENNA ARRAY

This paper presents the pattern and gain characteristics of a printed sub-array radiating element over a 4 to 1 frequency band.

We present the power handling capabilities (130 W C.W.) and the technological choice for designing this radiating element.

The purpose of this study is to design a vertical polarization radiating element with size limitation compatible with a H-plane scanning array of $\pm 50^\circ$.

The radiating element consists of four stripline notches fed by a corporate power divider structure.

The basic cell of the corporate feed consists of an in-line compensated three port power divider designed in two different technologies :

- stripline with air dielectric substrate,
- stripline with 0.8 mm PTFE dielectric substrate.

Finally we compare the performances of this radiating element to the performance of a H-plane sectoral horn of the same size.

1 - INTRODUCTION

Many small phased array antennas with vertical polarized radiators must be based upon the following considerations :

- The bandwidth is close to two octaves with a VSWR less than 3 : 1.
- The azimuthal size of the element is small enough to have reduced transmit grating lobes with an H-plane scanning of $\pm 50^\circ$.
- The elevation size of the element permits a minimum field of view of 20° (in the E-plane).
- The power handling capability (130 W CW) meets system requirements using mini TWT's.
- The physical construction of the Duroid radiator with aluminium structure is able to withstand environmental conditions (thermal, shock and vibration ...).

2 - DESCRIPTION OF THE MODEL

Figure 1 shows a photograph and a block diagram of the experimental sub-array radiating element.

The radiator consists of four stripline notches using a modified klopfenstein taper on the flared slot.

The printed sub-array fed by a corporate power divider structure is mounted in a mechanical support used as heat sink.

2.1. Corporate feed

The severe volume constraints, imposed by the close element spacing in elevation and the requirements in terms of power handling and bandwidth, have necessitated special care in the design of the power distribution network.

The basic cell of the corporate feed consists of an inline compensated three port power divider.

Figure 2 shows the basic cell in stripline technology with air/dielectric medium. VSWR and S12 (TRANSMISSION COEFFICIENT) are also presented from F_0 to $4 F_0$.

Figure 3 shows the basic cell in stripline technology with 0.8 mm Duroid dielectric substrate.

VSWR and S12 (TRANSMISSION COEFFICIENT) are also presented in the band F_0 to $4 F_0$. Finally we have designed the four way power divider using both technologies ; the input connector and the by-pass connection use coaxial lines with TFE reinforced by boron nitride.

2.2. Radiating element

The basic radiating element of the sub-array is the stripline notch antenna designed by coupling a strip transmission line to two outer conductors, etched on the opposite sides of the 0.8 mm thick boards supporting the notches.

Figure 4 shows the printed sub-array formed by four identical notches printed on a single circuit board and using a modified klopfenstein taper on the flared slot.

With this configuration, the E-plane line array is optimized in VSWR on each radiating element embedded in the array (passive VSWR).

Figure 5 shows the passive VSWR of each element from F_0 to $4 F_0$.

Figure 6 shows the E and H plane co-polarization pattern of center element at $1.3 F_0$; $2.4 F_0$ and $4 F_0$.

2.3. Sub-array results

The assembly of the four printed notches with the corporate feed was manufactured using a common case with by-pass connection in high temperature coaxial line.

Figure 8 gives the VSWR of the sub-array constructed, in the band F_0 to $4 F_0$; it was necessary to match this new radiating element by defining an active compensation of the notches.

Figure 9 shows the temperature raising of the case versus the input power of the sub-array at about $3.3 F_0$ with steps of 25 W CW every 30 mn for an ambient temperature of 25°C .

Figure 10 shows the E and H plane co-polarization pattern of the sub-array at $1.1 F_0$, $2.4 F_0$ and $4 F_0$.

Finally figure 11 gives the gain, and the 3 dB beamwidth of the sub-array at $1.1 F_0$, $2.4 F_0$ and $4 F_0$.

3 - COMPARATIVE RESULTS

We have manufactured an H-plane sectoral horn fed by an in-line adaptor TNC coax. to WRD (3.6 : 1). This partially compensated horn has comparable dimensions. It can be used as a radiating element of an E-plane phased array for a scanning up to $\pm 50^\circ$.

Figure 12 shows the comparative efficiencies of both radiating elements.

4 - CONCLUDING REMARKS

The feasibility of a compact power handling printed sub-array over a two octaves bandwidth has been demonstrated.

We have to experiment this radiating element in an H-plane array.

R E F E R E N C E S

- 1 - PEPE, C.D., POVINELLI, M.J., KOMIAK J.K.
WIDEBAND ACTIVE PHASED ARRAY

Proceedings of the 1987 Antenna Application Symposium Uroana, ILLINOIS.

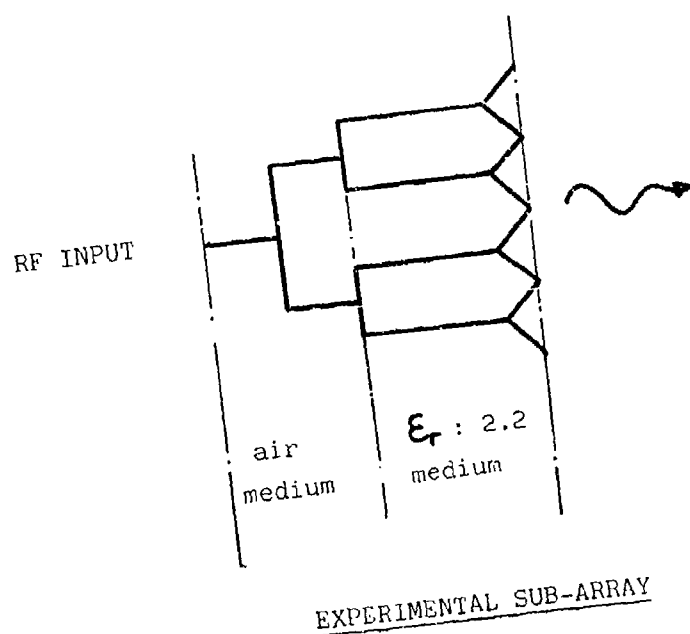
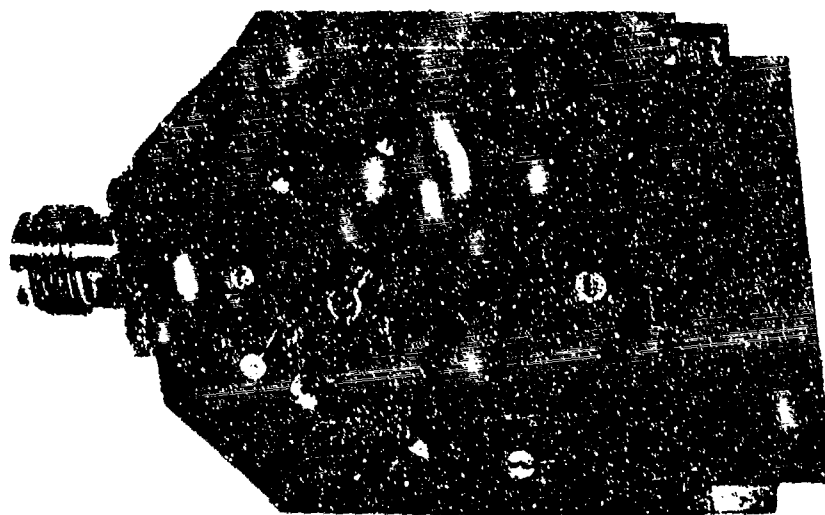
- 2 - MONSER, G.J.
PERFORMANCE CHARACTERISTICS OF NOTCH ARRAY ELEMENTS OVER
A 6/1 FREQUENCY BAND

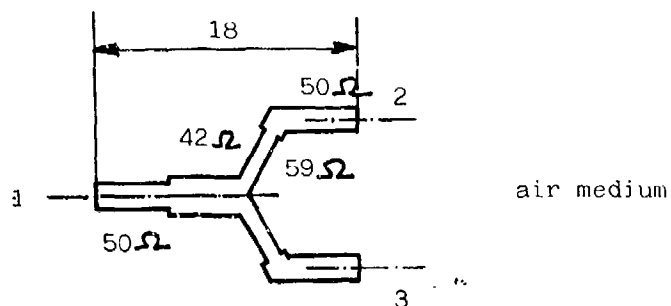
Proceedings of the 1987 Antenna Application Symposium Urbana, ILLINOIS.

- 3 - HOWE, HARLAN Jr (1974)
STRIPLINE CIRCUIT DESIGN

ARTECH HOUSE, DEDHAM, M.A.

Fig. 1





Basic cell of the air power divider

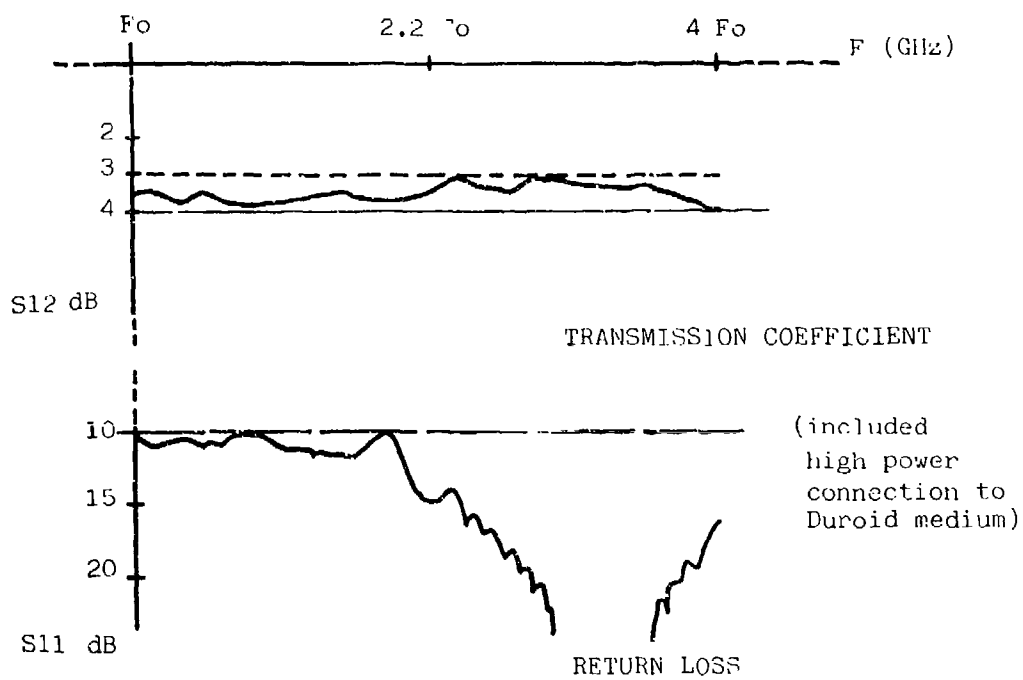
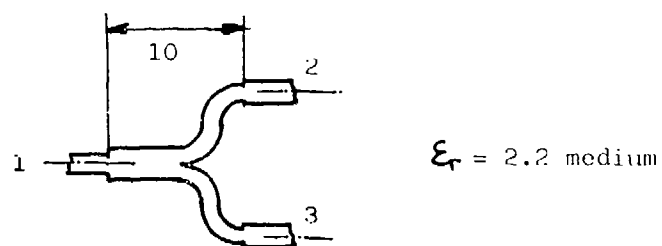
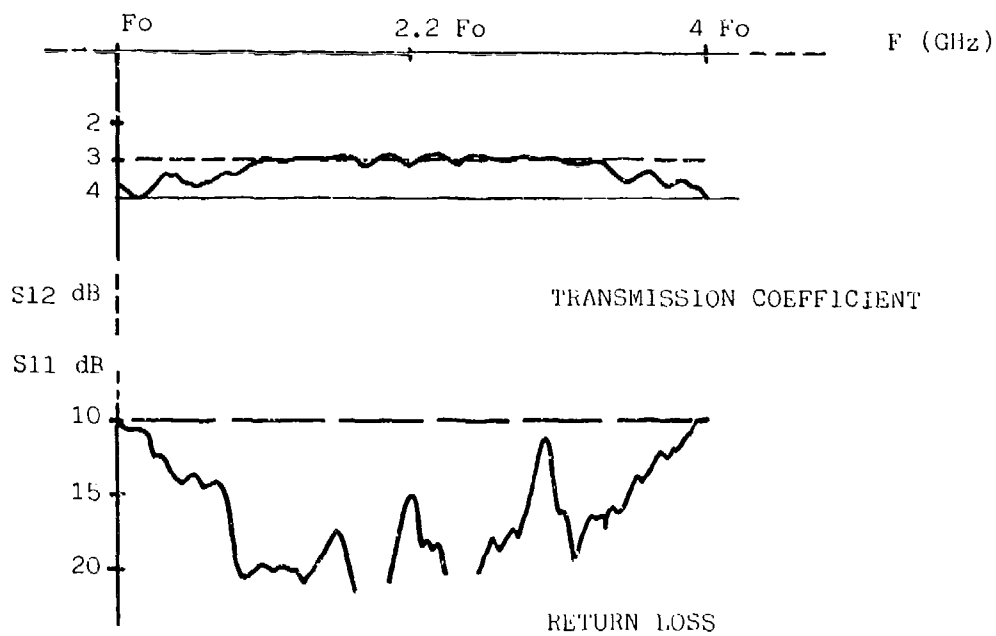
STRIPLINE AIR POWER DIVIDER

Fig. 3

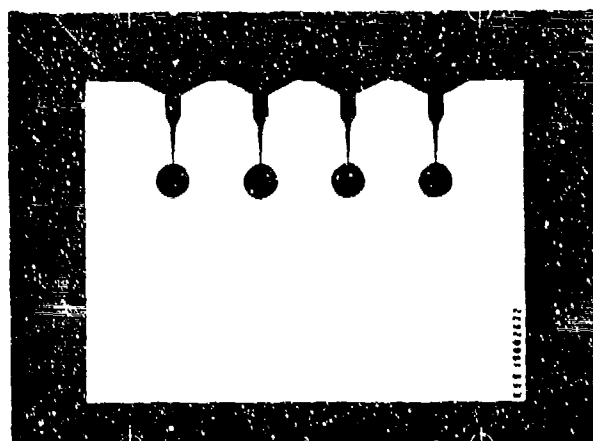


Basic cell of the Duroid power divider

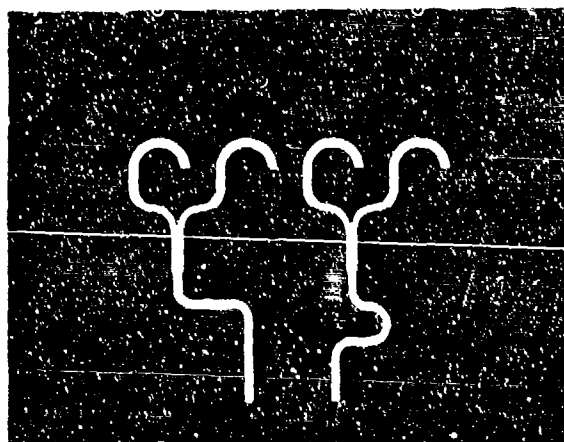


STRIPLINE DUROID POWER DIVIDER

Fig.4



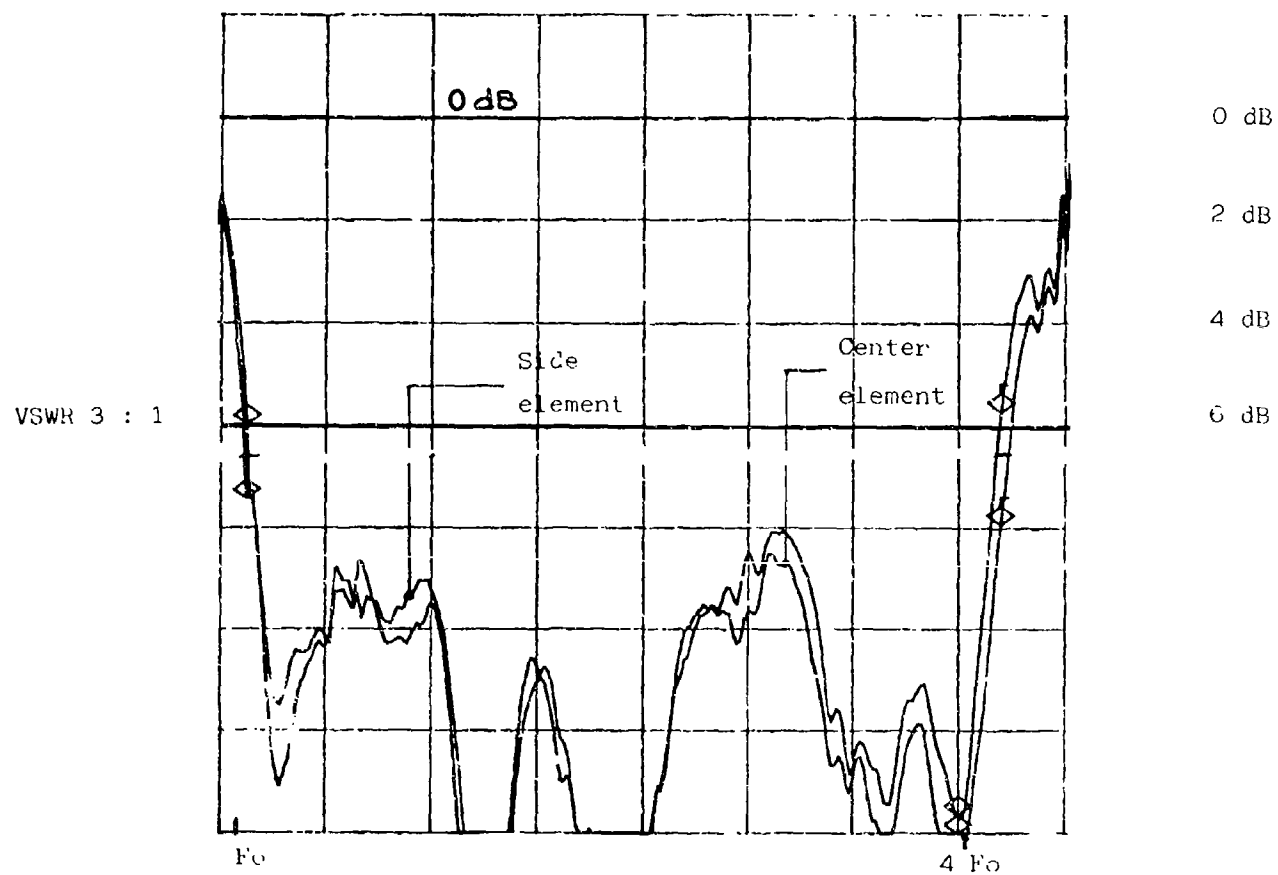
Notches drawn on the
ground plane



Stripline on the other side

PRINTED PART OF THE SUB-ARRAY

Fig. 5

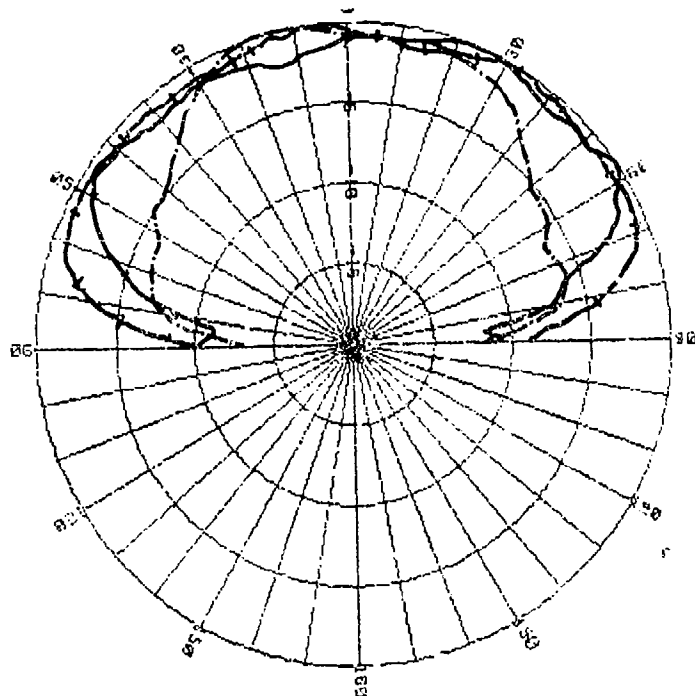
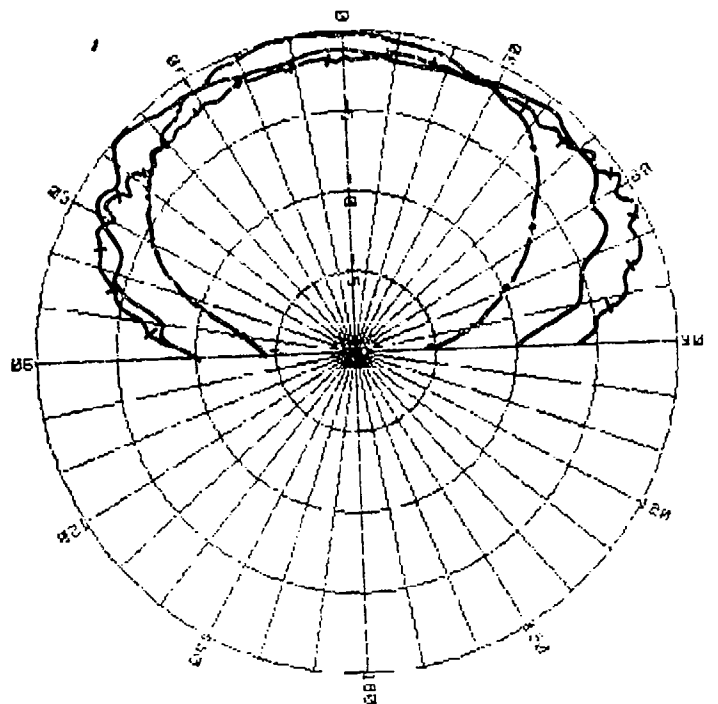


RETURN LOSS OF NOTCH ANTENNA

SCALE : 5 dB/div.

— 1.3 Fo
 —+— 2.4 Fo
 - - - 4 Fo

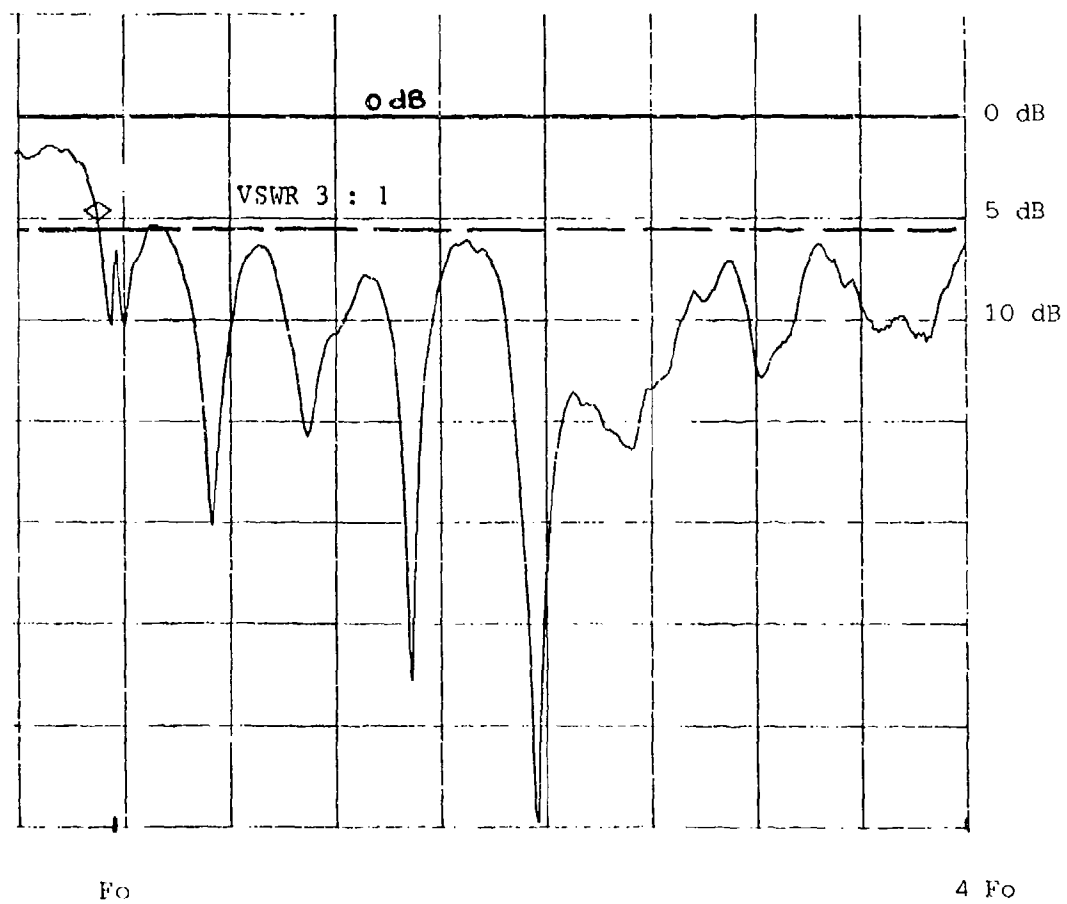
H-Plane



E-Plane

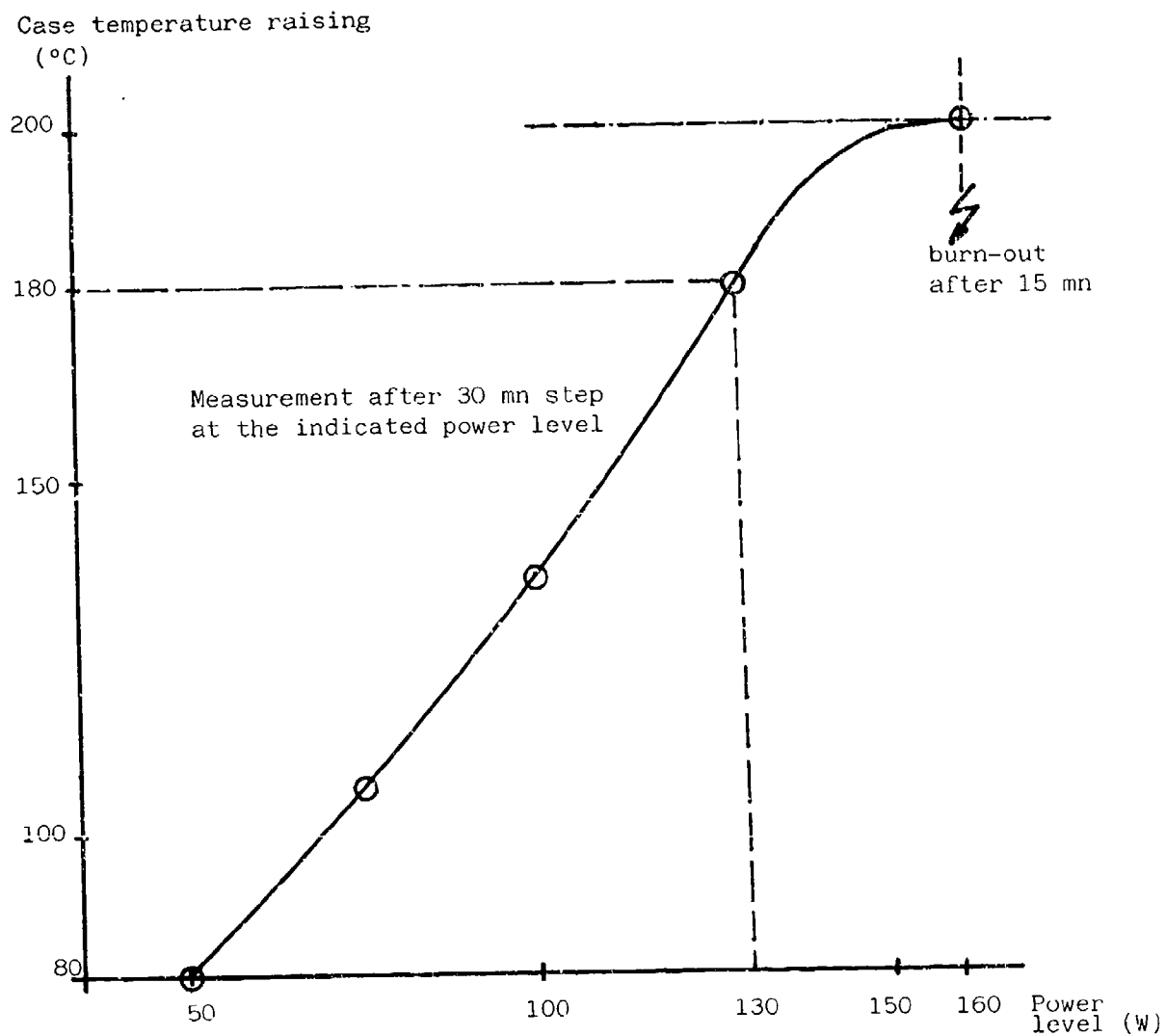
CENTER ELEMENT PATTERNS

Fig. 7



RETURN LOSS OF THE SUB-ARRAY

Fig. 8

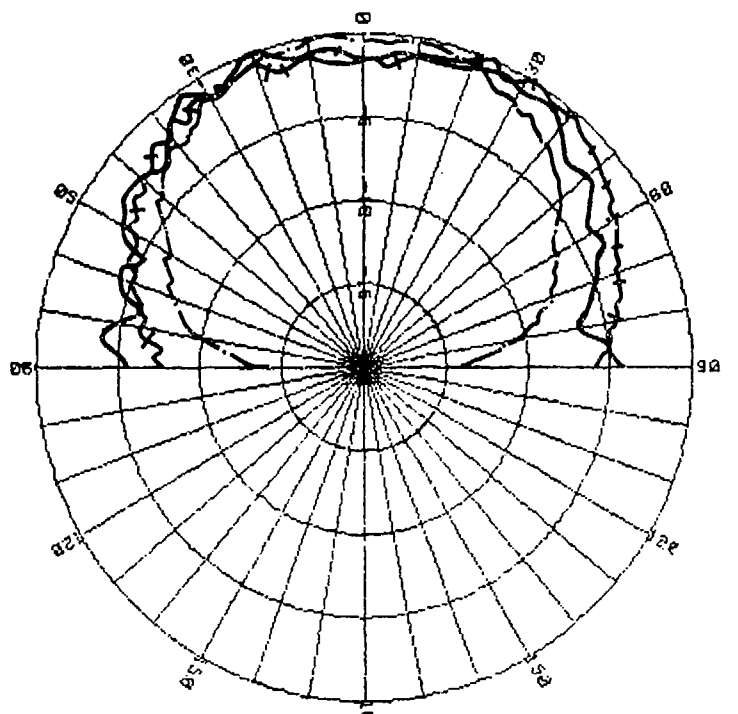


TEMPERATURE RAISING VS POWER LEVEL

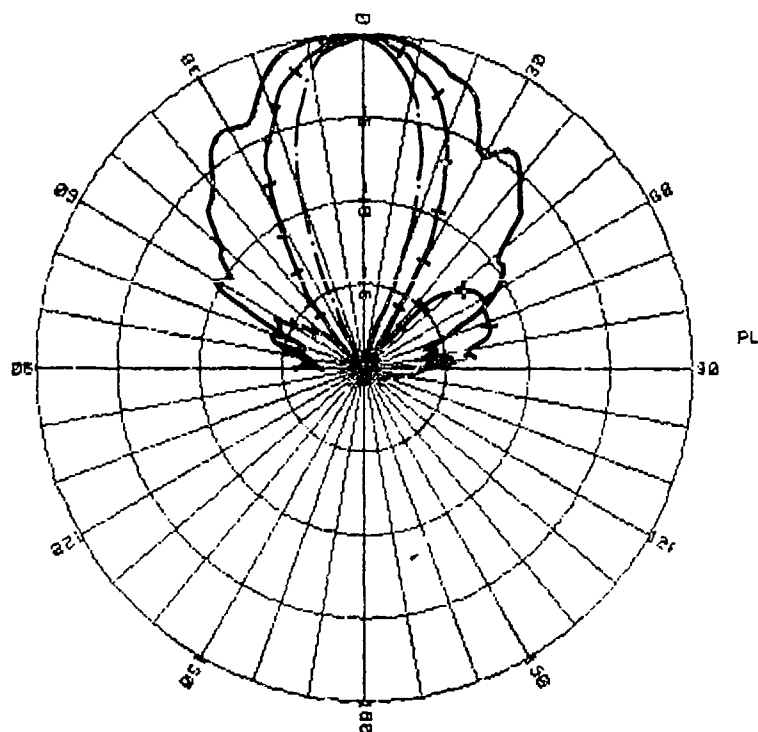
FOR 25° C AMBIENT TEMPERATURE

SCALE : 5 dB/div.

— 1.1 F_0
 + + + 2.4 F_0
 - - - 4 F_0



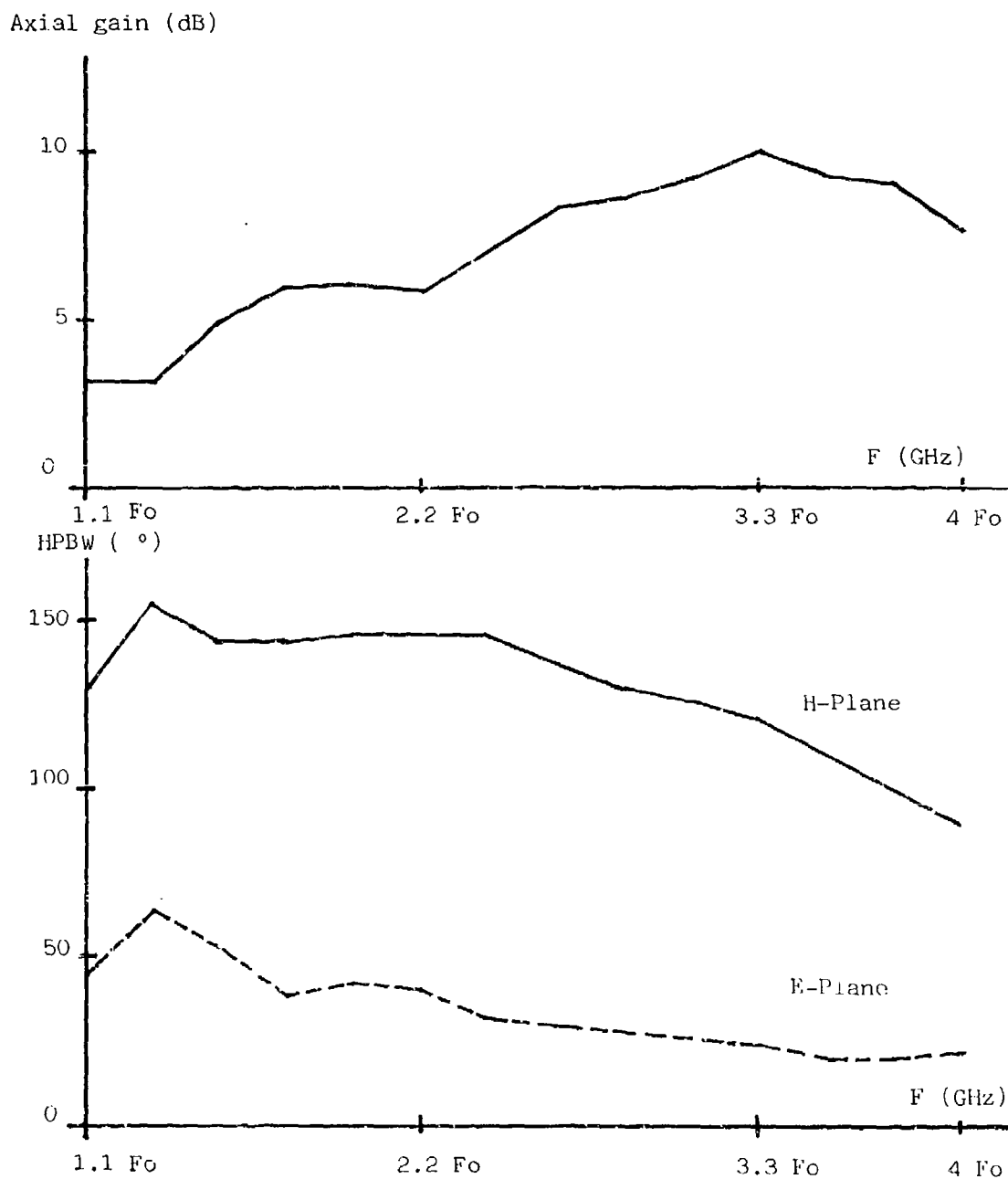
H-Plane



E-Plane

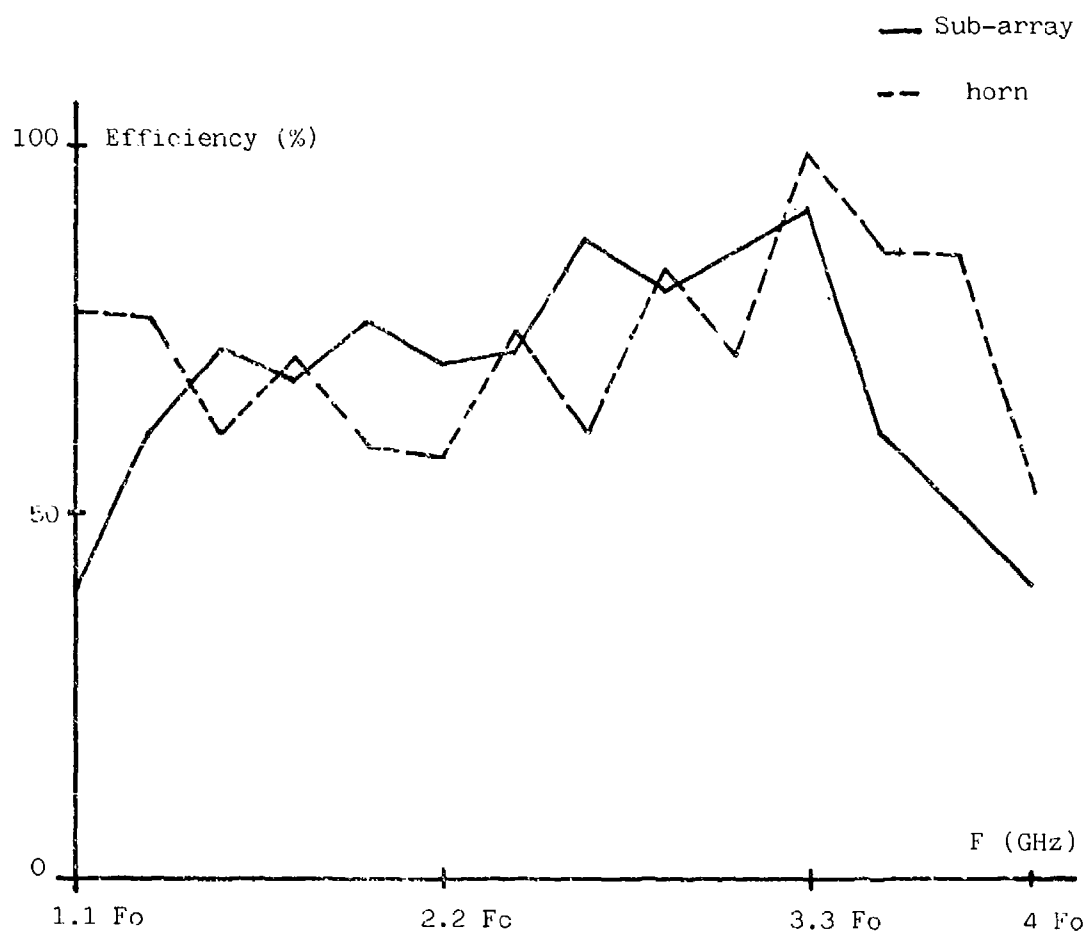
SUB-ARRAY PATTERNS

Fig. 10



PERFORMANCES OF THE SUB-ARRAY

Fig. 11



COMPARATIVE EFFICIENCIES BETWEEN SECTORAL HORN
AND SUB-ARRAY

PRINTED CIRCUIT ANTENNA DESIGNS

Daniel A. Mullinix, 1Lt, USAF and Paul M. Proudfoot, 2Lt, USAF

Rome Air Development Center, Electromagnetics Directorate

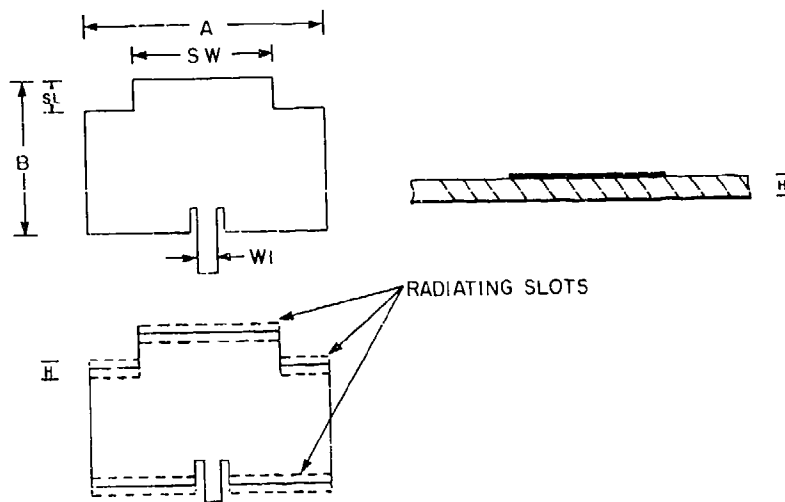
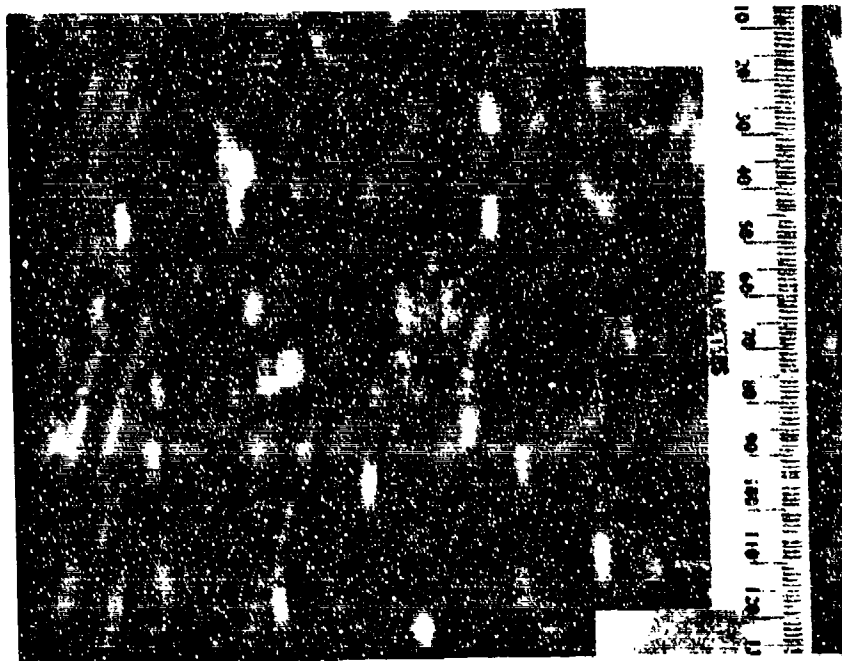
Hanscom AFB, Ma 01731

ABSTRACT

This paper is a summary of some of our current work in both broadside (conformal) and endfire printed circuit antennas. Many models exist for the design of conformal printed circuit antennas. The most complicated of these may take weeks or even months to develop and program. This paper will show that a simple transmission line model combined with segmentation methods can be used to predict the resonant frequency and input impedance of a surprising variety of elements with fair accuracy. Design equations, measured data and radiation patterns will be presented for stagger tuned elements, dual and circularly polarized inset feed patch elements, and even a circular patch modelled using rectangular segments. Measured data will be used to provide a feel for the range over which this model is a viable design candidate. We will also present additional measurement data (i.e. crosspolarization patterns, frequency dependence patterns and substrate selection information) on the printed circuit dipole presented in the 1986 proceedings by Rees and Edward.

1.1 STAGGER TUNED RECTANGULAR PATCH

It is an extremely well documented fact that conventional microstrip patch antennas are narrow band. The average bandwidth



Figures 1 and 2. Stagger Tuned Patch

of a microstrip patch is about 4% and bandwidths up to 10% can be achieved by increasing the electrical thickness of the substrate. However, the use of thick substrates in arrays is complicated due to the excitation of surface wave modes. We chose to model a stagger tuned element [1] because it promised an increased bandwidth over a standard rectangular patch for the same substrate thickness.

A stagger tuned patch with an inset coplanar feed line is shown in figures 1 and 2. It has an overall length and width of A and B respectively. The conductor thickness is T and the patch sits on top of a substrate of thickness, H. The length and width of the stagger tuned section is SL and SW respectively. In the transmission line model, this antenna is modelled as 3 slots (re. Fig 2) located on the edges of the patch perpendicular to the feedline. These slots are then connected to the feedpoint through the patch, which is modelled as sections of microstripline of width A and SW. The slots are assumed to have lengths (A-WI), (A-SW) and SW respectively. Harrington gives the admittance of a narrow H-plane slot as [2:183]:

$$Y_s = \pi A / \lambda \eta_0 (1 - k^2 H^2 / 24) + jA / \lambda \eta_0 [3.135 - 2 \ln(kH)] \quad (1)$$

$$= G_s + jB_s$$

where A is replaced by (A-WI), (A-SW) and SW for the admittances Y_{s1} , Y_{s2} and Y_{s3} of slots 1, 2 and 3 and $\eta_0 = 377\Omega$ is the impedance of free space. The main and stagger tuned sections of the patch are modelled as sections of microstripline of width

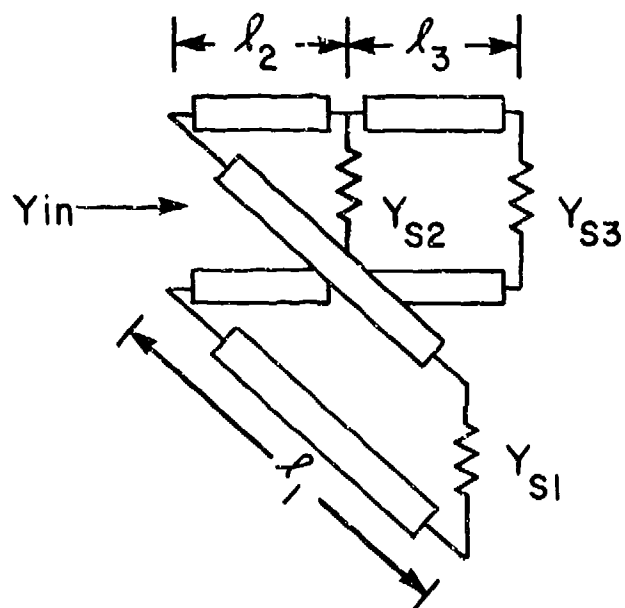


Figure 3. Equivalent Circuit of Stagger Tuned Patch

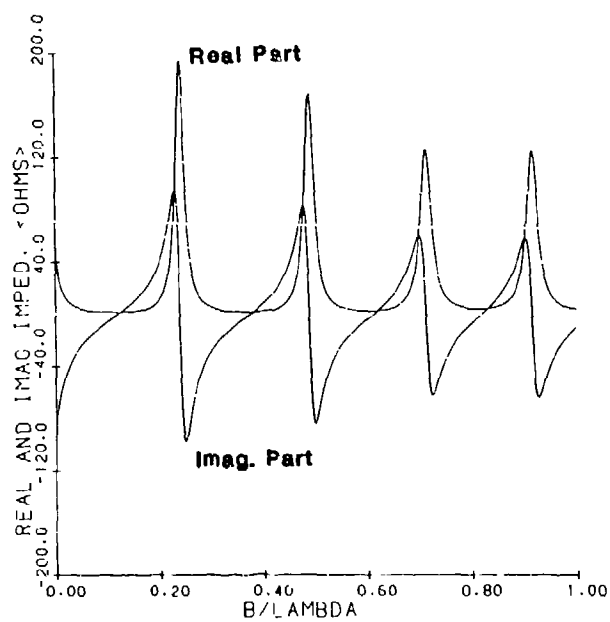


Figure 4. Stagger Tuned Patch Input Impedance vs. B/λ

A and SW. Their admittance is given by Schaubert et. al. as [3]:

$$Y_p = \sqrt{\epsilon_e} / \eta_0 [A/H + 1.393 + .667 \ln(A/H + 1.444)]^{-1} \quad (2)$$

where $\epsilon_e = (\epsilon_r + 1)/2 + (\epsilon_r - 1)/(2 \sqrt{1 + 10H/A})$

where A is equal to A for the admittance of the main patch section Y_p and A = SW for the admittance of the stagger tuned section Y_{ps} .

In a patch such as this, the input impedance varies from a high value at the edge (approx. 200 Ω) to zero at the center. It is not always convenient to use such a high impedance line. To use a feedline with a lower characteristic impedance Z_0 , we move the feedpoint inward from the patch edge by cutting two short slots parallel to the feedline as shown in figure 2, thus forming an inset feed. Then the admittance of all of the radiating slots is transformed to the location of the inset feed. Thus the input admittance of the patch is given by the equivalent circuit of figure 3. In equation form, the admittance at the intersection of the main patch and stagger tuned section is:

$$Y_2 = Y_{ps} [(e^{jkl_3} + \Gamma_3 e^{-jkl_3}) / (e^{jkl_3} - \Gamma_3 e^{-jkl_3})] + Y_{S2} \quad (3)$$

and therefore the admittance of the open circuit side of the patch is:

$$Y_{os} = Y_p [(e^{jkl_2} + \Gamma_2 e^{-jkl_2}) / (e^{jkl_2} - \Gamma_2 e^{-jkl_2})] \quad (4)$$

where $\Gamma_3 = (Y_{S3} - Y_{ps}) / (Y_{S3} + Y_{ps})$, $l_3 = SL \sqrt{\epsilon_e}$

$$\Gamma_2 = (Y_2 - Y_p) / (Y_2 + Y_p) , \quad l_2 = (B - D - SL) \sqrt{\epsilon_e}$$

similarly, the admittance of the feed side of the patch is:

$$Y_{fs} = Y_p [(e^{jkl_1} + \Gamma_1 e^{-jkl_1}) / (e^{jkl_1} - \Gamma_1 e^{-jkl_1})] \quad (5)$$

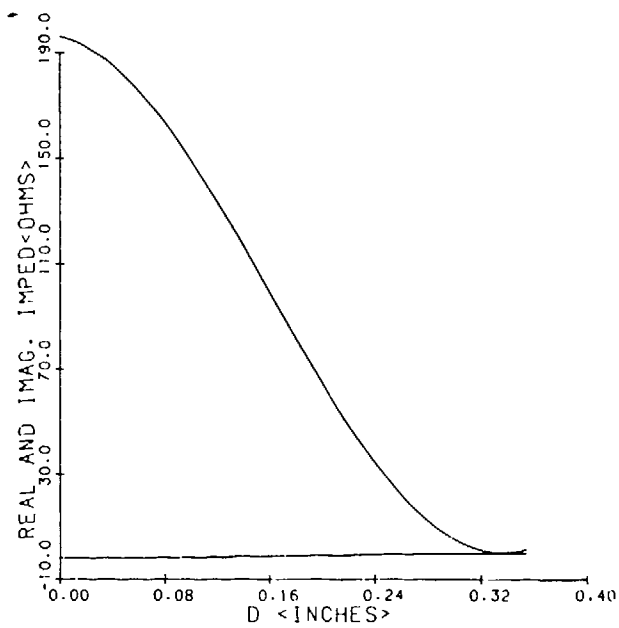


Figure 5. Stagger Tuned Patch Input Impedance vs. Inset Depth D

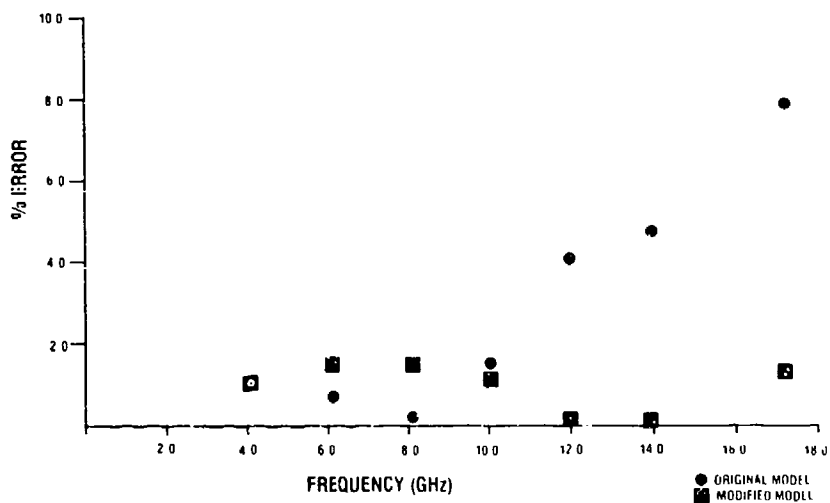


Figure 6. Stagger Tuned Patch Model Error

where $\Gamma_1 = (Y_{S1} - Y_p)/(Y_{S1} + Y_p)$, $\ell_1 = D \sqrt{\epsilon_e}$

Using Euler's relations,

$$Y_{fs} = \frac{Y_p G_1 \cos(k\ell_1) + j[B_1 \cos(k\ell_1) + Y_p \sin(k\ell_1)]}{[Y_p \cos(k\ell_1) - B_1 \sin(k\ell_1)] + j G_1 \sin(k\ell_1)} \quad (6)$$

$$Y_{os} = \frac{Y_p G_2^* \cos(k\ell_2) + j[B_2^* \cos(k\ell_2) + Y_p \sin(k\ell_2)]}{[Y_p \cos(k\ell_2) - B_2^* \sin(k\ell_2)] + j G_2^* \sin(k\ell_2)} \quad (7)$$

where

$$\begin{aligned} G_2^* + jB_2^* &= Y_2 \\ &= G_2 + jB_2 + \frac{Y_{ps} G_3 \cos(k\ell_3) + j[B_3 \cos(k\ell_3) + Y_{ps} \sin(k\ell_3)]}{[Y_{ps} \cos(k\ell_3) - B_3 \sin(k\ell_3)] + j G_3 \sin(k\ell_3)} \end{aligned} \quad (8)$$

Y_{in} is then:

$$Y_{in} = Y_{os} + Y_{fs} \quad (10)$$

where G_1 , G_2 , G_3 , B_1 , B_2 and B_3 are the real and imaginary parts of the slot admittances using eqn. (1). Figure 4 is a plot of patch input impedance vs. B/λ and figure 5 is a plot of patch input impedance vs. inset depth D . To determine the correct patch dimensions for a given resonant frequency and input impedance, we set $D = 0$ in eqn (9) and make successive guesses at B until the imaginary part equals zero. A good initial guess is $B = .49 \lambda_0 / \sqrt{\epsilon_r}$. Next, we adjust D until the real part equals the feedline characteristic impedance. A good initial guess for D is given by Carver and Mink [4] for a rectangular patch as:

$$D = (B/\pi) \cos^{-1}[R_0 / \sqrt{R_e}] \quad (11)$$

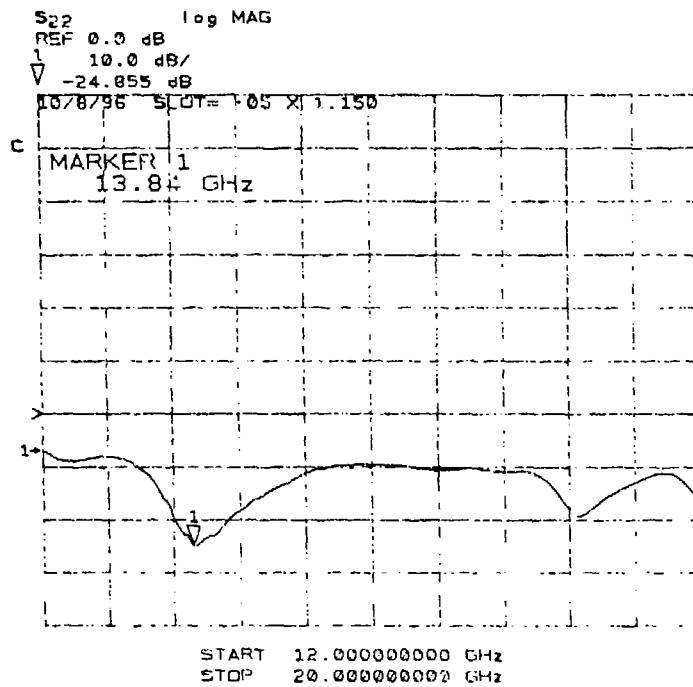


Figure 7. Stagger Tuned Patch Sample Return Loss Measurement

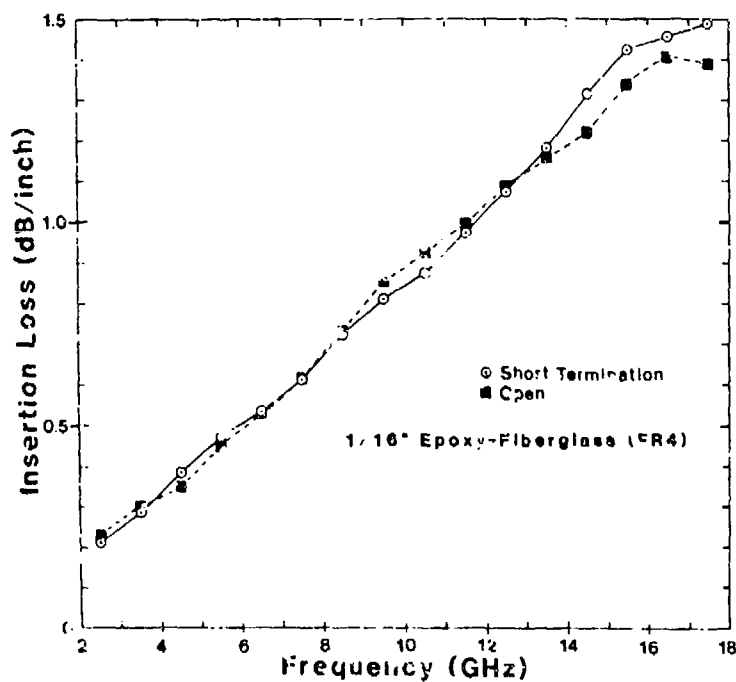


Figure 8. Loss Per Inch on Epoxy FR4

where R_0 equals Z_0 , the characteristic impedance of the feedline, and R_e is the edge input resistance of the patch without an inset feed. It is also necessary to apply a length extension since fringing fields cause the radiating slots at the patch edge to appear electrically some small distance beyond the edge of the patch. Hammerstadt [5] gives a very good approximation for apparent length extension of an open circuited microstrip transmission line as:

$$\Delta l = \frac{.412 H (\epsilon_e + .3)(W/H + .264)}{(\epsilon_e + .258)(W/H + .8)} \quad (11)$$

Our model was modified to account for this effect by using

$$l_1 = D \sqrt{\epsilon_e} + \Delta l/2, \quad l_2 = (B - D - SL) \sqrt{\epsilon_e} + \Delta l/2$$

and $l_3 = SL \sqrt{\epsilon_e} + \Delta l/2$.

1.2 STAGGER TUNED PATCH ANTENNA TEST RESULTS

In order to ensure a fair comparison of this patch to a standard rectangular patch, we used the same substrate material, connectors, and design frequencies that we used in the rectangular patch study [6]. In addition, the measurement equipment and calibration procedures were identical for each study.

Eight individual patch antennas with resonant frequencies between 2 and 18 GHz were constructed and tested. Figure 1 is a photograph of one of the antennas. The substrate used for this and the previous study was 1/16" thick FR4 epoxy-fiberglass with a relative dielectric constant of 4.4 and 1-oz. ($T=.0014$ ") copper

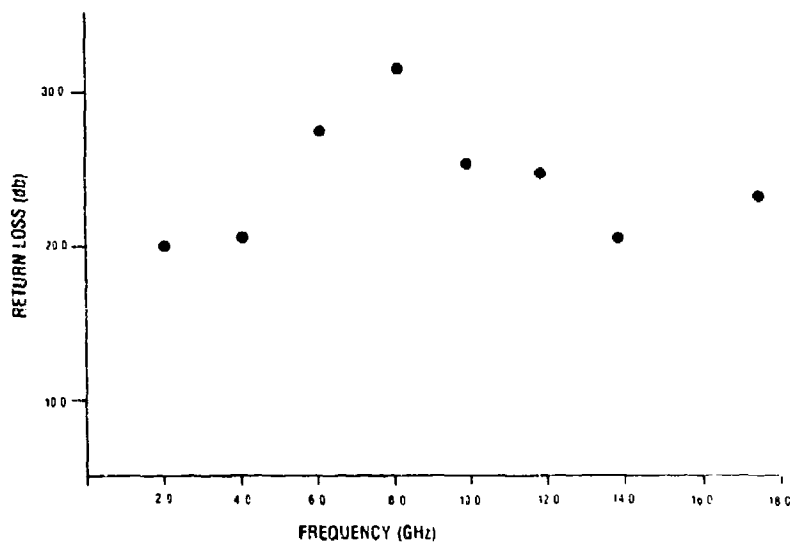


Figure 9. Stagger Tuned Patch Return Loss vs. Measured Frequency

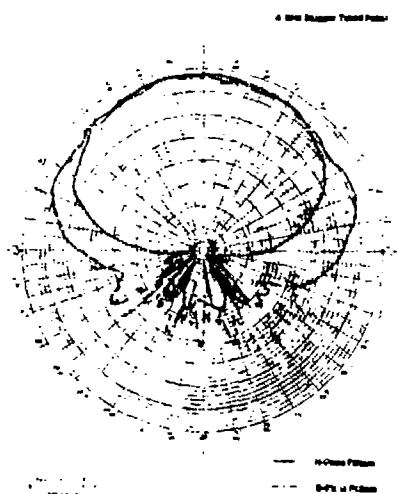


Figure 10. Stagger Tuned Patch E and H-Plane Patterns

cladding. The length and width of the stagger tuned section was chosen as 14% and 42% of the elements total length and width respectively. Figure 6 shows the model error between design and measured resonant frequencies for an original model and the modified model presented in this report which uses the effective dielectric constant and Hammerstadt's length extension. The modified model was very accurate for all frequencies used in this study.

Just as the resonant frequency measurement is a direct test of the model's accuracy in predicting the patch length, B, the return loss measurement tests its accuracy in determining the feed point location D. A sample return loss measurement for one of the stagger tuned antennas is shown in figure 7. To this measured return loss, we must add the two way attenuation in the microstripline between the network analyzer test port and the antenna's feed point, since that attenuation will tend to make the antenna's reflection coefficient appear smaller than it actually is. Figure 8 shows the loss per inch that we measured in a microstripline constructed on the same epoxy-fiberglass material as the antennas. The procedure used to measure the loss is documented in [7]. Figure 9 shows the corrected return loss vs. measured frequency for each of the eight antennas where the corrected return loss is the measured return loss corrected for the two way attenuation in the microstripline. All of the antennas had very good return losses ($>20\text{db}$) which

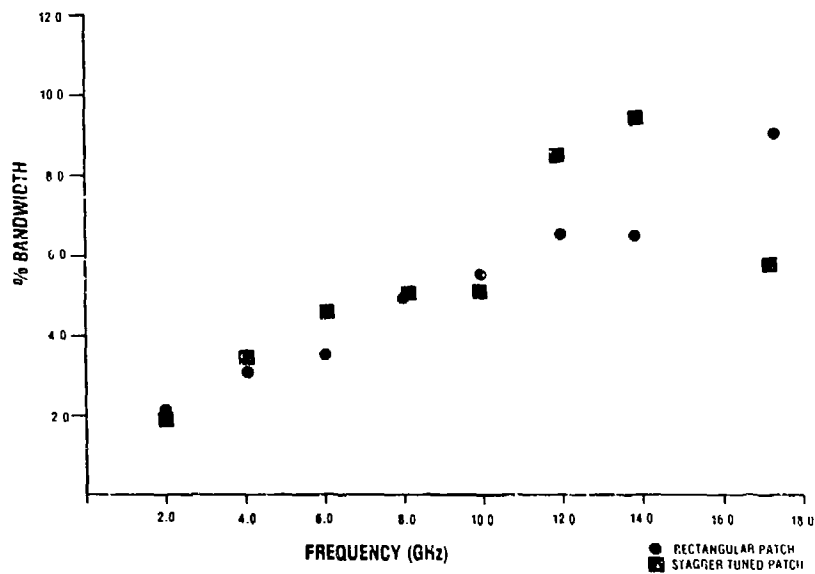


Figure 11. Stagger Tuned Patch Bandwidth

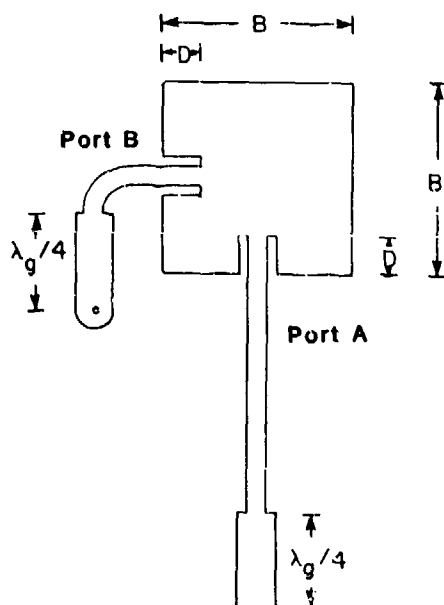


Figure 12. Dual Polarized Inset Feed Square Microstrip Patch

indicates: one, the depth of the inset feed is neither significantly inductive or capacitive since the feed point impedance is totally real, and two, the depth of the inset feed corresponds to a close impedance match with the 100 ohm feedline.

The E and H-plane patterns of the 8 GHz stagger tuned patch shown in figure 10 are typical patterns. A six wavelength (at 4 GHz) ground plane was used with the antennas to eliminate possible errors due to radiation from the substrate edge. With the addition of the ground plane, the characteristic periodic ripple associated with radiation at the edge of the ground plane in the E-plane of the patch becomes apparent and the periodicity of the ripple increases with frequency as it should. There is some irregularity in the E-plane pattern due to the edge launch connector.

The bandwidth for the eight individual patches is calculated between the 2:1 VSWR points of the corrected return loss measurement, and is shown in figure 11. The increasing bandwidth with frequency is due to the increasing electrical thickness of the substrate and is within the bounds we would expect from calculations by Bahl and Bhartia [8] on standard rectangular patches. From figure 11, you can see that although the measured bandwidth of the stagger tuned patch was generally greater, it was only by a small amount and not nearly the amount we had hoped for.

2.1 DUAL POLARIZED SQUARE PATCH

A dual polarized inset feed square microstrip patch is shown

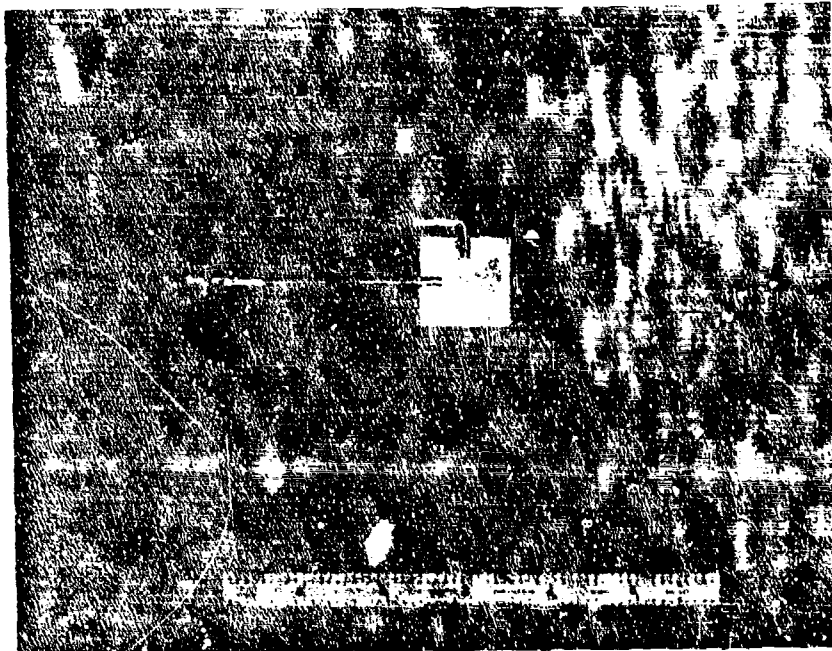


Figure 13. Photograph of Dual Polarized Patch

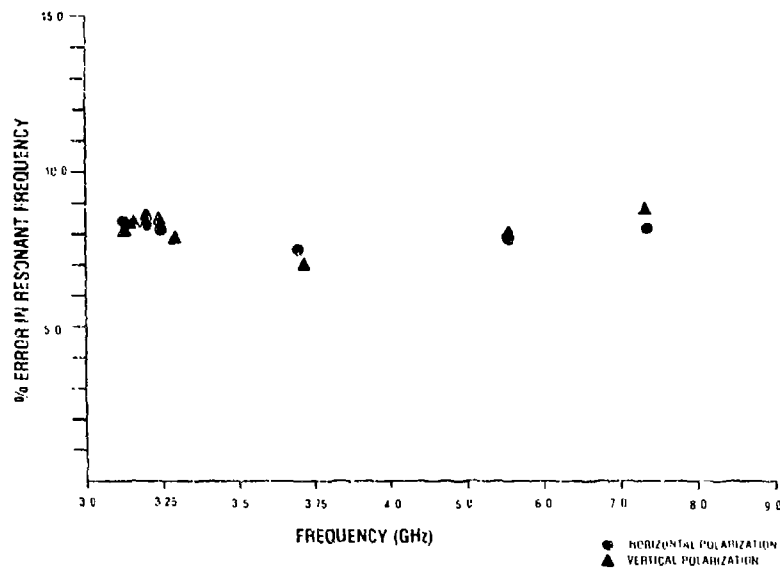


Figure 14. Model Error of Dual Polarized Patch

in figures 12 and 13. This patch was designed for a second generation dual polarized phased array for bistatic radar where one of the polarizations is probe fed and the other polarization is fed using a corporate microstripline feed. The substrate material for this effort was 1/16" thick OAK-602 with an ϵ_r of 2.5. To design this patch we assumed symmetry and used the same equations as in the stagger tuned patch except only two radiating slots. We expect the patch to radiate lower than the design frequency because the inset feed in the plane of the patch that is orthogonal to the polarization being fed lengthens the current path between the radiating edges of the patch.

2.2 DUAL POLARIZED PATCH TEST RESULTS

Nine individual dual polarized patches were built with operating frequencies between 3 and 10 GHz. Five of these patches were built in the 3.0-3.25 GHz range since this was the frequency at which the bistatic array would operate. The remaining four patches were built at approx. 4, 6, 8 and 10 GHz to test the patch over a wider range of frequencies and substrate parameters. All of the patches except one resonated between seven and nine percent below design frequency as shown in figure 14. This figure also indicates that the difference between the orthogonal polarization resonances was small enough that the bandwidth was unaffected. The corrected return losses, patterns and the performance of the patch in general were good for the lower frequency patches but degraded for the higher frequency patches

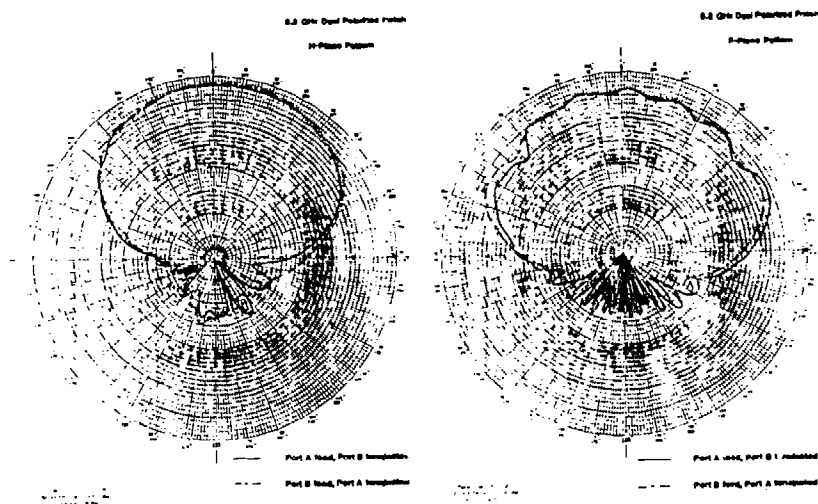


Figure 15. Dual Polarized Patch Antenna Patterns

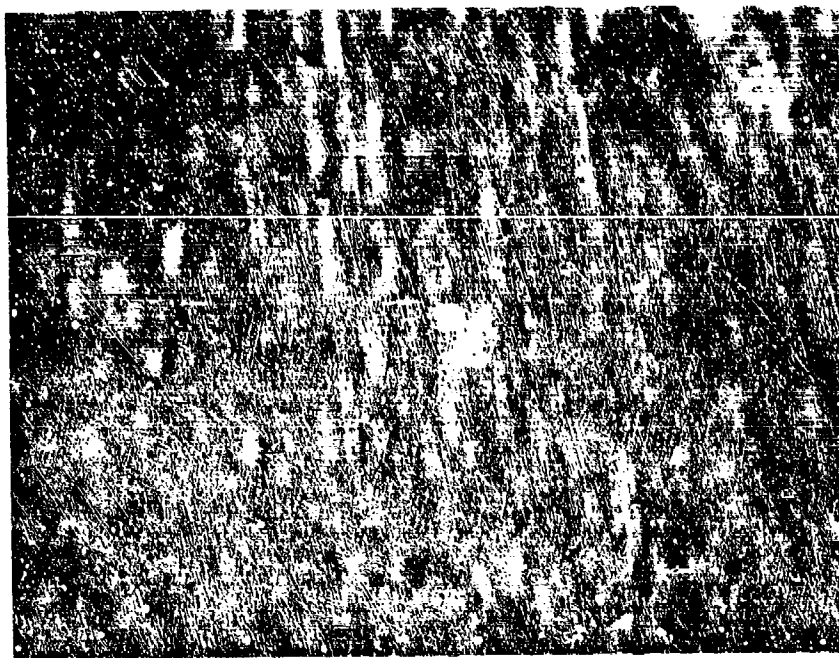


Figure 16. Circularly Polarized Hybrid Patch

probably because the width of the microstripline does not scale and thus the corner of the patch between the feedlines becomes isolated from the rest of the patch, hence changing the mode structure. Dual polarized patterns shown in figure 15 are typical of the lower frequency patches and have an axial ratio of about 1 dB.

3.1 CIRCULARLY POLARIZED PATCHES

Two different versions of circularly polarized square microstrip patches are shown in figures 16-17. Version 1 achieves circular polarization via a 90 degree hybrid corporate feed network and version 2 achieves it via an integrated diagonal slot in the patch [9]. The goal of this effort is a model with enough accuracy to build a patch for given frequency and substrate parameters in one or two iterations. In light of this, the two slot transmission line model used for the dual polarized patches will be used to model both versions of CP patches.

3.2 MEASUREMENTS

Three hybrid patches and three slot patches were built between 4 and 12 GHz on 1/16" Epoxy FR4, $\epsilon_r = 4.4$. Two of the three hybrid patches resonated between 6 and 8 percent below the design frequency as expected and had 18-25 dB return losses. However, the diagonal slot patches all resonated slightly higher than expected which is contrary to the results presented by Kerr [9] on a similar patch without the inset feed. This information and later radiation patterns that had a 25 dB axial ratio indicate that the inset feed is an unacceptable asymmetry. Radiation patterns for the hybrid

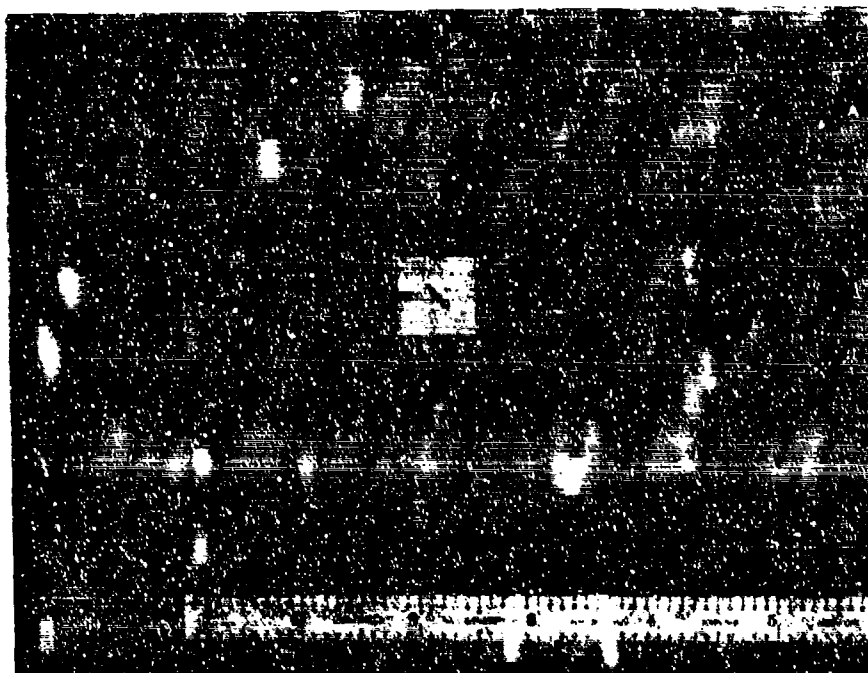


Figure 17. Circularly Polarized Slot Patch

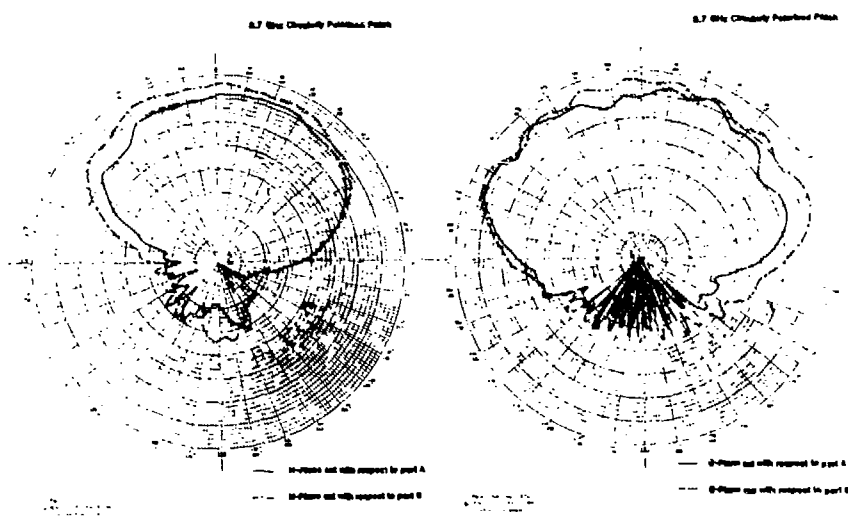


Figure 18. 3.7 GHz Circularly Polarized Hybrid Patch Antenna Patterns

design were fairly good at 3.7 GHz (figure 18), but were increasingly degraded for the 8 and 12 GHz patches no doubt due to the same isolated corner problem as found in the dual polarized patches.

4.1 RECTANGULAR SEGMENT MODEL CIRCULAR PATCH

The circular patch that was modelled is shown in figure 19. The patch contour was modelled by rectangular transmission line segments as shown in figure 20 where the radiating slots are located as shown in figure 21 (the inset feed design in figure 21 was abandoned because the input impedance was complex). Figure 22 shows the equivalent circuit of the model. In equation form, starting from the open circuit side of the patch at segment N and working toward the feed, we have:

$$Y_m = Y_{pm} [(e^{jkL_m} + \Gamma_{(m+1)} e^{-jkL_m}) / (e^{jkL_m} - \Gamma_{(m+1)} e^{-jkL_m})] + Y_{sm} \quad (12)$$

for $2 \leq m \leq N$

where $\Gamma_m = (Y_{sm} - Y_{p(m-1)}) / (Y_{sm} + Y_{p(m-1)})$, $m = N+1$

$$\Gamma_m = (Y_m - Y_{p(m-1)}) / (Y_m + Y_{p(m-1)}) \quad , \quad 2 \leq m \leq N$$

and finally,

$$Y_{in} = Y_{p1} [(e^{jkL_1} + \Gamma_2 e^{-jkL_1}) / (e^{jkL_1} - \Gamma_2 e^{-jkL_1})] + Y_{s1} \quad (13)$$

where Y_s and Y_p are defined by eqns. (1) and (2) respectively and L_m is equal to the length of each individual segment divided by the square root of ϵ_e for that segment. Note that the effective dielectric constant is different for each segment depending on the segment's width. Again, to determine the correct patch dimensions for given frequency and substrate parameters, the radius of the

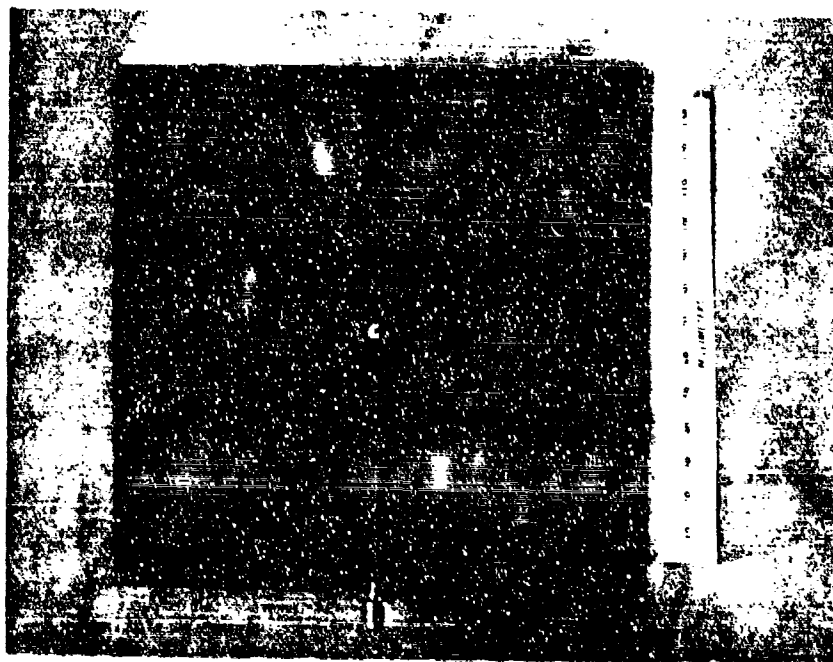


Figure 19. Photograph of Circular Patch

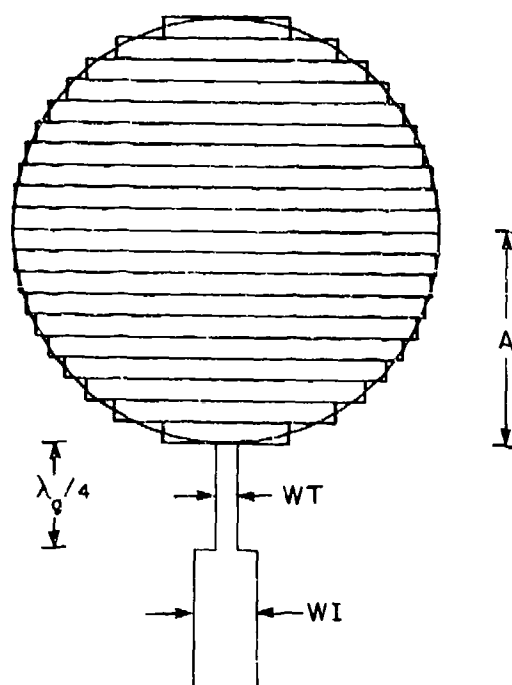


Figure 20. Location of Rectangular Segments with respect to Circular Patch Contour

patch A is successively changed until the imaginary part of eqn. (13) equals zero.

4.2 TEST RESULTS

Four patches like the one shown in figure 19 were built on 1/16" thick PTFE with an $\epsilon_r = 2.5$ over a range of 4-12 GHz. The corrected return losses of all of the patches were quite good (>18 dB). Figure 23 shows model error for the various segment models. Model accuracy improved as expected with an increasing number of segments to a point after which large increases in the number of segments made little improvement to the accuracy. Fringing fields at the edges of the patch make the patch electrically larger than it is. A radial length extension is required to compensate for this. Bahl and Bhartia give a radial length extension for their cavity model as [8:90]:

$$A_e = A [1 + (2H/A\pi\epsilon_r)(\ln(\pi A/2H) + 1.7726)]^{1/2} \quad (14)$$

In this transmission line model, the slot admittance Y_s partially compensates for fringing fields hence making the required length extension less than the extension required in a cavity model, hence:

$$A_{eff} = A + .35(A_e - A) \quad (15)$$

This equation resulted in model errors of less than 1% for all of the patches tested.

5.1 PRINTED CIRCUIT DIPOLE

The printed circuit dipole presented by Edward and Rees [10] consisted of a flat radiating dipole integrated with a double tuning balun. This effort discusses additional pattern measure-

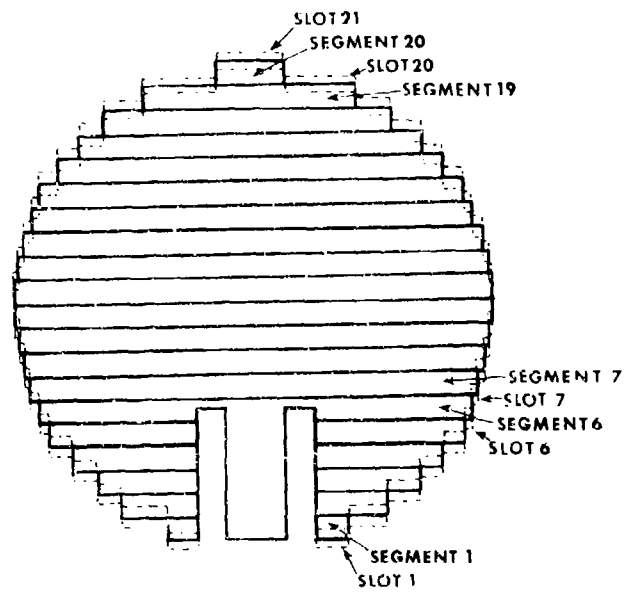


Figure 21. Location of Radiating Slots with respect to Contour

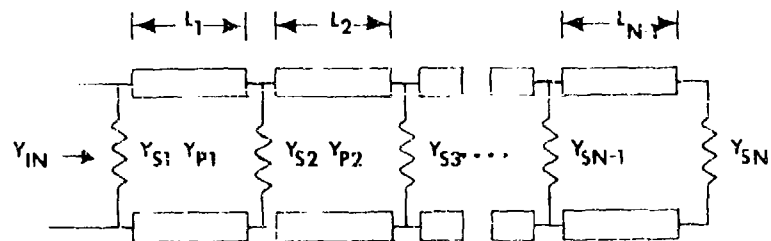


Figure 22. Equivalent Circuit of Rectangular Segment Transmission Line Model for Circular Patch

ments and substrate selection for this element. Antenna patterns (including cross-polarization patterns) will be presented at several frequencies over the operating band of the element.

Figures 24 and 25 show the dipole/balun geometry along with the coaxial equivalent circuit. In this circuit, the dipole input impedance is simply represented by a complex value Z_d . By inspection of the circuit of figure 25, the input impedance Z_{in} can be expressed as [12]:

$$Z_{in} = -j Z_a \cot(\theta_a) + \frac{j Z_d Z_{ab} \tan(\theta_{ab})}{Z_d + Z_{ab} \tan(\theta_{ab})} \quad (16)$$

where Z_a , θ_a , Z_{ab} and θ_{ab} are the characteristic impedance and electrical length of the microstrip and coupled microstrip lines respectively. By judicious selection of the parameters θ_a and θ_{ab} (i.e. the open end length and slot selection) in eqn.(16), one can achieve an impedance match over approximately a 40% bandwidth.

5.2 SUBSTRATE SELECTION

Selecting a suitable substrate is a critical step in the dipole/balun design. Once a substrate is selected, the designer has very little freedom to vary microstrip and coupled microstrip line widths. In the balun structure, the coupled microstripline acts as a ground plane to the microstripline (see figure 26). Note in this figure that virtually all of the fields beneath the microstripline of width W are contained within $3W$ [11]. Therefore, the width of the coupled microstripline must be greater than $3W$. Since there are two coupled lines, the dimension B (figure 26) must be greater

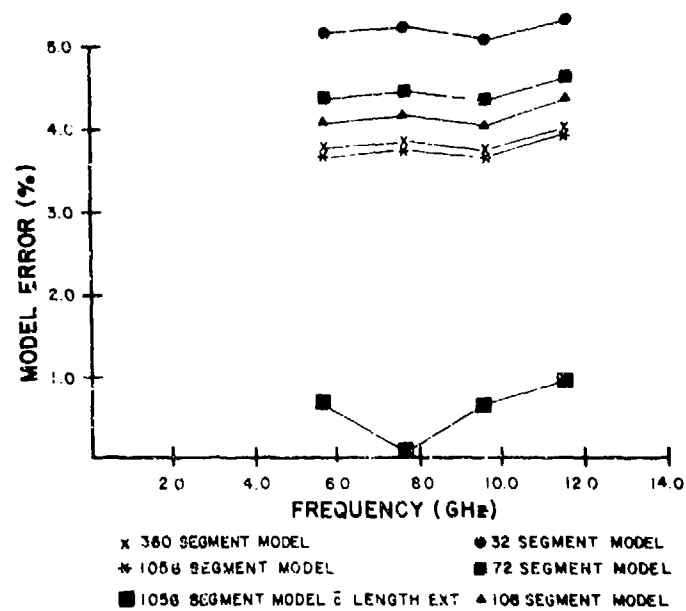


Figure 23. Circular Patch Model Error vs. Measured Frequency

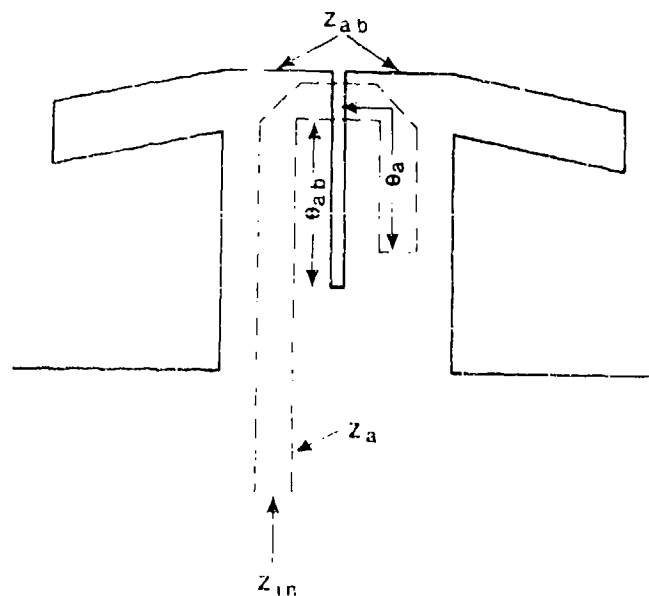


Figure 24. Dipole/Balun Geometry

than 6W. This transverse dimension B is now a major limitation to both the upper value of Z_{ab} and to the maximum frequency for which a dipole can be fabricated on a particular substrate. For example, the dipole length L is approximately $.43 \lambda_0$ or $.42''$ at 12 GHz. Clearly, this dipole could not be put on a substrate that yields a dimension B equal to $.6''$, because the two coupled microstriplines would be wider than the dipole. In order to keep all dipole/balun dimensions in proportion, it is suggested that $.4L < B < .5L$. Finally, a substrate should be selected such that $H/\lambda_g < .1$ to insure that the equations used in determining Z_a , θ_a , Z_{ab} and θ_{ab} will yield accurate results.

Five dipoles were designed, fabricated and tested. The dipoles range in frequency from 2-18 GHz. Three different substrates were used to cover this frequency range. The 2, 4 and 4.3 GHz dipoles were fabricated on $1/16''$ thick PTFE substrate with an ϵ_r of 2.54. A 15 GHz dipole was fabricated on $.02''$ PTFE with $\epsilon_r = 2.2$ and a 6 GHz dipole was fabricated on $1/16''$ epoxy, $\epsilon_r = 4.4$. To keep this portion of the report short, only the results of the 4 GHz dipole will be presented. However, these results are typical of the other four dipoles that were tested.

5.3 ANTENNA PATTERNS

Figure 27 shows the 4 GHz dipole mounted $\lambda_0/4$ above a $16'' \times 16''$ aluminum ground plane. It was noted while taking patterns that there should be good electrical contact between the aluminum ground plane

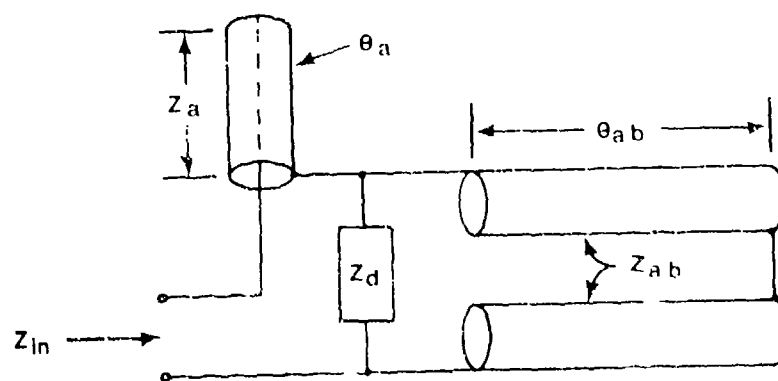


Figure 25. Coaxial Equivalent Circuit

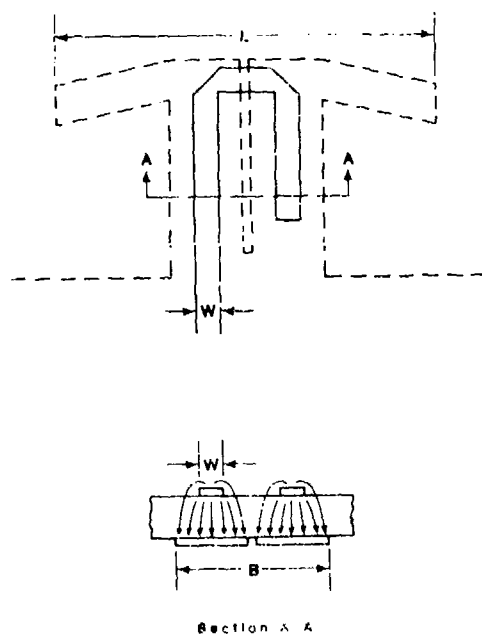


Figure 26. Fields Beneath the Bipole Microstrip Line Feed

and the substrate's ground plane. Patterns will be moderately degraded if this precaution is not adhered to. Also, a metal housing was used to enclose hardware located behind the aluminum ground plane. This eliminated any contributions to the antenna pattern from spurious radiation emitted by the feed line and coax-to-microstrip transition. Patterns were first taken of the 4 GHz dipole at the upper and lower end of the operating band to determine any frequency dependence of the patterns. The results are shown in figures 28 and 29. In comparing these figures note that the E-plane patterns became slightly broader as frequency is increased from 3.6 to 5.0 GHz, especially when the antenna is rotated more than 40 degrees from broadside. The only explanation for this seems to be that radiation from the dipole/halun configuration is more complicated than just that of the dipole itself. From the patterns taken, it was felt that radiation from the open-ended microstripline accounts for a good portion of the change in dipole patterns with frequency.

5.4 CROSS-POLARIZATION PATTERNS

Cross polarization patterns were taken next; the results are shown in figure 30. The trend here was two small lobes approximately 20 dB down occurring at ± 70 degrees from broadside in the H-plane and a single lobe approximately 15-20 dB down occurring near broadside in the E-plane. All dipoles tested exhibited similar cross-polarization patterns.

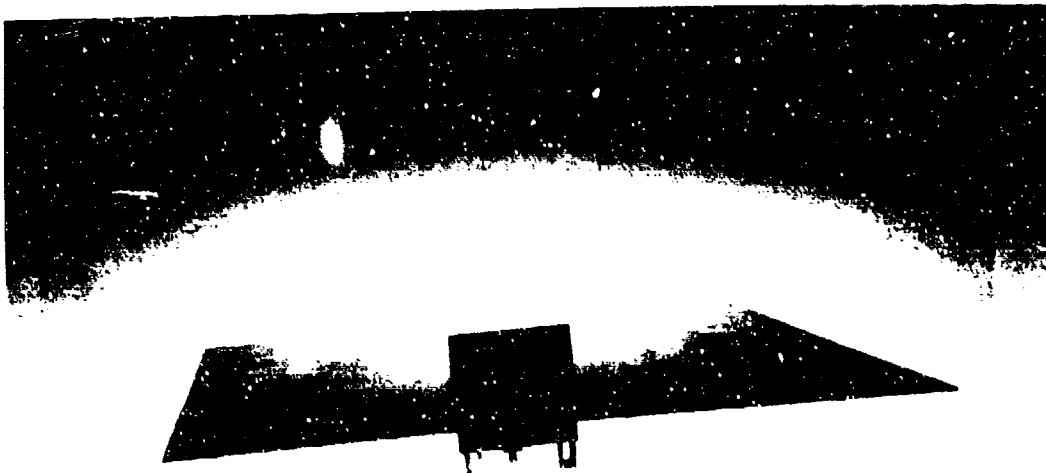


Figure 27. 4 GHz Dipole Mounted above a Ground Plane

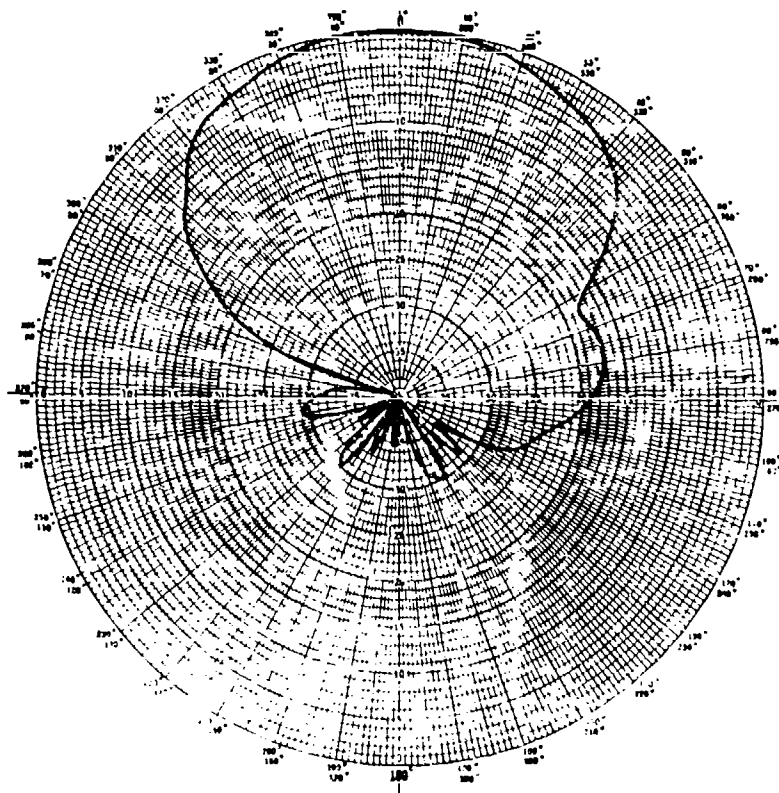


Figure 28a. F-Plane Dipole Pattern at 3.6 GHz

6.0 CONCLUSION

Six different types of antennas were designed, fabricated and tested in this paper. Five of these were successful from an operational standpoint with only the inset feed diagonal slot CP patch failing to make the grade. The segmentation transmission line model was very accurate in predicting the resonant frequency of both the stagger tuned and circular patches. The orthogonal inset feeds of both the dual polarized and CP hybrid patches caused these patches to resonate lower than the model frequency. However, the amount that they resonated low stayed fairly constant since the design input impedance was the same for all patches. This means that design curves can be generated from the data which reduces the number of iterations required to build a future patch for a specific frequency and substrate. This is important since these patches would be very difficult and time consuming to model using more precise models. The amount that the patches resonate low is a function of inset depth and therefore input impedance. Hence, the isolated corner problem of the higher frequency patches can be avoided by scaling the input impedance as the frequency is scaled up.

Additional information was presented on the Rees and Edwards printed circuit dipole. Antenna patterns show slight frequency dependence. Simple, easy-to-use design equations were presented that lend themselves nicely to computer-aided design. This element has many applications as a broad-band, low cost and lightweight antenna.

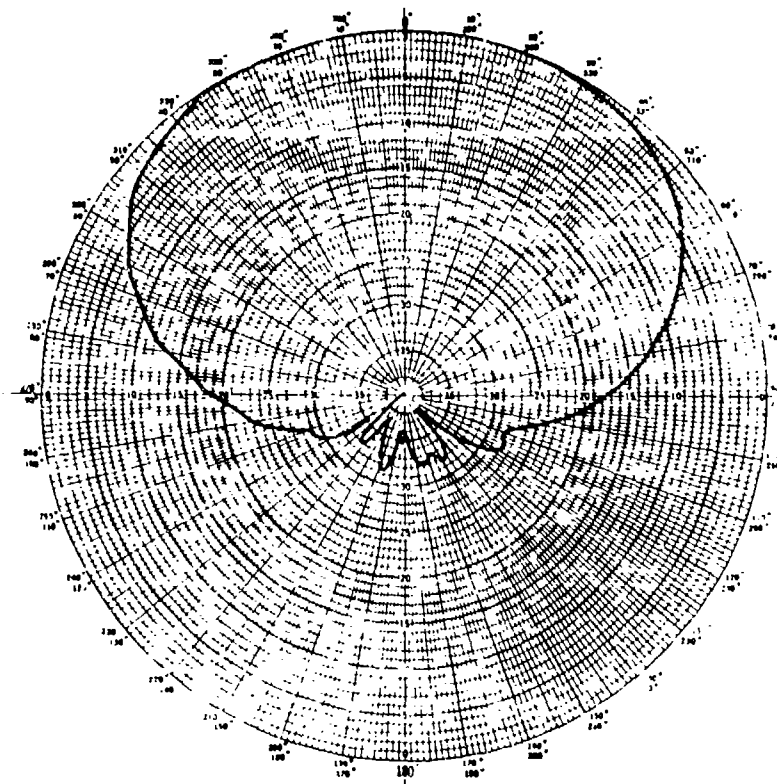


Figure 28b. H-Plane Dipole Pattern at 3.6 GHz

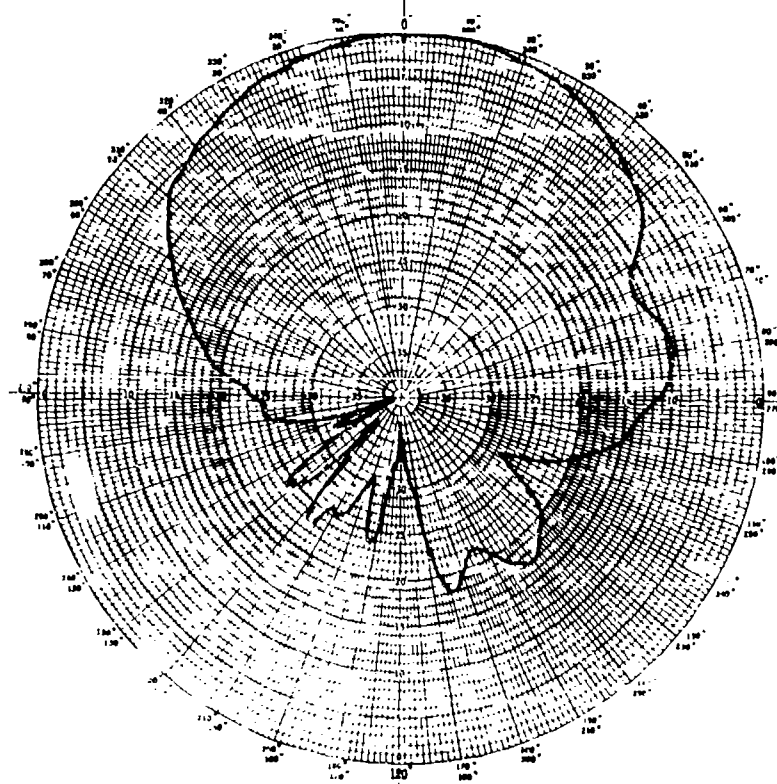


Figure 29a. E-Plane Dipole Pattern at 3.6 GHz

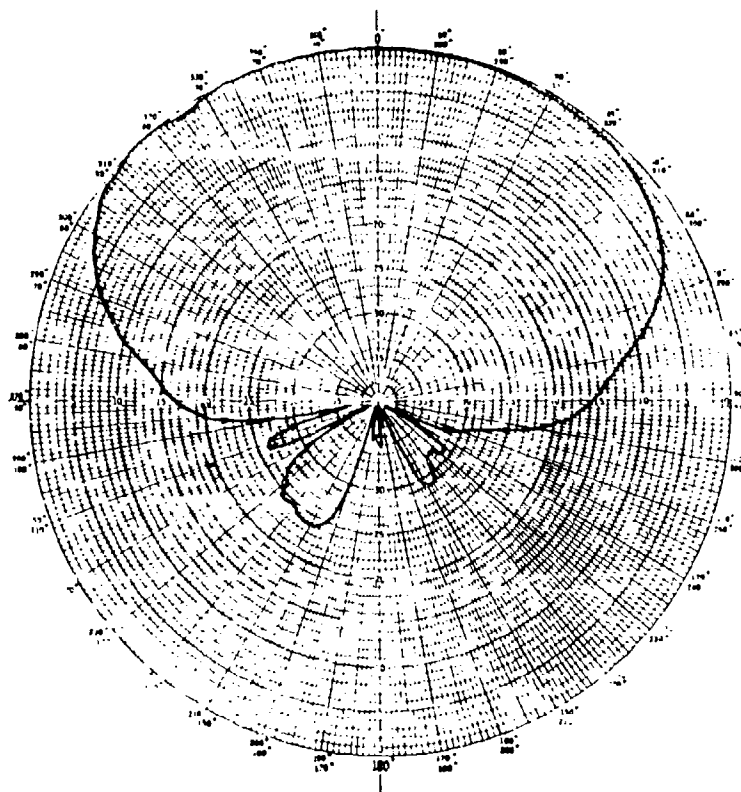


Figure 29b. H-Plane Dipole Pattern at 5.0 GHz

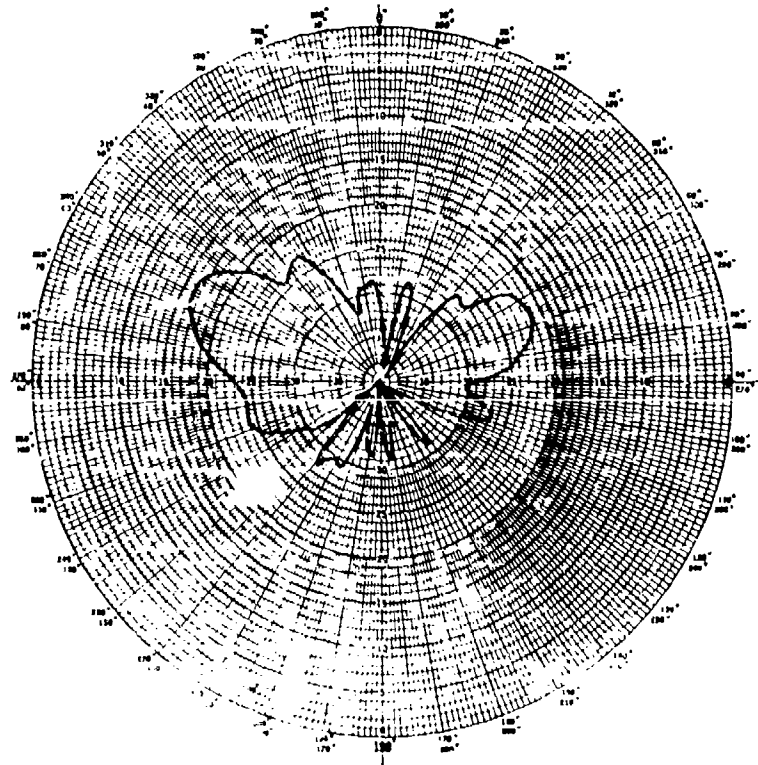


Figure 30a. E-Plane Cross-Polarization Dipole Pattern at 4.31 GHz

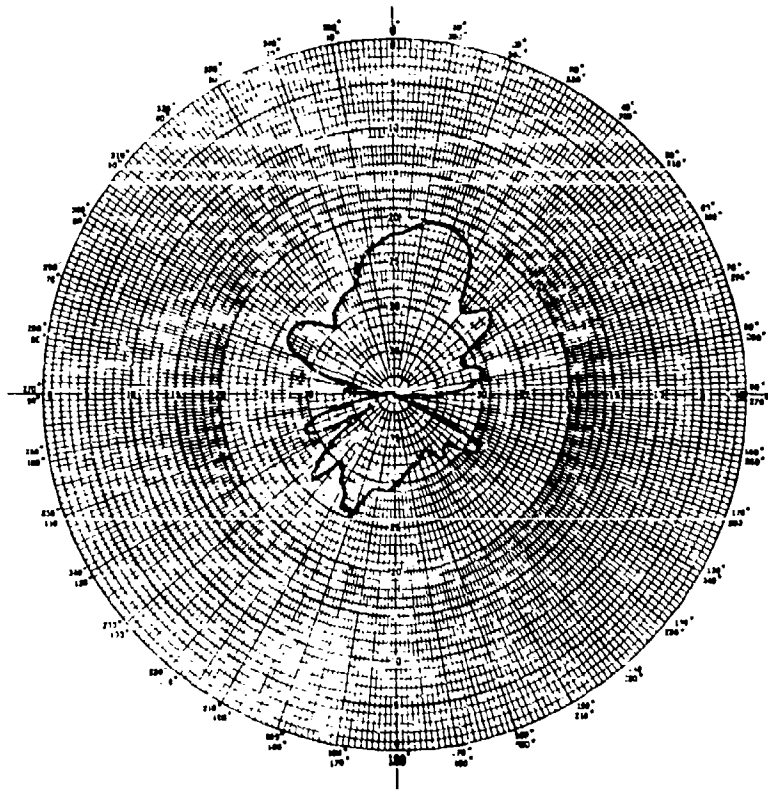


Figure 30b. H-Plane Cross-Polarization Dipole Pattern at 4.31 GHz

7.0 REFERENCES

1. Final Report, USAF Contract F19628-83C-0116 with Ball Aerospace Corporation to be published as an RADC Technical Report.
2. Harrington, R.F. (1961) Time Harmonic Electromagnetic Fields, McGraw Hill.
3. Schaubert, D.H., Farrer, F.G., Sindoris, A. and Hayes, S.T. (1981) "Microstrip Antennas with Frequency Agility and Polarization Diversity," IEEE Transactions on Antennas and Propagation, AP-29 pp. 118-123.
4. Carver, K.R. and Mink, J.W. (1981) "Microstrip Antenna Technology," IEEE Transactions on Antennas and Propagation, AP-29 pp. 1-24.
5. Gupta, K.C., Garg, R. and Chadha, R. (1980) Computer Aided Design of Microwave Circuits, Artech House.
6. Mullinix, D.A. and McGrath D.T. (1986) Rectangular Microstrip Patch Antenna Arrays, RADC Technical Report 86-151. NTIS# ADAL79170.
7. Kozak, F.E. and McGrath, D.T. (1985) Printed Circuit Transmission Line Transitions, RADC Technical Report 85-241. NTIS# ADAL69291.
8. Bahl, I.J. and Bhartia, P. (1981) Microstrip Antennas, Artech House.
9. Kerr, J.L. (1979) "Microstrip Antenna Developments," Proceedings of the Workshop on Printed Circuit Antenna Technology, pp. 3-1 thru 3-20.
10. Edward, B. and Rees, D. "A Broadband Printed Dipole with Integrated Balun," Microwave Journal, Vol 30, pp. 333-344 May 1987.
11. Roberts, W.K. "A New Wideband Balun," Proc IRE, Vol. 45, pp. 1628-1631, Dec. 1957.
12. Bawer, R. and Wolfe, J.J. "A Printed Circuit Balun for use with Spiral Antennas," IRE Transactions on Microwave Theory and Technology, Vol. MTT-8, pp. 319-325, May 1960.

A STUDY OF THE PROPAGATION AND RADIATION CHARACTERISTICS OF TAPE HELICAL STRUCTURES

Andrew F. Peterson, Bruce Greene and Raj Mittra
Electromagnetic Communication Laboratory
Department of Electrical and Computer Engineering
University of Illinois
1406 W. Green St.
Urbana, IL 61801

ABSTRACT: The characteristics of a helical geometry consisting of a tape helix separated from a concentric conducting core by a dielectric substrate are investigated. Assuming an infinitely long structure and an $e^{-j\beta z}$ dependence in all field components, the axial propagation constant β can be found as a complex root of the determinantal equation describing the boundary value problem. The k - β diagram of the helix provides information regarding the real-valued solutions for β that represent true axial propagation, as well as the complex-valued solutions that represent surface waves and leaky waves. Under the assumption that these same solutions exist on a finite-length structure, the current distribution and radiation pattern corresponding to a given β are obtained. The relationship between the complex-valued propagation constant and the resulting radiation characteristics will be discussed.

1 INTRODUCTION

Helical antennas have been widely used as broadband, practical radiating elements. Kraus discusses the so called normal and axial modes of operation [1].

Although it is difficult to rigorously analyze wire helical structures, the propagation characteristics of infinitely long tape and sheath helices (Figure 1) were studied during the 1950's by Sensiper [2], Watkins [3], and Hayes [4]. Assuming an $e^{-j\beta z}$ dependence in the field components, these models were used to generate the k - β diagram depicting the dispersion characteristics of the structure. In the 1960's, the existence of complex-valued solutions for β were discussed by Mittra [5] and Klock [6], who showed that helices support surface and leaky waves in addition to bound waves representing unattenuated axial propagation. The complex-valued solutions for β were subsequently used to study the leaky-wave radiation characteristics of helical antennas [7-9].

The work described above was limited to helices in free space, although the sheath helix with a concentric conducting core is discussed by Neureuther, Klock and Mittra [7]. They considered the case where the substrate medium is identical to the external medium. Other helical structures have been investigated by Ivanov and Ganchev, who considered a ferrite-loaded sheath helix with a concentric conducting core [10], and by Basu, Pal, Singh, and Vaidya, who considered a sheath helix with a concentric dielectric support [11].

In the present paper we consider a tape helix separated from a concentric conducting core by a dielectric substrate (Figure 2). In order to study the effect of the substrate and conducting core on the radiation characteristics of the helix, the k - β diagram is generated from the solution of the determinantal equation derived in Section 2. Section 3 describes the interpretation of the complex-valued propagation constants β by considering the fields in terms of a superposition of Fourier harmonics. Although the helix is basically a slow-wave device, and most of the harmonics represent non-radiating surface waves, typically one of the Fourier harmonics excites a radiating leaky wave. Expressions for the radiated fields are developed in Section 4. Numerical results are presented in Section 5 to illustrate the dependence of the k - β diagram and the radiation pattern on substrate permittivity and core size.

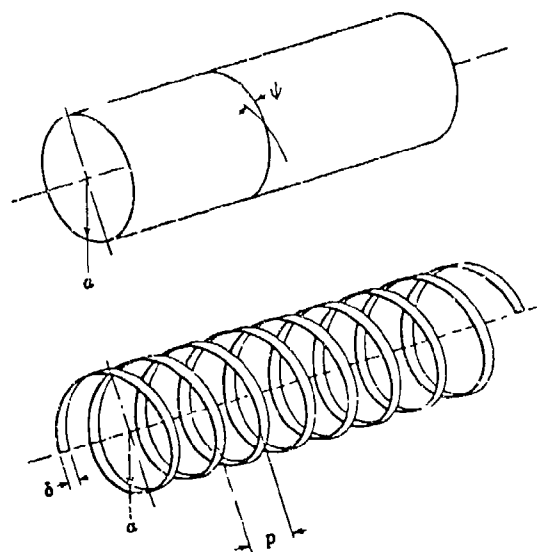


Figure 1 Sheath and tape models for the helix. The sheath model consists of an anisotropic conductor, so that current flow is restricted to the desired direction as defined by the pitch angle ψ . a) Sheath helix. b) Tape helix.

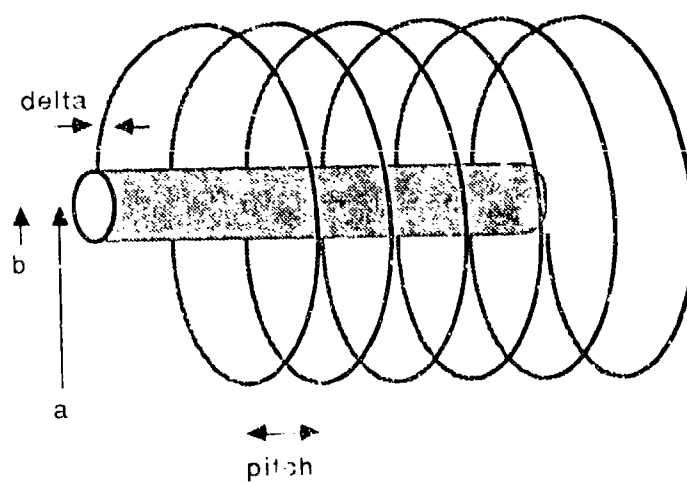


Figure 2. Helix with concentric conducting core.

2. DETERMINANTAL EQUATION FOR THE TAPE HELIX

Consider a tape helix having a concentric conducting core such as depicted in Figure 2. The tape helix is located at $\rho=a$ in a cylindrical coordinate system and the surface of the conducting core is located at $\rho=b$. A substrate material different from free space exists between the helix and the core ($b<\rho<a$). The tape width along z is denoted δ , and one period along z is known as the pitch p (Figure 1b). The centerline of the tape is defined by

$$x = a \cos \phi \quad (1)$$

$$y = a \sin \phi \quad (2)$$

$$z = \frac{p}{2\pi} \phi \quad (3)$$

Note that the tape helix is periodic in both ϕ and z . This suggests that the fields in the vicinity of the helix can be expanded in a Fourier series. However, a translation along z followed by a rotation in ϕ maps the structure onto itself. To account for this symmetry, it is convenient to introduce the variable ζ , where

$$\zeta = z + \frac{p}{2\pi} \phi \quad (4)$$

The location of the tape as a function of the variable ζ is

$$-\frac{\delta}{2} < \zeta < \frac{\delta}{2} \quad (\text{tape}) \quad (5)$$

$$\frac{\delta}{2} < \zeta < 1 - \frac{\delta}{2} \quad (\text{gap}) \quad (6)$$

Note that the geometry is also periodic in ζ .

We seek a solution having z -dependence $e^{-j\beta z}$. In a homogeneous, source-free region of space containing z -components of electric and magnetic fields of the form

$$E_z(\rho, \phi) e^{-j\beta z} \quad (7)$$

$$H_z(\rho, \phi) e^{-j\beta z} \quad (8)$$

the remaining field components are given by

$$E_\phi = \frac{-j\beta}{k^2 - \beta^2} \frac{1}{\rho} \frac{\partial E_z}{\partial \phi} + \frac{j\omega\mu}{k^2 - \beta^2} \frac{\partial H_z}{\partial \rho} \quad (9)$$

$$H_\phi = \frac{-j\omega\epsilon}{k^2 - \beta^2} \frac{\partial E_z}{\partial \rho} + \frac{-j\beta}{k^2 - \beta^2} \frac{1}{\rho} \frac{\partial H_z}{\partial \phi} \quad (10)$$

$$E_\rho = \frac{-j\beta}{k^2 - \beta^2} \frac{\partial E_z}{\partial \rho} + \frac{-j\omega\mu}{k^2 - \beta^2} \frac{1}{\rho} \frac{\partial H_z}{\partial \phi} \quad (11)$$

$$H_\rho = \frac{j\omega\epsilon}{k^2 - \beta^2} \frac{1}{\rho} \frac{\partial E_z}{\partial \phi} + \frac{-j\beta}{k^2 - \beta^2} \frac{\partial H_z}{\partial \rho} \quad (12)$$

In the region $b < \rho < a$, the fields can be expressed as

$$E_z = \left\{ \sum_{n=-\infty}^{\infty} [A_n I_n(\tau_{cn}\rho) + B_n K_n(\tau_{cn}\rho)] e^{-jn\frac{2\pi}{p}\zeta} \right\} e^{-j\beta z} \quad (13)$$

$$H_z = \left\{ \sum_{n=-\infty}^{\infty} [C_n I_n(\tau_{cn}\rho) + D_n K_n(\tau_{cn}\rho)] e^{-jn\frac{2\pi}{p}\zeta} \right\} e^{-j\beta z} \quad (14)$$

$$E_\phi = \left\{ \sum_{n=-\infty}^{\infty} \left[\frac{-\beta_n n}{\tau_{cn}^2} \{A_n I_n(\tau_{cn}\rho) + B_n K_n(\tau_{cn}\rho)\} + \frac{-j\omega\mu_c}{\tau_{cn}} \{C_n I_n'(\tau_{cn}\rho) + D_n K_n'(\tau_{cn}\rho)\} \right] e^{-jn\frac{2\pi}{p}\zeta} \right\} e^{-j\beta z} \quad (15)$$

$$H_\phi = \left\{ \sum_{n=-\infty}^{\infty} \left[\frac{j\omega\epsilon_c}{\tau_{cn}} \{A_n I_n'(\tau_{cn}\rho) + B_n K_n'(\tau_{cn}\rho)\} + \frac{-\beta_n n}{\tau_{cn}^2} \{C_n I_n(\tau_{cn}\rho) + D_n K_n(\tau_{cn}\rho)\} \right] e^{-jn\frac{2\pi}{p}\zeta} \right\} e^{-j\beta z} \quad (16)$$

where

$$\beta_n = \beta + n\frac{2\pi}{p} \quad (17)$$

$$\tau_{cn}^2 = \beta_n^2 - k^2 \mu_r \epsilon_r \quad (18)$$

μ_r and ϵ_r are the relative permeability and permittivity of the substrate, and I_n and K_n represent modified Bessel functions. In the region $\rho > a$, the fields have the form

$$E_z = \left\{ \sum_{n=-\infty}^{\infty} E_n K_n(\tau_{on}\rho) e^{-jn\frac{2\pi}{p}\zeta} \right\} e^{-j\beta z} \quad (19)$$

$$H_z = \left\{ \sum_{n=-\infty}^{\infty} F_n K_n(\tau_{on}\rho) e^{-jn\frac{2\pi}{p}\zeta} \right\} e^{-j\beta z} \quad (20)$$

$$E_\phi = \left\{ \sum_{n=-\infty}^{\infty} \left[\frac{-\beta_n n}{\tau_{on}^2} E_n K_n(\tau_{on} \rho) + \frac{-j\omega\mu_o}{\tau_{on}} F_n K_n'(\tau_{on} \rho) \right] e^{-jn\frac{2\pi}{p}\zeta} \right\} e^{-j\beta z} \quad (21)$$

$$H_\phi = \left\{ \sum_{n=-\infty}^{\infty} \left[\frac{j\omega\epsilon_o}{\tau_{on}} E_n K_n'(\tau_{on} \rho) + \frac{-\beta_n n}{\tau_{on}^2} F_n K_n(\tau_{on} \rho) \right] e^{-jn\frac{2\pi}{p}\zeta} \right\} e^{-j\beta z} \quad (22)$$

where

$$\tau_{on}^2 = \beta_n^2 - k^2 \quad (23)$$

To construct a dispersion relationship in the form of a determinantal equation for β , we first assume a form for the current density on the tape and solve for the field coefficients appearing in the above expression in terms of the current coefficients. Components of current parallel and perpendicular to the direction of the tape can be defined in terms of the pitch angle ψ (Figure 1) to produce

$$J_\perp = J_z \cos \psi - J_\phi \sin \psi \quad (24)$$

$$J_\parallel = J_z \sin \psi + J_\phi \cos \psi \quad (25)$$

Previous studies [2-3,5-6] have assumed a constant transverse dependence for the current density, i.e.,

$$J_\perp = 0 \quad (26)$$

$$J_\parallel = \begin{cases} J_0 e^{-j\beta \frac{p}{2\pi} \phi} & -\frac{\delta}{2} < \zeta < \frac{\delta}{2} \\ 0 & \text{otherwise} \end{cases} \quad (27)$$

The parallel component can be expressed in terms of a Fourier expansion as

$$J_{\parallel} = \left\{ \sum_{n=-\infty}^{\infty} J_n e^{-jn \frac{2\pi}{p} \zeta} \right\} e^{-j\beta z} \quad (28)$$

where

$$J_n = \frac{J\delta}{p} \frac{\sin\left(\beta_n \frac{\delta}{2}\right)}{\beta_n \frac{\delta}{2}} \quad (29)$$

and β_n is defined in Equation (17).

The tangential electric and magnetic fields must satisfy the boundary conditions

$$E_z(\rho=b) = 0 \quad (30)$$

$$E_{\phi}(\rho=b) = 0 \quad (31)$$

$$E_z(\rho=a^-) = E_z(\rho=a^+) \quad (32)$$

$$E_{\phi}(\rho=a^-) = E_{\phi}(\rho=a^+) \quad (33)$$

$$H_z(\rho=a^+) - H_z(\rho=a^-) = -J_{\phi} = -J_{\parallel} \cos \psi \quad (34)$$

$$H_{\phi}(\rho=a^+) - H_{\phi}(\rho=a^-) = J_z = J_{\parallel} \sin \psi \quad (35)$$

Enforcing these conditions produces the system

$$\begin{bmatrix} I_b & K_b & 0 & 0 & 0 & 0 \\ 0 & 0 & I_b' & K_b' & 0 & 0 \\ I & K & 0 & 0 & -K_o & 0 \\ -f_1 I & -f_1 K & -f_2 I' & -f_2 K' & f_3 K_o & f_4 K_o' \\ 0 & 0 & -I & -K & 0 & K_o \\ -f_5 I' & -f_5 K' & f_1 I & f_1 K & f_6 K_o' & -f_3 K_o \end{bmatrix} \begin{bmatrix} A_n \\ B_n \\ C_n \\ D_n \\ E_n \\ F_n \end{bmatrix} = \begin{bmatrix} 0 \\ 0 \\ 0 \\ 0 \\ -J_n \cos \psi \\ J_n \sin \psi \end{bmatrix} \quad (36)$$

where

$$I = I_n(\tau_{cn} a) \quad (37)$$

$$K = K_n(\tau_{cn} a) \quad (38)$$

$$I_b = I_n(\tau_{cn} b) \quad (39)$$

$$K_b = K_n(\tau_{cn} b) \quad (40)$$

$$K_o = K_n(\tau_{on} a) \quad (41)$$

$$f_1 = \frac{n\beta_n}{\tau_{cn}^2 a} \quad (42)$$

$$f_2 = \frac{j\omega\mu_c}{\tau_{cn}} \quad (43)$$

$$f_3 = \frac{n\beta_n}{\tau_{on}^2 a} \quad (44)$$

$$f_4 = \frac{j\omega\mu_o}{\tau_{on}} \quad (45)$$

$$f_5 = \frac{j\omega\epsilon_c}{\tau_{cn}} \quad (46)$$

$$f_6 = \frac{j\omega\epsilon_0}{\tau_{on}} \quad (47)$$

and primes denote differentiation with respect to the arguments of the modified Bessel functions. For each pertinent value of n , Equation (36) can be solved for the six unknown coefficients in terms of J_n . To find the complex-valued propagation constant β , we enforce the additional condition that the E-field component parallel to the tape vanishes in the center of the tape, i.e., at $\zeta=0$. This produces the determinantal equation

$$\begin{aligned} 0 = \sum_{n=-\infty}^{\infty} J_n \left[\cot' \psi f_2 f_4 K_0' W_4 (f_6 K_0' W_1 + f_5 K_0 W_3) \right. \\ \left. + (1 - f_1 \cot \psi)^2 K_0 W_1 f_4 K_0' W_2 \right. \\ \left. + (1 - \cot \psi)^2 K_0 W_1 f_2 K_0 W_4 \right] \\ \left[(f_4 K_0' W_2 + f_2 K_0 W_4) (f_6 K_0' W_1 \right. \\ \left. + f_5 K_0 W_3) + (f_3 - f_1)^2 K_0 K_0' W_1 W_2 \right]^{-1} \end{aligned} \quad (48)$$

where

$$W_1 = (K_b I - I_b K) \quad (49)$$

$$W_2 = (K_b' I - I_b' K) \quad (50)$$

$$W_3 = (K' I_b - I' K_b) \quad (51)$$

and

$$W_4 = (K' I_b' - I' K_b) \quad (52)$$

For a given value of k , Equation (48) can be solved numerically for the complex-valued propagation constant β .

In the special case where the interior medium is identical to the exterior medium, i.e., $f_1=f_3$, $f_2=f_4$, $f_5=f_6$, and $K_0=K$, the determinantal equation simplifies to

$$0 = \sum_{n=-\infty}^{\infty} \frac{J_n}{K_b' K_b} \left\{ -k^2 a^2 \cot^2 \psi K_b K' (K' I_b' - I' K_b) + \left(\frac{n\beta_n \cot \psi}{\tau_n} - \tau_n a \right)^2 K_b' K (K_b I - I_b K) \right\} \quad (53)$$

Equation (53) describes the dispersion characteristics of a tape helix separated from a concentric conducting core by free space. In both Equations (48) and (53), the current density is assumed to be constant in the direction perpendicular to the helix pitch angle ψ . The coefficients J_n can be modified to model a more accurate distribution if desired. We have been unable to find Equation (53) previously reported in the literature. However, in the limiting case as the radius b of the inner conductor vanishes, this equation simplifies to

$$0 = \sum_{n=-\infty}^{\infty} J_n \left\{ k^2 a^2 \cot^2 \psi K' I + \left(\frac{n\beta_n \cot \psi}{\tau_n} - \tau_n a \right)^2 K I \right\} \quad (54)$$

which is the determinantal equation for the tape helix derived by Sensiper [2] and Klock [6].

3. INTERPRETATION OF THE k - β DIAGRAM FOR THE TAPE HELIX

Figure 3 shows a k - β diagram depicting the real part of β for a tape helix without a core or substrate [6]. Straight lines appearing in the figure represent asymptotes for the case of vanishing tape width δ . Points along the asymptote $k\rho = \beta \sin \psi$ represent axial propagation, and account for the geometrical slowing of the wave due to currents flowing in the direction of the helix. Near the intersection of this asymptote with the asymptote $k\rho = -\beta\rho + 2\pi$, the curve labelled "Mode 1" deviates away from axial propagation and into the radiation region of the diagram. Solutions for β along this curve are complex valued. Since $\beta > k$, these solutions represent slow waves.

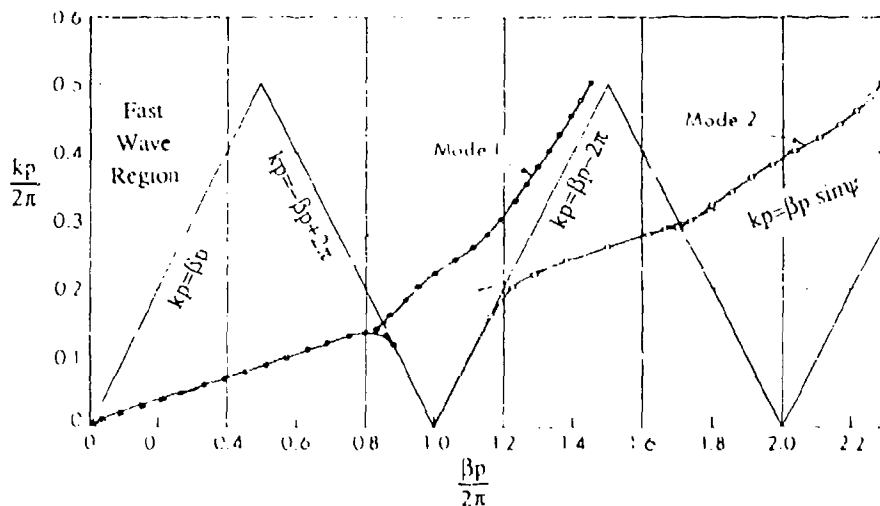


Figure 3. Real part of the k - β diagram for a tape helix with $\psi = 10^\circ$ and $(\delta/2a)\cot\psi = 0.1$ [6].

Although "Mode 1" is fundamentally a slow wave, because of the periodicity of the helix each term in the Fourier expansion of the fields acts as an independent harmonic with its own radiating or nonradiating character. By direct substitution, the functional dependence of the n -th harmonic can be written as

$$e^{-jn\frac{2\pi}{p}\zeta} e^{-j\beta z} = e^{-jn\phi} e^{-j\beta_n z} \quad (55)$$

where β_n is defined in Equation (17). Consider a point along the "Mode 1" curve where $\beta \cong 2\pi/p$. Although the $n=0$ harmonic is a slow wave with $\beta_0 \cong 2\pi/p$, the $n=-1$ harmonic has phase constant $\beta_{-1} \cong 0$ which is located in the fast wave region of the k - β diagram. In this case, the $n=-1$ harmonic is likely to excite a leaky wave. For the curve labelled "Mode 2," the $n=-2$ harmonic is such that β_{-2} is located in the fast wave region of the k - β diagram.

4. RADIATED FIELDS OF FINITE-LENGTH TAPE HELIX

Assuming that the fields have the form $e^{-j\beta z}$, the radiation pattern may be computed once the phase constant β is found from the dispersion relationship embodied in the determinantal equation. A finite length helix located along the z -axis with exactly N complete turns occupies the interval

$$-\frac{p}{2} < z < \frac{(2N-1)p}{2} \quad (56)$$

The presence of the conducting core and dielectric substrate complicate the calculation of far fields. However, given β , the near fields can be obtained from the expansions of Section 2. The far fields can be computed from equivalent sources located on the surface of the mathematical cylinder $\rho=a$, and defined in terms of the near fields. Neglecting radiation from the end-caps of the finite

mathematical cylinder, and assuming that only the harmonics between $n=-M$ and $n=M$ are significant, these equivalent sources have the form

$$K_{\phi}(\phi, z) = E_z(a, \phi, z) = \sum_{n=-M}^M E_{zn} e^{-j\beta_n z} e^{-jn\phi} \quad (57)$$

$$J_{\phi}(\phi, z) = -H_z(a, \phi, z) = - \sum_{n=-M}^M H_{zn} e^{-j\beta_n z} e^{-jn\phi} \quad (58)$$

$$K_z(\phi, z) = E_{\phi}(a, \phi, z) = \sum_{n=-M}^M E_{\phi n} e^{-j\beta_n z} e^{-jn\phi} \quad (59)$$

$$J_z(\phi, z) = -H_{\phi}(a, \phi, z) = - \sum_{n=-M}^M H_{\phi n} e^{-j\beta_n z} e^{-jn\phi} \quad (60)$$

and are truncated in z according to Equation (56). The coefficients are apparent from the field expansions from Section 2, i.e., $E_{zn}=E_n K_n(\tau_{0na})$, etc. The fields produced by these equivalent sources may be found in the usual manner from the magnetic and electric vector potentials [12]

$$\bar{A}(r, \theta, \phi) = \iint \bar{J}(\phi', z') \frac{e^{-jkR}}{4\pi R} a d\phi' dz' \quad (61)$$

$$\bar{F}(r, \theta, \phi) = \iint \bar{K}(\phi', z') \frac{e^{-jkR}}{4\pi R} a d\phi' dz' \quad (62)$$

where the integration is over the surface of the cylinder with $\rho=a$. For far-field calculations,

$$R \equiv r - a \sin \theta \cos(\phi - \phi') - z' \cos \theta \quad (63)$$

After substituting the preceding expansions into Equations (61) and (62), we arrive at the expressions

$$\begin{aligned} \bar{A}(r, \theta, \phi) = & \frac{e^{-jkr}}{4\pi r} e^{-j\gamma(N-1)} p\pi a \frac{\sin(N\gamma)}{\sin(\gamma)} \\ & \sum_{n=-M}^M \frac{\sin(\xi_n)}{\xi_n} j^n e^{jn\phi} \left\{ \hat{z} H_{0n} 2J_n(ka \sin \theta) \right. \\ & + \hat{\rho} H_{zn} [J_{n-1}(ka \sin \theta) + J_{n+1}(ka \sin \theta)] \\ & \left. + j \hat{\phi} H_{zn} [J_{n-1}(ka \sin \theta) - J_{n+1}(ka \sin \theta)] \right\} \end{aligned} \quad (64)$$

and

$$\begin{aligned} \bar{F}(r, \theta, \phi) = & \frac{e^{-jkr}}{4\pi r} e^{-j\gamma(N-1)} p\pi a \frac{\sin(N\gamma)}{\sin(\gamma)} \\ & \sum_{n=-M}^M \frac{\sin(\xi_n)}{\xi_n} j^n e^{jn\phi} \left\{ -\hat{z} E_{\phi n} 2J_n(ka \sin \theta) \right. \\ & - \hat{\rho} E_{zn} [J_{n-1}(ka \sin \theta) + J_{n+1}(ka \sin \theta)] \\ & \left. - j \hat{\phi} E_{zn} [J_{n-1}(ka \sin \theta) - J_{n+1}(ka \sin \theta)] \right\} \end{aligned} \quad (65)$$

where

$$\gamma = \frac{p}{2} (\beta - k \cos \theta) \quad (66)$$

$$\xi_n = \frac{p}{2} (\beta_n - k \cos \theta) \quad (67)$$

and J_n now denotes the Bessel function of the first kind.

In general, the helix will radiate an elliptically polarized wave. The far zone electric field components are proportional to

$$E_\theta(\theta, \phi) \propto e^{-j\gamma(N-1)} \frac{\sin(N\gamma)}{\sin(\gamma)} \sum_{n=-M}^M \frac{\sin(\xi_n)}{\xi_n} j^n e^{jn\phi} \\ \left\{ -\eta \sin\theta H_{\phi n} 2J_n(ka \sin\theta) + \eta \cos\theta H_{zn} [J_{n-1}(ka \sin\theta) \right. \\ \left. + J_{n+1}(ka \sin\theta)] + j E_{zn} [J_{n-1}(ka \sin\theta) - J_{n+1}(ka \sin\theta)] \right\} \quad (68)$$

and

$$E_\phi(\theta, \phi) \propto e^{-j\gamma(N-1)} \frac{\sin(N\gamma)}{\sin(\gamma)} \sum_{n=-M}^M \frac{\sin(\xi_n)}{\xi_n} j^n e^{jn\phi} \\ \left\{ -\sin\theta E_{\phi n} 2J_n(ka \sin\theta) + \cos\theta E_{zn} [J_{n-1}(ka \sin\theta) \right. \\ \left. + J_{n+1}(ka \sin\theta)] + j\eta H_{zn} [J_{n-1}(ka \sin\theta) - J_{n+1}(ka \sin\theta)] \right\} \quad (69)$$

Note the presence of an array factor due to the N-turn helix in the form

$$\frac{\sin(N\gamma)}{\sin(\gamma)} \quad (70)$$

where γ is complex-valued and defined in Equation (66). Because $\text{Re}(\beta) > k$, the main lobe of Equation (70) is not located in the visible region. The contribution from each harmonic contains the term

$$\frac{\sin(\xi_n)}{\xi_n} e^{jn\phi} \quad (71)$$

where ξ_n is defined in Equation (67). Based on the discussion from Section 3, we might expect that the harmonic exciting the leaky wave will be the main contributor to the far fields. Thus, it may be possible to approximate the far-field pattern using only that harmonic in Equations (68) and (69). A simple approximation to the pattern may be obtained by the product of Equations (70) and (71).

5. NUMERICAL RESULTS AND DISCUSSION

A computer program was created to solve Equation (48) for the values of β corresponding to a given k . This task involved finding zeros of a fairly complicated function in the complex plane, but was simplified somewhat because the solutions initially follow the asymptotes as suggested by Figure 3. Starting from these solutions, it is possible to increment k by small amounts in order to track β as the curve deviates from the line $k\rho = \beta p \sin \psi$. Figure 4 shows the k - β diagram obtained for a tape helix separated from a conducting core by free space, with $b/a=0.8$ and several pitch angles. As the solutions for β deviate from the line $k\rho = \beta p \sin \psi$, β becomes complex valued. However, Figure 4b illustrates that at some larger value of k , the solutions again become real valued. We only expect complex-valued solutions in this region of the k - β diagram, and these real-valued solutions are a spurious result caused by the numerical algorithm used to track β . In actuality, the algorithm employed for these preliminary results seeks a minimum of the right-hand side of Equation (48) rather than a true zero. We believe that the true curve stops at the point where β becomes real-valued, as suggested by some of the results of Klock [6].

Figure 5 shows a similar k - β diagram to illustrate the effect of differing core size. In common with Figure 4, the solutions deviate from the initial asymptote and become complex valued. They also subsequently become real-valued as k increases, suggesting that they no longer represent solutions of the determinantal equation and are a spurious result of the numerical algorithm. Figure 6 shows the effect of different substrate materials on the k - ρ diagram.

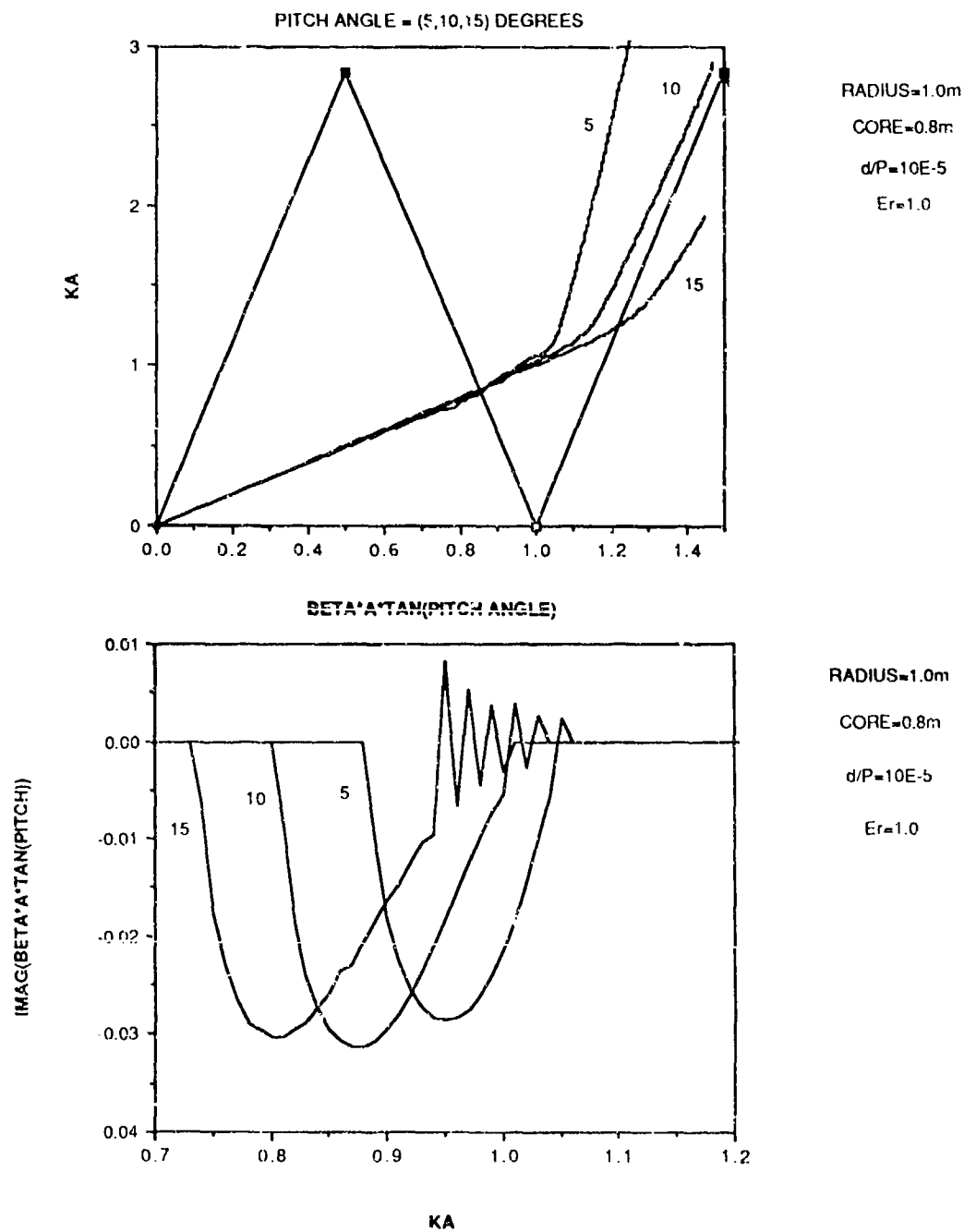


Figure 4. k - β diagram for a helix with $b/a=0.8$ and $\mu_r = \epsilon_r = 1$, for several pitch angles. a) $\text{Re}(\beta)$ versus k b) $\text{Im}(\beta)$ versus k

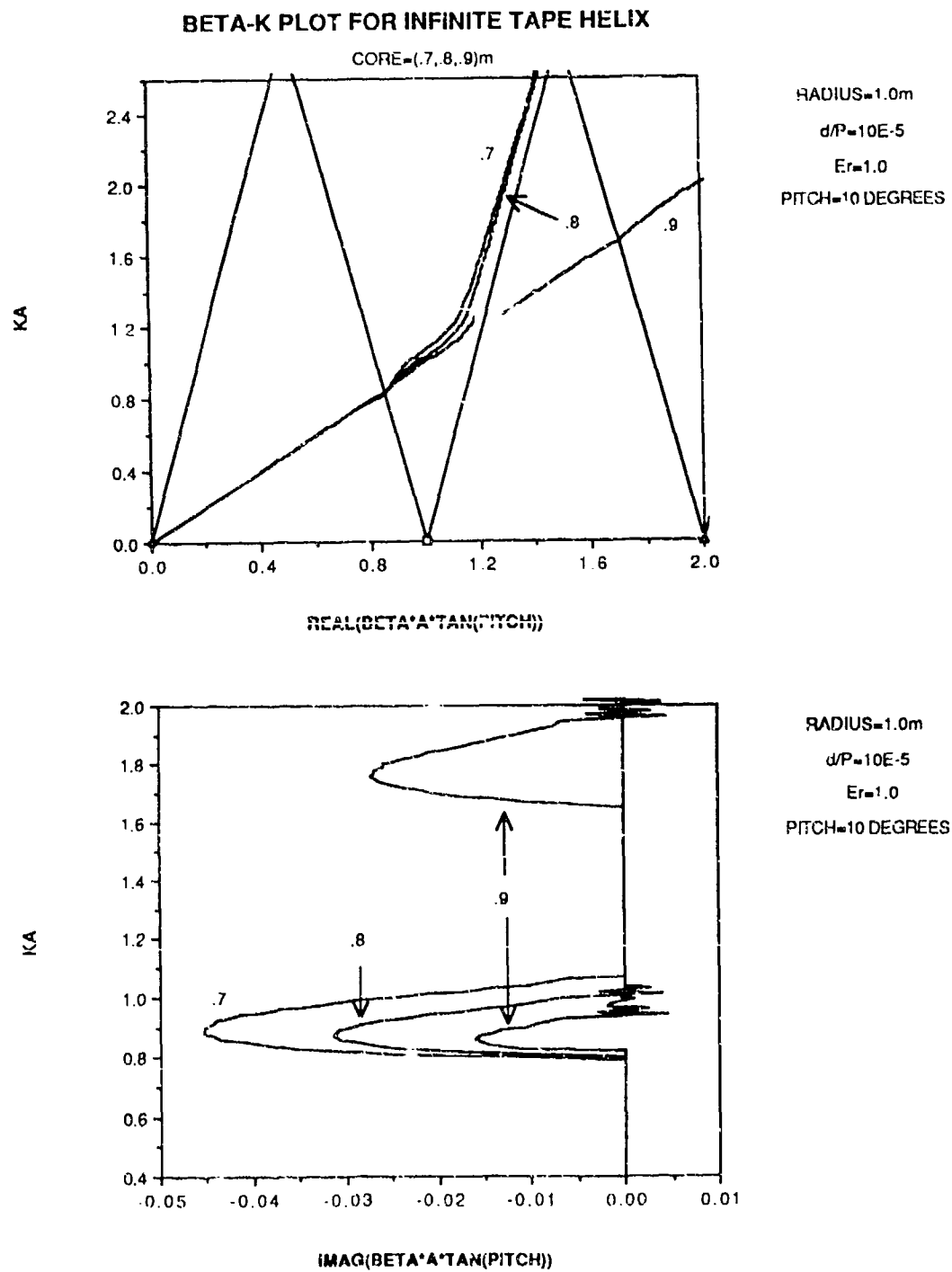


Figure 5. k - β diagram for a helix with $\psi=10^\circ$ and $\mu_r=\epsilon_r=1$, for several core sizes. a) $\text{Re}(\beta)$ versus k b) $\text{Im}(\beta)$ versus k

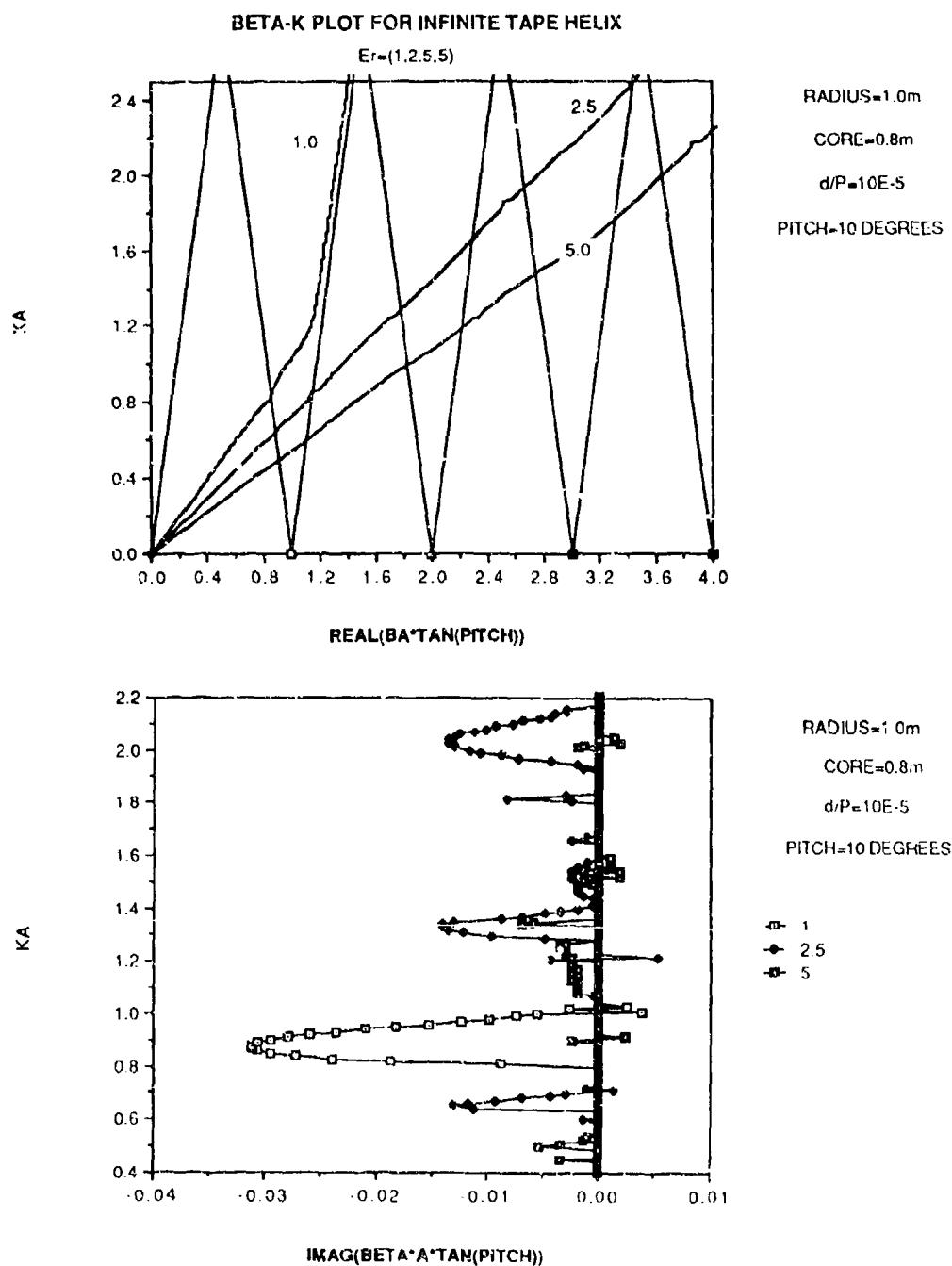


Figure 6. k - β diagram for a helix with $\psi=10^\circ$ and $b/a=0.8$, as a function of substrate permittivity. a) $\text{Re}(\beta)$ versus k b) $\text{Im}(\beta)$ versus k

Figure 7 shows power radiation patterns of a finite-length 10-turn helix with $b/a=0.8$ as a function of frequency. For $ka=0.8$, radiation is concentrated in the backward direction (Figure 7a). As frequency increases, the beam shifts to broadside (Figures 7d-g). To generate these patterns, Equations (68) and (69) were employed with $M=3$. Numerical experimentation revealed, however, that only the $n=-1$ harmonic contributes significantly to the patterns. Figure 8 shows the radiation patterns corresponding to two different pitch angles. Figure 9 shows similar patterns corresponding to different substrate materials. Although we have not verified these patterns experimentally, they agree qualitatively with Adams' results for a quadrifilar helix [8].

RADIATION PATTERN FOR TAPE HELIX

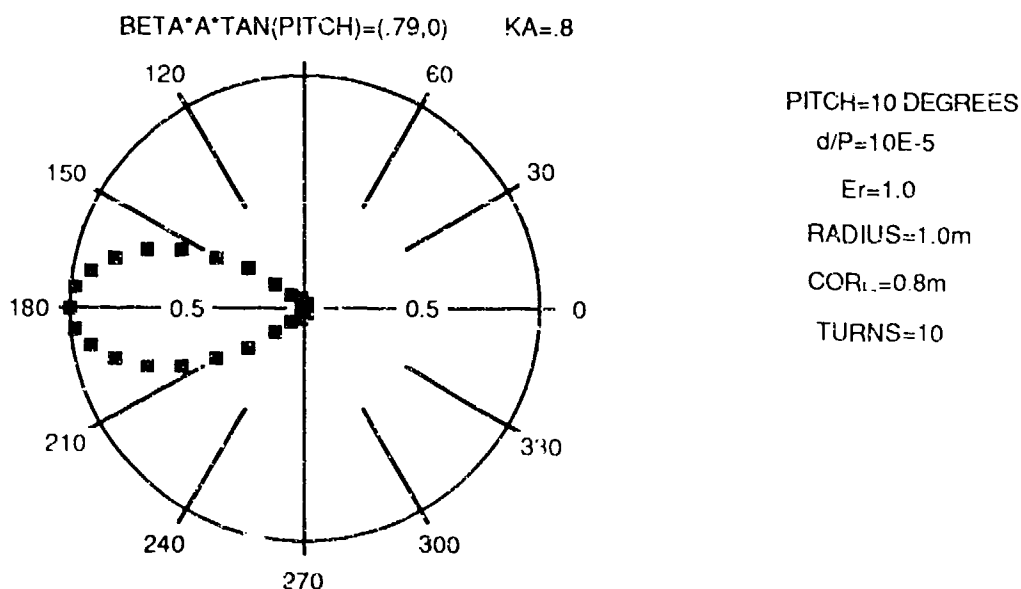
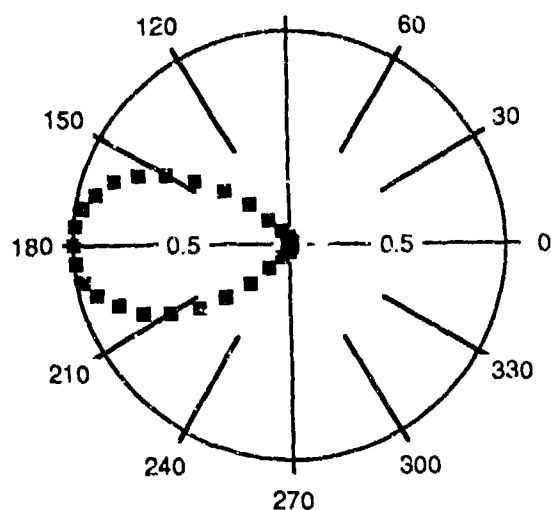


Figure 7. Radiation pattern of a 10-turn helix. a) $\beta = 0.79-j0.0$

RADIATION PATTERN FOR TAPE HELIX

$$\text{BETA} \cdot \text{A} \cdot \text{TAN}(\text{PITCH}) = (.8, -.01) \quad \text{KA} = .81$$



PITCH=10 DEGREES

$d/P = 10E-5$

$\epsilon_r = 1.0$

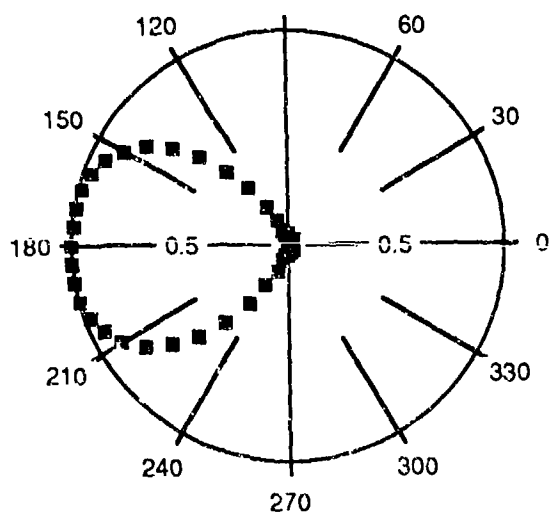
RADIUS=1.0m

CORE=0.8m

TURNS=10

RADIATION PATTERN FOR TAPE HELIX

$$\text{BETA} \cdot \text{A} \cdot \text{TAN}(\text{PITCH}) = (.84, -.03) \quad \text{KA} = .85$$



PITCH=10 DEGREES

$d/P = 10E-5$

$\epsilon_r = 1.0$

RADIUS=1.0m

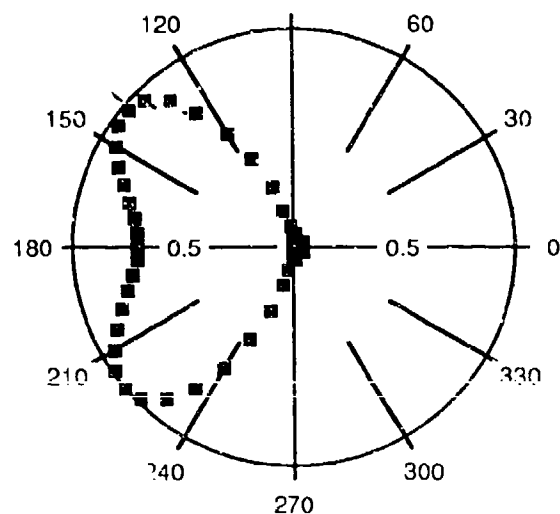
CORE=0.8m

TURNS=10

Figure 7. Radiation pattern of a 10-turn helix. b) $\beta = 0.8 - j0.01$ c) $\beta = 0.84 - j0.03$

RADIATION PATTERN FOR TAPE HELIX

$$\text{BETA} \cdot \text{A} \cdot \text{TAN}(\text{PITCH}) = (.89, -.03) \quad \text{KA} = .9$$



PITCH=10 DEGREES

$$d/P = 10E-5$$

$$\epsilon_r = 1.0$$

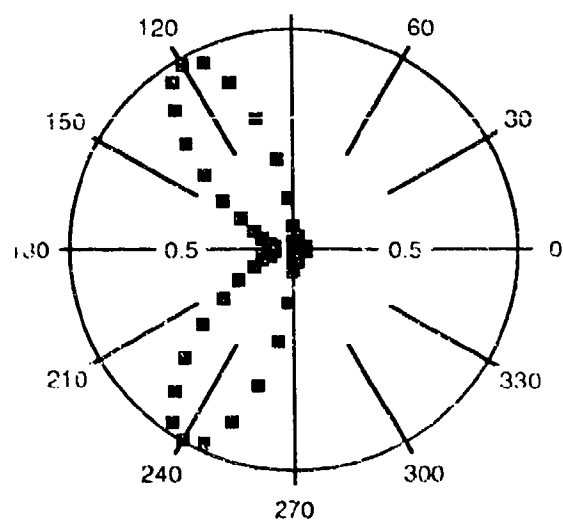
$$\text{RADIUS} = 1.0\text{m}$$

$$\text{CORE} = 0.8\text{m}$$

$$\text{TURNS} = 10$$

RADIATION PATTERN FOR TAPE HELIX

$$\text{BETA} \cdot \text{A} \cdot \text{TAN}(\text{PITCH}) = (.94, -.02) \quad \text{KA} = .95$$



PITCH=10 DEGREES

$$d/P = 10E-5$$

$$\epsilon_r = 1.0$$

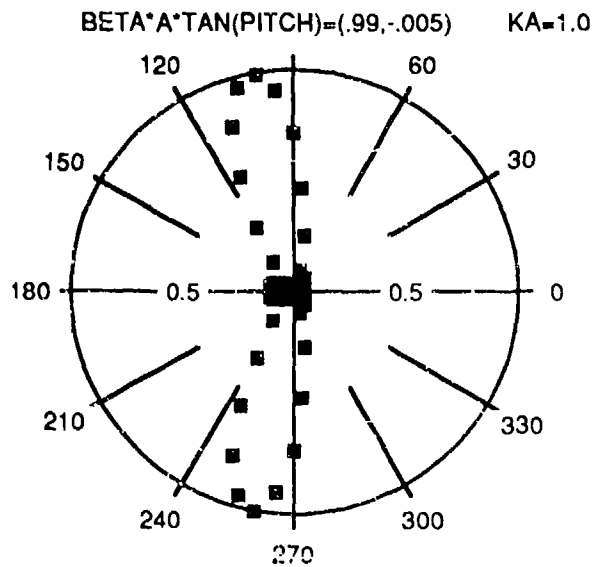
$$\text{RADIUS} = 1.0\text{m}$$

$$\text{CORE} = 0.8\text{m}$$

$$\text{TURNS} = 10$$

Figure 7. Radiation pattern of a 10 turn helix. d) $\beta = 0.89 - j0.03$ c) $\beta = 0.94 - j0.02$

RADIATION PATTERN FOR TAPE HELIX



PITCH=10 DEGREES

$d/P = 10E-5$

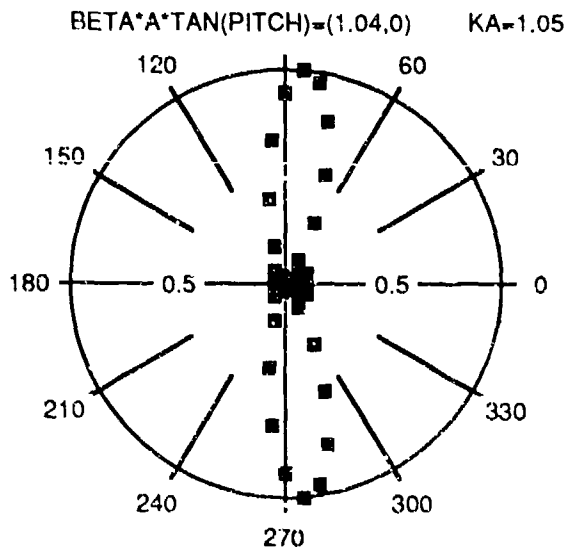
$\epsilon_r = 1.0$

RADIUS=1.0m

CORE=0.8m

URNS=10

RADIATION PATTERN FOR TAPE HELIX



PITCH=10 DEGREES

$d/P = 10E-5$

$\epsilon_r = 1.0$

RADIUS=1.0m

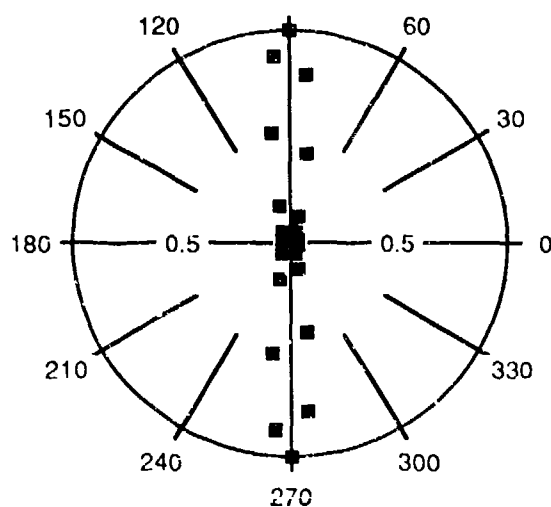
CORE=0.8m

URNS=10

Figure 7. Radiation pattern of a 10-turn helix. f) $\beta = 0.99 - j0.01$ g) $\beta = 1.04 - j0.0$

RADIATION PATTERN FOR A FINITE TAPE HELIX

$$\text{BETA} \cdot \text{A} \cdot \text{TAN}(\text{PITCH}) = (.998, -.003) \quad \text{KA} = 1.0$$



PITCH=15 DEGREES

$$d/P = 10E-5$$

$$\text{Er} = 1.0$$

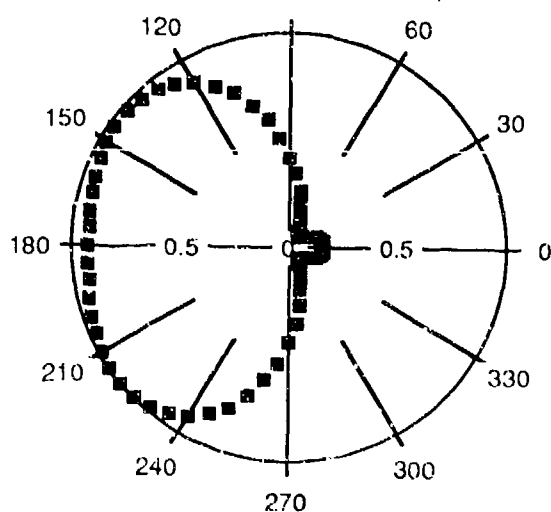
$$\text{RADIUS} = 1.0\text{m}$$

$$\text{CORE} = 0.8\text{m}$$

$$\text{TURNS} = 10$$

RADIATION PATTERN FOR A FINITE TAPE HELIX

$$\text{BETA} \cdot \text{A} \cdot \text{TAN}(\text{PITCH}) = (.956, -.022) \quad \text{KA} = 1.0$$



PITCH=5 DEGREES

$$d/P = 10E-5$$

$$\text{Er} = 1.0$$

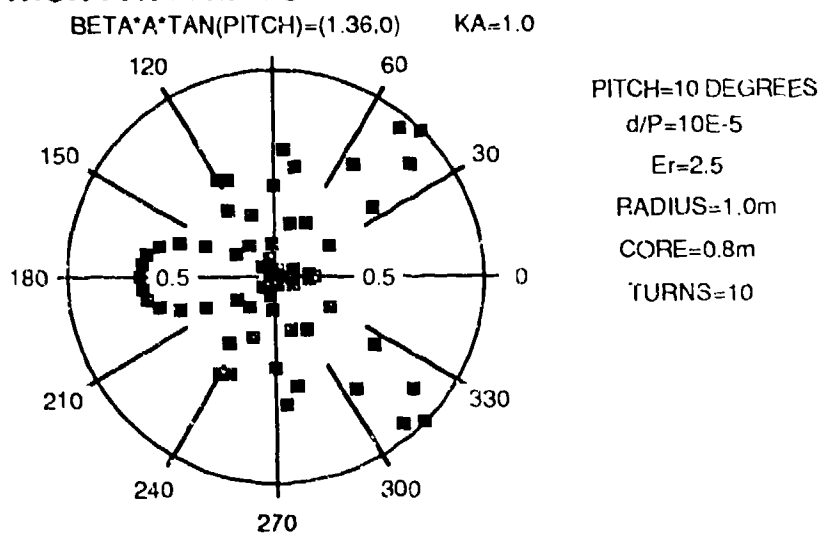
$$\text{RADIUS} = 1.0\text{m}$$

$$\text{CORE} = 0.8\text{m}$$

$$\text{TURNS} = 10$$

Figure 8. Radiation pattern of a 10-turn helix. a) $\psi = 15^\circ$ b) $\psi = 5^\circ$

RADIATION PATTERN FOR A FINITE TAPE HELIX



RADIATION PATTERN FOR A FINITE TAPE HELIX

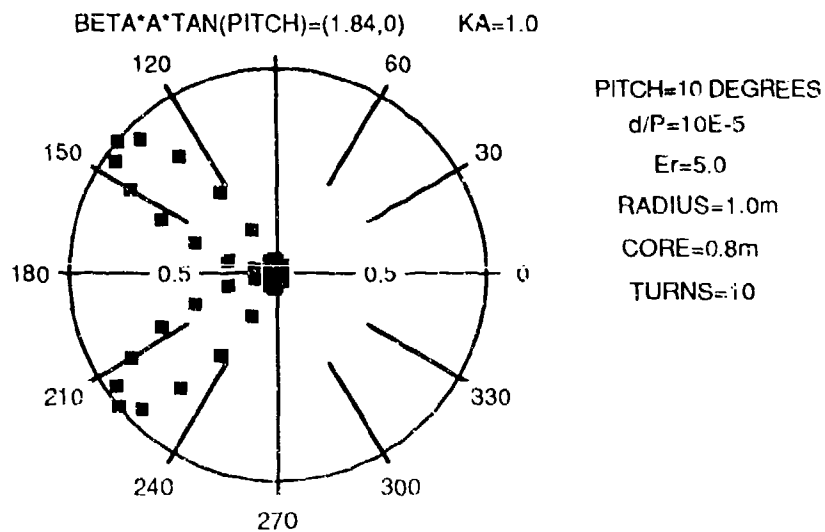


Figure 9. Radiation pattern of a 10-turn helix. a) $\epsilon_r = 2.5$ b) $\epsilon_r = 5.0$

6. CONCLUSIONS

The determinantal equation has been derived for an infinite tape helix separated from a concentric conducting core by a dielectric substrate. This equation can be solved to produce the k - β diagram describing propagation along the helix. Solutions for the complex-valued propagation constant β provide information about the excitation of leaky waves, and have been studied for several helical geometries. In addition, the radiation patterns of several finite-length helical structures have been estimated assuming the form of the fields along the helix.

7. REFERENCES

- [1] Kraus, J. D. (1950) *Antennas*. McGraw-Hill, New York.
- [2] Sensiper, S. (1955) "Electromagnetic wave propagation on helical structures," *Proc. IRE*, vol. 43, no. 2, pp. 149-161.
- [3] Watkins, D. A. (1958) *Topics in Electromagnetic Theory*. Wiley, New York.
- [4] Hayes, R. E. (1960) "Higher order modes in coupled helices," *IRE Trans. Microwave Theory Tech.*, vol MTT-8, no. 1, pp. 119-120.
- [5] Mittra, R. (1963) "Wave propagation on helices," *IEEE Trans. Antennas Propagat.*, vol. AP-11, no. 9, pp. 585-586.
- [6] Klock, P. W. (1963) "A study of wave propagation on helices," Ph.D. Dissertation, University of Illinois, Urbana, IL.

- [7] Neureuther, A. R., Klock, P. W., and Mittra, R. (1967) "A study of the sheath helix with a conducting core and its application to the helical antenna," *IEEE Trans. Antennas Propagat.*, vol. AP-15, pp. 203-210.
- [8] Adams, A. T. (1968) "Helix modes 1 and 2 of Klock," *IEEE Trans. Antennas Propagat.*, vol. AP-16, no. 7, pp. 491-493.
- [9] Hessel, A. (1969) "General characteristics of traveling-wave antennas," in *Antenna Theory*, R. E. Collin and F. J. Zucher, Eds., McGraw-Hill, New York.
- [10] Ivanov, K. P. and Ganchev, S. I. (1971) "Ferrite-loaded helical line with coaxial inner conductor," *IEEE Trans. Microwave Theory Tech.*, vol. MTT-19, no. 9, pp. 784-786.
- [11] Basu, B. N., Pal, B. B., Singh, V. N. and Vaidya, N. C. (1984) "Optimum design of a potentially dispersion-free helical slow-wave circuit of a broad-band TWT," *IEEE Trans. Microwave Theory Tech.*, vol. MTT-32, no. 4, pp. 461-463.
- [12] Harrington, R. F. (1961) *Time Harmonic Electromagnetic Fields*. McGraw-Hill, New York.

ADVANCED ARCHITECTURE FOR A MONOPULSE
ACTIVE APERTURE ARRAY*

Peter D. Hrycak
Ann C. Sullivan
Dr. Gary E. Evans

Westinghouse Electric Corporation
Electronic Systems Group
Development and Operations Division
Baltimore, Maryland 21205

Abstract

A unique architecture for an active aperture array with monopulse capability is described in this paper. The traditional approach requires three beamforming networks: uniform transmit, receive ultra-low sidelobe sum, and receive ultra-low sidelobe difference. This architecture exploits the potential inherent in the next generation MMIC T/R module to: reduce the required beamformers from three to two, simultaneously error correct the receive monopulse beams, and to simplify the beamformers. A noise figure analysis of this technique will be presented which compares the noise figure of this new architecture to that of a conventional single beam active array.

* The work described herein was supported by the United States Air Force, Electronic Systems Division, Hanscom AFB, through contract no. F19628-88-C-0116 and under the direction of Mr. John Antonucci.

1.0 Introduction and Summary

The next generation of airborne surveillance arrays is foreseen to have T/R modules, radiators, and beam formers embedded into the contoured skin of the aircraft, with rf, logic, and power distributed in compact flush networks. The sophistication of the T/R modules is steadily increasing as microprocessors and MMICs rapidly decrease in size. The limiting components are, or soon will be, the radiators, networks, and perhaps the circulators, which have fundamental physical size and shape requirements for good electrical performance. These conflict with the physical constraints of the embedded, conformal configuration. The objective of the study on which this paper is based has been to exploit the potential of the new generation of T/R modules to overcome these limitations. This has been done at length, resulting in a new beam former architecture. It was assumed that the system requirements are such that 3 beamforming networks are required in the elevation plane: uniform amplitude on transmit, low sidelobe sum beam and difference beams on receive. A new architecture has been conceived which reduces the number of beamformers from three to two, simplifies the construction of these networks, and allows simultaneous error correction for both sum and difference which relaxes the network manufacturing precision.

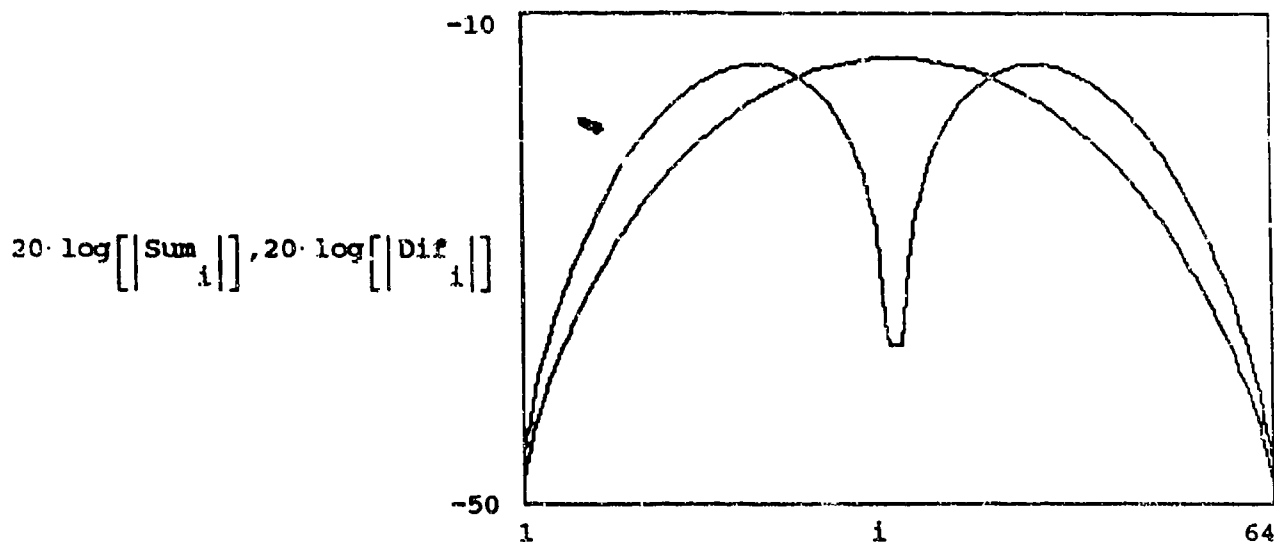
2.0 Architecture Selection

Most architectures for airborne surveillance arrays depend on beam manipulation in azimuth to eliminate jamming, which is concentrated near the horizon. Consequently, the azimuth networks are complex and the hardware is minimized by collecting first in many columns rather than in many rows. Thus the many column beamformers make up the bulk of the r.f. combining network, and simplification of that architecture has the highest priority. It is assumed that independent transmit and receive signals are involved, and that monopulse is necessary. It would appear that 3 independent combiners are necessary, with independent errors to be compensated. Closer examination shows that with the flexibility of a controllable T/R module coupled with optimal beam former architecture selection, this can be significantly simplified.

In this paper, four elevation beamforming architectures will be compared; the conventional architecture, a Westinghouse architecture, Poirier's method of manifold elimination [1], and a fourth approach which combines the Westinghouse architecture and Poirier's method of manifold elimination. It is important to note that planar array distributions were used only for the comparison of architectures, but the results apply equally to a curved array.

2.1 Conventional Architecture

Existing architectures employ three beamforming networks in the elevation plane: a uniform amplitude beamforming network used for transmit, a receive Sum beamforming network, and a receive Difference beamforming network as shown in Figure 2.1-1. On receive, one can correct errors within one of the receive beamforming networks, let us for sake of argument say the Sum network, by using the phase and amplitude controls within the T/R modules, but these errors will be translated into the receive Difference network which will further degrade the sidelobe performance of this beam. Below is a plot of both the Sum and Difference illumination tapers for a low sidelobe set of monopulse beams for a planar array with 64 elements in the elevation plane. The sum taper is for a pattern where the first three sidelobes are at -50 dB down from the main lobe and the rest fall off as $1/R$. The difference taper is for a pattern where the first three sidelobes are at -48 dB from the difference main lobes with the rest falling off as $1/R$.



[1] "Simplified MMIC Active Aperture Feeding", J. Leon Poirier, Internal Report Rome Air Development Center, Date Unknown.

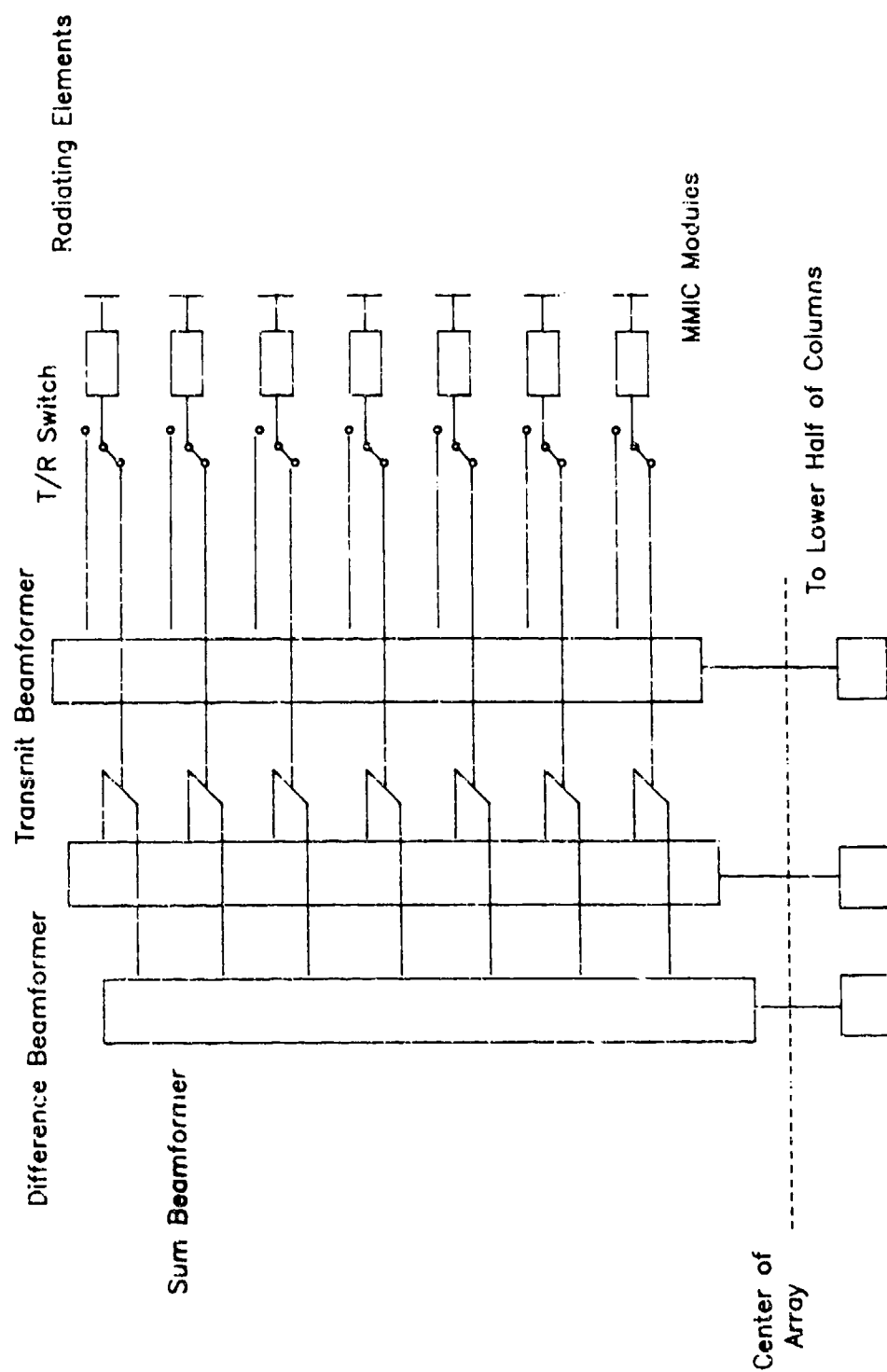


Figure 2.1-1. Conventional Architecture

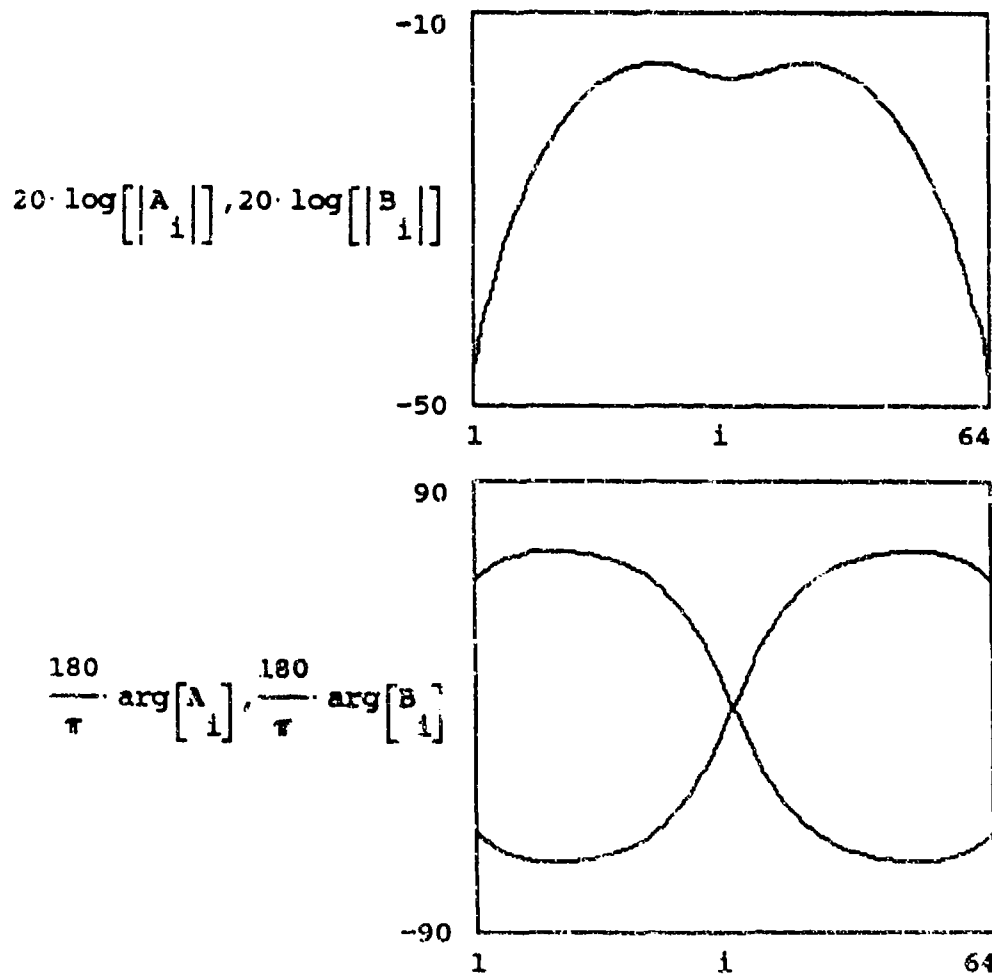
.2 Westinghouse Architecture

A Westinghouse architecture is shown in Figure 2.2-1 which has the potential of simultaneously correcting the Sum and Difference receive beams. This architecture consists of forming "Sum + j Difference" and "Sum - j Difference" beamformers. In order to better understand this architecture, let's take the Sum and Difference tapers described in section 2.1 and add them in quadrature. Hence, we'll have two new functions.

$$A_1 := \text{Sum}_1 + j \cdot \text{Dif}_1$$

$$B_1 := \text{Sum}_1 - j \cdot \text{Dif}_1$$

These two new functions are obviously the complex conjugate of each other. In terms of these functions being implemented within a microwave distribution network, the two networks are identical, but physically flipped as can be shown in the plots of these two functions below.



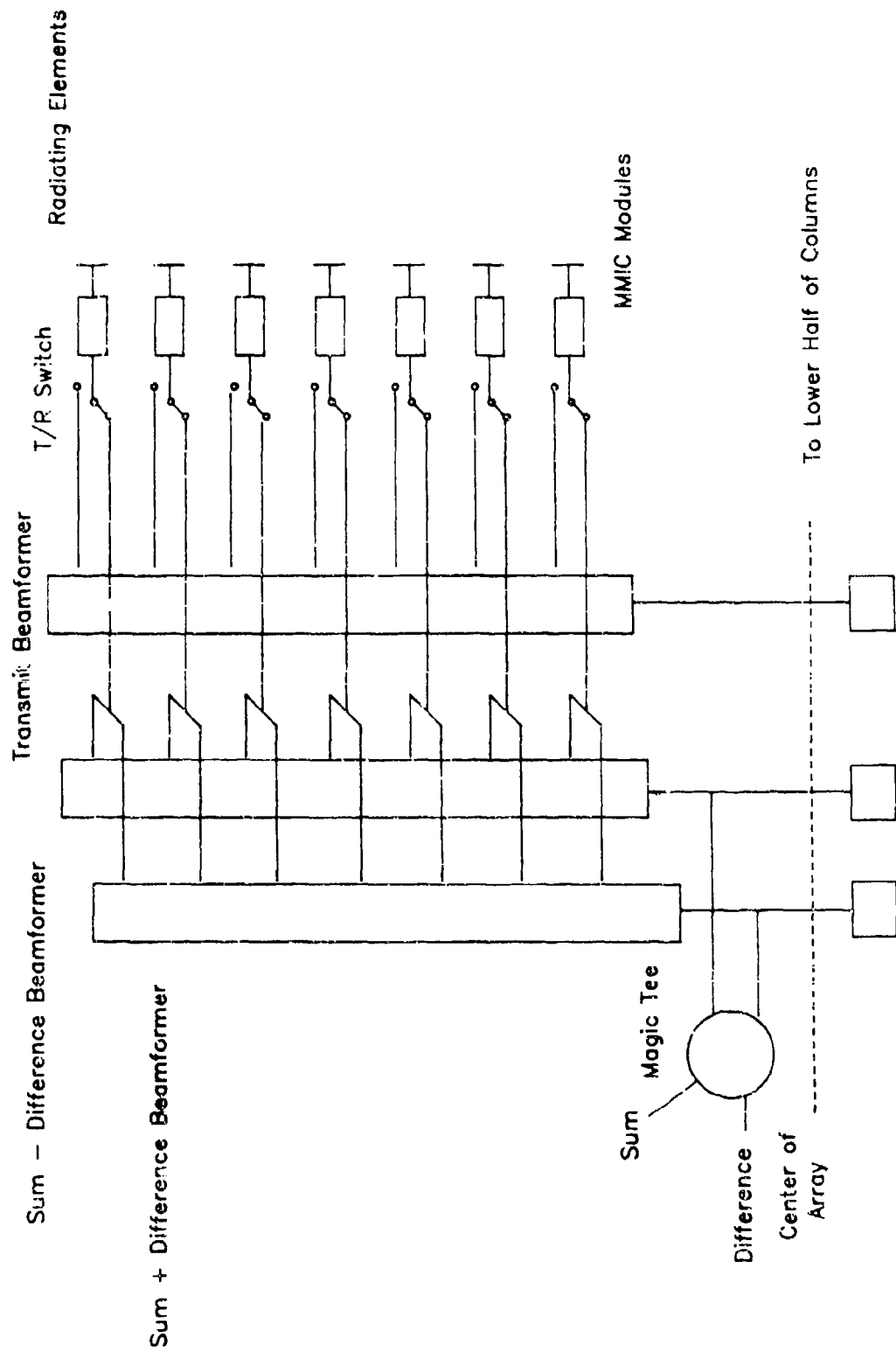
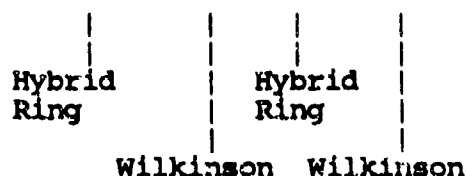


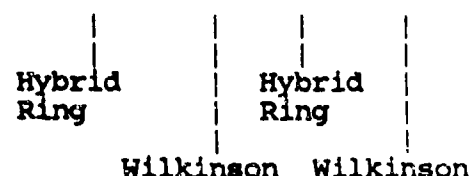
Figure 2.2-1 Baseline Architecture

In order to extract the original sum and difference functions, we need to implement a magic tee into the overall beamforming network. Before we get to the radiating element, we need to go through a -3.01 dB Wilkinson combiner. The mathematical formulation of this network is shown below.

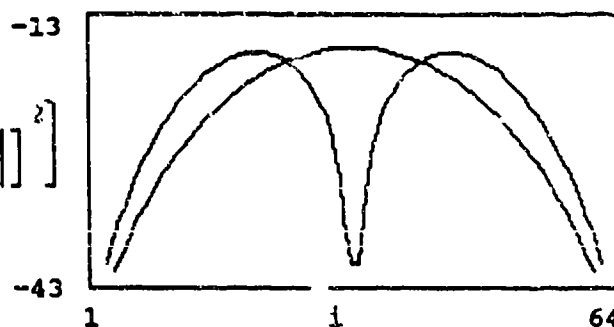
$$\text{Sumnew}_1 := \frac{1}{\sqrt{2}} \cdot A \cdot \frac{1}{\sqrt{2}} + \frac{1}{\sqrt{2}} \cdot B \cdot \frac{1}{\sqrt{2}}$$



$$\text{Difnew}_1 := \frac{1}{\sqrt{2}} \cdot A \cdot \frac{1}{\sqrt{2}} - \frac{1}{\sqrt{2}} \cdot B \cdot \frac{1}{\sqrt{2}}$$



$$10 \cdot \log \left[\left| \left| \text{Sumnew}_1 \right| \right|^2 \right], 10 \cdot \log \left[\left| \left| \text{Difnew}_1 \right| \right|^2 \right]$$



It should be noted that we have extracted the original illumination functions. For an active aperture, a -3.01 dB additional return loss in the receive chain should have a minimal if not inconsequential impact. The key features of this architecture are:

1. Only one network needs to be developed and used twice.
2. Since the topology of the network is such that it is symmetric about the center (with the exception of the output phases), it is possible for us to compensate for any errors within the manifolds with the controls available within the T/R modules. The output phasing should be able to be manufactured with great accuracy since they are only line lengths.

This architecture simplifies the overall receive beamforming network, but three beamforming networks are still required.

Poirier, in his paper, described an architecture (Figure 2.3-1) which reduces the number of beamforming manifolds from 3 to 2. This architecture exploits the use of a variable attenuator within the T/R module to use the uniform amplitude transmit network to perform the tapering required for the low sidelobe receive beam. In order to form a low sidelobe difference beam, a modified difference beamformer is used which when combined with the attenuation provided by the T/R modules, forms a low sidelobe difference receive beam. As with the architecture described in section 2.2, one suffers a -3.01 dB receive beamsharing loss, the impact of which can be reduced by the use of a high gain, low S/N LNA in the T/R module. However, as Poirier points out in his paper, if one uses the T/R modules for network error compensation for the sum beam, the errors get translated into the difference beamformer. Simultaneous beam correction would not be possible with a conventional T/R module.

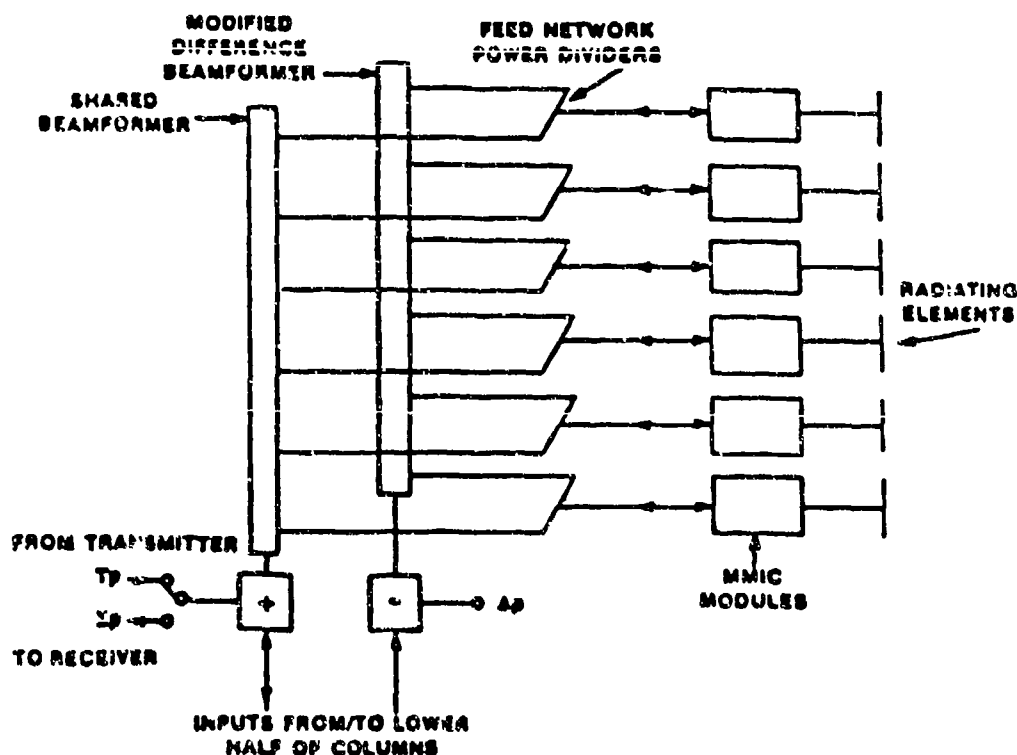


Figure 2.3-1 Poirier's method of manifold elimination

2.4 Combination Architecture

The Westinghouse architecture described section 2.2 simplifies the overall receive beamforming network, but three beamforming networks are still required for an active aperture system with receive monopulse. A means of reducing the required networks from 3 to 2 would be to build a beamforming network with uniform amplitudes, but with the phase tapers described for the A_1 and B_1 networks. Since the amplitude is uniform, one of these networks would be used for the transmit function with the transmit phase shifters being used to collimate the beam in a desired direction. On receive, we would use a modification of the Westinghouse architecture with the exception that the attenuators within the T/R module would form the final illumination taper for both sum and difference receive beams. This new architecture is shown in Figure 2.4-1.

Let us consider two new networks: C and D with uniform amplitudes and the phase tapers found in the A and B networks.

$$C_1 := \frac{1}{\sqrt{64}} \left[\cos[\arg[A_1]] + j \cdot \sin[\arg[A_1]] \right]$$

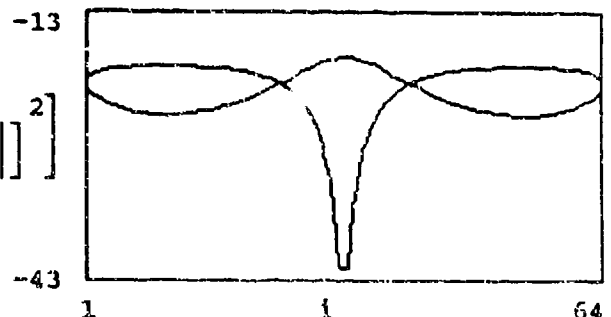
$$D_1 := \frac{1}{\sqrt{64}} \left[\cos[\arg[B_1]] + j \cdot \sin[\arg[B_1]] \right]$$

If we use a network for the above two dividers comparable to the one defined for the A and B system of receive networks, (figure 2.2-1) we obtain:

$$\text{Sumnear}_1 := \frac{1}{\sqrt{2}} C_1 \cdot \frac{1}{\sqrt{2}} + \frac{1}{\sqrt{2}} D_1 \cdot \frac{1}{\sqrt{2}}$$

$$\text{Difnear}_1 := \frac{1}{\sqrt{2}} C_1 \cdot \frac{1}{\sqrt{2}} - \frac{1}{\sqrt{2}} D_1 \cdot \frac{1}{\sqrt{2}}$$

$$10 \cdot \log \left[\left| \left| \text{Sumnear}_1 \right| \right|^2 \right], 10 \cdot \log \left[\left| \left| \text{Difnear}_1 \right| \right|^2 \right]$$



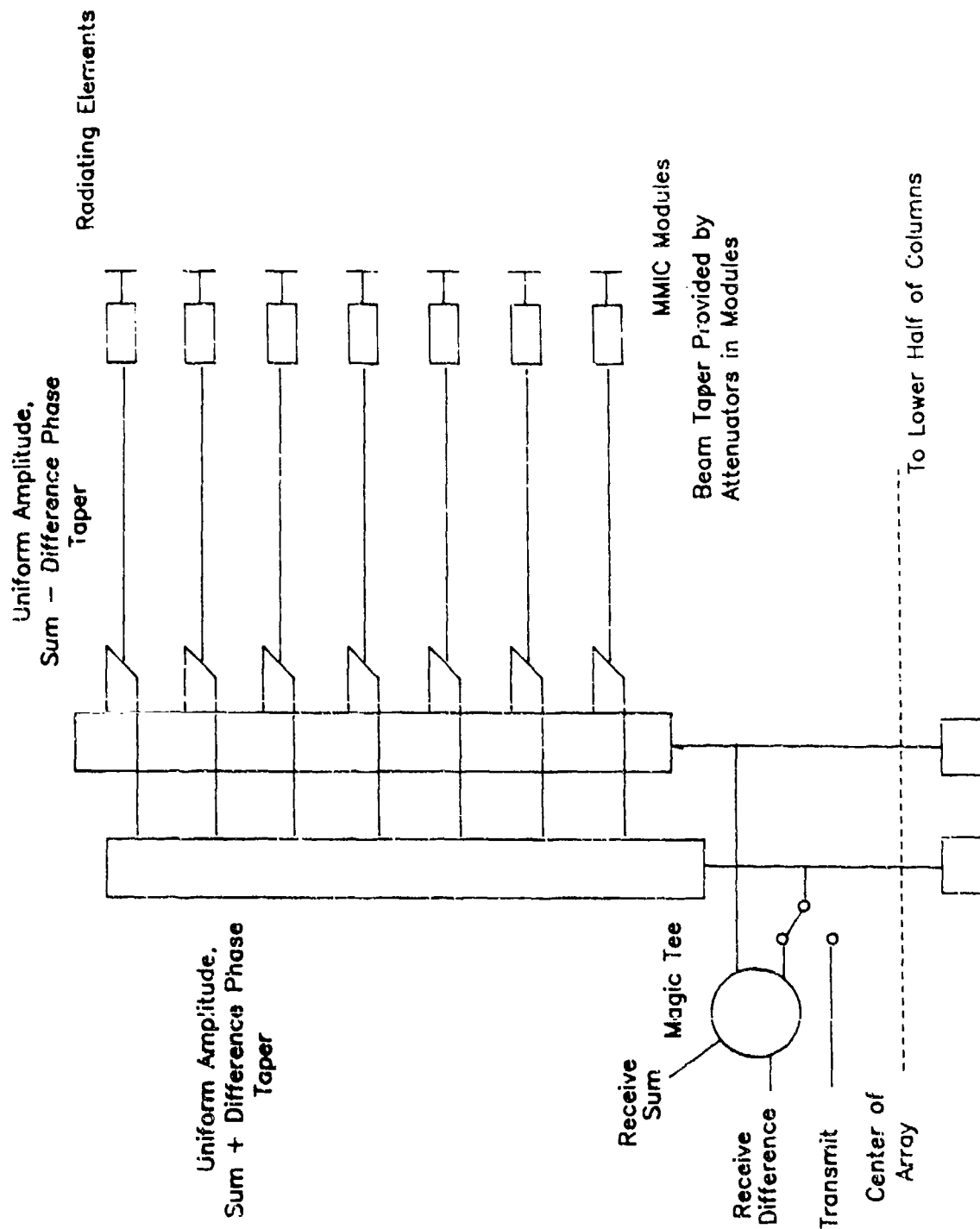
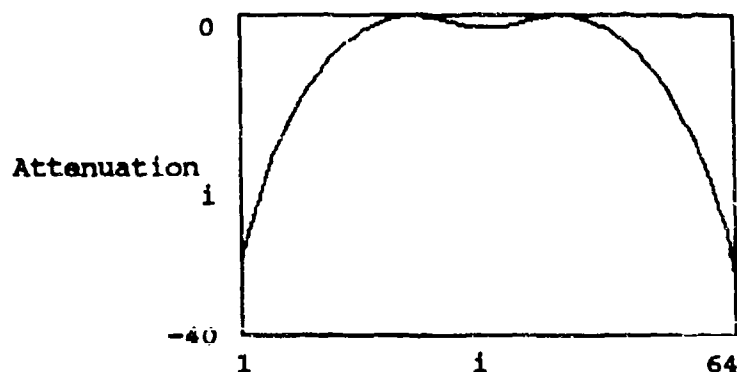


Figure 2.4-1 Advanced Architecture

Let us add the attenuation available to us due to receive attenuators in the T/R modules. Since the center elements have the peak value for the sum taper, we will apply zero attenuation to these ports and add attenuation to only the outlying ports. The offset between these two functions is:

$$\text{Offset} := -3.01 \quad \text{dB}$$

$$\text{Attenuation}_i := 10 \cdot \log \left[\left[\left| \text{Sumnew}_i \right| \right]^2 \right] - 10 \cdot \log \left[\left[\left| \text{Sumnear}_i \right| \right]^2 \right] + \text{Offset} \quad \text{dB}$$



The signals out of this new beamformer are:

$$\text{Sumfinal}_i := \frac{\text{Sumnear}_i \cdot 10^{\frac{\text{Attenuation}_i}{20}}}{1}$$

$$\text{Difinal}_i := \frac{\text{Difnear}_i \cdot 10^{\frac{\text{Attenuation}_i}{20}}}{1}$$

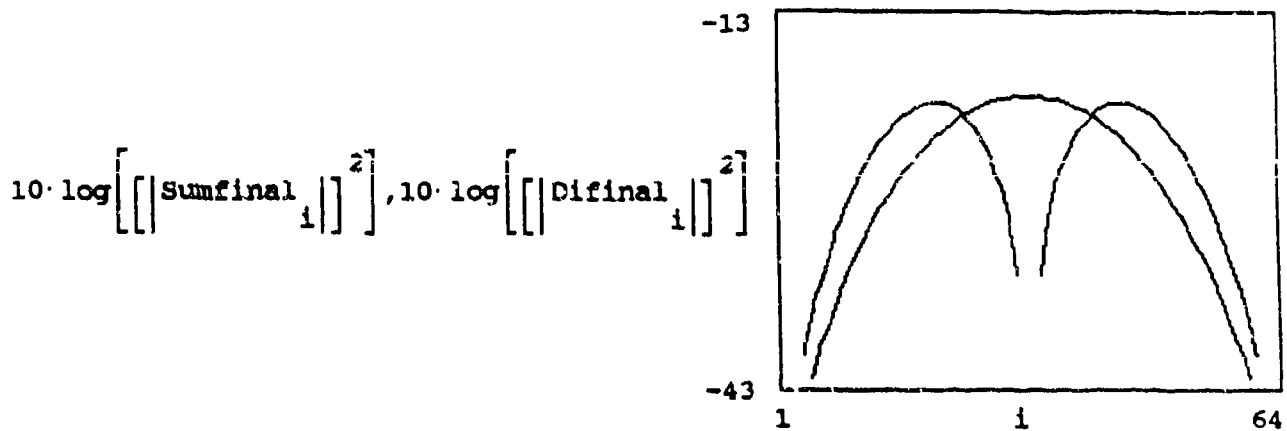
Let us now compute the losses due to forming beams using this technique.

$$\text{Sumloss} := 10 \cdot \log \left[\sum_i \left[\left| \text{Sumfinal}_i \right| \right]^2 \right] \quad \text{Difloss} := 10 \cdot \log \left[\sum_i \left[\left| \text{Diffinal}_i \right| \right]^2 \right]$$

$$\text{Sumloss} = -6.02 \quad \text{dB}$$

$$\text{Difloss} = -6.02 \quad \text{dB}$$

To verify that we end up with the desired patterns, a plot of both the final sum and difference illumination tapers formed by this architecture are shown below.



It should be noted that we have extracted the original illumination functions at a cost of -6.02 dB receive beamformer loss. The proper design of the T/R module will have the impact of minimizing the impact on the system noise figure. The key features of this new architecture are:

1. We have reduced the number of beamformers from three to two.
2. Only one network needs to be developed and used twice.
3. Each network has a uniform amplitude taper.
4. Since the topology of the network is such that it is symmetric about the center (with the exception of the output phases), it is possible to simultaneously error correct both receive beams if the beamformers are manufactured with precise output phases.

2.5 Noise Figure Calculations

The use of tapering in the modules adds loss, made practical by the low noise amplifier (LNA) gain. A comparison was made of the noise figure performance of a simple single beam system to the one described in section 2.4. The definition of noise figure is the ratio of available signal-to-noise power at the antenna input terminals to the available signal-to-noise power at the output terminals reduced by the antenna gain. The equivalent circuit used for this calculation is shown in Figure 2.5-1. The calculation was completed for a single column of the antenna. As is generally done, the input terminals of the antenna were assumed to be at $T_0 = 290$ deg K (reduced sky noise factors are treated separately) and bandwidth effects were neglected for both configurations. It was assumed that all noise sources were uncorrelated and therefore, the noise powers are additive. The mismatch and ohmic losses of the antenna element are represented by the resistance L_1 . The noise input to each row is represented by N_{in} . The noise at the output of L_1 is N_a which equals N_{in} , since the input temperature and the temperature of the resistance L_1 are the same. The signal input to each row is defined as S_{in} , which is normalized to 1.

$$\begin{aligned} N_{in} &:= k \cdot T_0 \cdot B & S_{in} &:= 1 \\ N_a &:= k \cdot T_0 \cdot B & S_a &:= \frac{1}{L_1} \end{aligned}$$

where B = bandwidth of the system

$T_0 = 290$ deg K

k = Boltzmann's constant

Each row has an LNA with gain G and noise figure F_a . F_a is represented as a noise source positioned before the amplifier. The gain of the amplifier includes the receive phase shifter insertion loss and the T/R switch. At the output of the amplifier the noise (N_b) and signal (S_b) levels in each row are equivalent to those of the other rows (NOT EACH OTHER).

$$\begin{aligned} N_b &:= G \cdot F_a \cdot k \cdot T_0 \cdot B & S_b &:= \frac{G}{L_1} \end{aligned}$$

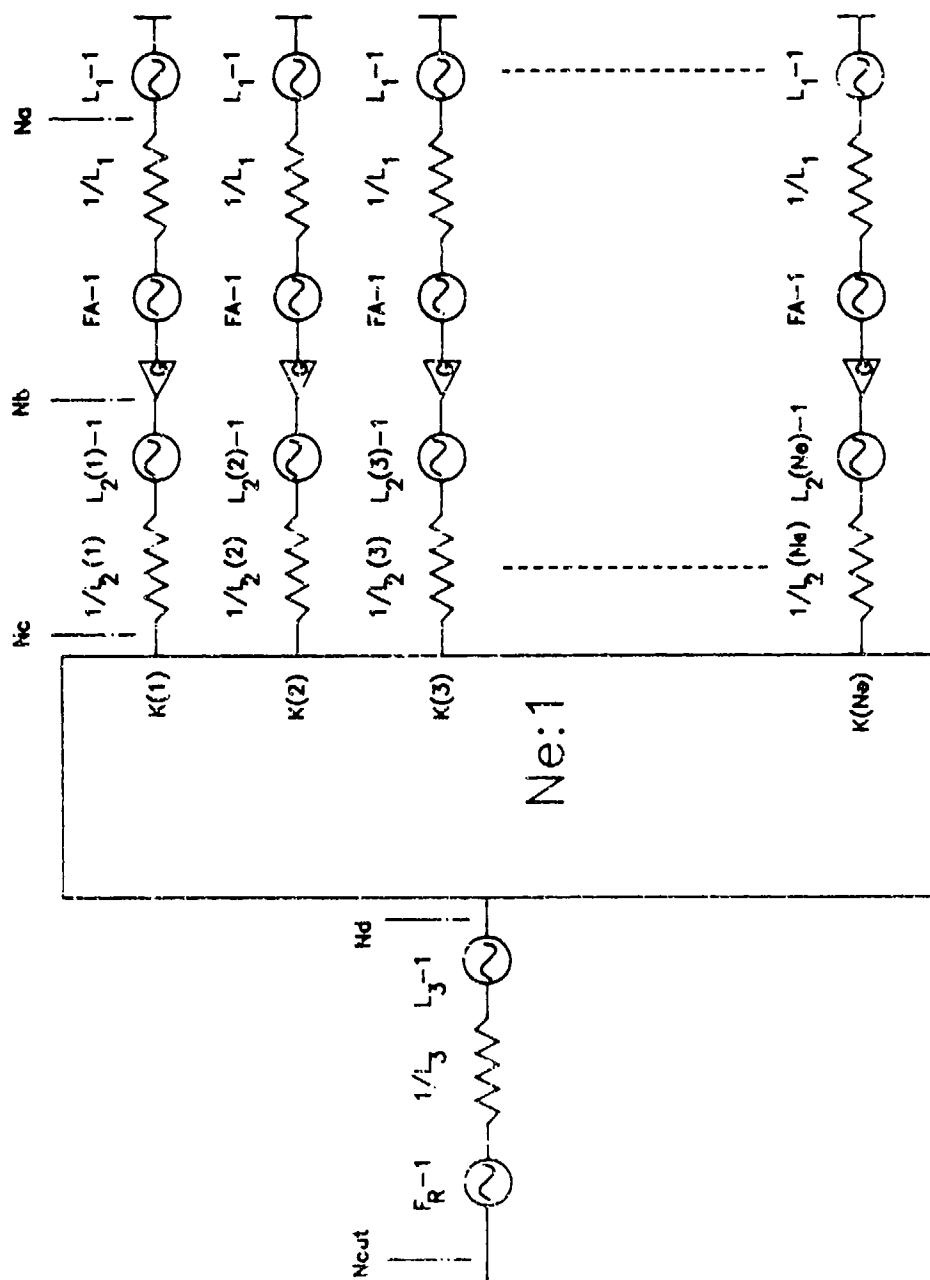


Figure 2.5-1 Equivalent Circuit for Noise Figure Calculations

An attenuator in each row is represented by $L2_n$, where n is the row number with the peak row having an attenuation of 0dB. These attenuators model the formation of the sum taper by attenuators in the receive path of the T/R module and represent from the output of the LNA to the output of the magic tee. The noise present at the output of the attenuator is represented by Nc and the signal by Sc . The attenuator reduces the available noise power by the value of its attenuation. The attenuator also contributes noise power which is a function of its value. [2]

$$Nc_n := \frac{1}{L2_n} \left[Nb + \left[L2_n - 1 \right] \cdot k \cdot T_0 \cdot B \right]$$

where

$$L2_n := \frac{P_n}{P_{peak}}$$

P_n is the power of the row
 P_{peak} is the power of the peak row

$$Sc_n := \frac{G}{L1_n \cdot L2_n}$$

[2] "Equivalent Circuits of Noisy Networks", Leo Young, April, 1958, Electronic Engineering

At the output of the beamformer the NE noise contributions are summed up uniformly since this beamformer does not introduce a taper, and power wise as the noise adds noncoherently (N_d). The signal is summed up in voltages since it adds coherently on the peak of the sum peak (S_d).

$$N_d := \sum_n \frac{N_c}{NE}$$

$$S_d := \frac{1}{NE} \left[\sum_n \sqrt{S_c} \right]^2$$

The resistance L_3 represents the combiner and circulator ohmic loss. The noise figure of the remainder of the receiver (mixer, cable losses, second amplifier) is lumped together in the noise figure, Fr . The noise and signal at the output of the system are calculated as follows:

$$N_{out} := \frac{1}{L_3} \left[N_d + (L_3 - 1) \cdot k \cdot T_0 \cdot B \right] + (Fr - 1) \cdot k \cdot T_0 \cdot B$$

$$S_{out} := \frac{S_d}{L_3}$$

Since we assumed that the $S_{in} = 1$ and the $N_{in} = kT_0B$, the overall noise figure is calculated as follows:

$$NF := \frac{\frac{S_{in}}{N_{in}}}{\frac{S_{out}}{N_{out}}} \cdot G_{af}$$

where G_{af} is the array factor in the gain of the antenna.

$$NF := N_{out} \cdot \frac{G_{af}}{k \cdot T_0 \cdot B \cdot S_{out}}$$

The array factor in the gain of the antenna must now be calculated. After normalization of the power, this factor can be shown to be:

$$G_{af} := \frac{V_{pk}^2}{P_{in}}$$

$$G_{ant} := \frac{\left[\sum_n \sqrt{L2_n} \right]^2}{\sum_n L2_n}$$

Substituting the equation for antenna gain, noise output and signal output into the equation for noise figure, we obtain a reduced equation for noise figure. To compute noise figures, typical values of all parameters were chosen, $L1 = .5$ dB, $G = 20$ dB, $Pa = 2$ dB, $L3 = 1.3$ dB, and $Fr = 6$ dB. For these values, the new architecture has a noise figure of 2.85 dB.

$n := 1 \dots 32$... half the array

$NE := 32$

$$L2_n := \left[\frac{\text{Sum}_n}{\text{Sum}_{32}} \right]^2$$

Sum is the desired sum illumination taper. The center element must have a value of 1 for these calculations.

$$NF := 10 \cdot \log \left[\frac{L1}{G} \cdot \left[L3 \cdot NE \cdot \frac{Fr}{\sum_n L2_n} + (G \cdot Fa - 1) \right] \right]$$

The noise (Nb) and the signal (Sb) levels are the same for both architectures to the output of the INA. No attenuators are present in the conventional architecture. For the conventional architecture the manifold produces the taper with each row having a power coefficient represented by K_n . The noise output of the conventional architecture is:

$$Nout := \frac{k \cdot T_0 \cdot B}{L3} \cdot \left[(L3 - 1) + G \cdot Fa \cdot \sum_n K_n \right] + (Fr - 1) \cdot k \cdot T_0 \cdot B$$

Since the sum of the coefficients is equal to one, this expression can be reduced to:

$$Nout := k \cdot T_0 \cdot B \left[1 + \frac{G \cdot Fa - 1}{L3} \right] + (Fr - 1)$$

The next two expressions solve for the signal output and the array factor in the gain of the conventional antenna architecture.

$$Sout := \frac{G}{L1 \cdot L3} \cdot \left[\sum_n \sqrt{k(n)} \right]^2$$

$$Gaf := \left[\sum_n \sqrt{k(n)} \right]^2$$

The noise figure of the conventional architecture is calculated by the following expression:

$$NF := 10 \cdot \log \left[\frac{L1}{G} \cdot (L3 \cdot Fr + (G \cdot Fa - 1)) \right]$$

For the typical parameters given previously, the noise figure of this configuration is 2.62 dB. In order to determine the impact of amplifier gain on noise figure, noise figure was calculated as a function of amplifier gain for both architectures. The plots which follow show that in order for the attenuator architecture to achieve the 2.62 dB noise figure of the conventional architecture, the amplifier gain must increase 4 dB. It should be noted that any transmit taper reduces the attenuator loss rapidly.

Let us compute the noise figure as a function of gain for the two architectures.

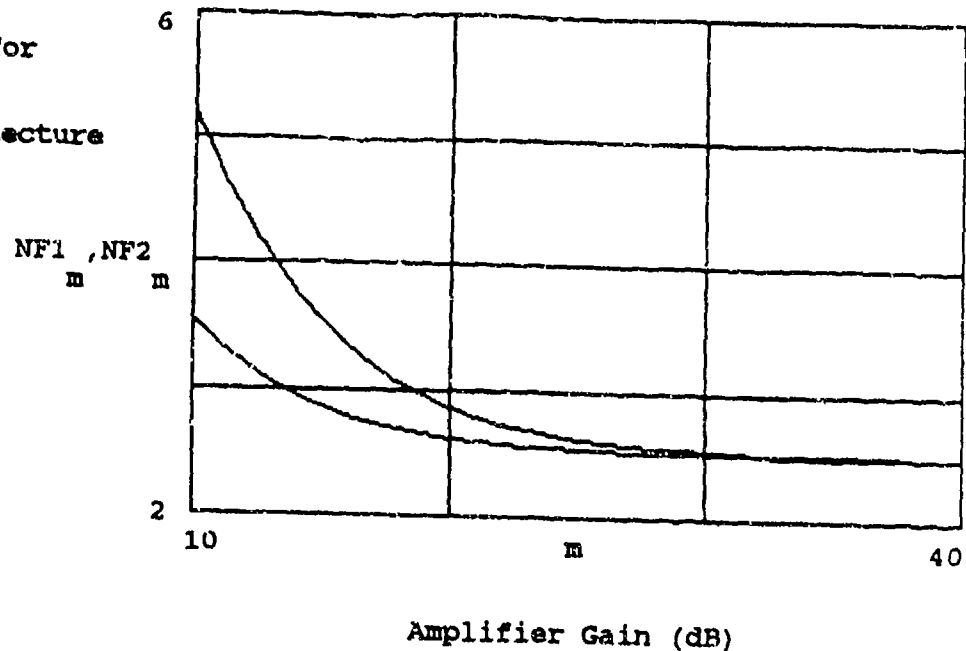
$m := 10 \dots 40$ Amplifier Gain in dB

$G_m := 10^{\frac{m}{10}}$ Amplifier Gain as a Power ratio

$$NF1_m := 10 \cdot \log \left[\frac{L1}{G_m} \left[L3 \cdot Fr + \left[G_m \cdot Fa - 1 \right] \right] \right] \quad \text{Noise figure relationship for conventional architecture}$$

$$NF2_m := 10 \cdot \log \left[\frac{L1}{G_m} \left[L3 \cdot NE \cdot \frac{Fr}{\sum_n L2_n} + \left[G_m \cdot Fa - 1 \right] \right] \right] \quad \text{Noise figure relationship for advanced architecture}$$

Noise Figure (dB) for
Conventional NF1
and Advanced Architecture
NF2



2.6 Summary

Westinghouse studied beamforming architectures in elevation with multiple beam capability and low sidelobe monopulse. The surface of these beamformers was assumed to be planar for comparative purposes only. This methods include; Conventional Method, Poirier's Method of Manifold Elimination [1], a Westinghouse architecture, and a combined approach of two architectures. The conventional approach is to use a separate transmit and receive manifold for a total of 3 manifolds in a monopulse system. Poirier's approach suggest : by using one of the manifolds on both receive and transmit that the beamforming can be accomplished in 2, rather than 3 networks. He uses the T/R module to generate the illumination function for one of the receive beams. However, since only one set of phase and amplitude controllers exist, errors can only be corrected in one of the networks, but not both.

The Westinghouse architecture addresses the problem of error correcting 2 beamformers with one set of phase and amplitude controllers. The architecture consists of a magic tee, a transmit switch, two similar power dividers, 3.01 dB Wilkinson couplers and the T/R modules. This architecture adds the sum and

difference tapers in quadrature to create $S+jD$ and $S-jD$ functions (S and D are assumed to be in phase quadrature). Since the amplitudes of the two functions are equal and symmetric about the center, the only difference between the two networks is the phase front. Both functions have the same phase magnitude, but opposite sign. Therefore, the same network can be used to generate both tapers, but one of the networks will be physically flipped about the center element. Since the phase taper is set by the number of bends in the stripline, it can be manufactured to great precision and will not be a significant error contributor. Therefore, by measuring the amplitude on the input to both networks random manufacturing errors can be averaged and considerably reduced. These average numbers can be stored in the T/R module and any manufacturing errors will be reduced to a minimal level by compensation in the T/R module. This allows for simultaneous compensation for errors in two networks by using the T/R module, but a separate uniformly illuminated transmit network would be required. In order to form the desired sum and difference beams, the outputs of the $S+jD$ and $S-jD$ networks are fed into a magic tee.

The 3.01 dB Wilkinson divider which splits the receive energy between the two beamformers, introduces a receive loss of 3.01 dB. The T/R switch in this architecture avoids this loss on transmit by switching in the transmit power divider. The 3.01 dB coupler and T/R switch will be included in the T/R module.

The fourth approach combines Poirier's method and the Westinghouse method. The key features of this approach is that it reduces the number of manifolds from three to two and maintains the potential of compensating for errors in the receive sum and difference patterns simultaneously. The architecture contains the same components as the previously described Westinghouse architecture except for different power divider characteristics. The power dividers have a uniform amplitude taper and the phase taper of the $S+jD$ and $S-jD$ networks. Again one network is the complex conjugate of the other network which implies that we need to develop only one network (e.g. $S+jD$). The second network ($S-jD$) will be flipped about the center element. The transmit function requires a uniform taper in order to run the high power amplifiers in the T/R modules to saturation. One of the networks can be used for the transmit function and the transmit phase shifter will take out the phase shift built into the network as well as steering the beam. The receive operation is similar to that of the previously described Westinghouse

architecture with the exception that the beamformers have uniform amplitude. The S+jD and S-jD networks in conjunction with the 3 dB Wilkinson dividers and the Magic Tee set the ratio of the amplitudes for the sum and difference beams. The receive attenuators in the T/R modules set the proper attenuation simultaneously for the sum and difference beams. Hence, we have reduced the number of beamformers from 3 to 2 while retaining the capability of simultaneously correcting errors in both the sum and difference beams. The loss on receive associated with this architecture was found to be 6.02 dB. On transmit, we encounter a -3.01 dB driver loss due to the Wilkinson dividers. We can eliminate this loss on transmit by incorporating a T/R switch before one of the coupler legs. Both the -3.01 dB Wilkinson divider and the T/R switch could be incorporated into the T/R modules.

Noise figure calculations were done to compare the conventional architecture and the use of attenuators to form a taper on receive. A planar array distribution was used for comparative purposes. To maintain the same overall noise figure as the conventional architecture, the attenuator architectures require an INA with an additional 4.0 dB of gain. However, in order to avoid driving the end elements into the noise floor, an additional 10 dB of gain is suggested.

Table 2.6-1 summarizes the architecture comparisons. The architecture which combines Poirier's method of architecture manifold elimination and the Westinghouse architecture (Figure 2.3-1) was selected. This architecture reduces the number of beamformers required from 3 to 2 and is able to correct errors in both the sum and difference beams.

Table 2.6-1 Architecture Comparison

<u>Architecture</u>	<u>Number of Beamformers</u>	<u>Error Correct Both Sum and Difference</u>	<u>Additional System Receive Loss</u>	<u>LNA Gain Increase</u>
Conventional	3	No	0 dB	0 dB
Poirier's Method	2	No	---	4 dB
Westinghouse	3	Yes	3.01 dB	0 dB
Combination	2	Yes	6.02 dB	4 dB

BROADBAND MMIC T/R MODULE/SUBARRAY PERFORMANCE

D. Brubaker
D. Scott
S. Ludvik
Teledyne Monolithic
Microwave
Mountain View, California

M. Lynch
H.H. Chung
W. Foy
S.Y. Peng
Teledyne Ryan Electronics
San Diego, California

ABSTRACT

Increased availability of monolithic microwave integrated circuits (MMIC) has generated interest in active phased array systems. Continuing component developments are providing more complex functions on-chip and lower MMIC costs that can make realization of large array practical. Future systems are projected to operate over wide bandwidths and implement advanced concepts such as shared apertures in which several RF functions (EW, radar, communications, etc.) are performed on a single aperture. This paper presents the results of the development of broadband T/R Modules operating over frequencies from 6 to 18 GHz. In addition, the development of a 4-element broadband subarray and the integration with the modules are also included. A 5-bit delay line phase shifter has been developed for steering the subarrays over a ± 60 degrees scan sector. Both calculated and measured T/R Module and subarray pattern data have been compared and discussed.

1.0 INTRODUCTION

The current phased array technology demands for a wideband ($\geq 300\%$), shared-aperture phased-array to meet the present and future needs in many critical application areas. The ultimate goal is to make the Phased Array Antenna Systems affordable and reliable. It is envisioned that such a broadband shared-aperture phased-array offers many advantages, such as reducing real estate required for airborne applications, reducing scattering cross-sections, performing multiple missions, etc. The challenge to materialize these antenna systems, however, is developing the required key components. These key components are subarrays, T/R (Transmit/Receive) modules, beamforming network and its associated control circuits to say the least.

The purpose of this paper is to present results on the development of broadband (6-18 GHz) Transmit/Receive (T/R) module and subarray components. The broadband T/R Module developed consists of T/R switches, high power amplifiers, low noise amplifiers, and a 5-bit delay line phase shifter. The subarray developed is a 6-element printed-circuit dielectric notch radiator. For the integration test, there are 6 subarrays mounted on the top of a common ground plane. Center four subarrays were connected to 4 T/R Modules mounted behind the ground plane, with outer two subarrays resistively terminated.

Typical data measured for each subcomponent of T/R Modules are discussed in Section 2.0. Simulated subarray patterns using the measured T/R Module data are presented in Section 3.0. Brief description of T/R Module/subarray integration test is given in Section 4.0. Measured integration test pattern performance is summarized in Section 5.0, followed by conclusions and recommendations in Section 6.0.

2.0 T/R MODULE PERFORMANCE

2.1 T/R MODULE DESIGN

The T/R Module developed consists of a "transmit" power amplifier chain and a "receive" low noise amplifier chain that share a common 5-bit delay shifter and antenna via a pair of SPDT switches. It was designed for an 8-element array, operating from 6.0 to 18.0 GHz. The element spacing used is 0.492 inch. This design was scaled directly from an L-band phased-array, operating from 0.6 to 1.8 GHz, which was developed at Teledyne during the years of 1983 and 1984. Figure 1 shows a general block diagram of a broadband T/R Module, which includes a polarity switch to provide the polarization diversity capability. For the developed T/R Module, however, the polarity switch was not included, as shown in Figure 2. This figure shows the basic layout of the developed T/R Module. Note that the key subcomponents are high

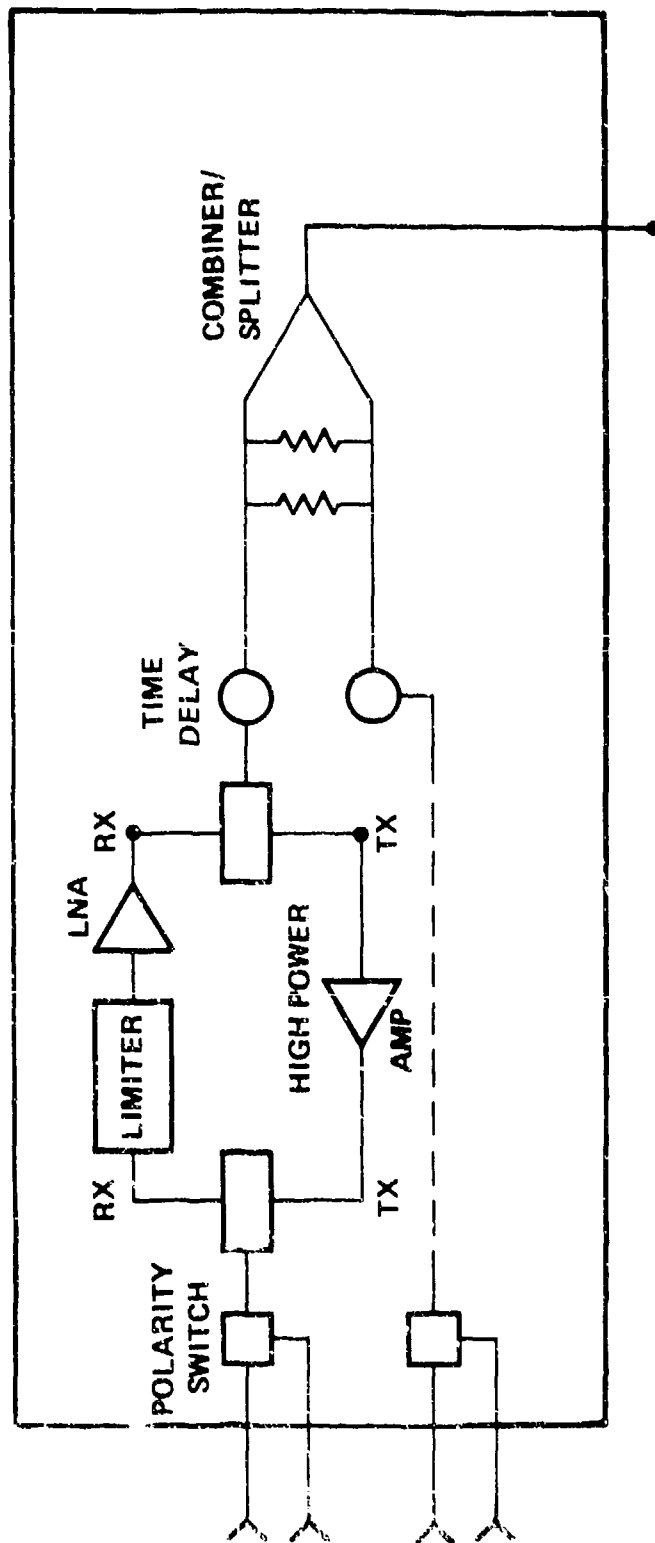


Figure 1. A General Block Diagram of a Broadband T/R Module

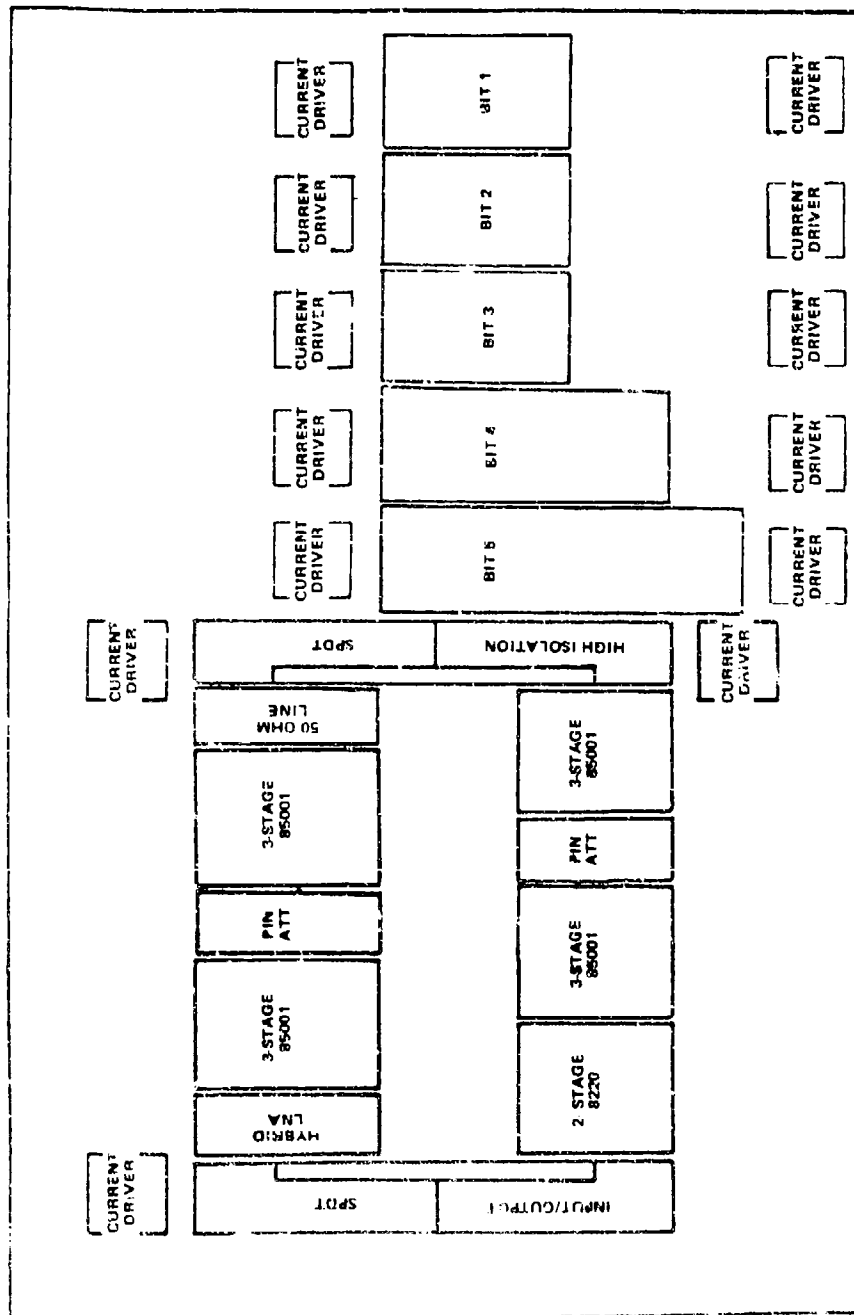


Figure 2. Layout of T/R Module

power amplifiers, low noise amplifiers and a 5-bit delay line phase shifter. Figure 3 shows a photo of the hardware developed.

2.2 DELAY LINE PHASE SHIFTER

For broadband frequency (300% bandwidth) operation, delay line phase shifters are required to provide frequency independent beam scanning capability. This concept is illustrated in Figure 4 which shows a 4-element subarray with beam scanning to an angle θ . Note that the θ is given by:

$$\theta = \text{SIN}^{-1} \left(\tau \frac{c}{d} \right) \quad (1)$$

where τ is the time delay difference between any two adjacent elements, c is speed of light in free space and d is element spacing. The beam steering is dependent on time delay τ and element spacing d , not on operating frequencies.

For the selected element spacing, $d = 0.492$ inch, and the desired scan coverage of ± 60 degrees from the 8-element array broadside, the 5-bit delay line bit sizes required are 8.5, 17.1, 34.1, 68.2 and 136.4 pico seconds. Figure 5 shows the measured net time delay states of the complete T/R Module for the receive path over the entire operating frequency range. Results are similar for the transmit path. It should be pointed out that the measured data for each state showed good flatness

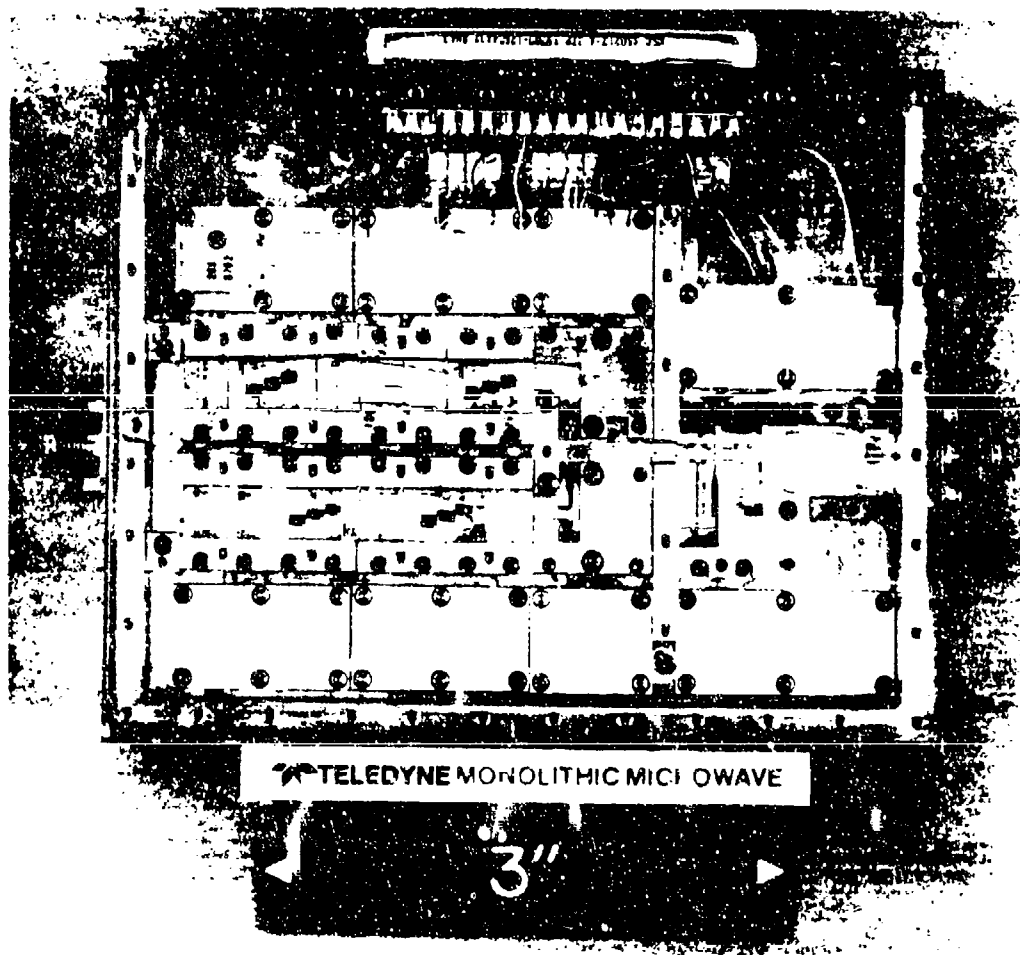


Figure 3. A Photo of the Developed TMM Module Hardware

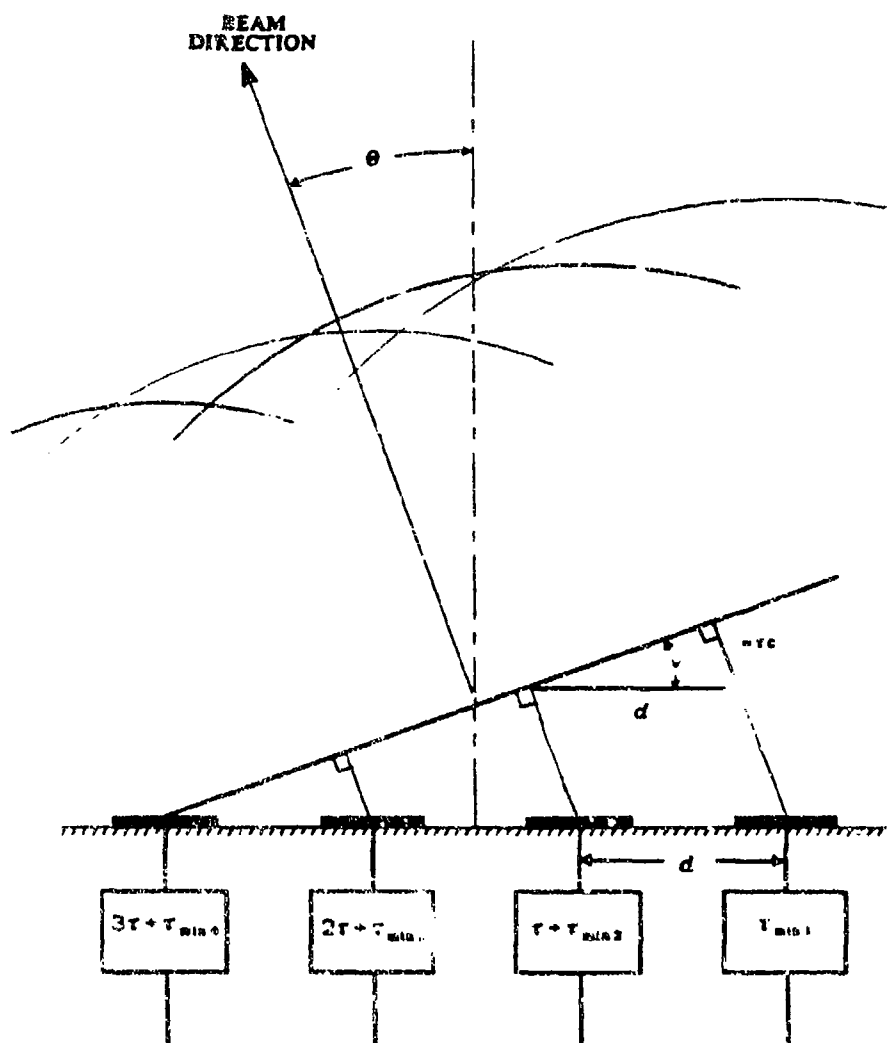


Figure 4. Beam-Steering with Time Delay Line Phase Shifters

over the frequency range as desired. The difference between any two adjacent state should be constant and equal to the least bit size of 8.5 pico seconds. The measured data did show that this condition has generally been met with some minor errors.

One of the important criteria for T/R Modules is their performance repeatability from module to module. Figure 6 shows the measured net delay of 5-bit states for all four T/R Modules. Note that each bit tracked well from module to module.

2.3 RECEIVE MODE

The measured performance of the receive mode operation is shown in Figure 7. Note that the key performance items are gain, gain control, and noise figure. In addition, the gain tracking from module to module is important. The measured data showed good gain of 35 dB, with a 20 dB gain control. The noise figure measured is about 6.5 dB. The gain tracking is about 5 dB.

2.4 TRANSMIT MODE

The measured performance of the transmit mode operation is given in Figure 8. The key transmit mode performance items are gain, gain control and transmit power. Note that the measured typical transmit gain is 37 dB with a 20 dB gain control range.

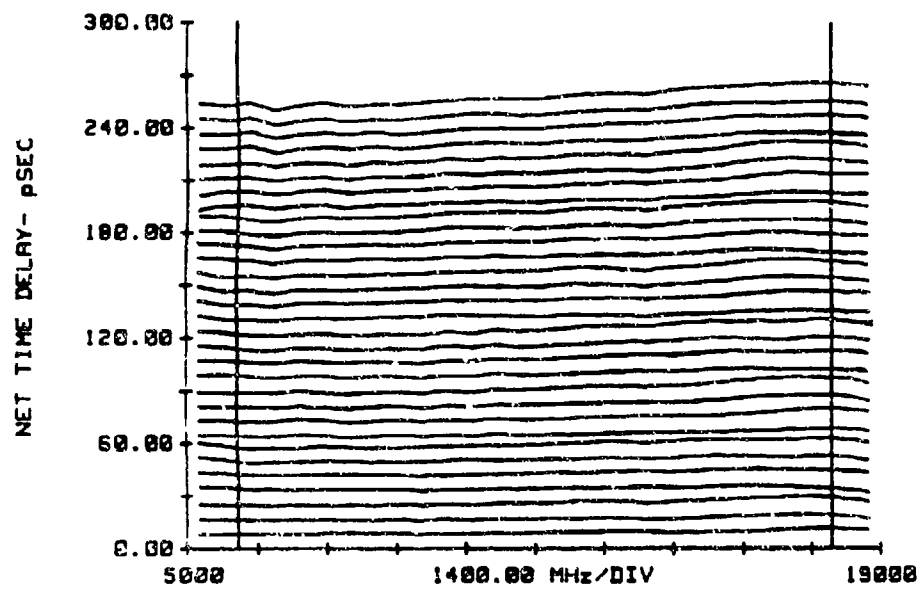


Figure 5. Measured Net Time Delay States for a Typical T/R Module

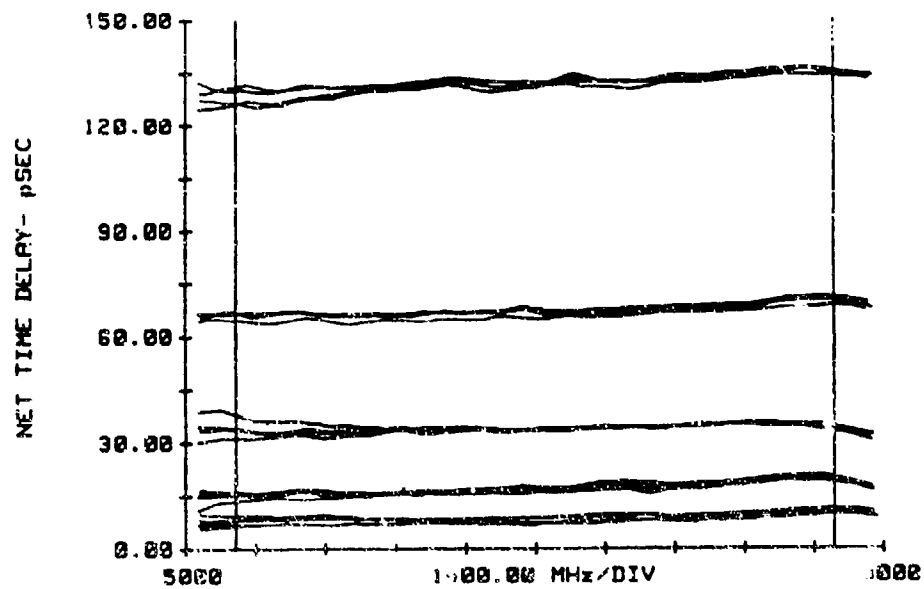


Figure 6. Measured Net Time Delay of 5 Bit States for all Four Modules

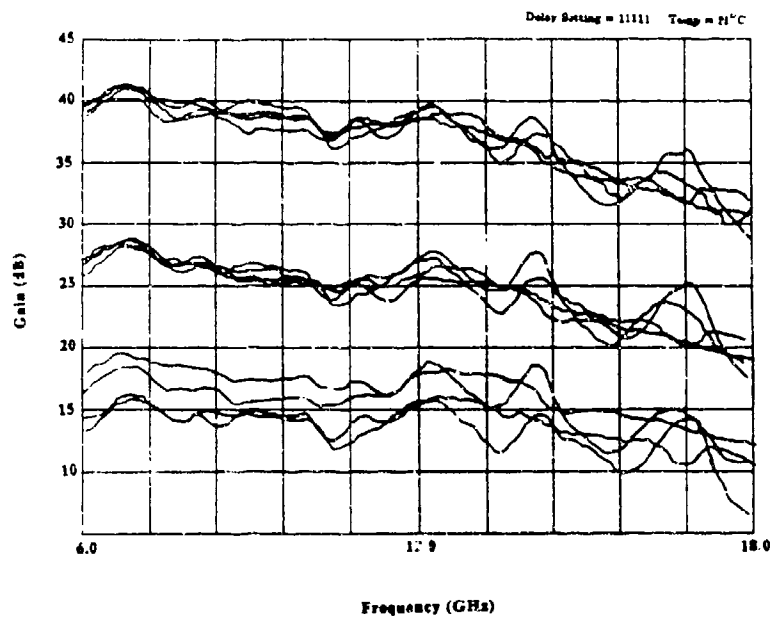


Figure 7. Measured Receive Path Gain Tracking for 3 Different Gain Control Settings

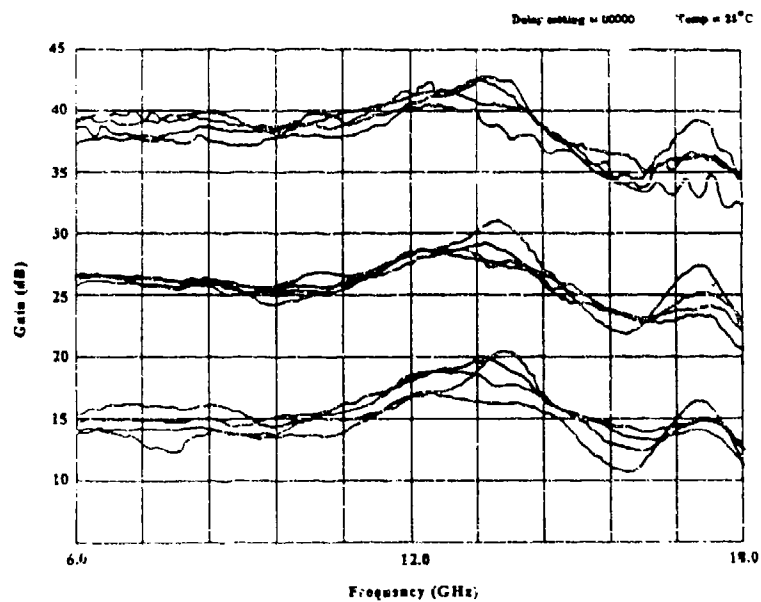


Figure 8. Measured Transmit Path Gain Tracking at Three Gain Control Settings

The module to module amplitude tracking is mostly less than 5 dB over the frequency range for 4 T/R Modules. The transmit output power will be saturated at about 25 dBm. A desired increase in output power can be achieved by reducing the input switch insertion loss, increasing the power amplifier gain and increasing the output power of the driver amplifiers.

2.5 MODULE PERFORMANCE SUMMARY

Table 1 provides a summary of the measured data performance for the developed four T/R modules. The measured data meets most of the design goals. Improvements, however, are needed in both amplitude tracking and 5-bit delay line error tolerance.

3.0 SIMULATED SUBARRAY PATTERNS

Before the T/R Modules/Subarrays integration test, subarray patterns were simulated using the measured T/R Module time delay data. Figure 9 shows a 4-element subarray fed by 4 T/R Modules via a 1:4 corporate feed circuit. In the pattern simulation, uniform amplitude illumination was assumed and the mutual coupling effect was not included. The calculated patterns are shown in Figures 10-16. The corresponding relative aperture phase measured and designed for each frequency and beam angle is also shown in each figure. These aperture phase errors determine subarray pattern performance and provide understanding of the phase error effect on beam shaping.

Table 1. Comparison of Achieved Performance and Goals

Parameter	Goal	Measured
Frequency (GHz)	6-18 GHz	6-18 GHz
Port Match, Antenna and Feed	2:1	2:1
Gain, Transmit and Receive	30 dB	35 dB
Gain Control 10 dB	20 dB	
Transmit Power Output	23 dBm	25 dBm
Receive Noise Figure	6 dB	6.5 dB typ.
Phase Match: (at 6 GHz)		
Unit-to-Unit	±30 degrees	±29 degrees
Transmit-to-Receive	±30 degrees	±33 degrees
Switchable Delay:		
Bit 1 (psec)	8.5 ±3%	8.3 ±15%
Bit 2 (psec)	17.1 ±3%	17.3 ±7%
Bit 3 (psec)	34.1 ±3%	33.3 ±6%
Bit 4 (psec)	68.2 ±3%	68.8 ±4%
Bit 5 (psec)	136.4 ±3%	131.8 ±4%
Gain Flatness Vs. Frequency	±3 dB	±5 dB
Gain Variation Vs. Delay Setting	±2 dB	±1.5 dB
Gain Tracking, Unit-to-Unit	Not specified	±2.5 dB
Not Delay Tracking, Unit-to-Unit	Not specified	±19% on Bit 1 decreasing to ±2% on Bit 5
Time Tracking, Unit-to-Unit	Not specified	Receive path: ±6.5 psec. Transmit Path: ±22.5 psec

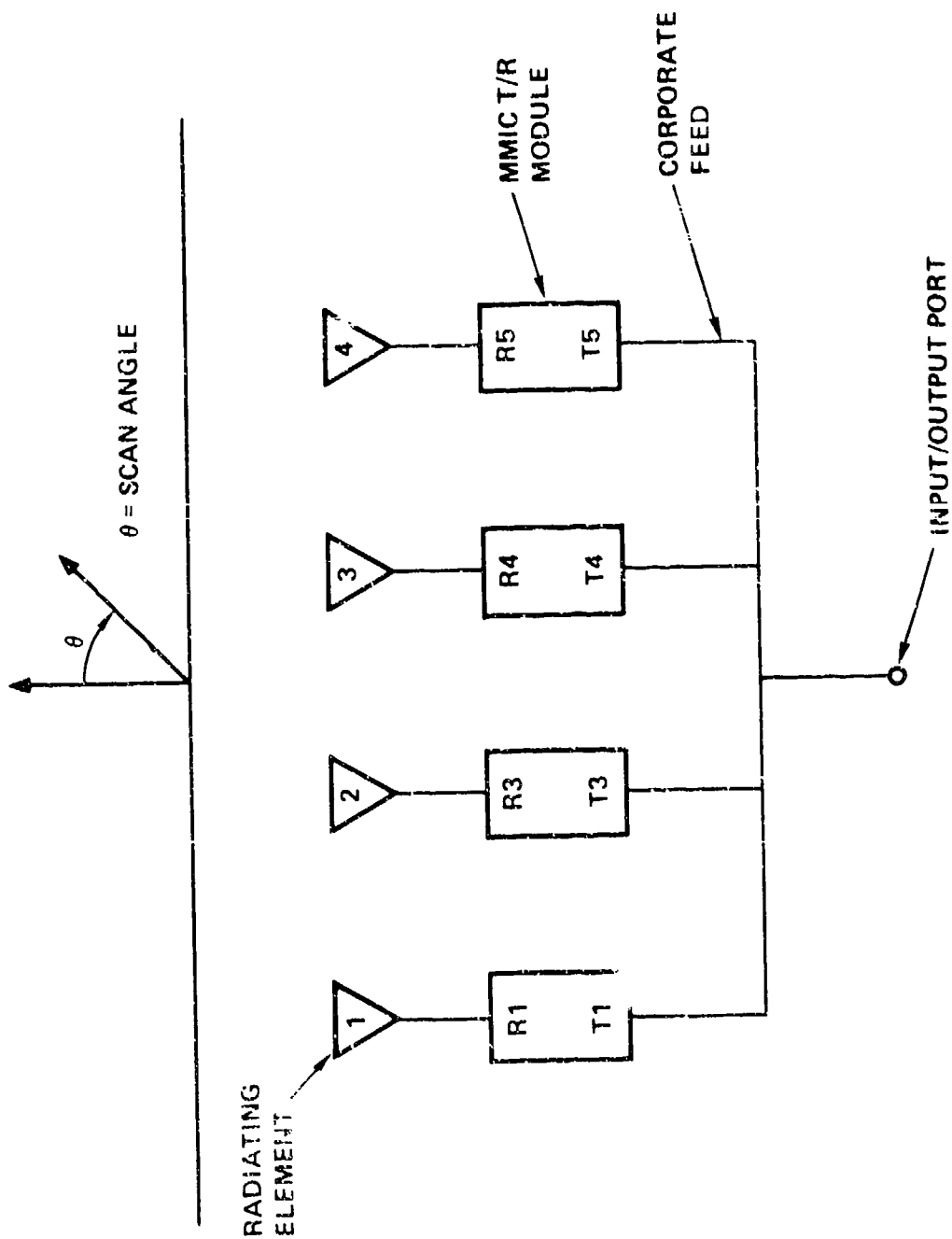


Figure 5. A Sketch to Show a 4-Element Subarray Fed by 4 T/R Module via a 1:4 Corporate Feed Circuit

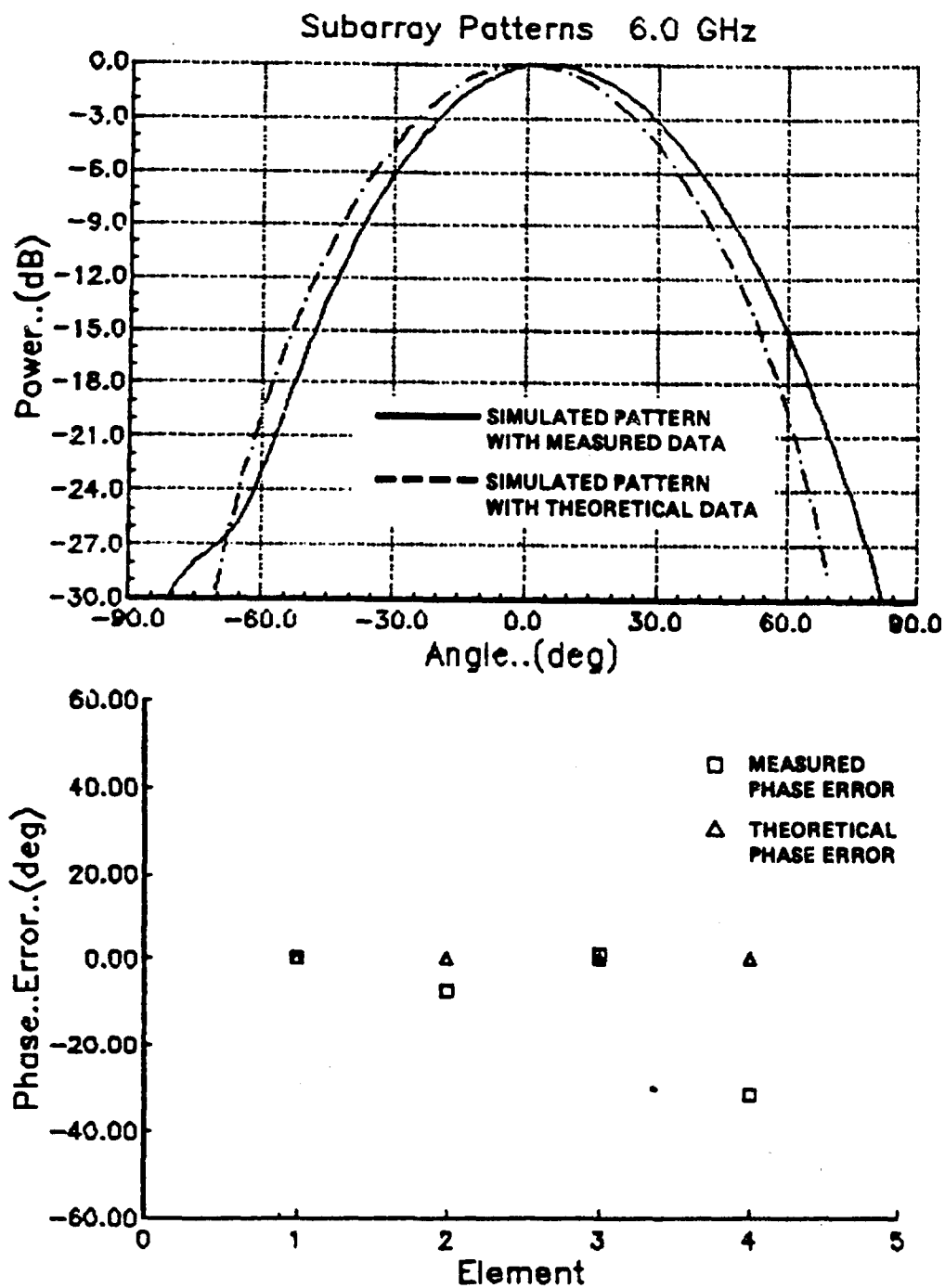


Figure 10. Simulated Subarray Patterns and Aperture Phase Distributions at 6 GHz and 0 Degree Scan Angle

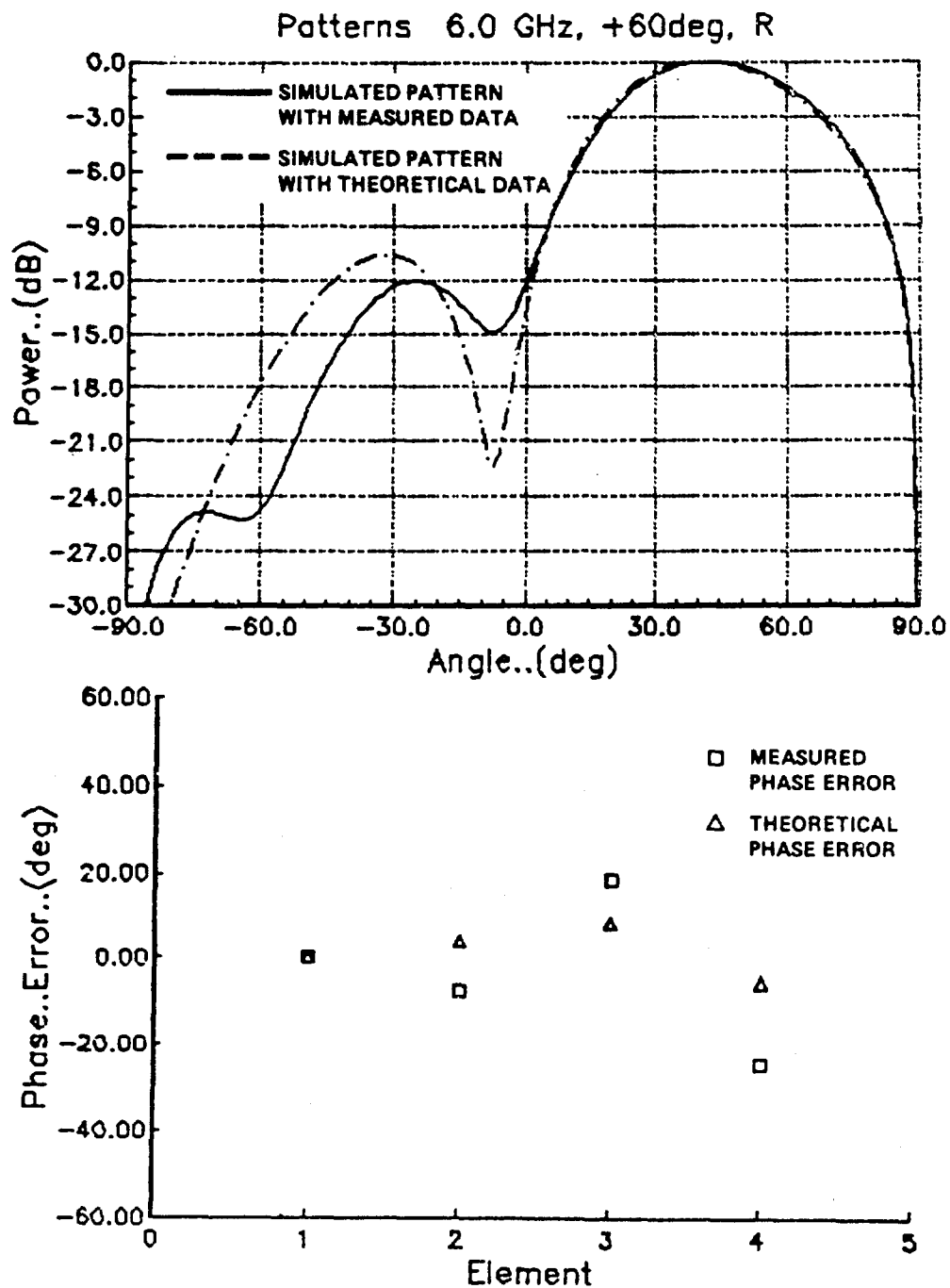


Figure 11. Simulated Subarray Patterns and Aperture Phase Distributions at 6 GHz and 60 Degrees Scan Angle

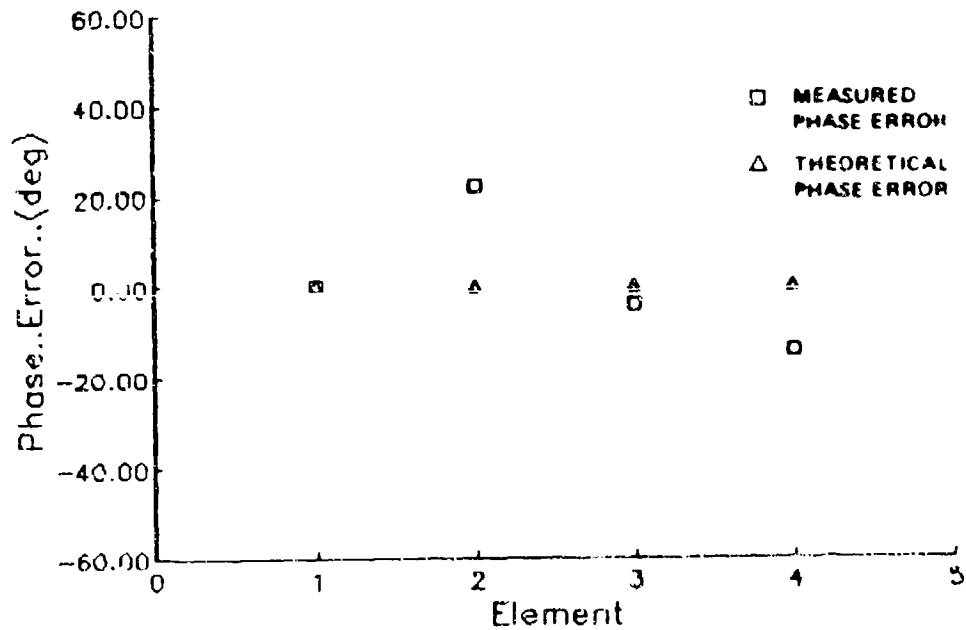
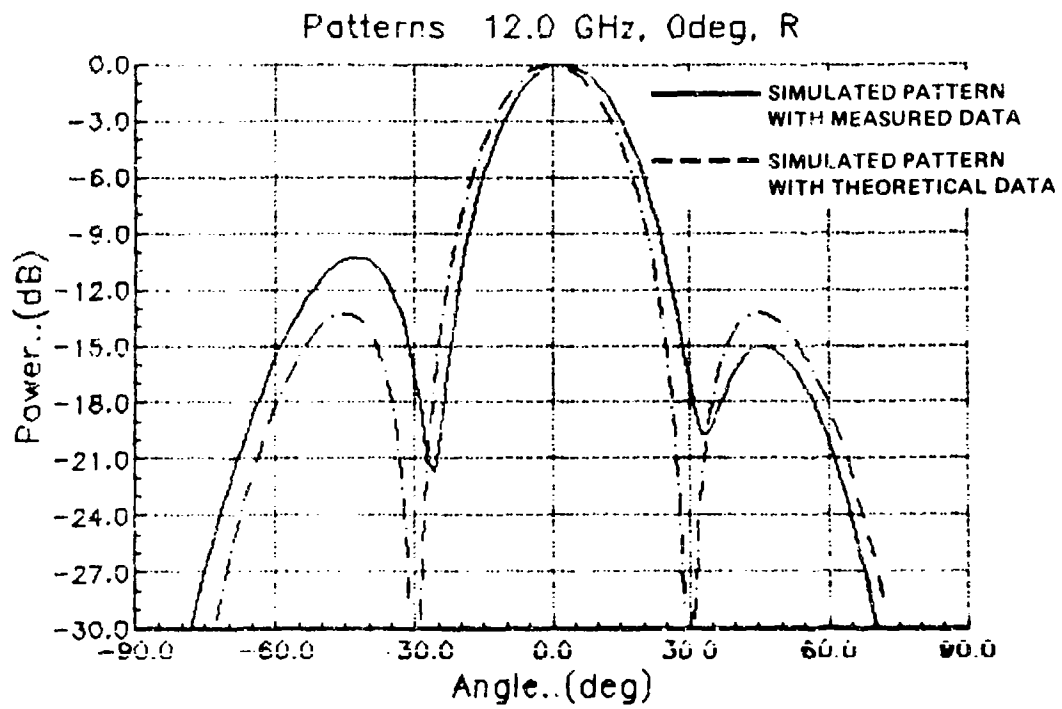


Figure 12. Simulated Subarray Patterns and Aperture Phase Distributions at 12 GHz and 0 Degree Scan Angle

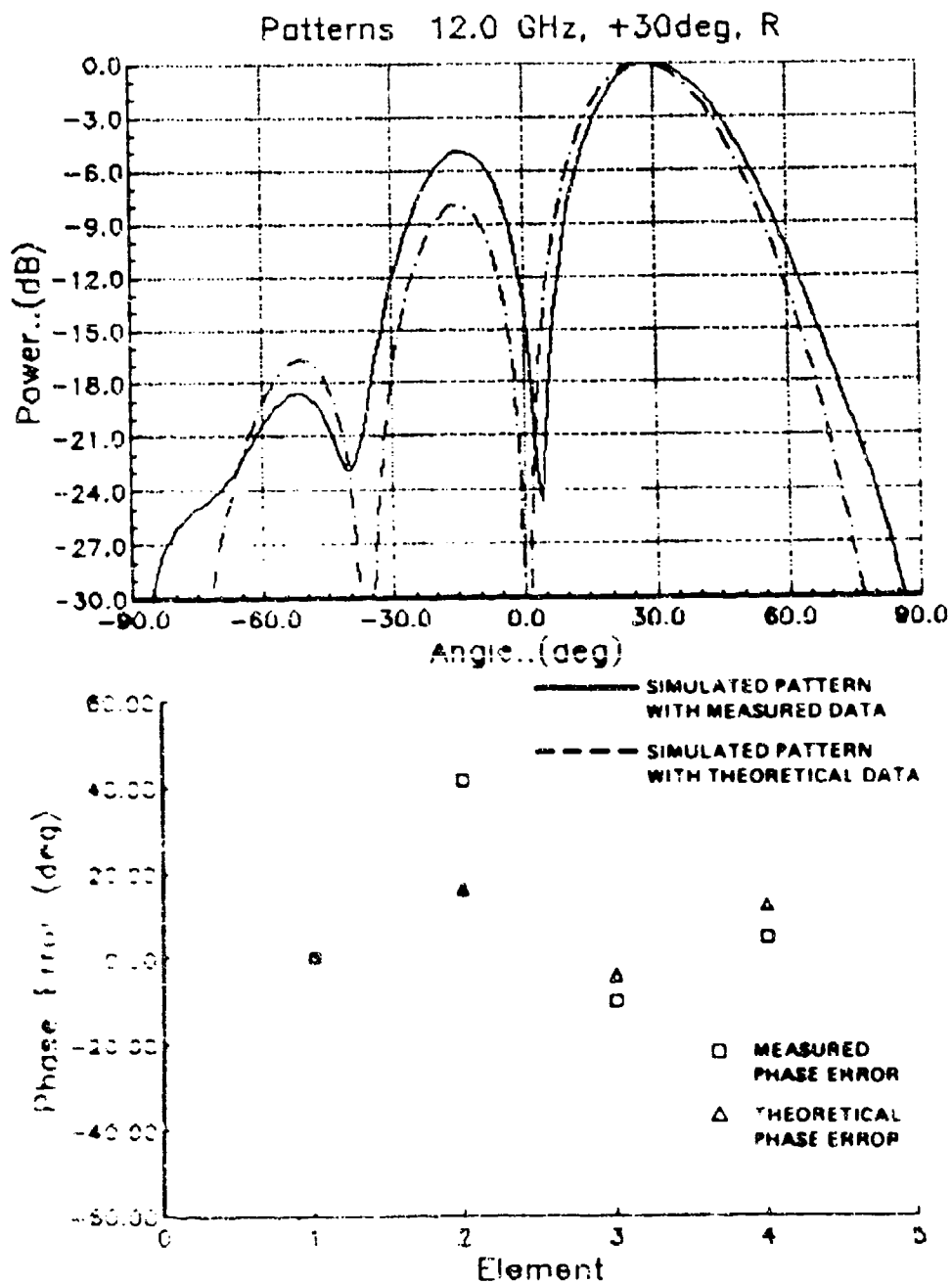


Figure 13. Simulated Subarray Patterns and Aperture Phase Distributions at 12 GHz and 30 Degrees Scan Angle

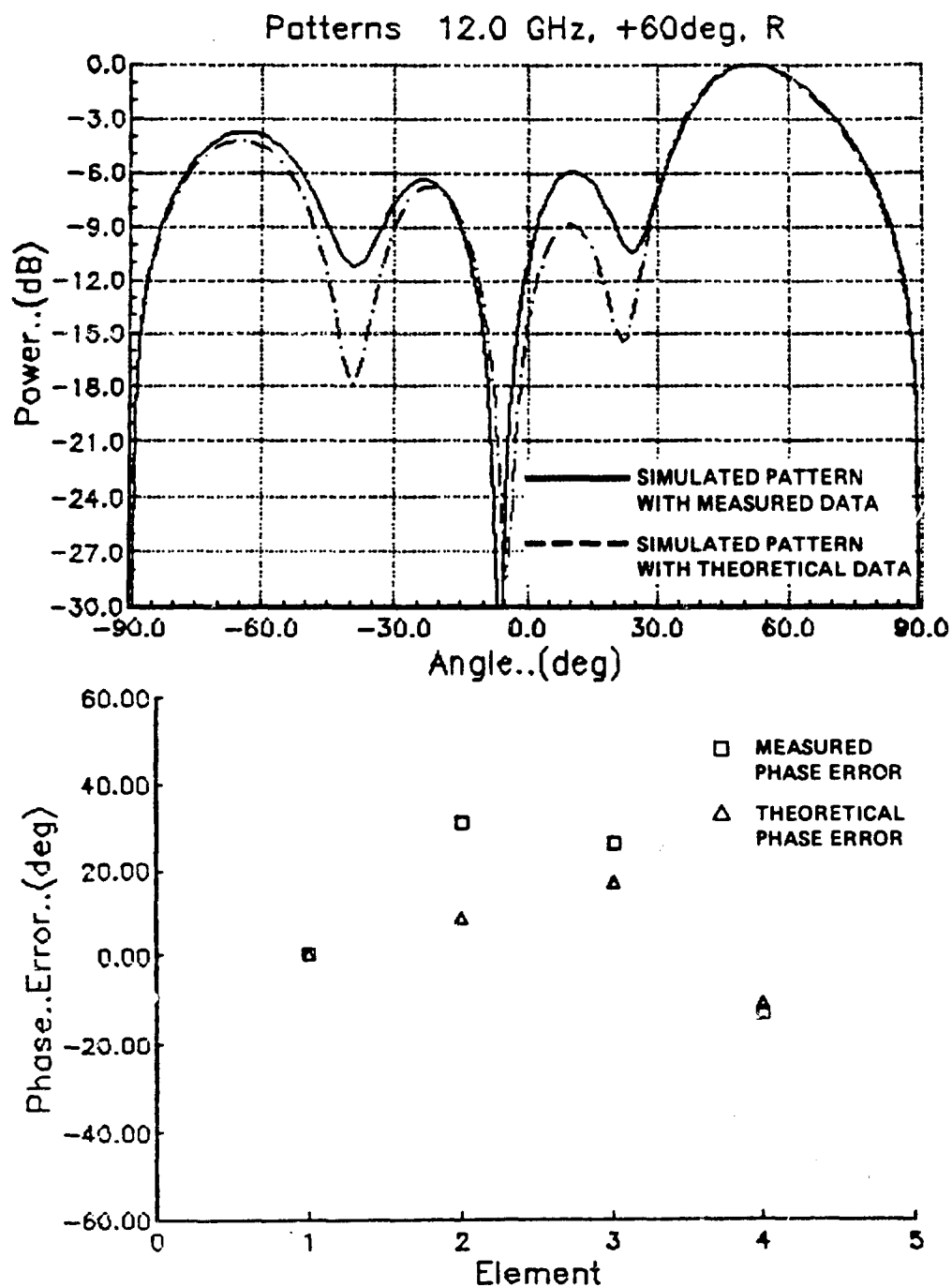


Figure 14. Simulated Subarray Patterns and Aperture Phase Distributions at 12 GHz and 60 Degrees Scan Angle

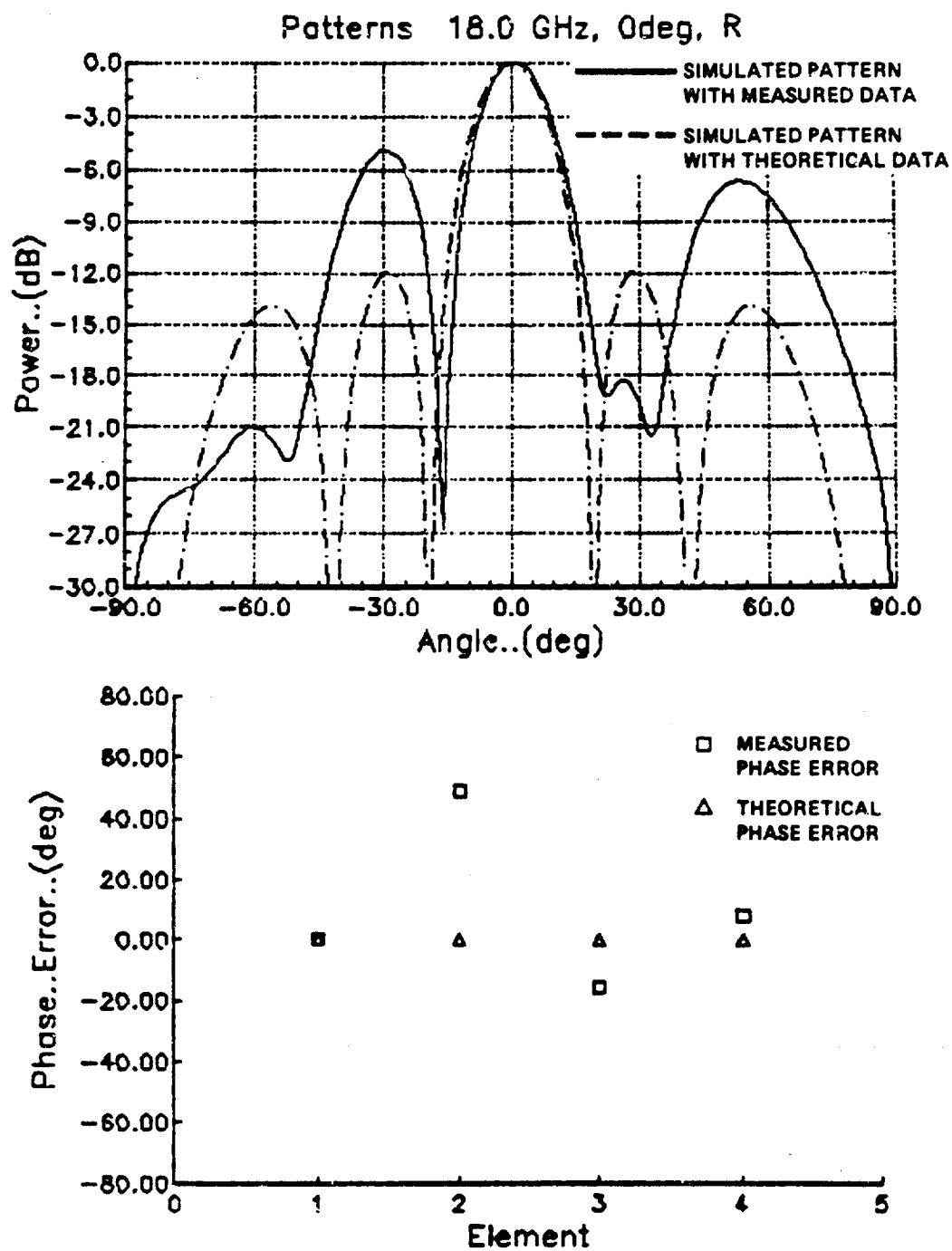


Figure 15. Simulated Subarray Patterns and Aperture Phase Distributions at 18 GHz and 0 Degrees Scan Angle

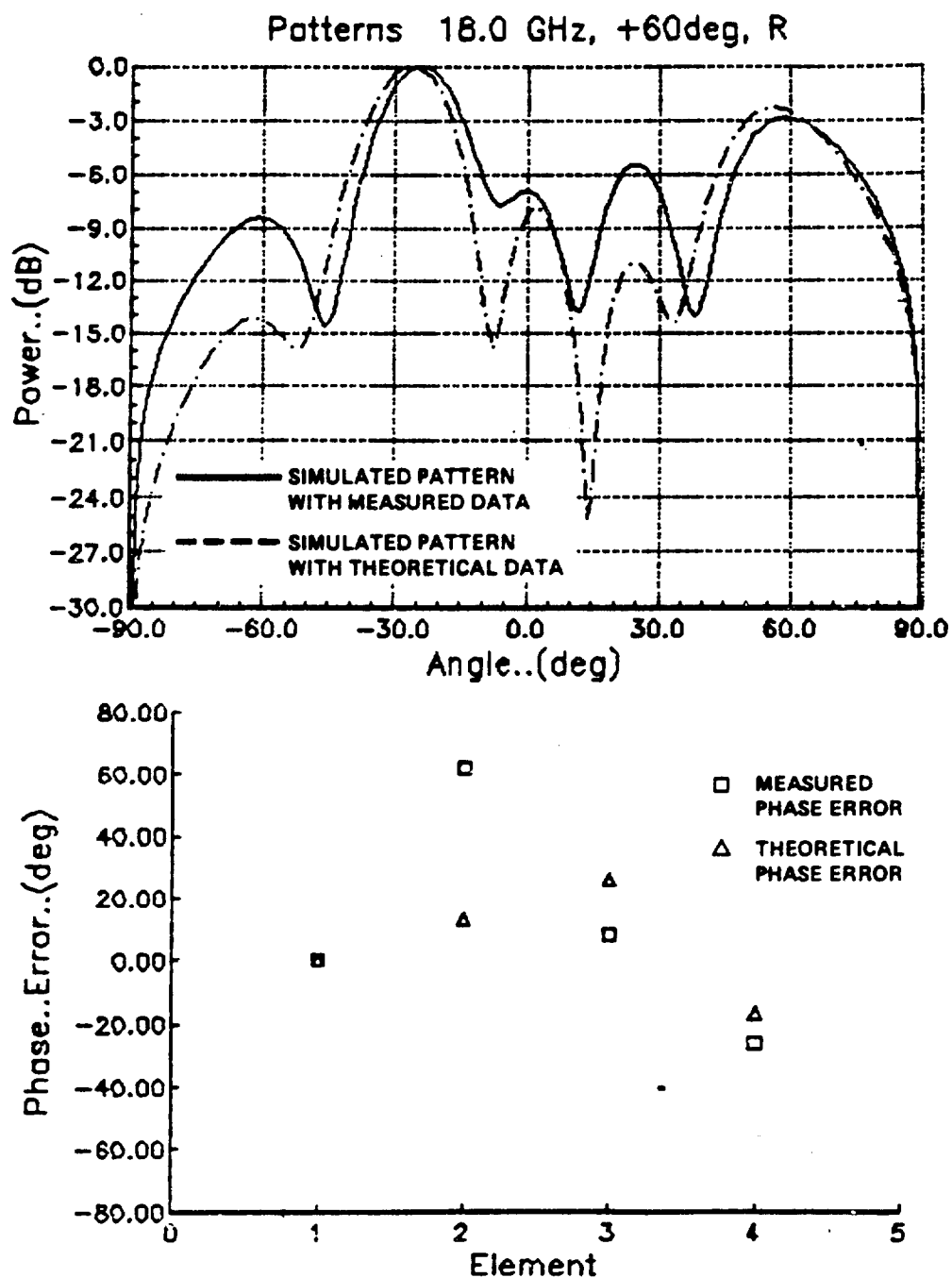


Figure 16. Simulated Subarray Patterns and Aperture Phase Distributions at 18 GHz and 60 Degrees Scan Angle

Figures 10 and 11 show the simulated subarray patterns (solid lines) based on the measured T/R Module phase data (as given by squares). The frequency used is 6 GHz and beam angles are 0 (Figure 11) and 60 degrees (Figure 12). For comparison purpose, the theoretical phase data were also shown in the figure (as given by triangles). Note that only one out of four T/R Modules has larger phase error (about 30 degrees as shown in Figure 10). The simulated subarray patterns using the theoretical phase data were shown by the dashed lines. Good agreement between the dashed line and solid line subarray patterns has been obtained. It should be mentioned that there were no grating lobes at 60 degrees scan angle (Figure 11), due to the small element spacing.

Figure 12, 13 and 14 show the simulated subarray patterns for the frequency of 12 GHz and beam angles of 0, 30 and 60 degrees, respectively. The simulated patterns with the measured and theoretical aperture phase data again agree well, except sidelobes. The higher sidelobe levels shown in these figures are mainly caused by large phase errors at element No. 2. Figures 15 and 16 show the simulated patterns for the frequency of 18 GHz and beam angles of 0 and 60 degrees, respectively. Note that the phase error at element No. 2 increases to about 50 degrees for broadside beam (Figure 15) and 65 degrees for beam at 60 degrees (Figure 16). As a result, the subarray pattern sidelobes for the measured phase data are much higher than that of the theoretical phase data. For future development, the No. 2 T/R Module

phase error can be corrected and the corresponding sidelobe level of subarray patterns will be improved. The grating lobes are shown in Figures 14 and 16 for scan angle at 60 degrees at frequencies of 12 and 18 GHz. These grating lobes are expected due to the large element spacing at higher frequencies.

4.0 T/R MODULE/SUBARRAY INTEGRATION TEST

4.1 PHYSICAL INTEGRATION

To verify the simulated subarray patterns, four T/R Modules were integrated with a 6 x 6 subarrays as shown in Figure 17. The 6 x 6 subarrays were mounted on the top of a 12 x 12 inches ground plane. The four T/R Modules were mounted behind the ground plane. Four coaxial cables were used to provide RF connections between the four T/R Modules and the center four subarrays. The outer two subarrays were terminated by RF loads. Each subarray contains 6 dielectric notch radiator which was developed to operate from 6 to 18 GHz.

The input VSWR for each embedded element is better than 2:1. The spacing between any two adjacent subarrays is 0.492 inch. To provide structure support, foam spacers were placed between two adjacent subarrays.

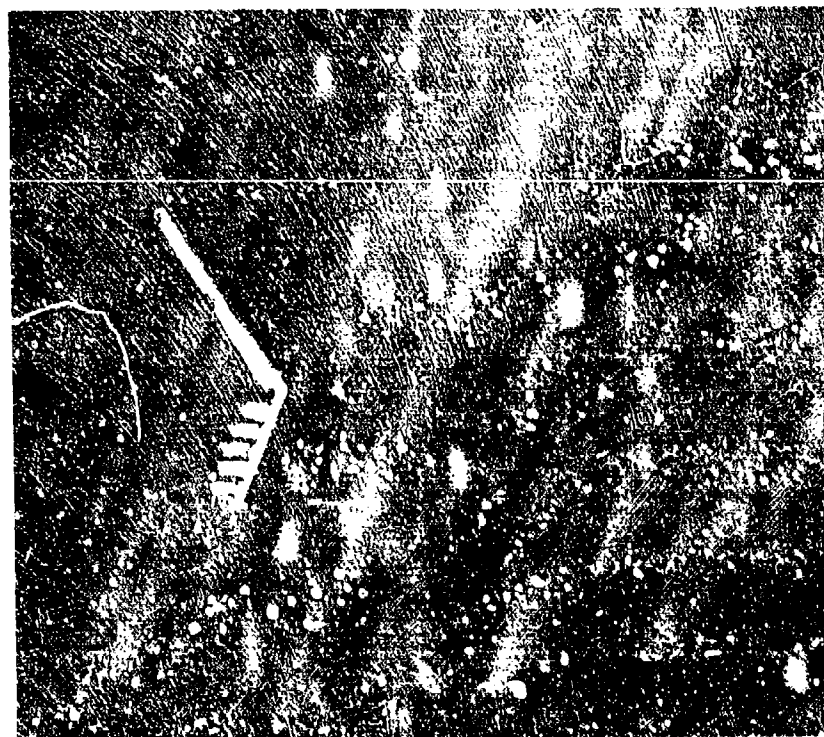


Figure 17. A Photo to Show the Subarrays Integrated with the T/R Modules for Pattern Test

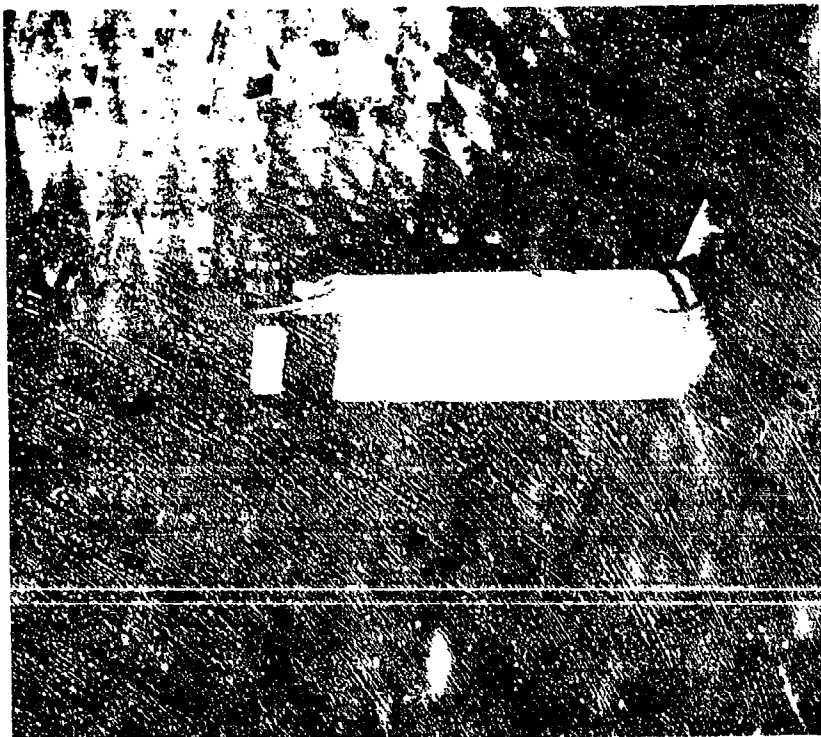


Figure 13. A Photo to Show the Integrated T/R Module/Subarray Mounted on a Foam Column for Pattern Test Inside an Anechoic Chamber

4.2 TESTING CONDITIONS

The integrated T/R Module/Subarray was mounted on top of a foam column pedestal inside an anechoic chamber for subarray pattern measurement, as shown in Figure 18. The power supply and T/R Module control circuits were placed on a rack and placed outside the anechoic chamber. The module gain level settings were adjusted to provide a uniform gain distribution across the array. This involved adjusting attenuation levels to compensate for individual temperature deviations due to the position of each module in the subarray. Gain levels were adjusted to maintain a nominal gain of 30.0 dB for both transmit and receive modes. The accuracy of this gain level is within ± 0.5 dB for each module.

5.0 MEASURED SUBARRAY PATTERNS

The integrated T/R Module/Subarray patterns were measured for frequencies of 6, 12 and 18 GHz and beam angles of 0, 30 and 60 degrees. Typical data were shown in Figures 19, 20 and 21. For comparison purposes, the simulated subarray patterns using the theoretical element phase data were also plotted in these figures. In general, the measured beamwidth is smaller than that simulated. This may be caused by the fact that the outer two subarrays were excited by

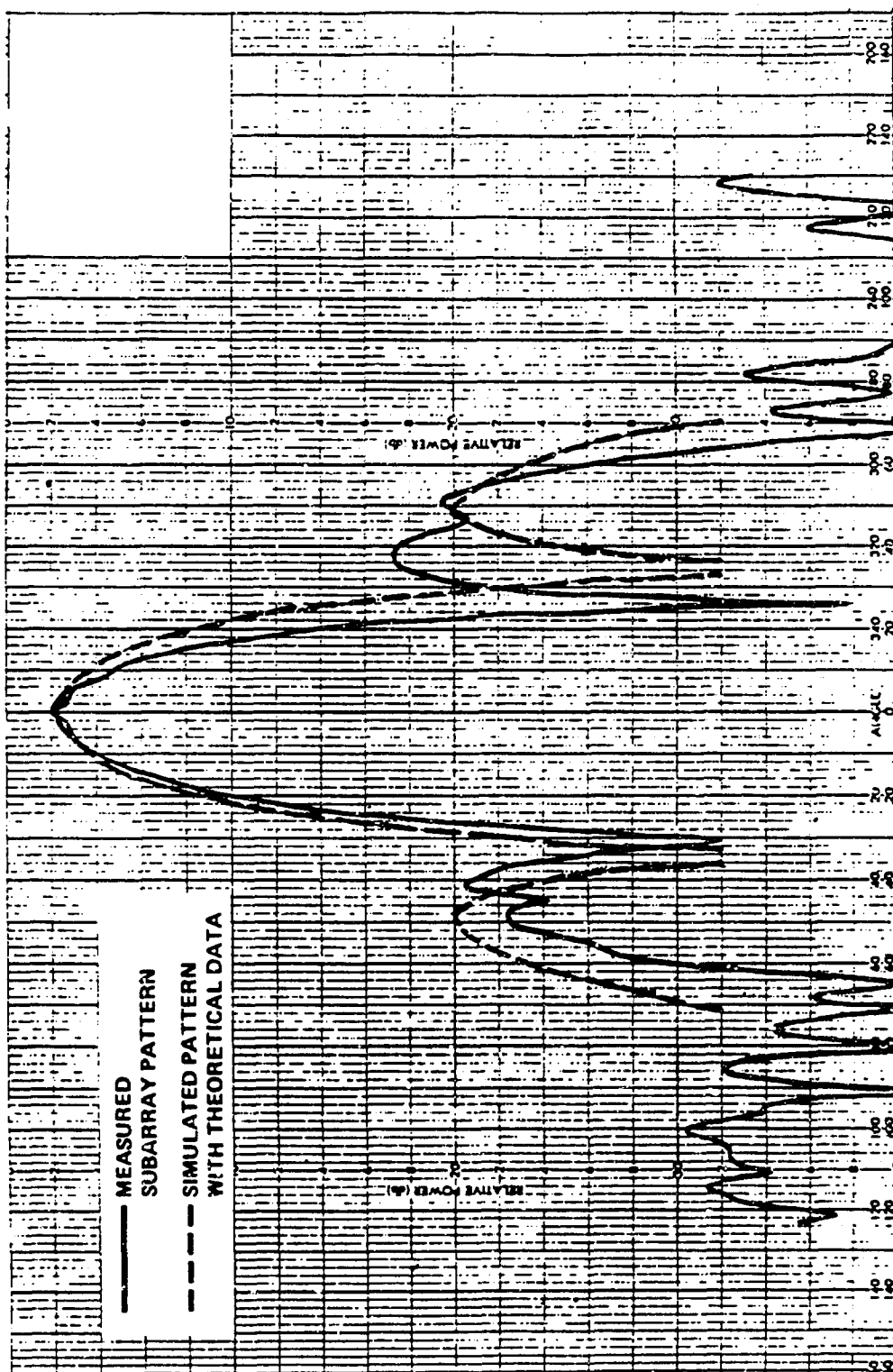


Figure 19. Measured Subarray Pattern at 12 GHz and 0 Degree Scan Angle

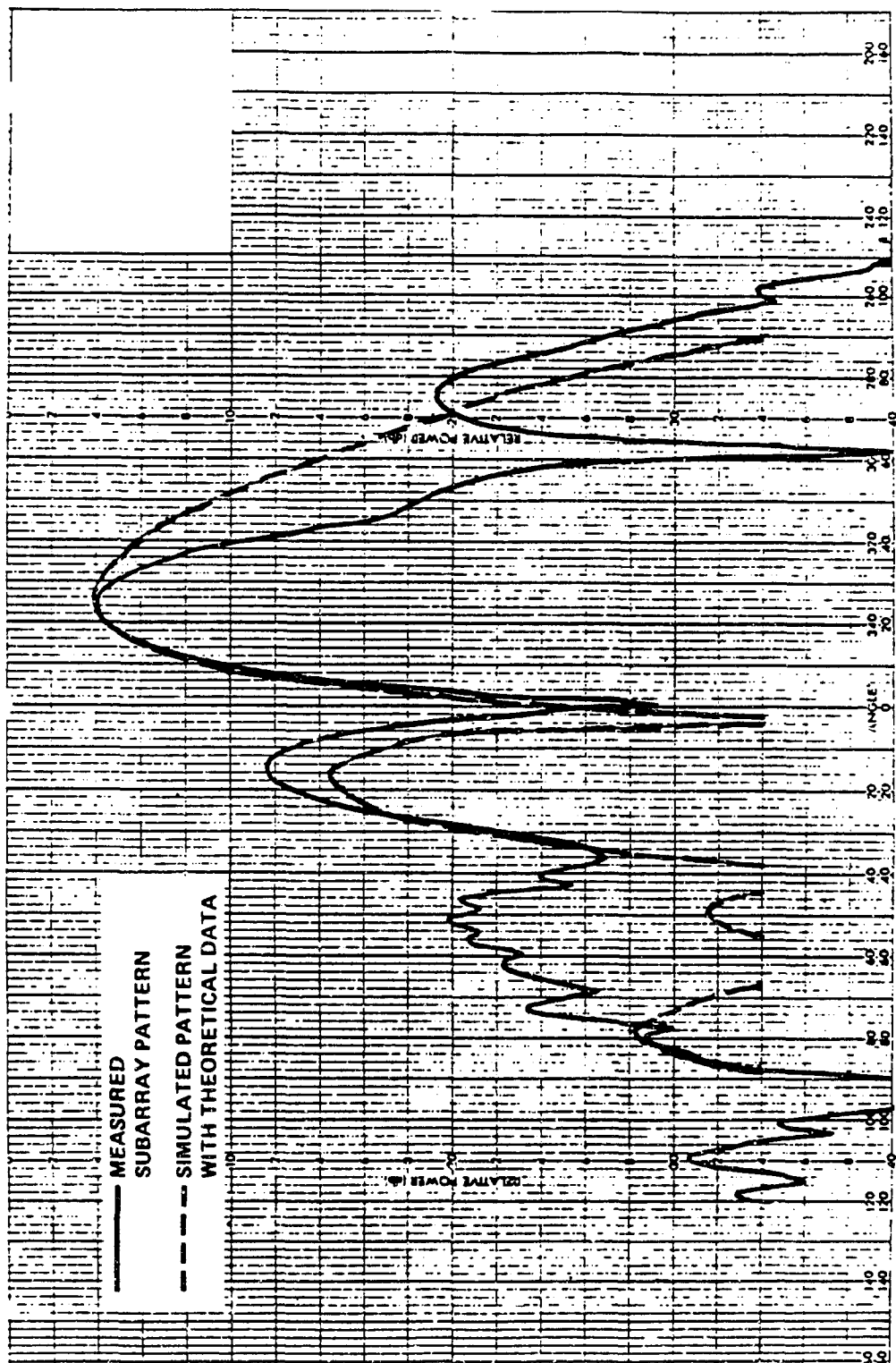


Figure 20. Measured Subarray Pattern at 12 GHz and 30 Degrees Scan Angle

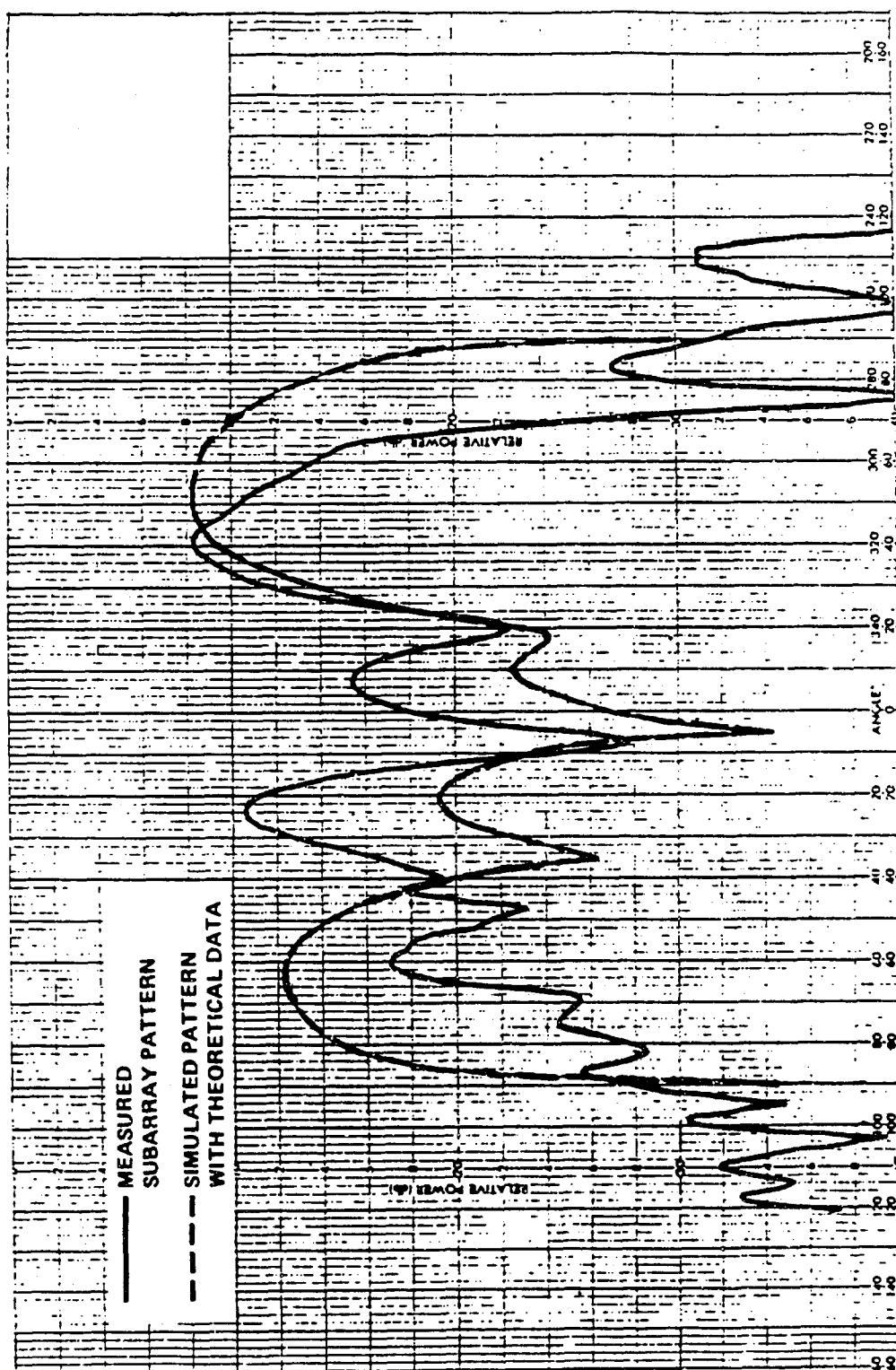


Figure 21. Measured Subarray Pattern at 12 GHz and 60 Degrees Scan Angle

mutual coupling effect from the center four active subarrays. As a result, the effective subarray aperture increases which will reduce the beamwidth.

It is also noted that the sidelobes and grating lobes of the measured subarray patterns are higher than that simulated. This may be caused by aperture phase error as discussed in Section 3.0. However, the beam did scan to the desired directions using the developed 5-bit delay line phase shifter.

6.0 CONCLUSIONS AND RECOMMENDATIONS

6.1 CONCLUSIONS

A 5-bit true time delay MMIC/hybrid 6-18 GHz T/R Module has been developed for phased array EW and shared aperture applications. Saturated output power is typically +25 dBm. Receive and transmit path gains are approximately 35 dB each, with 20 dB of gain control. Each T/R Module may be switched into one of 31 net time delay states. Unit-to-unit net delay tracking for four units is within 7 psec while gain tracking is within 5 dB.

Based on the measured and simulated subarray pattern performance, it is concluded that the broadband T/R Module does provide the beam steering capability over the designed frequency range (from 6 to

18 GHz) and the space angle coverage (± 60 degrees from array broadside).

6.2 RECOMMENDATIONS

Three main areas for improvement have been identified. First, FEDs should be used instead of PIN diodes for all switching elements, including delay shifters. Second, control of the module needs to be analyzed and integrated, as much as possible, into the module. Third, packaging needs to be studied and improved. In addition, the phase tracking from module to module needs further improvement to reduce subarray aperture phase error. The improvement in gain tracking is also recommended.

7.0 ACKNOWLEDGEMENT

Thanks are due to Mr. R. E. Chapman and Dr. G. Schaffner for their support in this IR&D program.

ARRAY TRADE-OFF STUDY USING MULTILAYER
PARASITIC SUBARRAYS

by

A. Zaman, R. Q. Lee, R. A. Acosta

NASA Lewis Research Center

Cleveland, OH 44135

ABSTRACT:

The use of multilayer parasitic patch subarrays in a microstrip phased array offer many potential advantages. In this paper an analytical study of microstrip arrays with high gain multilayer parasitic patch subarrays and conventional patch antennas is presented. It is indicated that a thinned array of half as many multilayer parasitic patch subarrays (per row and column) at twice the spacing will perform as well as the full array of ordinary patch antennas. The criterion for comparison was array gain, 3 dB beamwidth and sidelobe level. The attendant reduction in the required number of patch antennas and consequently, MMIC phase shifters is very significant in terms of array complexity, cost and power loss.

INTRODUCTION:

It has been reported in the literature that the presence of parasitic patch elements adjacent to excited ones enhances the gain of the patch antenna [1-3]. Recent experimental studies have established that parasitic patch subarrays with overlaying stack of parasitic patches above an excited one can produce gain several dB higher than that of the single excited patch itself [4]. Using these higher gain multilayer patch subarrays as the basic radiating unit for a large array with MMIC (Monolithic Microwave Integrated Circuits) phase and amplitude control offer many advantages. For beam pointing and sidelobe level control in a large array of patch antennas, the number of MMIC's required is proportional to the number of patches comprising the array. The resulting beam forming network introduces complex feed architecture, high power loss, spurious radiation in the feed network and high cost due to MMIC's. To alleviate these problems, higher gain parasitic patch subarrays can instead be employed that will meet the array design criterion with fewer number of elements and hence fewer number of MMIC devices.

The aim of this paper is to study the feasibility of using a reduced number of such high gain elements to maintain the design performance in large MMIC phased array. The result of this study will serve as a reference performance basis in large array design where array architecture is modified, addressing critical configuration and performance issues.

ARRAY TRADE-OFF ANALYSIS:

In the simulation, the trade-off performance of a (16 x 16) array of microstrip patch elements in the broadside direction was studied. The 34 dB array gain was realized with the above array of 256 patch elements with 10 dB individual gain and aperture dimension of $(7.5\lambda \times 7.5\lambda)$. Figure 3 shows such an array. If instead, the multilayer parasitic patch subarrays with 15 dB individual gain were chosen as the basic radiating unit then the array performance goal (i.e. gain, sidelobe level, beamwidth) is achievable with only 81 elements; resulting in a substantial reduction in the number of MMIC required.

Figures 1 and 2 show the far-field patterns of a single patch and a multilayer parasitic patch subarray respectively. For analysis; the element patterns were approximated by appropriate cosine powered functions. Then two-dimensional array patterns were computed using generalized array theory.

Figures 5 through 10 show the H-plane cut of the far-field plots for different array configurations. For comparison, only the H-plane plots have been displayed. Gain for each array was computed by integrating the total radiated power.

RESULT AND DISCUSSION:

The trade-off comparison for a planar array of mentioned gain, sidelobe level, beamwidth is displayed in Table 1. The first three columns in Table 1 correspond to the array configurations with 34 dB array gain. The next three columns give an alternate look at the array if element savings are not taken

into consideration. The resulting increase in array gain of 39 dB is associated with higher gain elements at the expense of a larger number of MMIC devices or with a large number of standard gain elements and proportional number of MMIC devices. The study results indicate that an array of standard gain patch elements reconstructed with reduced number of higher gain parasitic elements within the same array aperture and consequently at increased element spacing will produce same directivity, 3 dB beamwidth and lower sidelobe envelope. Hence for a large array, an improvement of 5 dB in element gain will reduce the number of MMIC required by 66% to operate at the design performance level.

The above study does not take into consideration the effect of mutual coupling or radiation from the feed lines which would likely degrade the anticipated performance and lower the array gain.

The performance degradation can be recovered somewhat without additional MMIC devices by an array of (16×16) multilayer parasitic subarrays and connecting the subarrays into groups of two. Each such group can be controlled by an MMIC device as indicated in Figure 4. Though the resulting array has the same number of radiating elements as its conventional counterpart but requires fewer number of MMIC devices. Such an array produces even higher overall gain and lower sidelobe envelope with identical 3 dB beamwidth and null location.

REFERENCES:

1. Entschladen, H. and Nagel, U. (1984) Microstrip Patch Array Antennas, Electron. Lett., 20: 931-933.
2. Lee, K. F., Acosta, R. J. and Lee, R. Q. (1987) Microstrip Antenna Array with Parasitic Elements, IEEE/AP-5 International Symposium, Blacksburg, VA.
3. Lee, R. Q. Acosta, R. J. and Lee, K. F. (1987) An Experimental Investigation of Parasitic Microstrip Arrays (1987) Symposium on Antenna Application, Monticello, IL.
4. Lee, R. Q. and Lee, K. F. (1988) Gain Enhancement of Microstrip Antennas with Overlaying Parasitic Directors, Electron. Lett., 24: 656-658.

Gain: Array	34 dB			39 dB		
	10 dB	15 dB	15 dB	15 dB	10 dB	10 dB
Element						
Array:						
Number	(16 x 16)	(9 x 9)	(9 x 9)	(16 x 16)	(29 x 29)	(29 x 29)
Aperture	(7.5λ x 7.5λ)	(7.5λ x 7.5λ)	(4λ x 4λ)	(7.5λ x 7.5λ)	(7.5λ x 7.5λ)	(14λ x 14λ)
Spacing	0.5λ	0.94λ	0.5λ	0.5λ	0.27λ	0.5λ
Feature	Reference Array	Aperture Constant	Spacing Constant	Spacing Aperture Constant	Aperture Constant	Spacing Constant
θ _{3H}	6.2°	6.2	10.5°	6.2°	6.36°	3.4°
1st Zero	7.05°	6.8°	12.3°	6.8°	7.27°	9.1°
S.L.L.:						
3rd	-23 dB	-24.5 dB	-27.5 dB	-26 dB	-24 dB	-22 dB
5th	-31.5 dB	-36 dB		-41 dB	-34.5 dB	-25.5 dB

TABLE I

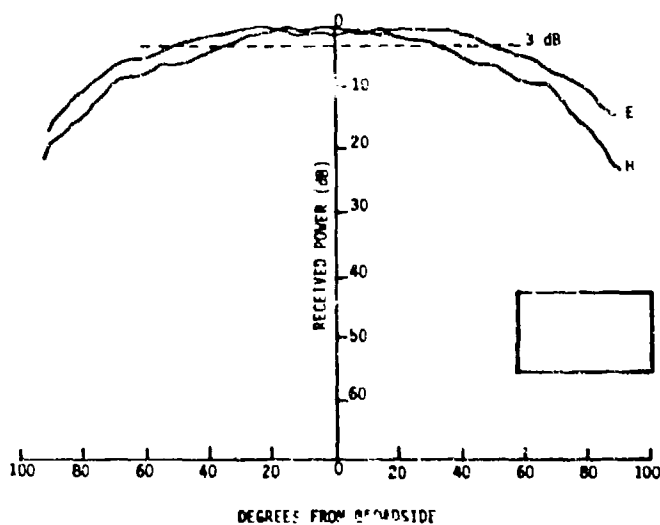


FIGURE 1: E AND H-PLANE PATTERNS FOR A SINGLE PATCH ELEMENT.

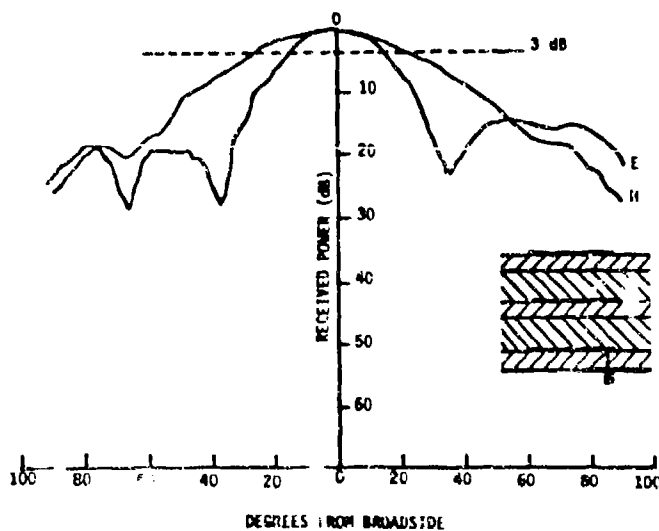


FIGURE 2: E AND H-PLANE PATTERNS FOR A MULTILAYER PARASITIC SUBARRAY ELEMENT.

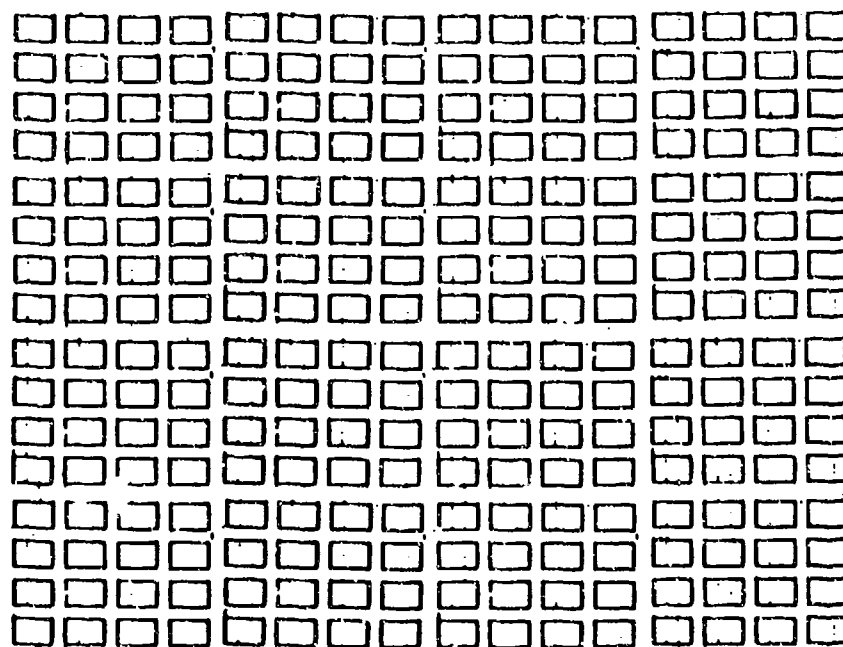


FIGURE 3: (16 x 16) ARRAY OF SINGLE PATCHES.

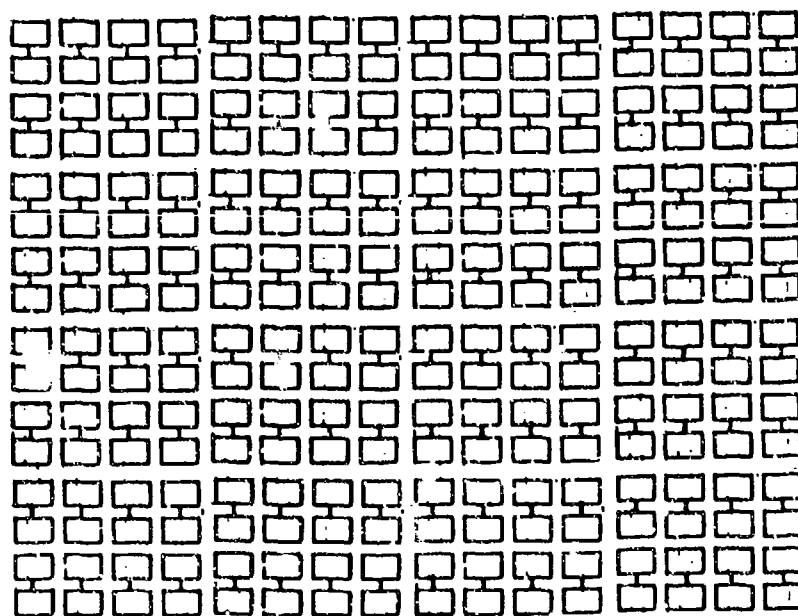


FIGURE 4: (16 x 16) ARRAY OF MULTILAYER
PARASITIC SUBARRAYS. SUBARRAYS
CONNECTED INTO GROUPS OF TWO.

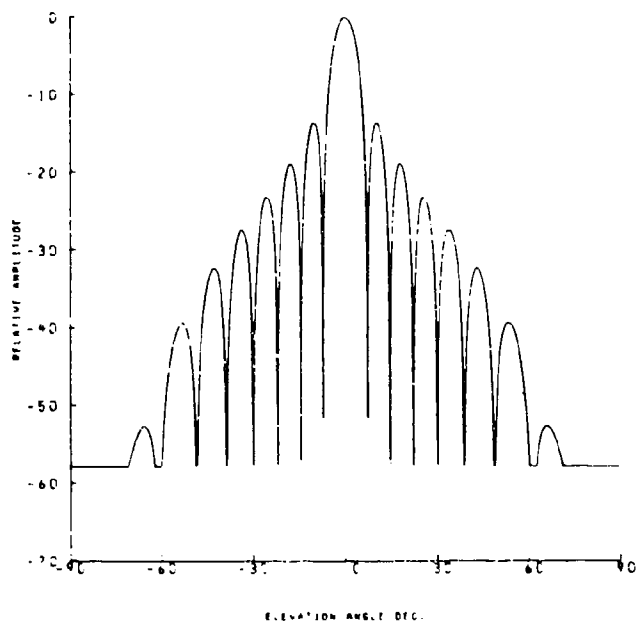


FIGURE 5: H-PLANE PATTERN FOR A (16 x 16) ARRAY OF SINGLE PATCHES AT 0.5λ ELEMENT SPACING.

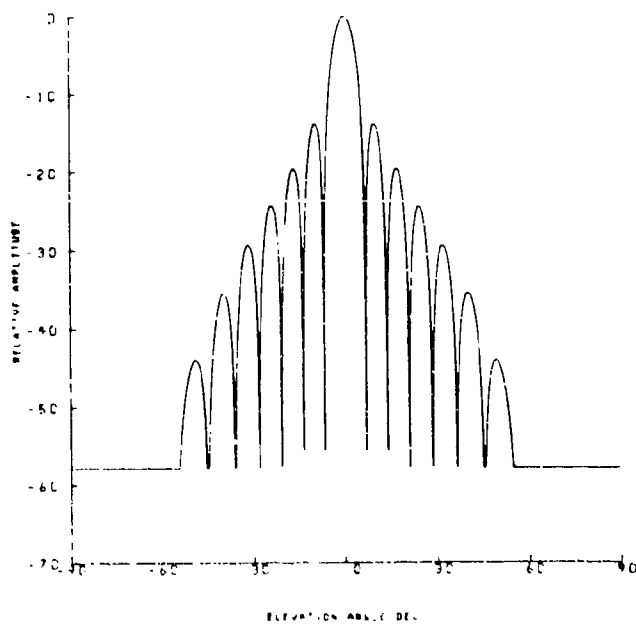


FIGURE 6: H-PLANE FOR A (9 x 9) ARRAY OF MULTILAYER PARASITIC SUBARRAYS AT 0.94λ ELEMENT SPACING.

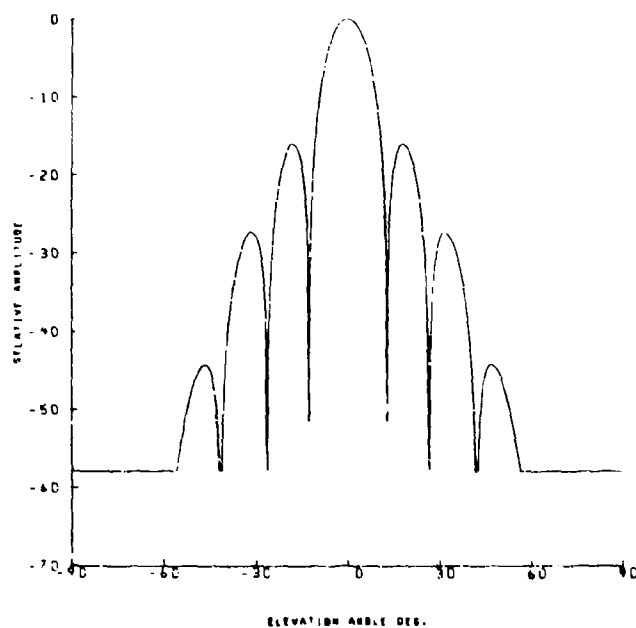


FIGURE 7: H-PLANE PATTERN FOR A (9 x 9) ARRAY OF MULTILAYER PARASITIC SUBARRAYS AT 0.5λ ELEMENT SPACING.

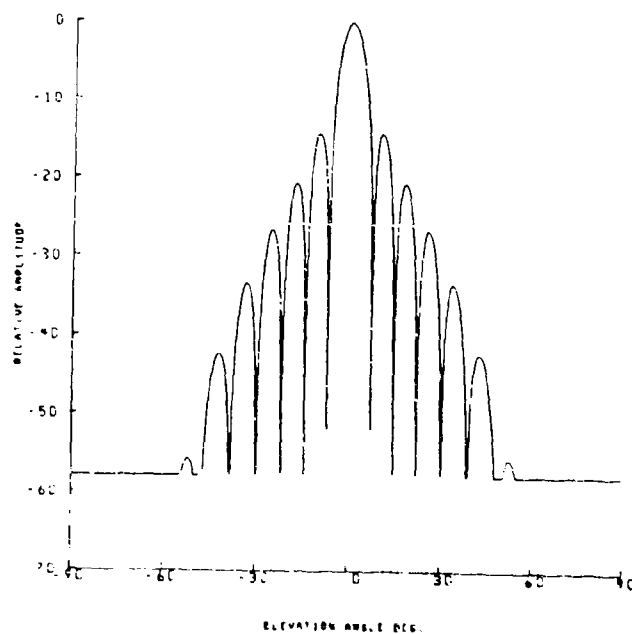


FIGURE 8: H-PLANE PATTERN FOR A (16 x 16) ARRAY OF MULTILAYER PARASITIC SUBARRAYS AT 0.5λ ELEMENT SPACING

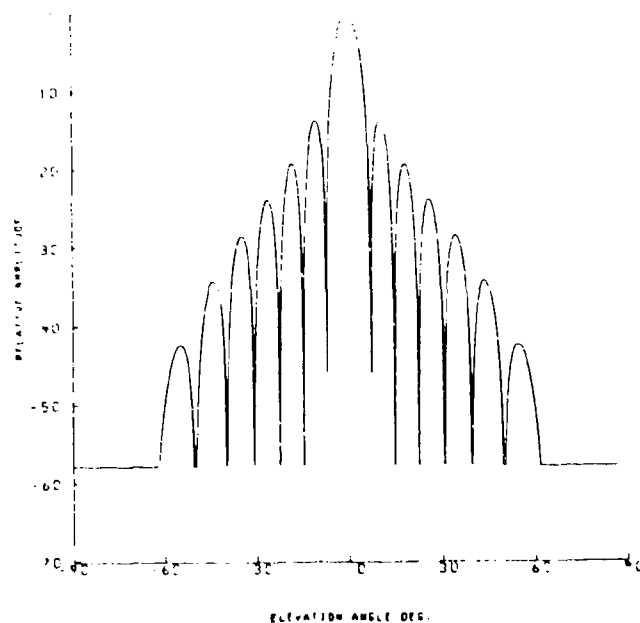


FIGURE 9: H-PLANE PATTERN FOR A (7 x 29) ARRAY OF SINGLE PATCHES AT 0.7λ ELEMENT SPACING

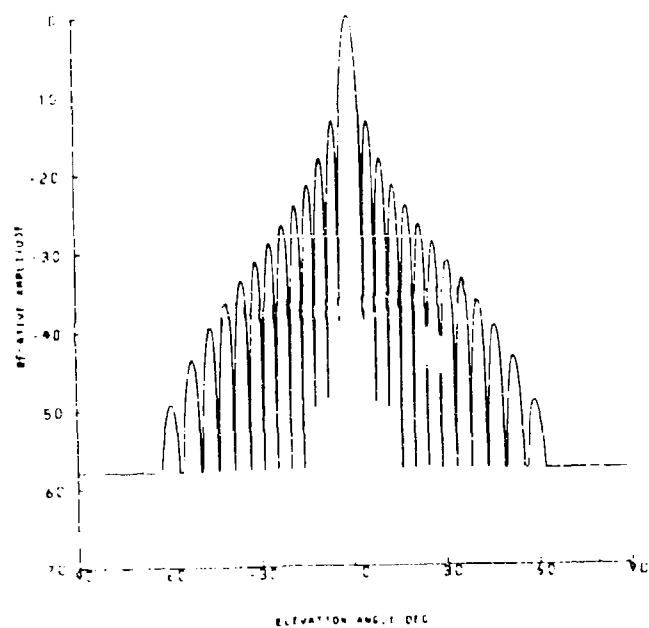


FIGURE 10: H-PLANE PATTERN FOR A (29 x 29) ARRAY OF SINGLE PATCHES AT 0.5λ ELEMENT SPACING.

C. DONN, A. E. BOLLESEN AND S. H. WONG
ROCKWELL INTERNATIONAL CORPORATION
ANAHEIM, CALIFORNIA 92803

1. INTRODUCTION

In recent years, Rockwell has been developing SHF/EHF monolithic active phased array technology. Recent advances in the GaAs monolithic microwave integrated circuit (MMIC) technology in the SHF/EHF bands suggest the feasibility of very "thin" active phased arrays which are ideal for conformal applications (1,2,3). Rockwell completed a study for Rome Air Development Center, Hanscom AFB, Massachusetts which defined a design approach for the K-band monolithic active receive array (4,5,6). A 16-element subarray was utilized to demonstrate and evaluate the design, fabrication and integration of the recommended array architecture and technology. This presentation reports the performance of this 16-element monolithic active receive array.

2. ARRAY DESCRIPTION

A photo of the 16-element array hardware components, which are: the array, phase shifter control box and power supply box, is shown in Figure 1; an RF functional diagram is illustrated in Figure 2.

Photos of subarray aperture and the detail of a single radiating element cell are shown in Figure 3. Each individual element cell consists of a cavity radiating element excited orthogonally (to produce circular polarization) by outputs from a Lange coupler; a single GaAs monolithic microwave integrated circuit consisting of a low noise amplifier, a buffer amplifier and a 3-bit phase shifter.

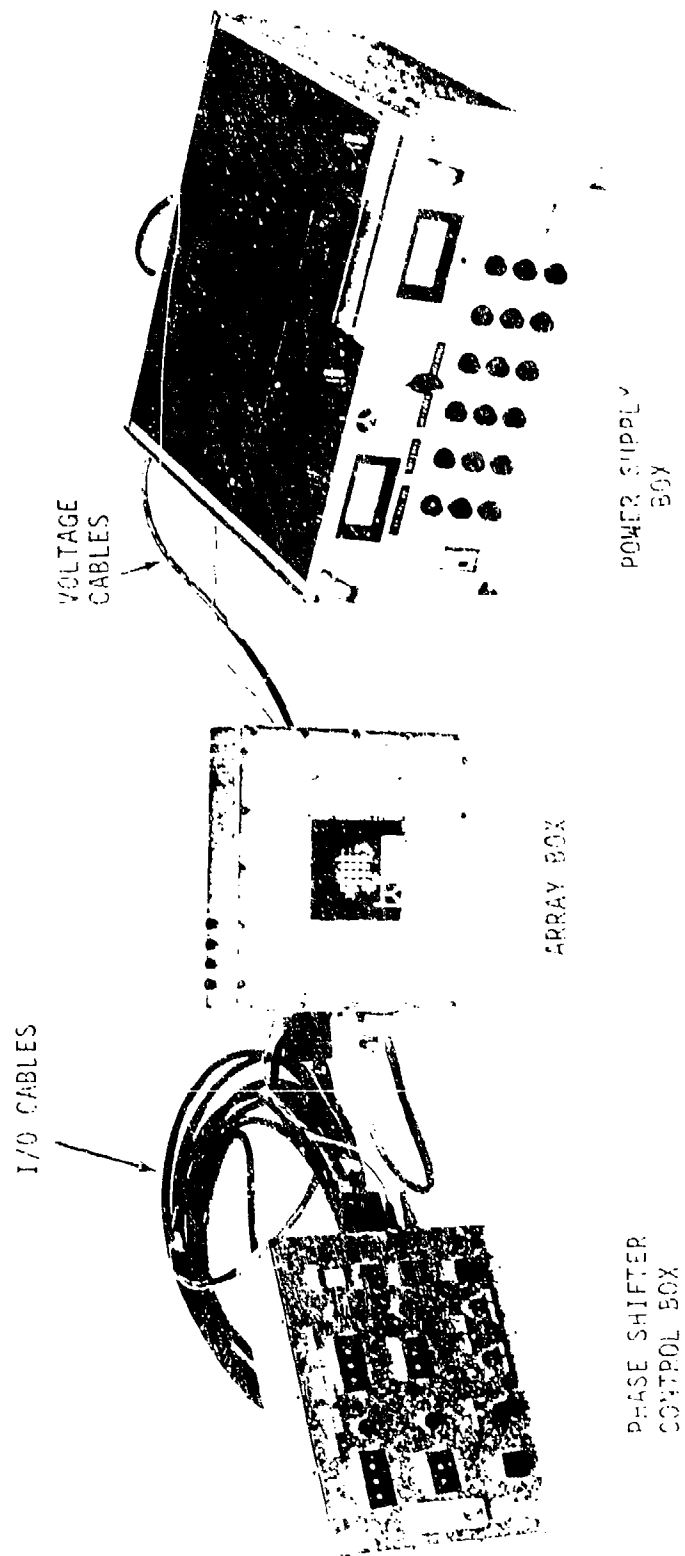


FIGURE 1 THE 16-ELEMENT MMIC PHASED ARRAY HARDWARE COMPONENTS

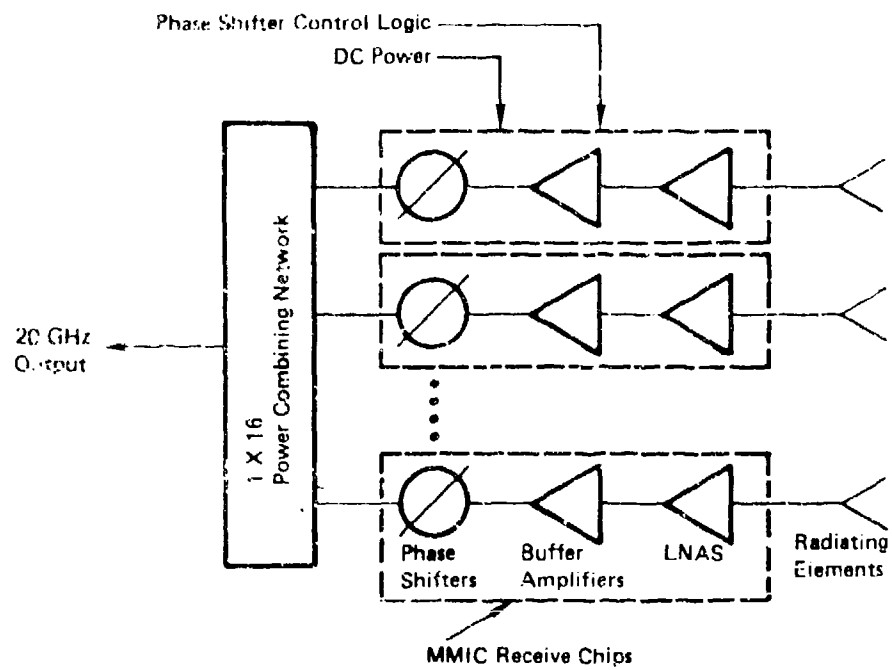


FIGURE 2 RF FUNCTIONAL DIAGRAM OF THE 16-ELEMENT SUBARRAY

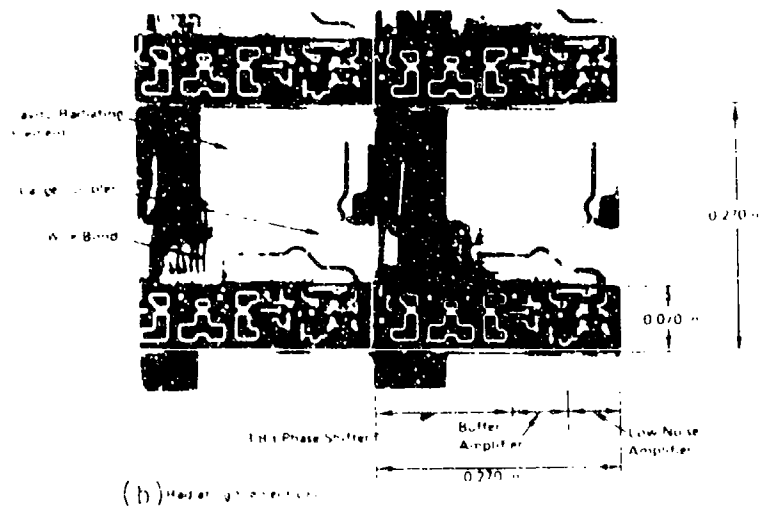
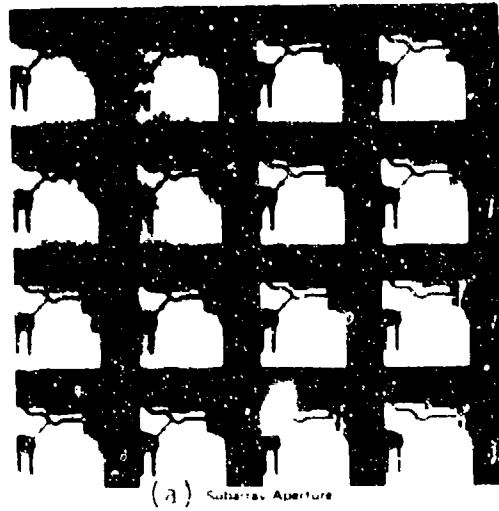


Figure 3 Photo of the 16 Element Subarray

All 16 radiating elements are connected to the RF distribution network via vertical RF feed thrus. The array also provides interconnections to control the MMIC functions. The array was designed with uniform distribution and the antenna control was mechanized into the control box rather than "on element" control modules.

3. RECEIVE MODULE

The 20 GHz MMIC receive module (or chip) contains a low-noise amplifier, a 3-bit phase shifter and a buffer amplifier all integrated in a single monolithic GaAs chip. The overall dimensions of the chip are 0.070"X0.270" with a thickness of 0.005". The goals for design performance were as follows:

Low-Noise Amplifier	Gain	10 dB
	Noise Figure	4 dB
Buffer Amplifier	Gain	10 dB
	Noise Figure	5 dB
Phase Shifter	Isolation Loss	9 dB max. (3 dB per bit)
	Phase	45°, 90°, 180° (per bit)

FABRICATION PROCESS

Gallium arsenide monolithic microwave integrated circuit (MMIC) fabrication technology at Rockwell is based on direct, localized ion implantation for active layer formation, projection, direct-step-on-wafer (DSW) photolithography. This DSW photolithography was used for all patterning steps including FET gates, plasma-enhanced chemical vapor deposition (PECVD) of silicon nitride for metal-insulator-metal (MIM) capacitors, low capacitance crossovers, through-substrate via holes for ground connections, and

a refractory metal-based metallization system for high reliability. All processing is carried out on 3-inch wafers, using automated high throughput equipment, in a closely monitored pilot production environment. FET gates, 0.5 μm -long, are patterned using a proprietary dummy-gate process. Dry processing techniques including ion milling, reactive ion etching and plasma etching are used extensively. This has led to the development of a high yield process with state-of-the-art circuit performance. Tight control of all important fabrication steps is maintained through an extensive use of test patterns on the wafer. Further control over device performance is offered by the availability of in-house-grown semi-insulating GaAs and a strong internal program in materials technology. A CALMA GDS II computer-aided design system is used for design and layout of IC masks, producing the pattern generator tapes required for mask fabrication. Mask fabrication is carried out at a Rockwell-owned entity, OPTOMASK, which also provides service to commercial semiconductor companies.

GaAs MESFETs are used as active devices and Schottky diodes are used for level shifting applications. Except for very small values, resistors are formed by ion implantation (300-100 Ω/\square). Small value resistors are fabricated using ohmic metallization with a sheet resistance of 1.5 Ω/\square . The dissimilar active layer requirements of different types of FETs, diodes, and resistors are met by multiple, localized ion implantation.

MIM capacitors, with plasma-enhanced CVD silicon nitride as dielectric are used for both RF tuning and bypassing due to good control ($\pm 10\%$) on capacitance per unit area. A capacitance of 130 pF/mm² is currently used, although higher values are possible by thinning the dielectric layer which may reduce reproducibility due to small variations in lithography.

Wafer fabrication is done on 635 μm -thick substrates (to minimize breakage). Before etching via holes from the backside, the substrates are thinned to 125 μm . Thinning is accomplished by a combination of lapping and polishing that leaves a mirror finish on the final surface. This helps in reducing RF losses in the microstrip ground plane which is formed by metallizing the backside by electroless and electro-plating (3 μm gold). Backside metallization also plates all the via holes, thereby providing ground points at appropriate locations on the chip. Transmission lines are constructed in the form of microstrip. The fabrication process incorporates a two-level metallization scheme with low capacitance crossovers. The second metallization level which forms all the microwave circuitry, top plates of MIM capacitors and many interconnects, is gold plated to a thickness of approximately 3 μm to minimize RF losses. An air bridge technology for 3-inch wafers using projection lithography has recently been developed and implemented as part of the baseline process. The interlevel dielectrics (silicon oxynitride) is also used to passivate all active devices. No organic materials (e.g., polyimide) are present on the MMIC chip. The wafer is diced from the back, with a high

speed diamond saw, since it is not feasible to demount a 5 mil thick 3-inch wafer from the carrier substrate and remount it face-up without excessive breakage. A specialized pattern in the via mask defines the saw streets. A flow chart of the process showing cross-sections of devices after completion of the major process steps is provided in Figure 4.

A single 3" wafer, containing 44 fields with each field having a layout as shown in Figure 5, was processed. Each field contains three chips, two are of the latest design and the third is the prototype design included as a back-up if required. The wafer was DC probed prior to thinning and backside processing. Eighty-seven (87) of the eighty-eight (88) possible chips with the latest design passed the DC screening.

TEST RESULTS

A cascade probe connected to a HP8510 was used to test all chips. The cascade probe is a specially designed RF probe which allows accurate RF measurement without the bonding of chips onto a test fixture and thus chips were free of possible physical damage after the RF testing. A preliminary RF screening consisted of measuring RF signal at chip output port through all 3-bit phase states was performed on the 87 chips. Thirty-six chips failed this preliminary RF screening. The remaining 52 chips underwent a complete S-parameter characterization from 19 GHz to 21 GHz. Based on the preliminary scrutinization of the test data, nine chips were deemed to be unacceptable due to either very low gain or large phase

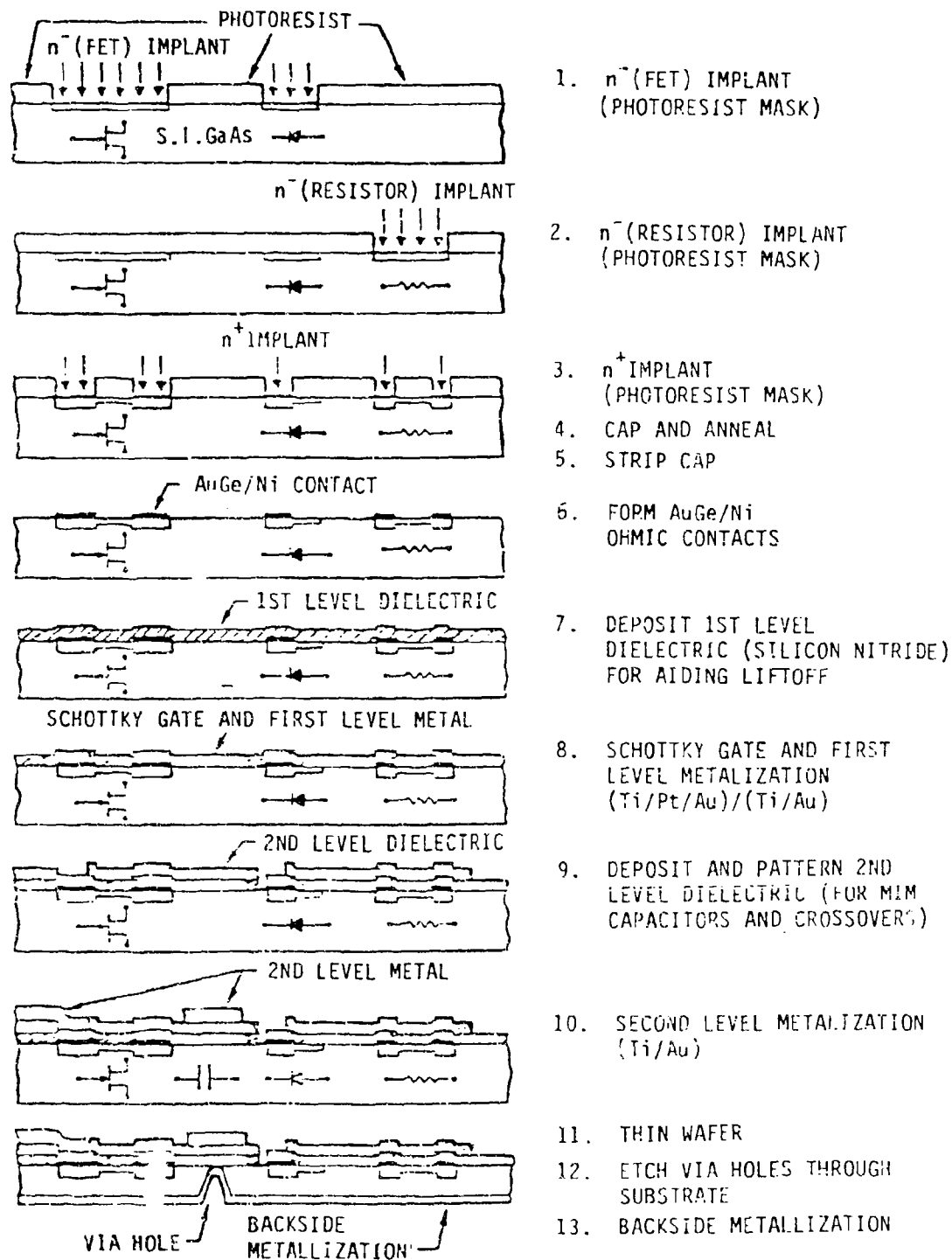


Figure 4 Schematic MMIC Cross Section After Completion of Various Processing Steps

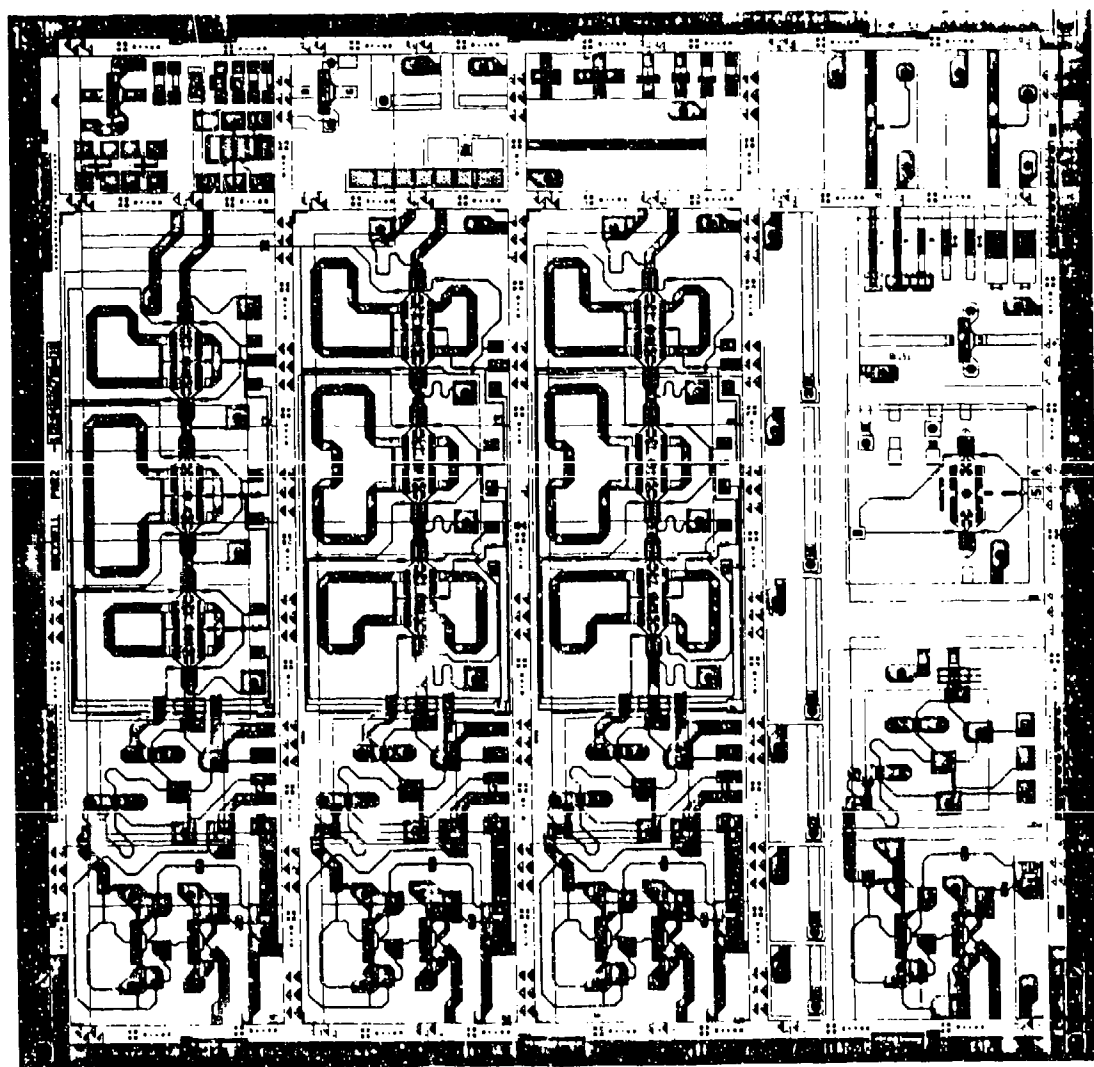


FIGURE 5 20 GHz RECEIVE MODULE MASK LAYOUT

variation or a combination of both. The remaining test data of 42 chips were analyzed to determine peak gain for each chip, the frequency where the peak gain occurred, the gain variation across the eight phase states, and the phase delay (referenced to the zero-degree phase state for each phase state). The means, maximum, minimum and standard deviation are tabulated in Table 1. It should be noted that except for the peak gain, the statistics are based on the data at 20 GHz only.

TABLE 1 20 GHz MMIC CHIP TEST DATA SUMMARY

Parameter	Data Summary (42 devices)				
	Units	Mean	Max	Min	Standard Deviation
Peak S(21) Gain	dB	9.1	12.8	7.0	1.3
Freq @ Peak S(21) Gain	GHz	19696	19920	19440	.128
S(21) Gain Spread (8 phases)	dB	1.4	1.7	1.1	.165
S(21) Angle (45 State)*	Degrees	39.9	42.3	37.5	1.01
S(21) Angle (90 State)*	Degrees	87.7	90.8	84.4	1.50
S(21) Angle (135 State)*	Degrees	126.5	130.2	121.8	2.06
S(21) Angle (180 State)*	Degrees	184.9	188.9	179.6	2.04
S(21) Angle (225 State)*	Degrees	225.6	229.6	220.1	2.52
S(21) Angle (270 State)*	Degrees	271.3	276.5	265.3	2.78
S(21) Angle (315 State)*	Degrees	314.5	319.5	308.6	3.05
*Referenced to S(21) Angle in the 0 degree phase state					

Additional analyses were performed on the 16 chips selected for the integration onto the array. The gain and phase measurement data are listed in Tables 2 and 3 for 19.5 GHz and in Tables 4 and 5 for 20 GHz. The numbers 1 - 16 in the Tables correspond to the position on the array. Good uniformity can be seen in the data both across the 16 devices for each phase state and especially across the phase states of each individual chip. The absolute values do not match the design goals; however, considering that this is the first quantity lot of a higher order MMIC (several functions on a single chip) produced (to our knowledge anywhere), the results are extremely encouraging.

While gathering the raw data, it was noted that the frequency response was lower than desired. The gain and phase shift across the frequency band from 19.2 to 20.6 GHz for a single chip is shown in Figures 6 and 7 respectively. The slope on the phase shift is to be expected and is not of major concern as long as it is linear and consistent from phase state to phase state because a correction for frequency can be implemented in a large array.

The gain and absolute phase shift values are indicative of the state of modeling at the higher frequencies. Although models are well established at lower frequencies and for individual circuits, the same degree of confidence has not been achieved at the higher frequencies. There is sufficient evidence, however, to believe that with the S-parameter data obtained from this iteration, an MMIC can be produced to meet the design goals with little risk.

Table 2 Element Amplitude Excitation at 19.5 GHz

Element No.	MMIC Identification	CHIP GAIN IN dB FOR PHASE STATE									
		0°	45°	90°	135°	180°	225°	270°	315°	\bar{M}	σ
1	23B	4.21	5.10	4.94	5.86	3.81	4.50	3.95	4.99	4.67	.64
2	32D	8.03	8.93	8.70	9.55	7.75	8.51	8.00	8.98	8.56	.51
3	14F	4.58	5.76	5.60	6.62	4.44	5.11	4.49	5.62	5.28	.70
4	13H	6.60	7.77	7.47	8.44	6.55	7.21	6.45	7.53	7.25	.68
5	21G	7.72	8.63	8.38	9.12	7.56	8.16	7.51	8.36	8.18	.52
6	22A	10.19	11.09	11.00	11.79	9.91	10.55	10.06	11.03	10.70	.64
7	33H	7.42	8.56	8.31	9.23	7.29	8.06	7.41	8.48	8.10	.57
8	21F	5.59	6.60	6.51	7.46	5.36	5.96	5.38	6.48	6.17	.66
9	24F	5.17	6.34	6.13	7.22	5.00	5.68	5.06	6.24	5.86	.68
10	43D	6.57	7.64	7.47	8.40	6.42	7.20	6.54	7.62	7.23	.67
11	42H	9.63	10.82	10.50	11.51	9.36	10.24	9.42	10.63	10.26	.71
12	32G	4.34	5.14	5.30	6.29	4.21	4.92	4.20	5.29	4.96	.68
13	41H	3.71	4.84	4.62	5.54	3.53	4.20	3.52	4.55	4.31	.69
14	44E	6.11	7.27	7.07	8.13	5.89	6.60	5.95	7.12	6.77	.70
15	22E	6.64	7.63	7.47	8.45	6.37	7.08	6.49	7.58	7.21	.70
16	34H	6.31	7.54	7.38	8.19	6.31	6.96	5.85	7.36	6.99	.71
TOTAL											
\bar{M}		6.42	7.48	7.30	8.24	6.24	6.93	6.27	7.37	$\bar{M} = 6.94$	
σ		1.81	1.80	1.78	1.72	1.78	2.28	1.81	1.79	$\sigma = 2.15$	

Table 3 Element Phase Excitation at 19.5 GHz

Element No.	MMIC Identification	CHIP PHASE VALUE IN DEGREES FOR PHASE STATE							
		0°	45°	90°	135°	180°	225°	270°	315°
1	23B	0	40.1	92.5	125.7	181.2	221.0	264.2	307.3
2	32D	0	41.9	87.1	127.7	183.2	224.5	267.5	311.5
3	14F	0	46.4	84.8	123.7	180.6	215.0	262.8	304.8
4	13H	0	42.5	86.5	126.0	181.1	220.9	261.9	304.5
5	21G	0	42.7	86.8	128.2	182.2	224.4	266.4	311.6
6	22A	0	40.6	84.7	124.7	179.5	220.4	261.2	305.3
7	33H	0	39.2	85.4	124.1	185.1	218.2	261.6	304.2
8	21F	0	40.5	83.9	124.9	179.9	219.6	260.1	302.8
9	24F	0	38.0	84.3	122.0	179.1	216.8	260.7	302.0
10	43D	0	38.5	81.8	122.9	180.5	220.2	262.4	306.1
11	42H	0	39.6	83.6	123.7	176.6	216.2	258.0	301.9
12	32G	0	38.9	85.5	123.7	179.1	217.6	261.8	303.7
13	41H	0	46.2	91.3	130.1	184.9	224.4	267.4	310.2
14	44E	0	40.1	86.1	125.3	181.0	220.5	263.6	306.8
15	22E	0	40.6	85.8	128.2	183.7	223.8	266.6	310.4
16	34H	0	37.5	83.9	122.0	176.2	216.0	257.3	300.5
\bar{M}			40.83	85.88	125.2	180.9	220.0	262.7	305.9
σ			2.53	2.63	3.35	2.7	3.07	3.03	3.42

Table 4. Element Amplitude Excitation at 20 GHz

Module #	CHIP GAIN IN dB FOR PHASE STATE									
	REF (0 Deg)	45	90	135	180	225	270	315	\bar{M}	σ
1	5.0	5.5	5.5	6.2	4.7	4.9	4.8	5.3	5.24	.46
2	5.5	6.1	6.0	6.8	5.1	5.5	5.1	5.8	5.74	.53
3	6.0	6.6	6.6	7.3	5.8	6.0	5.7	6.3	6.29	.50
4	4.5	5.3	5.2	6.0	4.3	4.7	4.2	4.9	4.89	.56
5	5.3	6.0	5.7	6.5	5.0	5.4	4.9	5.6	5.55	.49
6	4.8	5.4	5.3	6.2	4.4	4.7	4.3	5.1	5.03	.58
7	5.0	5.7	5.7	6.5	4.8	5.1	4.8	5.5	5.39	.54
8	7.6	7.9	8.2	8.6	7.4	7.4	7.4	7.7	7.98	.41
9	8.2	8.6	8.7	9.3	8.0	8.0	7.9	8.3	8.38	.44
10	6.6	7.2	7.1	7.9	6.4	6.7	6.4	7.1	6.93	.47
11	5.4	6.2	6.0	6.9	5.1	5.4	5.0	5.7	5.71	.59
12	4.8	5.5	5.5	6.2	4.6	4.8	4.5	5.1	5.13	.54
13	3.8	4.6	4.5	5.3	3.7	4.0	3.6	4.3	4.23	.53
14	6.9	7.4	7.5	8.1	6.6	6.7	6.6	7.0	7.10	.49
15	7.0	7.5	7.5	8.2	6.8	7.0	6.8	7.4	7.28	.44
16	3.6	4.3	4.3	5.1	3.4	3.6	3.3	4.0	3.95	.56
TOTAL										
\bar{M}	5.625	6.24	6.21	6.94	5.38	5.62	5.23	5.84	5.91	
σ	1.29	1.17	1.24	1.15	1.21	1.20	1.30	1.20	1.33	

Table 5. Element Phase Excitation at 20 GHz

Module #	CHIP PHASE VALUE IN DEGREES FOR PHASE STATE							
	REF	45	90	135	180	225	270	315
1	0	40	89	128	186	227	274	315
2	0	40	89	128	187	228	275	316
3	0	40	89	127	186	227	273	315
4	0	42	90	129	186	226	270	313
5	0	41	90	130	187	229	275	319
6	0	39	88	125	185	225	271	313
7	0	39	88	126	184	225	271	314
8	0	40	88	126	184	225	270	312
9	0	39	89	125	184	224	271	313
10	0	38	85	124	185	225	271	315
11	0	38	86	124	181	222	268	311
12	0	40	89	128	186	225	271	315
13	0	40	89	126	184	224	270	313
14	0	41	89	129	185	227	272	316
15	0	40	90	130	188	229	276	319
16	0	40	87	125	181	222	267	309
TOTAL								
\bar{M}		39.8	88.4	126.9	184.8	225.6	271.6	314.4
σ		1.01	1.37	1.96	1.83	2.06	2.47	2.69

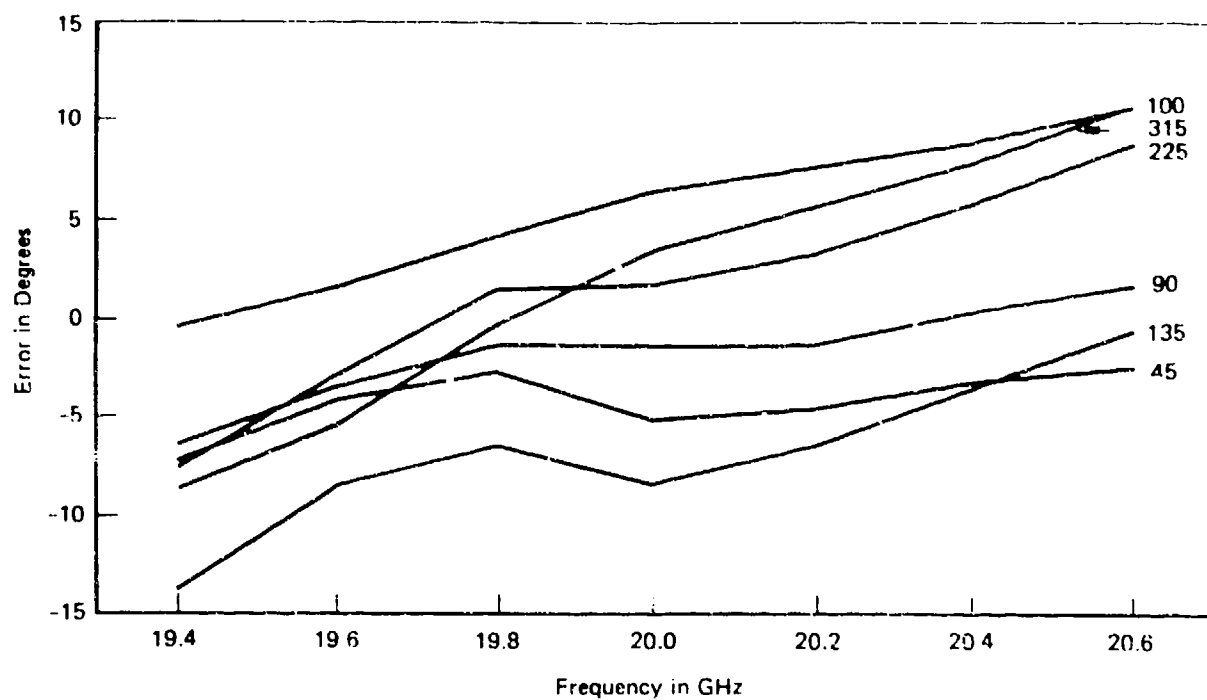


Figure 6 Phase Error Referenced to Zero State at Each Frequency (RIC 4 F)

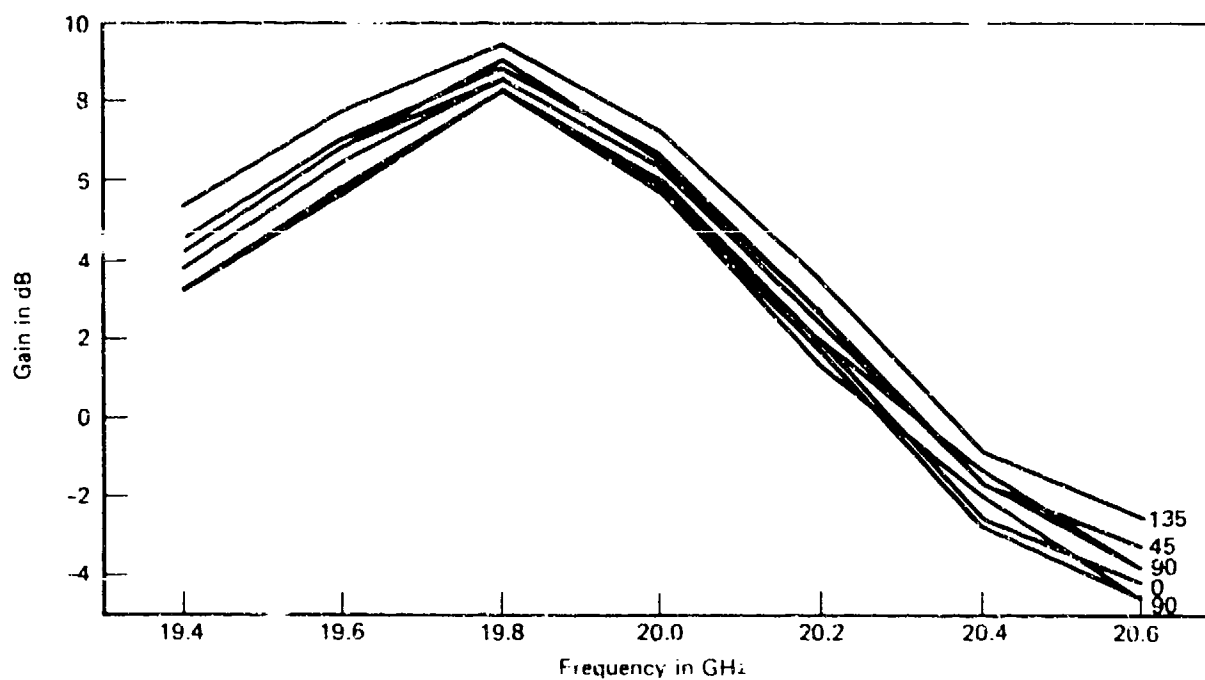


Figure 7 MMIC Gain (RIC 4 F)

4. RADIATING ELEMENT

The performance specifications of 20 GHz radiating element were as follows:

Frequency	20 GHz
Bandwidth	± 0.5 GHz
VSWR	1.5:1
Size	$\leq 1/4$ Wavelength

In view of the 5% bandwidth and the array scan angle coverage of 0 degree to ± 60 degrees requirements, a dielectric loaded cavity radiating element was selected. A phased array with cavity radiating elements will not experience a "blind spot" as that with patch radiating elements. This is because there is no dielectric medium to support the generation of surface wave under the radiating aperture while the beam is scanned beyond ± 30 degrees from broadside direction. The selected cavity radiating element, shown in Figure 8, has a size of 0.131" (length) X 0.131" (width) X 0.075" (depth) and is loaded with alumina material. Two 0.048" X 0.039" "ears" are used to provide accessible ports for exciting the orthogonal polarizations. For circular polarization, a Lange coupler was used to feed the two orthogonal linear ports ("ears") thru two 50-ohm microstrip lines.

5. ARRAY INTEGRATION AND PERFORMANCE

The array in a size of 1.08"X1.08"X0.24" consists of 16 radiating element cells arranged in a 4X4 matrix with a 0.27" spacing between

adjacent cells. Each radiating cell, shown in Figure 9, consists of a cavity radiating element of size 0.131"X0.131"X0.075" excited by a Lange coupler, a GaAs MMIC receive chip of size 0.270"X0.070"X0.005" consisting of a low-noise amplifier, a buffer amplifier, and a 3-bit phase shifter. All 16 radiating cells are connected to a power combining network via a vertical RF feed-thru. A cross section of array with a RF feed-thru is shown in Figure 10. The length of the feed-thru, 0.238", is determined by the impedance matching requirement. The RF feed-thru is simply a piece of coax cable that slips into a pre-drilled 0.056" diameter hole in the carrier plate. The center conductor is 0.010" in diameter.

DC/Logic connections for each MMIC chip are provided on the corresponding cell surface routed from the backside of the array via a thru-hole. The array vertical integration scheme is shown in Figure 11 and was integrated into a single hardware unit designated as Antenna Box. However, the DC/Logic control function was mechanized into a separate control box designated as a Phase Shifter Control Box rather than the preferred "on-chip" control module to provide flexibility and shorten the design/implementation time during this initial demonstration program. For ease of identification of MMIC chip locations in the array, the radiating elements are numbered from 1 to 16 as shown in Figure 12. These identification numbers are used for setting the phase values of individual elements in the Phase Shifter Control Box.

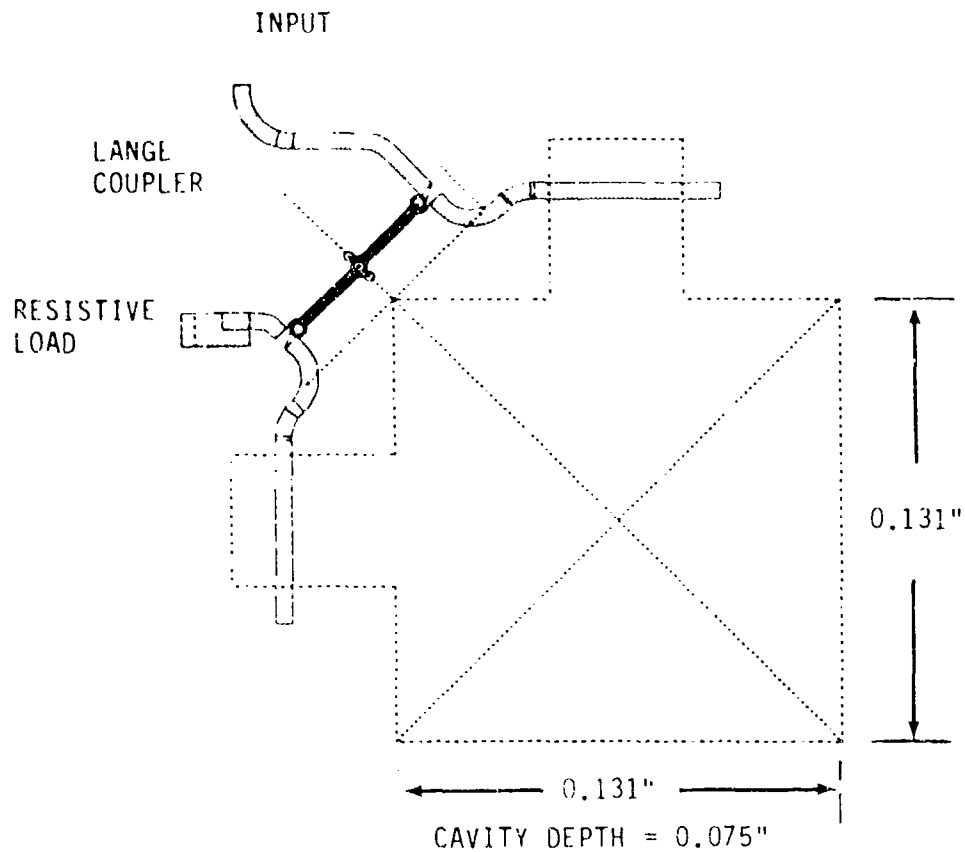


FIGURE 8 CIRCULARLY POLARIZED CAVITY RADIATING ELEMENT DESIGN

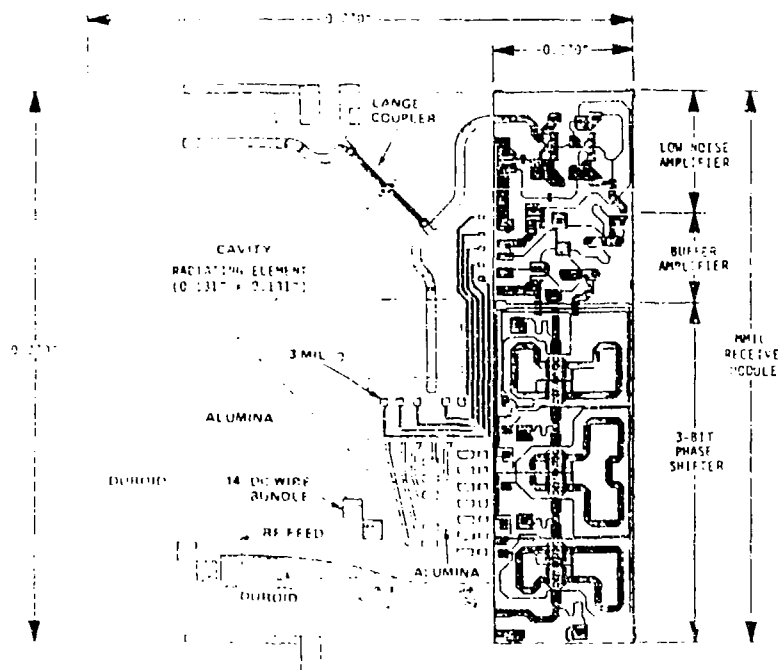
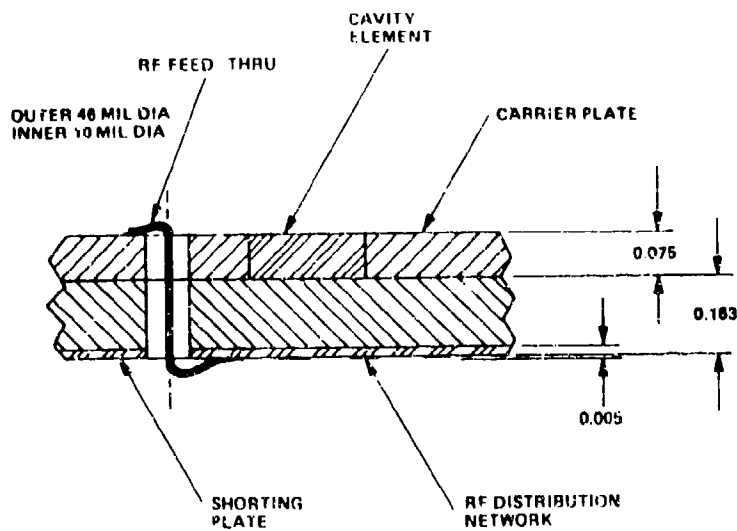


Figure 9 Detail Configuration of a Single Radiating Cell

CROSS-SECTION OF ARRAY SHOWING RF FEED-THRU



8807010

FIGURE 10

INTERCONNECTION OF ANTENNA WITH ANTENNA CONTROLLER BOARD

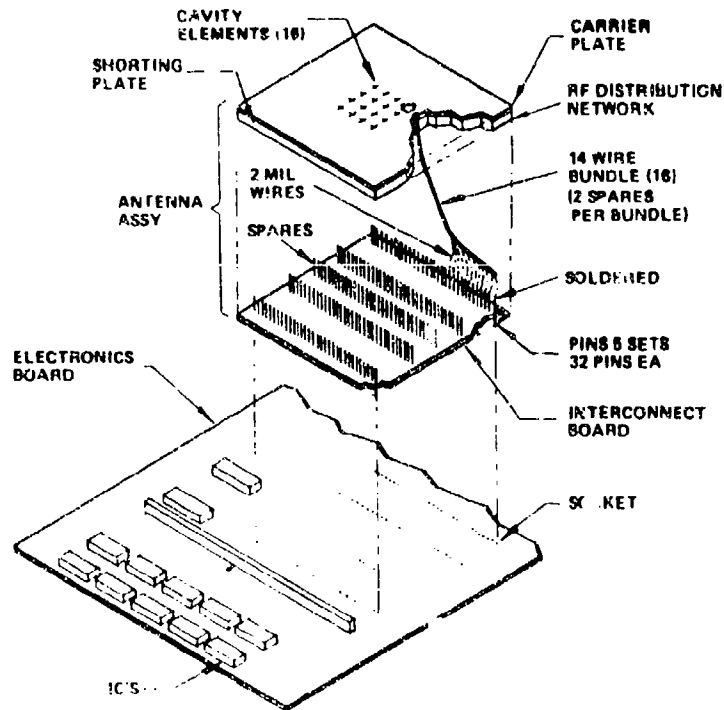


FIGURE 11

ARRAY PERFORMANCE

Gain calibrations of the broadside beam for the 16-element array at three frequencies were performed by comparing the array with a standard gain horn. The measured circular polarization gains of the broadside beam, referenced to the output port of the power combining network shown in Figure 2 after corrections for the broadside axial ratio are summarized in Table 6. Measured gain values at 19.5 GHz, 20 GHz, and 20.3 GHz are, respectively, 10.9 dBic, 9.5 dBic, and 6.2 dBic.

Axial ratio radiation patterns for beams scanned from 0 (broadside) to 60 degrees with a 20-degree increment in various phi-plane cuts were recorded at 19.5, 20.0, and 20.3 GHz. Figure 13 shows the measured scan beam patterns at 0, 10, 20, 40, 50, 60 degrees in the phi=45-degree plane at 19.5 GHz. They are well behaved.

Theoretical active array pattern and gain performance with the effect of all MMIC chips can be accounted for by using the actual gain and phase shift values of the 16 MMIC chips as the actual excitations for the corresponding radiating elements. The theoretical gain values then need to be adjusted for the dissipative, reflective, and other loss factors encountered in the array. A comparison was made between the theoretical and measured array performance. Theoretical active array gain and pattern performance at 19.5 GHz were calculated by using the measured chip data in Tables 2 and 3 as element excitations. The calculated gain was then adjusted for the dissipative, reflective, and other loss

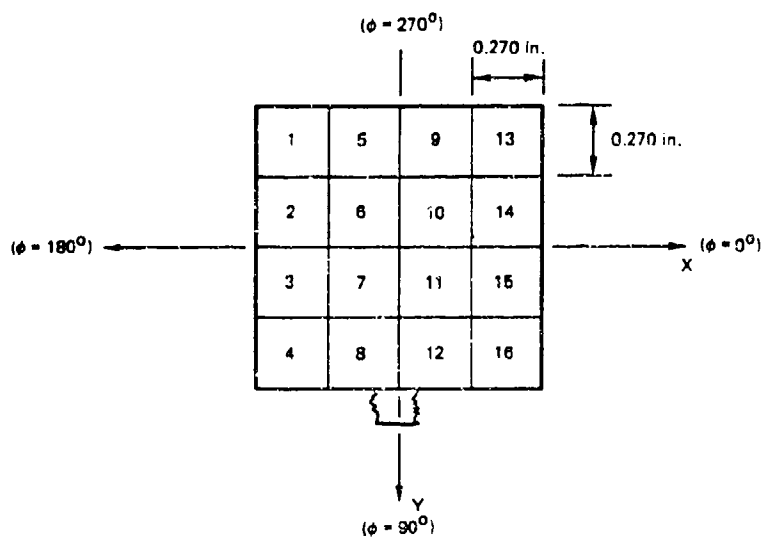


Figure 12 Subarray Element Identification

Table 6 Measured Circular Polarization Gain of the 16-Element Subarray

Parameters	Measured Gain		
	19.5 GHz	20 GHz	20.3 GHz
Measured Peak Linear Gain (dB)	9.3	7.9	4.8
Correction for Axial Ratio (dB)*	+1.6	+1.6	+1.4
Circular Polarization Gain (dBic)	10.9	9.5	6.2

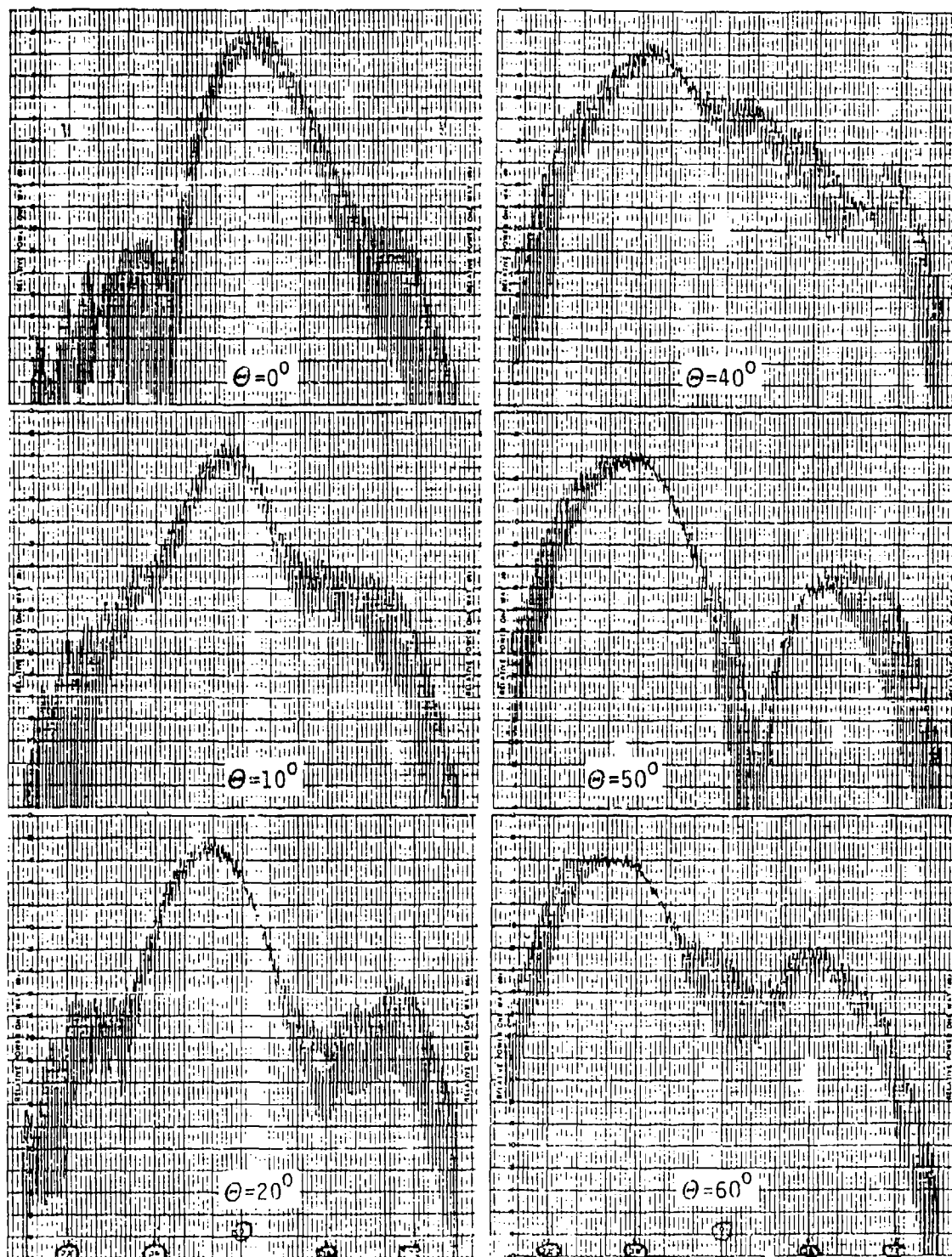


Figure 13 Measured Scan Beam Patterns at 19.5GHz in $\phi=45^\circ$ Plane

factors encountered in the array as tabulated in Table 7. The estimated active array losses for beams at broadside and $\theta = 20^\circ$ are, respectively, -5.8 dB and -7.1 dB. Assuming a perfect circular polarization, the calculated active array broadside beam gain is 16 dBic without accounting for the array loss. Thus, the calculated array gain adjusted for the loss for the broadside beam is 10.2 dBic compared with 10.9 dBic measured. For the beam scanned to $\theta = 20^\circ$, they are 8.9 dBic calculated and 8.9 dBic measured. The comparison of the calculated and measured gain values is excellent. The calculated and measured patterns are in good agreement except for the sidelobes. Although the sidelobe level is fair, the discrepancy is due to amplitude and phase errors not accounted for in the theoretical modeling. In particular, the phase setting for each chip was referenced to zero degree. The zero degree point was not verified experimentally. Table 8 summarizes the calculated and measured array performance.

6. CONCLUSION AND RECOMMENDATION

Based on these test results, the design, fabrication, and integration of a K-band MMIC phased array was demonstrated with this 16-element subarray hardware. The MMIC receive chip performance was less than desirable; however, improvement can easily be achieved with additional iterations. A successful MMIC processing approach has also been demonstrated with a yield of 48 percent (42 RF functional chips out of 87 total from a single wafer), a very high yield on a complex analog GaAs MMIC module at K-band.

TABLE 7 ACTIVE ARRAY LOSSES (dB)

Parameters	Broadside Beam	Beam Scanned At $\theta = 20^\circ$
<u>Reflection</u>		
Power Divider (1.6:1 Avg.)	0.9 (Avg.)	"
Element 2.1:1	0.6	"
<u>Dissipative Losses</u>		
Quartz Line (1.5 dB/in.)	0.4	"
Power Divider (1.2 dB/1.1)	2.9	"
Feed-thru	0.3	"
Wire Bonds (0.1 dB/bond)	0.2	"
<u>Other Losses</u>		
Cross-Pol	0.5	"
Phase Quantization	-	0.9
Beam Scan at 20°	-	0.4
TOTAL LOSS	5.8 dB	7.1 dB

Table 8 Calculated and Measured Antenna Pattern Performance at 19.5 GHz

Pattern Performance	Broadside		Main Beam Scanned To ($0^\circ, 20^\circ$)	
	Measured	Calculated	Measured	Calculated
Gain (dBic)	10.9	10.2	8.9	8.9
Beamwidth (Deg.)	30.0	29.0	28.0	31.2
SLL (dB)	-18.0	-37.5	-12.0	-24.3

For the 16-element array hardware, there are a total of 768 wire bonds performed for the DC/Logic connections (4 wire bonds per control line X 12 lines per chip X 16 chips). This is definitely prohibitive in terms of reliability and cost for practical array applications. An on-chip digital module for DC/Logic control functions is recommended to reduce the number of wire bonds.

7. ACKNOWLEDGEMENT

This work was sponsored by Rome Air Development Center, Hanscom AFB under the contract F19628-83-C-0108. The authors wish to thank Dr. A. K. Gupta for the 20 GHz GaAs MMIC receive chips and Mr. J. F. Pedersen, Hazeltine Corporation for the array hardware.

8. REFERENCE

1. R. J. Mailloux, "Phased Array Architecture for Millimeter Wave Active Arrays, IEEE APS Newsletter, February 1986, pp. 4-7
2. R. J. Mailloux, "Antenna and Radar", Microwave Journal, March 1988, pp. 28-33
3. J. F. McIlveana, "Monolithic Phased Arrays for EHF Communication Terminals", Microwave Journal, March 1988, pp. 113-125
4. I. K. Petroff, M. K. Mikasa, G. R. Kaelin and A. K. Gupta, "Monolithic Microwave Integrated Circuits for a Conformal 20 GHz Receive Phased Array", IEEE Military Communications Conference, October 1984, Los Angeles, California
5. I. K. Petroff, M. K. Mikasa, and J. F. Pedersen, "A K-Band Monolithic Active Receive Array", Phased Arrays 1985 Symposium, October 1985
6. C. Donn and A. E. Bollesen, "A 16-Element, K-Band Monolithic Active Receive Phased Array Antenna", 1988 IEEE APS International Symposium Digest, pp. 188-191

**SIDE LOBE REDUCTION VIA MULTI-APERTURE
MICROWAVE SYSTEMS**

Steven M. Watson, James P. Mills, and David H. Stone

Air Force Institute of Technology, Department of Engineering
Physics, Wright-Patterson AFB, Ohio 45433

Abstract

The far-field antenna patterns of array microwave systems can generate large side lobe irradiances. The purpose of this research was to design array systems which had far-field patterns which exhibited side lobe irradiances less than that of a perfectly transmitting circular antenna and central lobe widths no greater than that of a single large antenna of an equivalent diameter. Antenna array systems composed of 19, 37, 61, and 91 antennas satisfied these performance criteria. Further analysis indicated that central obscurations lowered the maximum side lobe irradiance in the 19 antenna arrays. Also, random dephasing of the antennas caused degraded performance of the arrays. The ability to steer the arrays using phase variations was investigated. The effects of a nonfunctioning antenna in the 19 antenna array was studied.

Introduction

INTRODUCTION

The purpose of this research was to design and analyze multi-element systems (phased arrays) which exhibited maximum side lobe gain to central lobe gain ratios which were less than that of a single large antenna; i.e. -17.6dB. In addition, the resulting far-field antenna patterns would have central lobe widths which were equal to or less than that of a single large antenna of equivalent diameter.

There are many applications of phased array antenna systems. One application of phased array systems is that of power transmission. To maximize irradiance on a target or another receiving antenna, a high gain antenna is required, typically a parabolic dish in a Cassegrain configuration. There are, unfortunately, manufacturing limits when building extremely large antennas, especially when mobility of the system may be required. In addition, practical limits of the effective aperture arise when considering air breakdown when transmitting at high powers. Arrays of circular antennas may provide a suitable alternative to single large antennas.

Toraldo Di Francia¹ examined the reduction of side lobes in proximity to the central lobe while narrowing the central

lobe of the far-field diffraction patterns of a single optical aperture. Although Di Francia's results considered optical frequencies, the results are equivalent to the microwave frequencies if one allows the λ/D ratio to remain constant where D is the size of the optic or antenna.

The research reported here extended Toraldo Di Francia's summation of complex field amplitudes generated by concentric rings to array (antenna array) systems. The approach consisted of designing antenna array systems composed of concentric rings of identical circular antennas which were analogous to the concentric thin rings on a single large aperture. These systems were comprised of one to six rings of antennas yielding antenna totals of 19, 37, 61, and 91. In all cases, the secondary maxima gain to central lobe gain ratios of the far-field antenna patterns for each antenna array was less than that of the perfectly transmitting single large antenna. In addition, the central lobe widths generated by these systems were equal to that of a single large aperture of equivalent diameter. This was expected, of course, because the various arrays of antennas were constrained in size to just fit within the single large antenna.

Theory

The analysis consisted of examining the far-field antenna patterns produced by imaging a point source through each antenna array. The electric field pattern of an individual circular element in the far-field is given by :

$$E(u,v) = \frac{2\pi a^2 J_1[(u^2 + v^2)^{1/2}]}{(u^2 + v^2)^{1/2}} \quad (1)$$

where

$$u = \frac{2\pi ax}{\lambda R} \quad \text{and} \quad v = \frac{2\pi ay}{\lambda R} \quad (2)$$

and "a" = the element radius, x and y are the cartesian coordinates in the target plane, λ is the wavelength, and R is the distance to the focal plane.

In the case of an array of circular antennas, the electric field in the far-field is given by:

$$E_N(u,v) = \frac{2\pi a^2 J_1[(u^2 + v^2)^{1/2}]}{(u^2 + v^2)^{1/2}} \times \sum_{n=1}^N \exp[-i(up_n \cos\theta_n + vp_n \sin\theta_n)/a]. \quad (3)$$

This electric field pattern, excluding nonessential proportionality factors, is proportional to the Fourier transform of the transmittance of the array pattern². The array pattern can be expressed as the convolution of one of the antennas with an array of delta functions which describe the location of the centers of each antenna.³⁻⁶ The antennas were

contained within each array were identical circular antennas. In this analysis, N was the number of antennas in the system, θ_n was the angular position of each antenna in degrees from the x axis; and p_n was the radial distance of the n th antenna from the origin of the system and was expressed in terms of multiples of the antenna radius. Uniform, monochromatic illumination of these apertures was assumed.

A. Far-Field Antenna Patterns for Concentric Rings of Apertures

The antenna array systems examined were comprised of concentric rings of identical circular antennas with a single antenna at the origin. The single antenna was surrounded by six antennas which just contacted each other and the center antenna (Figure 1). All of the array systems were constrained to just fit inside of a single large antenna of constant radius a_{ref} . As a result, the subantenna radii of the array systems had to be adjusted appropriately.

In order to describe the far-field diffraction patterns of these systems, a geometric analysis was performed for the concentric rings of identical circular antennas. This analysis was combined with equation (1) to yield:

$$E_m(u,v) = \frac{2\pi a_{ref}^2 J_1[(u^2 + v^2)^{1/2}]}{[(2)(rings)+1]^2 (u^2 + v^2)^{1/2}} \times \sum_{n=1}^N \exp[-im(up_n \cos \theta_n + vp_n \sin \theta_n)/a], \quad (4)$$

which describes the antenna pattern generated by each ring of antennas. Some of the variables in this equation are: rings - number of rings which comprise a particular array system "m" represents a particular ring beginning with $m = 1$ as the ring closest to the origin at an antenna radius of $2a$ (Figure 2a), $m = 2$ as the next ring with a radial distance of $4a$ (Figure 2b), etc. The frequency of the complex field amplitudes generated by each ring is determined by the argument of each exponential. For the rings that are further from the origin, i.e. as $2m$ increases, the antenna patterns exhibit higher frequencies. However, the rings located in proximity to the origin produced lower frequency field amplitudes.

The total antenna pattern of the array system is a summation of the complex field amplitudes of each of the rings. This coherent summation of the electric field amplitudes yields the following complex field amplitude at the focal plane:

$$E_M(u,v) \approx E_0(u,v) + E_1(u,v) + E_2(u,v) + \dots + E_m(u,v), \quad (5)$$

where $E_0(u,v)$ is the electric field pattern for the single antenna located at the origin.

The far-field irradiance patterns were calculated using the relationship:²

$$I(u,v) = E(u,v)E^*(u,v). \quad (6)$$

Equations (3), (4), and (5) formed the basis for the

calculations of the far-field antenna patterns which, in turn, were used to determine the performance of the concentric ring antenna array systems.

RESULTS

The purpose of this research was to design and analyze antenna array systems which had far-field antenna patterns characterized by maximum side lobe to central lobe gain ratios which were less than that of a single large antenna; i.e. -17.6dB. In the resulting antenna patterns, the central lobe widths were evaluated. The theoretical far-field antenna patterns of arrays composed of three to 91 elements (antennas) were examined. Far-field calculations and side lobe comparisons were performed for these arrays with and without obscurations. Dephasing of individual elements (jitter) and steerability were examined for the 19 (rotated), 37, 61, and 91 element systems. Finally, the 19 antenna (rotated) system was examined for its far-field performance with nonfunctioning elements.

Figure 3 displays the antenna arrays which were analyzed as well as the equivalent single aperture. The antenna array labeled "19 elements (rotated)" differed from the standard 19 element array in that the outer ring of 12 antennas were rotated 6.75° with respect to the inner ring. In each case, the radius of each antenna array system was equal to that of the single large antenna.

In this research, it has been assumed that there was no coupling between the individual antennas and that each antenna was at least 10 wavelengths in diameter. This last assumption

ensures that there are minimal effects on the far-field diffraction patterns due to edge effects⁷. For each antenna system, the antenna radiation patterns were calculated using equation (6) and converted to dB. Each antenna pattern was normalized to a unity peak mainlobe gain so that the side lobe to main lobe comparisons could be made.

Figure 4 is the diffraction pattern for a single large element plotted in units of dB. The first sidelobe is the largest at 17.6dB below that of the mainlobe (because of the low sampling rate along the U axis, the lobe structure will appear to be jagged). The single antenna pattern is circularly symmetric. However, the multi-antenna patterns are not. The succeeding array gain patterns are displayed using this format. Each figure represents a planar cut of the pattern which includes the largest sidelobe.

Side Lobe to Central Lobe Gain Analysis

Representative patterns are shown in Figures 5a, b, and c. These are the far-field patterns for the 4(square), 7, and 19 (rotated) antenna arrays, respectively. The maximum sidelobes for the 4 element array were only 10.0dB below the mainlobe and 15.8dB below the mainlobe for the 7 antenna array. These two systems did not exhibit side lobe to main lobe ratios less than that of the single large antenna system. However, The 19, 19 (rotated), 37, 61, and 91 array systems exhibited maximum side lobe to central lobe gain ratios which were less than -17.6dB.

The 19 antenna (rotated) array exhibited the lowest side lobe gain; i.e. -18.6dB. As the number of antennas increased, the side lobe to central lobe gain ratios increased, but did not exceed the single large antenna value of -17.6dB. Figure 6 depicts the results of this analysis for both clear apertures and apertures with a 20% central obscuration (the obscuration simulates the addition of feed horns or Cassegrain secondary reflectors).

Figures 7a through c illustrate the reason for the reduced maximum side lobe to central lobe gain ratios. Values for these particular configurations of the antennas. The 19 antenna system, depicted in the upper right-hand corner, was used to illustrate this effect. Figure 7a is the calculated electric field amplitude in the far-field due to the outer ring composed of 12 antennas. Figure 7b represents the addition of the field amplitudes from the outer (12 antennas) and inner (6 antennas) rings. Figure 7c is the field amplitude generated by all 19 antennas. The side lobe heights are considerably less than that generated solely by the outer ring. (It should be noted that there is a considerable difference between the side lobe irradiances of the arrays being examined in this research and a 19 antenna close-packed array system (Figure 8). Even though this system is very similar to the 19 antenna (rotated) system, the close-packed system yields a maximum side lobe irradiance value of 16.6dB below that of the central lobe gain. This maxima is 61% greater than that of the 19 antenna array with the outer ring rotated 6.75°).

Figures 9a through f illustrate the far-field radiation patterns of the single large, 19, 19 (rotated), 37, 61, and 91 antenna systems, respectively. Each pattern is the calculated far-field modulus which is the square root of the irradiance of equation (4)). As the number of antennas increased from 19, the structured side lobes, evidenced by the pronounced peaks, moved further from the central lobe. The irradiance of these structured lobes decreased as the number of antennas increased. As the number of antennas increased, the antenna patterns more closely resembled that of the single large antenna. In addition, the irradiance of the side lobe ring nearest the central lobe increased. For the 37, 61, and 91 antenna systems, the maximum side lobe values were located in the first rings. As depicted in Figure 6, as the number of antennas increased, the value of the first side lobe disk approached the value of the first side lobe disk of the single large antenna.

Central Lobe Width Analysis

Using Figures 9a through f, each of the antenna patterns was analyzed to determine the central lobe width generated by each array and compared to the central lobe width of the single large antenna. The results indicated that the central lobe widths were equal. Harvey⁴ et. al. arrived at the same conclusions using close-packed synthetic-antenna systems composed of 3, 7, and 19 subapertures which had the same

equivalent diameter as a single large aperture. Also, O'Neill⁸ illustrated that the central lobe width of a synthetic array was "characterized by its largest dimension."

Central Peak Irradiance Analysis

The next portion of this analysis was an examination of the central peak irradiance ratios of the antenna arrays. The peak gain for a circular antenna array will be less than that of a single antenna which circumscribes the array. The electric field pattern of the single large antenna (equation (2)) is directly proportional to the area of this antenna of radius a_{ref} . On the other hand, the electric field pattern of an array of antennas which just fit inside of this large antenna is proportional to the area of one of the antennas (πa^2) which comprise the array times the summation of plane waves generated by each antenna (equation (3)). In order to find the central peak irradiance ratios, the far-field irradiance patterns (I) were calculated for the focal plane coordinates $u = v = 0.0$. This yields:

$$\frac{I_N(0,0)}{I_S(0,0)} = \frac{(N\pi a^2)^2}{(\pi a_{\text{ref}}^2)^2} \quad (7)$$

where N is the number of antennas in the particular antenna array. Table 1 displays the irradiance ratios for the arrays considered.

Table 1

Peak Irradiance Ratios for Multi-Element Arrays

<u>Array</u>	<u>$I_N(0,0)/I_S(0,0)$</u>
Single	1.000
3	0.417
4	0.197
4(square)	0.471
7	0.605
19	0.578
37	0.570
61	0.567
91	0.566

The 7 element system exhibited the largest central lobe peak irradiance ratio whereas the 4 element array displayed the lowest ratio.

Jitter Analysis

The far-field patterns generated by the multi-element arrays were sensitive to the relative dephasing of the array elements⁹⁻¹⁴. To illustrate this dephasing, the outer ring of antennas of the 7 antenna system was shifted in phase by $\lambda/10$ with respect to the central element. A close examination of Figures 10a and b indicate that the relative dephasing caused the sidelobe patterns to symmetrically increase in amplitude and shift in position. Dephasing two of the outer ring elements (separated by 1 element) by $\lambda/10$ with respect to the rest of the array has an adverse affect on the far-field diffraction pattern (Figure 10c). The sidelobe patterns exhibit a marked asymmetry with an increase in amplitude.

Calculations were then performed to analyze the random element-to-element jitter for the 19 (rotated), 37, 61, and 91 element arrays. Jitter, in this context, is defined as the random shifting of phase through the elements with respect to each other into and out of the antenna plane. The calculations were performed using:

$$E_N(u,v) = E(u,v) \cdot \sum_{n=1}^N \exp[-i(up_n \cos \theta_n + vp_n \sin \theta_n)/a] \exp(i\phi_n) \quad (8)$$

where $E(u,v)$ is the electric field generated by any single antenna of the array and ϕ_n is the phase associated with each antenna. The phase values for each element, in terms of λ , were randomly generated using a Gaussian distribution and ranged between the following values:

-0.0125 λ -- +0.0125 λ
 -0.0250 λ -- +0.0250 λ
 -0.0375 λ -- +0.0375 λ
 -0.0500 λ -- +0.0500 λ

where the extreme ranges are the 3 sigma values.

Figure 11 illustrates the effect of the jitter on the far-field diffraction pattern on the 19 element (rotated) array. The effect is manifested by asymmetry and increased amplitude of the sidelobe patterns.

Figure 12 is a compilation of maximum side lobe values generated by the 19 (rotated), 37, 61, and 91 element systems experiencing varying degrees of jitter. For each range of jitter values, the maximum side lobe value was determined 10

times. The RMS value was computed from these side lobe irradiances. The x axis reflects the total range of the 3 sigma values that were mentioned previously. In all cases, as seen in Figure 12, the magnitude of the maximum side lobe increased as the jitter value increased. The 19 element (rotated) system exhibited the lowest side lobes for each jitter value up to a jitter value of approximately 0.075λ . This superior performance can be attributed to the fact that this system had the lowest side lobe irradiances before jitter was introduced. However, it is evident that the rate at which the side lobes grew was inversely proportional to the number of elements in the system. This is apparent in the slopes of the curves, particularly between 3 sigma jitter values of $.050\lambda$ and $.100\lambda$.

Steerability

The next portion of this research was an examination of the ability to steer the central lobes using phase variations of the individual elements of each of the multi-element systems. Crockett and Strange¹⁵ examined the ability to steer the central lobe of a seven element close-packed system by smoothly and linearly varying the phase across its face. This research utilizes the same steering technique where each antenna was assigned a discrete phase value. Tilting the incoming plane wave, which illuminated each of the systems, is another way of visualizing the varying phase difference across

the face of the antenna array systems. The magnitudes of the phase difference, i.e. the steering magnitudes, across the face of these systems were:

0.0λ	--	$\lambda/2$
0.0λ	--	λ
0.0λ	--	$3\lambda/2$
0.0λ	--	2λ

where the 0.0λ value was at one edge of the element system and the maximum phase magnitude value is located at the opposite edge. Equation (8) was used to calculate the far-field antenna patterns for this steering technique.

Figures 13a and b illustrate the effects of steering the central lobe of the 19 (rotated) and 91 element systems using the technique described above. The first plot of each series is the ideal far-field diffraction pattern for each system without attempting to phase steer the central lobe. The second plot employs the 0.0λ to λ phase difference across the face of the multi-element system. Finally, the third plot of each series illustrates the 0.0λ to 2λ steering magnitude. The dashed curves on the second and third plots are the envelope functions which were generated by a single element of each respective system. These plots indicate that the movement and relative gain of the central lobes were constrained by the envelopes of each system. In addition, the further the central lobe was moved from the optical axis, the greater the gain of the side lobes. Since the central lobe dimension of envelope function of the 19 element (rotated) system was considerably narrower than that of the 91 element system, the central lobe

experienced an accelerated gain loss as compared to the 91 system.

Nonfunctioning Elements

The final portion of this research examined the performance of the 19 antenna (rotated) array with one of the 19 elements nonfunctioning. The far-field antenna patterns were examined when each of the 19 antennas had, in turn, zero transmittance. The performance of the system was determined using the maximum side lobe values. The maximum sidelobe values ranged from -15.85 to -15.43dB with an RMS value of -15.68dB.

Figures 14a and b illustrate the modulus of the far-field diffraction patterns for the cases of a nonfunctioning antenna in the inner and outer rings, respectively. In both cases, the patterns exhibited an increase in the side lobe values. The most noticeable effects occurred in the side lobes which were in proximity to the central lobe.

Conclusions

This research examined array systems which, according to two criteria, could perform as well as a single large antenna with an equivalent diameter. The array systems examined were composed of 19, 37, 61, and 91 circular antennas arranged in concentric circles.

The secondary maxima for each of these systems was less than that of the single large antenna. The 19 antenna system with the outside ring rotated 6.75° exhibited the lowest maximum side lobe gain with a value of 18.6dB below the central lobe. In all cases, the antenna radiation patterns of the array systems had central lobe widths equal to that of the single large antenna system.

This research also analyzed the far-field antenna patterns for the effects of central obscurations in each of the antennas, random phase fluctuations (jitter), steerability using a smoothly and linearly phase difference across the face of each system, and nonfunctioning elements. The results indicated that for central obscurations, side lobe values actually were reduced for the 19 and 19 (rotated) element systems when compared to the perfectly transmitting system. When jitter was introduced into each of the systems, the side lobe values increased and the far-field antenna patterns exhibited asymmetry. The 19 element (rotated) system was able

to sustain the greatest amount of jitter and continue to exhibit side lobe values equal to or less than -17.6dB. The multi-element systems are capable of being phase steered, however, the side lobe values began to increase rapidly with a corresponding decrease in central lobe gain. The 91 antenna system exhibited a superior steering ability when compared to the other multi-element systems. Finally, single nonfunctioning elements in the 19 element (rotated) system caused a degradation in far-field antenna patterns with an increase in side lobe values.

It has been demonstrated that array (antenna) systems can exhibit large side lobes. This analysis has demonstrated that there are multi-telescope/antenna designs which actually reduce side lobes below that of a single large telescope (antenna). When used for imaging applications, such as Ladar, Radar, and astrophysical observations, reduction of the side lobes could improve the two point resolution of these systems. The antenna arrays discussed in this research could also be utilized for power transmission.

In addition to the array approach to this research, one could interpret these systems as single large antennas that have a form of edge tapering. Reducing the transmittance of certain small portions of the antenna to 0.0 will reduce the side lobe values as compared to that of a single large antenna with no tapering and improve the imaging properties.

References

1. Toraldo Di Francia, G. "Super-Gain Antennas and Optical Resolving Power," Supplmento Al Vol.IX, Series IX Del Nuovo Cimento, 426, 1952.
2. Goodman, Joseph W. Introduction to Fourier Optics. San Francisco: McGraw-Hill, 1968.
3. Fender, J.S. "Synthetic Apertures: An Overview," Synthetic Aperture Systems, Proc. SPIE, 440, 2-7 (1983).
4. Harvey, J.E., MacFarlane, M.J., and Forgham, J.L. "Design and Performance of Ranging Telescopes: Monolithic Versus Synthetic Aperture," Optical Engineering, Vol. 24, No. 1, 183-188 (Jan/Feb 1985).
5. Chow, W.W. "Far-Field Intensity of a Partially Locked Optical Phased Array," Applied Optics. 23, 4332-4338 (1984).
6. Watson, Steven M. Two-Point Resolution Criterion for Multi-Aperture Optical Telescopes. MS Thesis. Air Force Institute of Technology, Wright-Patterson Air Force Base, Ohio, 1987.

7. Silver, Samuel. "Microwave Aperture Antennas and Diffraction Theory", Journal of the Optical Society of America, Vol. 52, No. 2, 131-139 (Feb 1962).
8. O'Neill, G.K. "A High Resolution Orbiting Telescope," National Academy of Sciences, Synthetic Aperture Optics, Vol. 2, Woods Hole Summary Study (National Academy of Sciences - National Research Council Advisory Committee to the AFSC), Washington, D.C. (1967).
9. Palma, G.E. and Townsend, S.S. "Performance and Phasing of Multiline Synthetic Apertures," Synthetic Aperture Systems, Proc. SPIE, 440, 68-76 (1983).
10. Waite, T. and Sun, K. "Physical Understanding of Synthetic Aperture Arrays Via Simple Models," Synthetic Aperture Systems, Proc. SPIE, 440, 52-55 (1983).
11. Crockett, G.A. and Strange, D.A. "Computer Model for Evaluating Synthetic Aperture Propagation," Synthetic Aperture Systems, Proc. SPIE, 440, 77-84 (1983).
12. Harvey, J.E., Silverglate, P.E. and Wissinger, A.B. "Optical Performance of Synthetic Aperture Telescope Configurations," Southwest Conference on Optics, Proc SPIE, 540, 110-118 (1985).

13. Butts, R.R. "Effects of Piston and Tilt Errors on the Performance of Multiple Mirror Telescopes," Wavefront Distortions in Power Optics, 293, 85-89 (1981).

14. Shellan, J.B. "Phased-Array Performance Degradation Due to Mirror Misfigures, Piston Errors, Jitter, and Polarization Errors," J. Opt. Soc. Am. A, Vol. 2, No. 4, 555-567 (April 1985).

15. Crockett, G.A. and Strange, D.A. "Computer Model for Evaluating Synthetic Aperture Propagation," Synthetic Aperture Systems, Proc. SPIE, 440, 77-84 (1983).

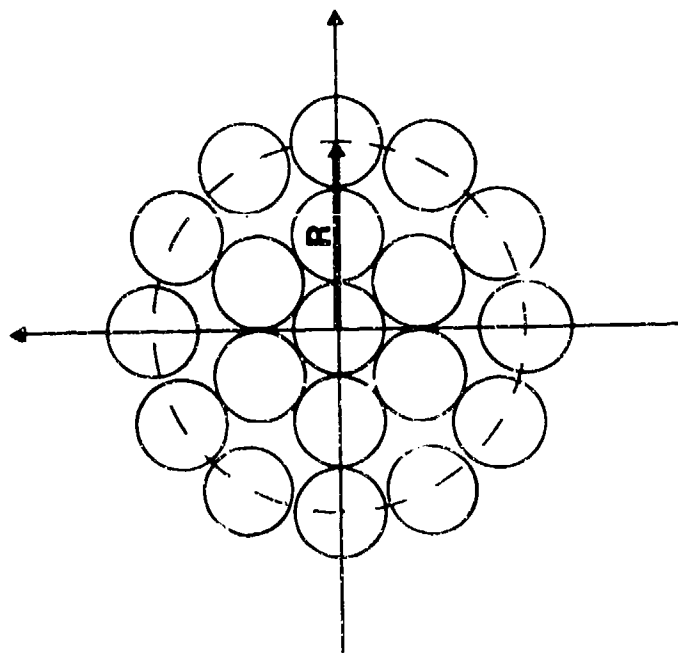


Fig. 1. A 19 antenna system illustrating the distance (R) from the origin to the circle on which the centers of each antenna of the outside ring were placed.

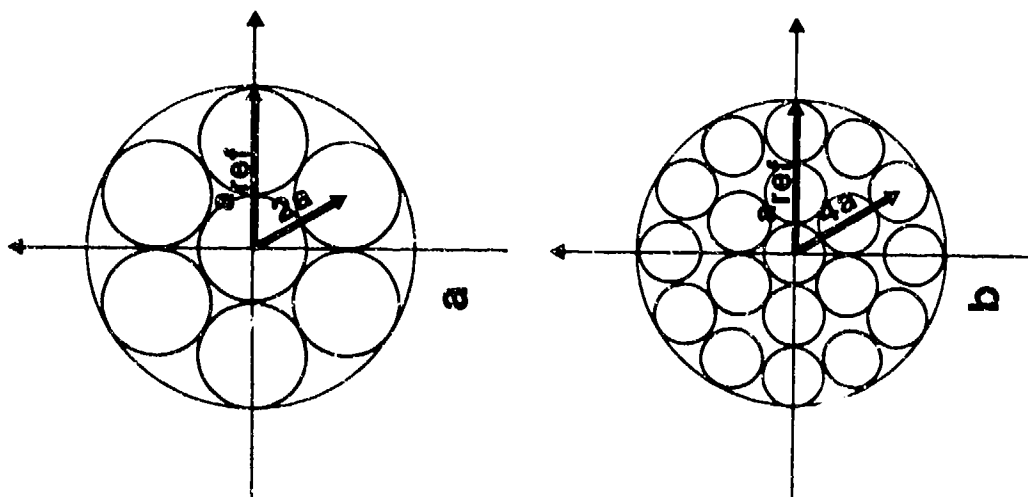
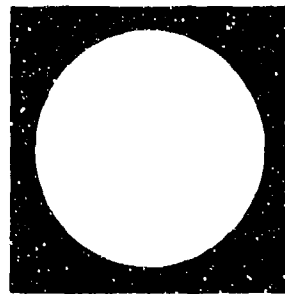
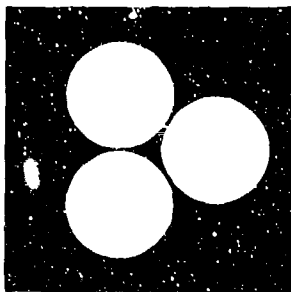


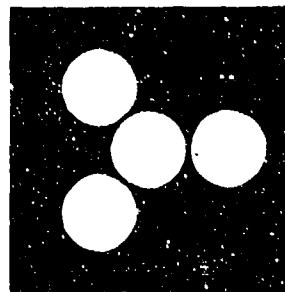
Fig. 2. a) Seven and b) 19 antenna systems comparing the subantenna radii with r_{ref} .



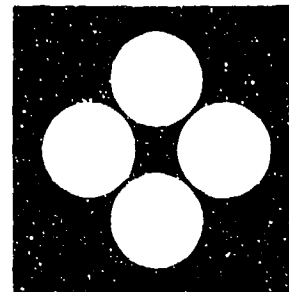
1 element



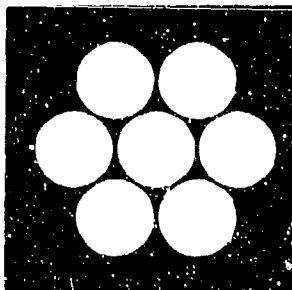
3 elements



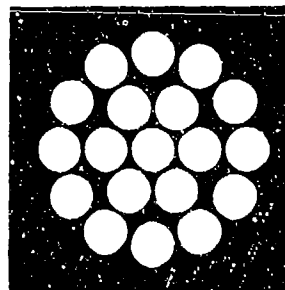
4 elements



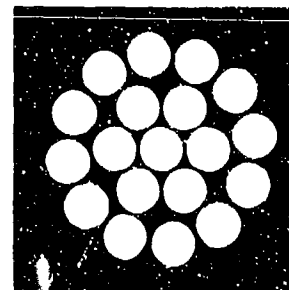
4 elements
(square)



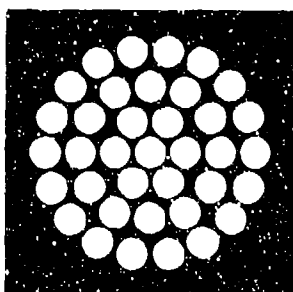
7 elements



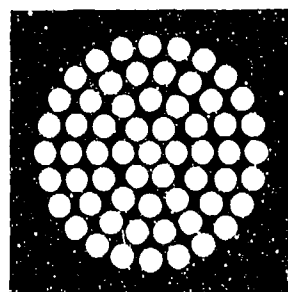
19 elements



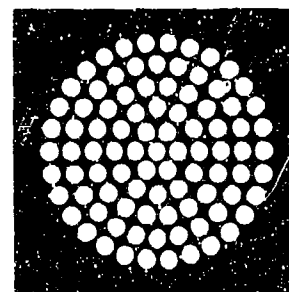
19 elements
(rotated)



37 elements



61 elements



91 elements

Fig. 3. Antenna arrays which were analyzed.

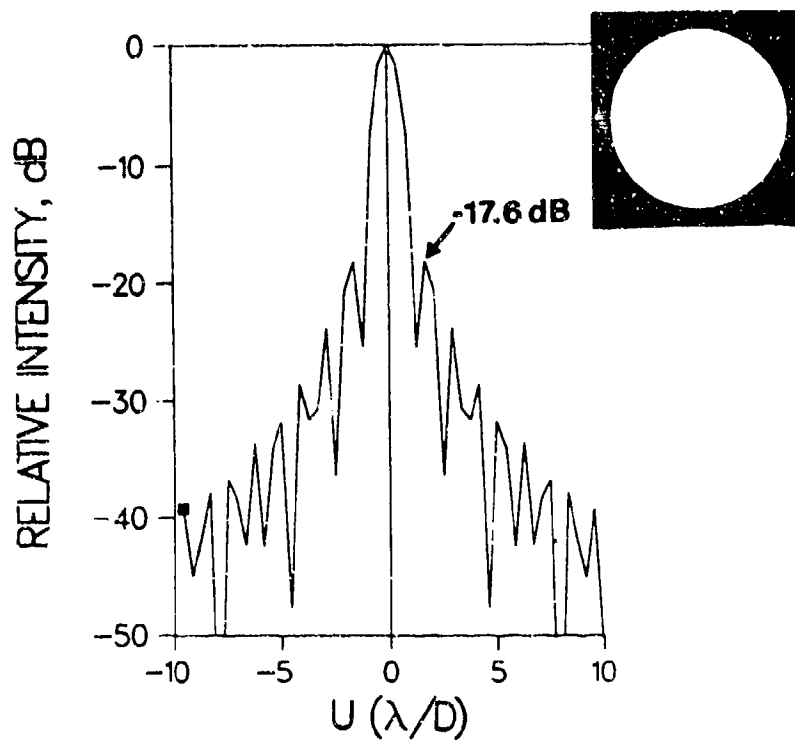


Fig. 4. Single large antenna far-field diffraction pattern in units of B .

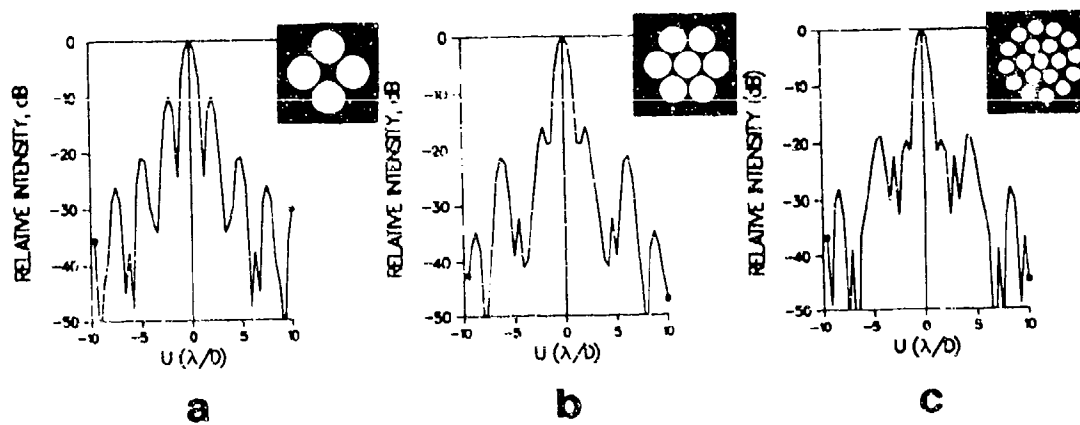


Fig. 5. Far-field antenna patterns for the a) 4 (square), b) 7, and c) 19 (circular) element arrays.

MAX SIDE LOBE COMPARISON

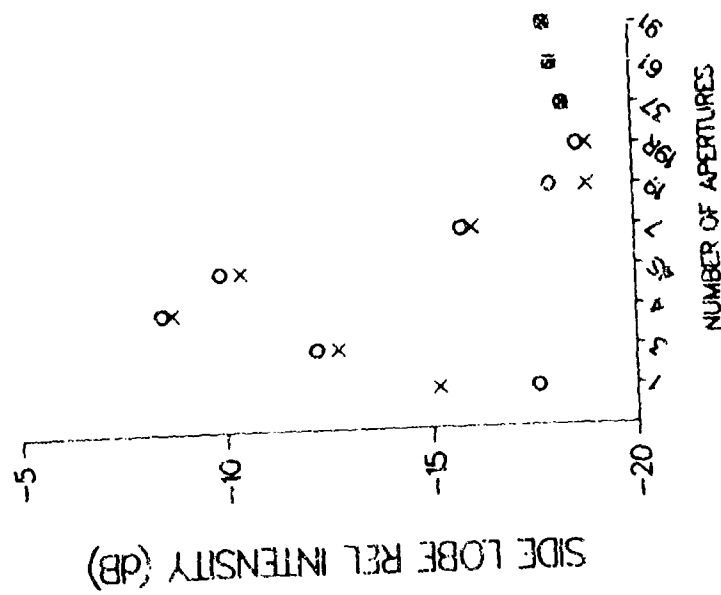


Fig. 6. Comparison of maximum side lobe values (O - without central obstruction, X - with 20° central obstruction) for the analysed arrays.

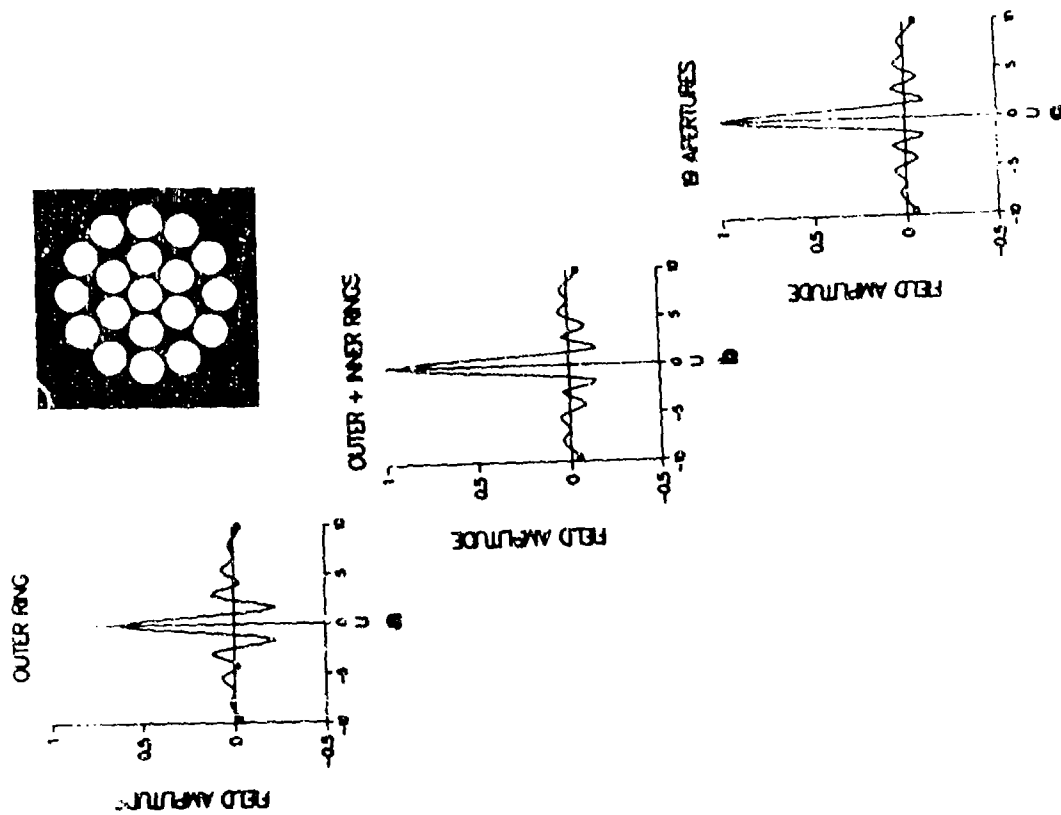


Fig. 7. a) field amplitude of outer ring of 19 antenna system, b) summation of field amplitudes from inner and outer rings of 19 antenna system, and c) resultant field amplitude from summation of all 19 antennas.

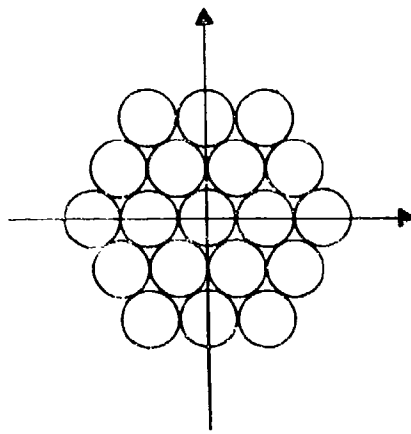


Fig. 8. 19 antenna close-packed system.

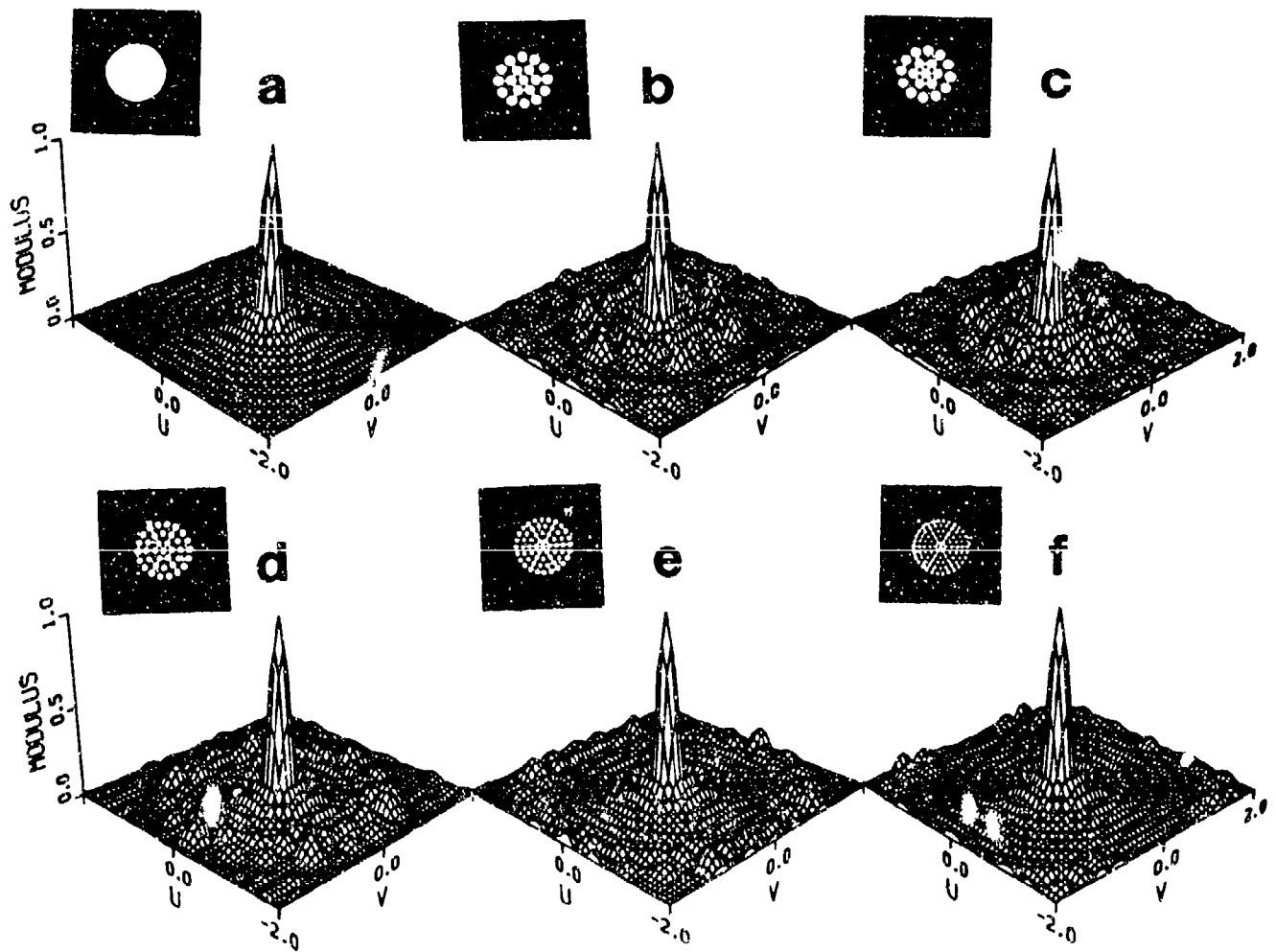


Fig. 9. Far-field antenna radiation patterns (displayed as the modulus) for the a) single large, b) 19, c) 19 (rotated), d) 37, e) 61, and f) 91 antenna systems.

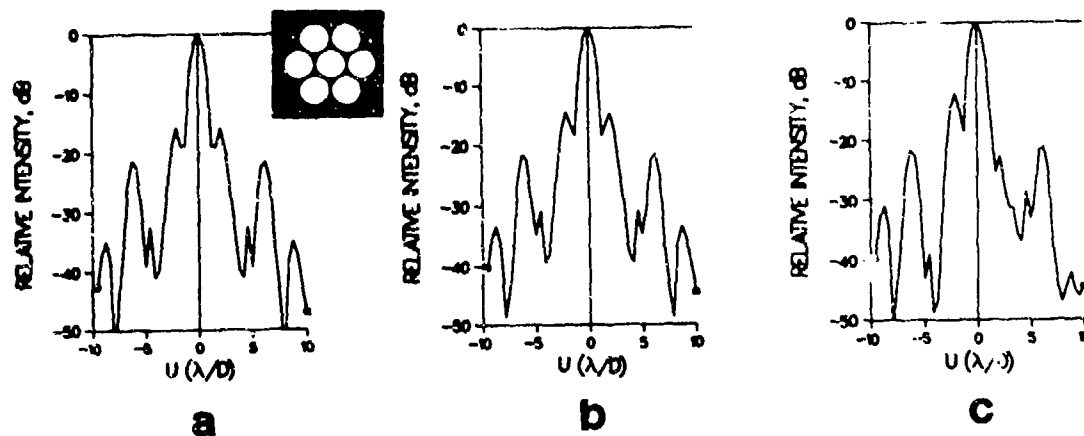


Fig. 10. Far-field antenna radiation pattern of a 7 antenna array a) without dephasing and b) with the outer ring of elements shifted in phase by $\lambda/10$ with respect to the central element, and c) two elements of the outer ring (separated by one element), dephased by $\lambda/10$ with respect to the remaining antennas.

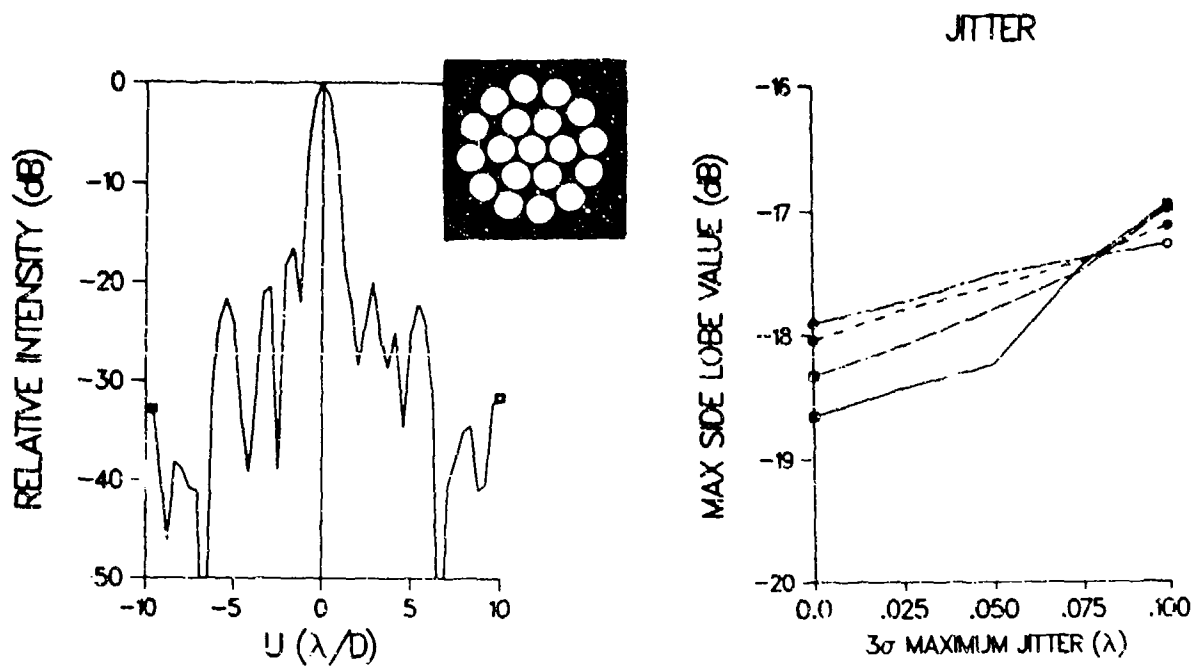


Fig. 11. Far-field antenna radiation pattern for the 19 antenna (rotated) array experiencing a 3 sigma jitter value of .12.

Fig. 12. Side lobe irradiances generated by the antenna array systems experiencing jitter (— = 19 (rotated) antennas, --- = 37 antennas, ··· = 61 antennas).

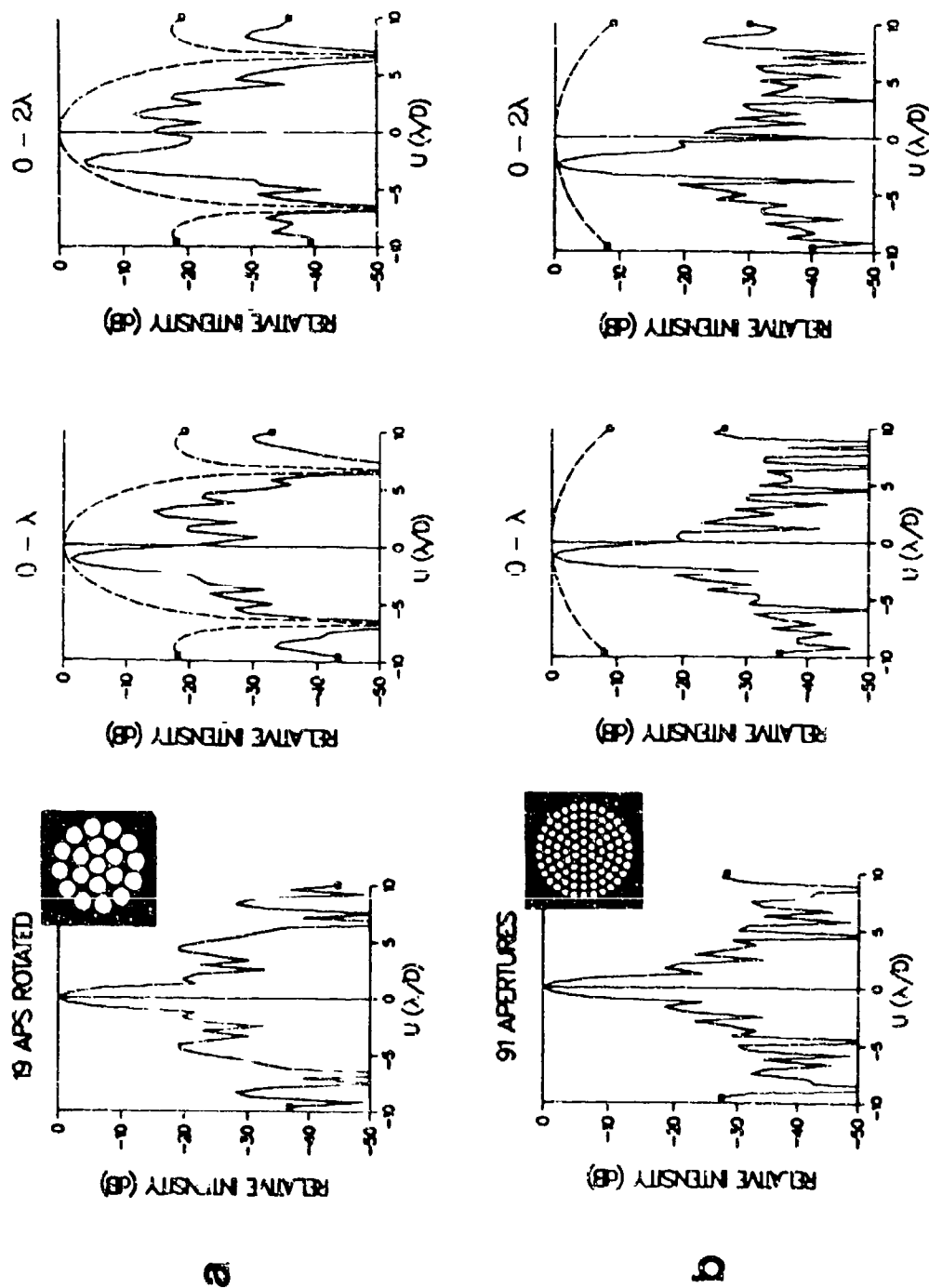


Fig. 13. Far-field antenna radiation patterns of the a) 19 (rotated) and b) 91 antenna systems with the following phase steering magnitudes: 0.0λ , 0.0λ , $-\lambda$, and 0.0λ (dashed curve = envelope function generated by a single antenna of each respective array).

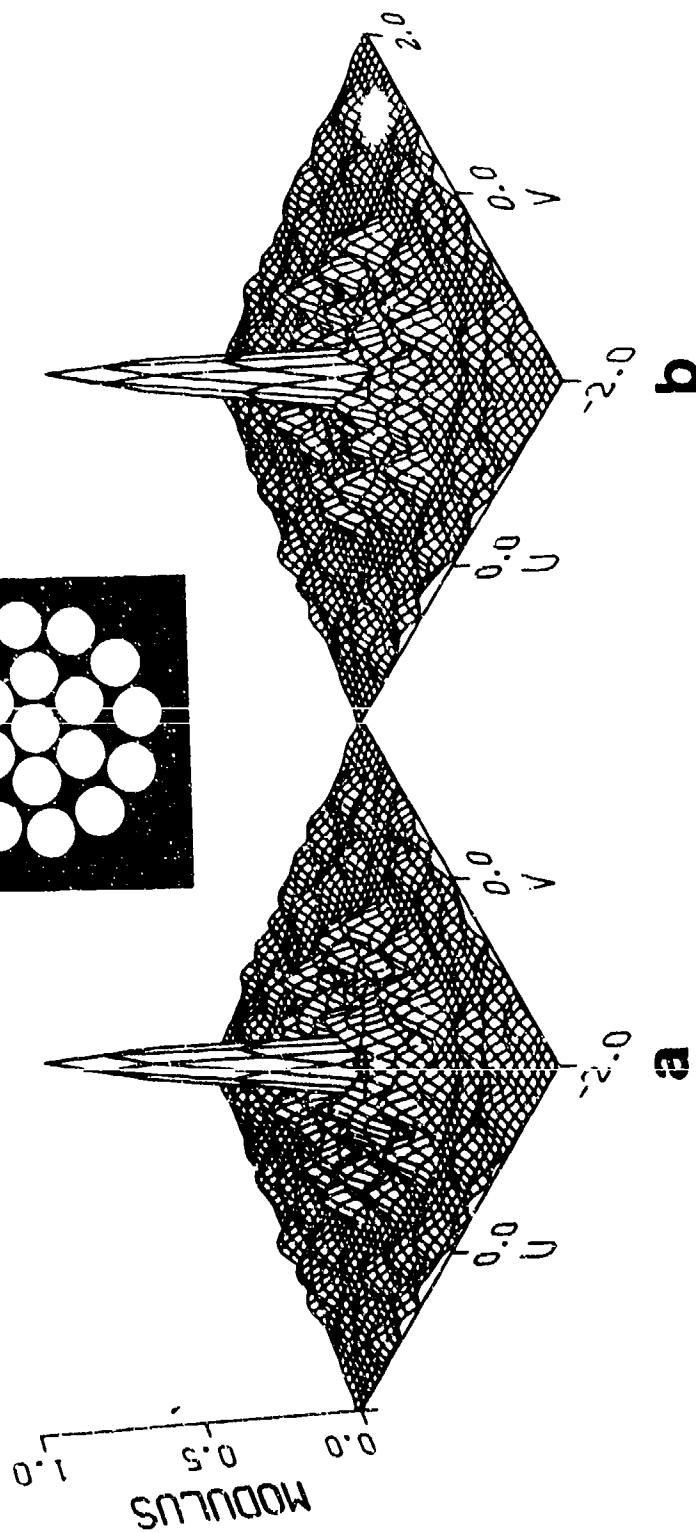


Fig. 14. Far-field antenna radiation patterns for the 19 antenna (rotated) system with a single nonfunctioning element located in the a) inner ring and b) outer ring.

DUAL-POLARIZED, COMMON-APERTURE MONOPULSE ANTENNA

R. Kliger, R. Mariano, N. Sa, J. Toth

Missile Systems Division
Raytheon Company
Bedford, MA

DUAL-POLARIZED, COMMON-APERTURE MONOPULSE ANTENNA

R. Kliger, R. Mariano, N. Sa, J. Toth

ABSTRACT

A unique, linearly polarized microstrip antenna has been developed and tested. This antenna has the capability of being used as a light-weight, thin profile, overlay retrofit to existing linearly polarized, slotted waveguide arrays. Together, the two apertures constitute an antenna system that provides two independent, orthogonal, linear polarizations.

The microstrip antenna consists of an array of microstrip dipoles, capacitively fed by feedlines running underneath the dipoles. The dipoles are grouped in "subarrays" and are fed from common feedlines routed midway between the ends of the waveguide slots. In order to minimize coupling between the feedlines and the slots, the feedlines are positioned very close to the microstrip groundplane. The microstrip dipole sub-arrays are strategically positioned such that the dipoles lie between the waveguide slots. Cutouts in the microstrip antenna located above the waveguide slots allow the slots to radiate undisturbed. Measurements have shown negligible degradation in performance of either antenna when integrated in a single aperture.

INTRODUCTION

For typical linearly polarized monopulse seeker antennas, receive signal depolarization introduces unacceptably large error in the

determination of the direction to the target (i.e., the direction indicated by the processed monopulse data will differ from the true boresight direction). For seekers mounted within highly curved radomes, incident signal depolarization effects result in induced boresight error in the monopulse system. This situation becomes intolerable when the incident signal polarization is nearly orthogonal to the expected antenna polarization and produces large swings in boresight error.

One method of reducing the susceptibility of radome enclosed seeker antennas to depolarization effects is to provide a means of detecting the orthogonal polarization component. It can be shown that a complete set of orthogonally polarized monopulse system outputs can be processed to eliminate seeker polarization dependence. For this case, the seeker antenna requires separate sum and difference channel outputs for two orthogonal polarizations. The antenna configuration presented herein is one approach for providing this dual polarization capability.

Other dual polarization antenna configurations (reflectors, flatplates, etc.) have been developed in the past; but in most cases, these systems were large, cumbersome and settled for degraded primary polarization performance to achieve the additional capability. The common aperture monopulse antenna presented here provides orthogonal

polarization performance by superimposing a microstrip dipole aperture over a conventional waveguide flatplate seeker antenna without significant performance degradation to the primary antenna. A diagram of the combined waveguide/microstrip radiating structure is shown in Fig. 1.

The composite microstrip/waveguide flatplate aperture provides a very low profile, high performance antenna configuration. The waveguide flatplate primary antenna provides the typical high gain, pencil beam performance required by present day seekers. The microstrip antenna (which can be designed as a retrofit to an existing waveguide antenna) provides a low height add-on aperture with a design topology allowing the primary antenna slots to radiate with minimum obstruction. Although the microstrip aperture provides less gain due to increased feed losses, other performance parameters (such as beamwidth, monopulse slope and sidelobes) can be maintained.

Both waveguide and microstrip apertures utilize partially integrated array feed networks to minimize loss, each aperture can be easily connected to an appropriate 3 (or 4) channel monopulse network to provide a very compact, reliable, dual polarized monopulse system. In addition, each component and system can be manufactured and tested prior to final integration allowing high yield at final assembly.

INDIVIDUAL ANTENNA CONSIDERATIONS

A major advantage of the present approach is that the design of each aperture (waveguide and microstrip) can be performed fairly independently. The design of slotted waveguide antennas is a well-documented field ¹⁻³ and hence is not discussed here. In comparison, the design of microstrip antennas of the present type ^{4,5} is a relatively new area of interest.

The microstrip antenna consists of dipole sets grouped in sub-arrays and fed from common feedlines (Fig. 2). As in the design of a slotted-waveguide sub-array, the microstrip dipole sub-array is modelled by shunt elements having assigned impedances on an equivalent transmission line. Dipole excitations and input impedances are calculated using standard transmission line methods. Individual dipole impedances are controlled by adjusting the dipole length and the dipole offset from the feedline (Fig. 3). To a first order approximation, a dipole's resistance is controlled by the offset while the reactance is controlled by the length. Other parameters of interest are the feedline groundplane spacing and the dipole groundplane spacing.

The dipole ground plane spacing is a key parameter in a trade-off between dipole bandwidth and effective dipole impedance control. A large dipole groundplane spacing results in enhanced bandwidth characteristics, but reduces the dynamic range of realizable dipole impedances. The range over which dipole impedances may be varied is critical to the control of sub-array input impedances and to antenna sidelobe levels. The antenna bandwidth is primarily affected by two factors - the dipole groundplane spacing (dipole bandwidth) and the length of the microstrip feed lines (feed bandwidth). Figure 4 shows the effect dipole groundplane spacing has on the dipole bandwidth under conditions used in a recent design. The role that feedline length plays on bandwidth is due to phase dispersion across a given sub-array at the edges of the frequency band.

The location of microstrip dipoles must be chosen with great care as to avoid grating lobes in antenna far-field radiation patterns. These are undesirable and are caused by large unpopulated spaces between microstrip dipoles. Normally, grating lobe problems are not found in small aperture antennas (approximately 5 wavelengths in diameter). However, in larger aperture antennas, a greater number of microstrip dipoles are required to fill the aperture area. This requires more sub-arrays which in turn necessitates a more complex feed network. The number of sub-arrays may be reduced by modifying the manner in which dipoles are fed from the feedlines.

Figure 5 shows two possible sub-array configurations as well as a cross section view of a sub-array showing a dipole, the feedline, and the ground plane. In Fig. 5a, the dipoles are all fed from the same side of the feedline and spaced a dielectric wavelength apart. In order to use this geometry, microstrip feedlines are placed between every adjacent pair of waveguide slots in a direction perpendicular to the axis of the slot (Fig. 1). In order to reduce the number of sub-arrays, dipoles can be spaced at intervals of half a wavelength and are alternately fed from both sides of a given feedline (Fig. 5b). With this configuration, feedlines are placed between every other pair of adjacent slots as in Fig. 2. The decreased number of sub-arrays greatly reduces the complexity of the feed network. However, such a configuration spaces dipoles far enough apart to result in the presence of grating lobes in the radiation characteristics of the microstrip antenna.

Figure 2 shows the overlay of the microstrip antenna feed line and dipole layers on the waveguide slots for a recently developed 13 wavelength diameter antenna. The irregular spacing of the microstrip dipoles is a result of the problems discussed above. Figure 6 is a view showing the complexity of the feed network for this antenna. This antenna does have grating lobes in its radiation characteristics but they are low enough and far enough from the main beam not to adversely affect system performance.

Measured and calculated sum channel contour plots of that antenna are shown in Figs. 7 and 8 respectively. The grating lobes mentioned above occur in planes approximately ± 15 degrees with respect to the horizontal. Figure 9 is a phot graph showing both a 5 wavelength antenna aperture and the 13 wavelength aperture discussed above. The smaller antenna does not exhibit any grating lobe problems due to the relaxation of the above constraints occurring in a small aperture.

COMBINED ASSEMBLY CONSIDERATIONS

The key problem in designing a dual-polarized antenna assembly using this technique⁶ is to insure that the desired performance of each individual antenna is achieved without degrading the performance of the other. Since the waveguide antenna is in most cases previously designed, the microstrip antenna must be designed around the existing "host" waveguide antenna. The primary design task is to locate the microstrip dipoles in areas of the aperture which would not interfere with the radiation of the waveguide slots. A minimum, safe waveguide slot/microstrip dipole distance can be established via a series of careful laboratory measurements. The microstrip sub-array feedlines should be positioned midway between adjacent slots (as in Fig. 2) and as close to the ground plane as practical. This is done to minimize stray radiation coupling into the waveguide array or radiating into free space.

Dielectric loading of the waveguide slots by the microstrip antenna is avoided by cutting away the dielectric material directly over the waveguide slots. Antenna pattern measurements have shown that this technique does not seriously affect the performance of either antenna. If both antennas are being designed from the start, the waveguide slots may be designed such that the dielectric loading is taken into account avoiding the necessity to remove the dielectric material.

E-plane far-field radiation patterns of the 5 wavelength diameter waveguide antenna are shown in Figs. 10 and 11, respectively. Figure 10 shows sum and difference channel patterns for the waveguide antenna without the microstrip antenna. Figure 11 shows the same data for the case where the microstrip antenna was added. Only minor discrepancies between the two sets of data are observable. Sum channel sidelobe levels are affected minimally by the presence of the microstrip aperture, and an excellent difference channel null depth is preserved.

Figures 12 and 13 show the larger, 13 wavelength microstrip antenna E-plane, far-field radiation patterns for the profiled and unprofiled cases respectively. Profiling the microstrip aperture includes the machining of many slots in the dielectric material. These slots are located at positions that would be directly above waveguide slots when the two apertures are integrated. Thus, the microstrip groundplane is interrupted at many locations by these slots. Nevertheless, negligible

differences in the radiation patterns are observed between the profiled and unprofiled cases. Unfortunately, at the time of this writing, radiation patterns of the two 13 wavelength antennas, when integrated, were not available. Previous data on the smaller 5 wavelength antenna indicated that no appreciable changes in performance occurred.

Feedthru (RF connections between the microstrip aperture and the feed network) locations for the assembly are also critical. Since the feedthrus must penetrate thru the waveguide antenna, they must be placed in areas that do not affect performance. Ideally, this would be in areas outside the waveguide slot radiating area. In large arrays, this is not entirely possible. In these cases, feedthrus must be located within the outer limits of the waveguide array. Feedthrus have been positioned within the waveguide walls of the array without serious degradation.

Antennas of this type can be made for new systems or as a retrofit to existing systems. In retrofit cases, the waveguide arrays must be modified to include the feedthru areas and any support bosses at the rear of the antenna. These bosses are used to hold the microstrip antenna feed network in place. The microstrip aperture is affixed to the assembly by bonding it over the waveguide aperture.

CONCLUSION

Cross polarization jamming and radome induced depolarization of received signals can cause large target boresight errors for linearly polarized seeker antennas. A compact, high performance, dual polarized antenna approach has been developed which reduces seeker susceptibility to depolarization effects. The antenna, as configured, provides a complete set of superimposed orthogonally polarized monopulse channels which can be processed to eliminate the seeker polarization dependence.

Conventional waveguide flatplate and stripline/microstrip manufacturing techniques can be employed during fabrication of the antenna system components. The microstrip aperture can be designed in conjunction with a new waveguide flatplate configuration or as a low height retrofit to an existing waveguide antenna. Radiation patterns of recently developed 5 and 13 wavelength circular dual polarized antennas have shown that the integration of the two apertures does not present any significant degradation to the performance of either antenna.

In general, far-field radiation performance of this dual polarized antenna structure is dependent on the individual application and design constraints, but full aperture performance from both antennas is achievable. Typically, the waveguide antenna provides the primary polarization and achieves the best overall performance, while the flexibility of the microstrip antenna configuration is used to provide the secondary polarization and to allow easy integration of the two apertures.

References:

- 1) R.S. Elliott, Antenna Theory and Design, Prentice-Hall, Englewood Cliffs, N.J. 1981, Chapter 8.
- 2) R.S. Elliott and L.A. Kurtz, "The Design of Small Slot Arrays", IEEE APS, Vol. AP-26, 1978, pp. 214-219.
- 3) P.N. Richardson and N.Y. Yee, "Design and Analysis of Slotted Waveguide Antenna Arrays", Microwave Journal, June 1988, pp. 109-125.
- 4) W. Miccioli, J. Toth, N. Sa, and M. Lewis, "Microstrip Monopulse Dipole Array", 1984 Symposium on Antenna Applications, Urbana, Illinois, September 19-21, 1984.
- 5) J. Lane, N. Sa, and J. Toth, "Resonant Microstrip Dipole Arrays", 1985 Symposium on Antenna Applications, Urbana, Illinois, September, 1985.
- 6) United States Patent 4,700,193; Norbert Sa, William F. Miccioli, A. R. Chinchillo, John F. Toth; "Cross Polarized Antenna"; 13 Oct. 1987.

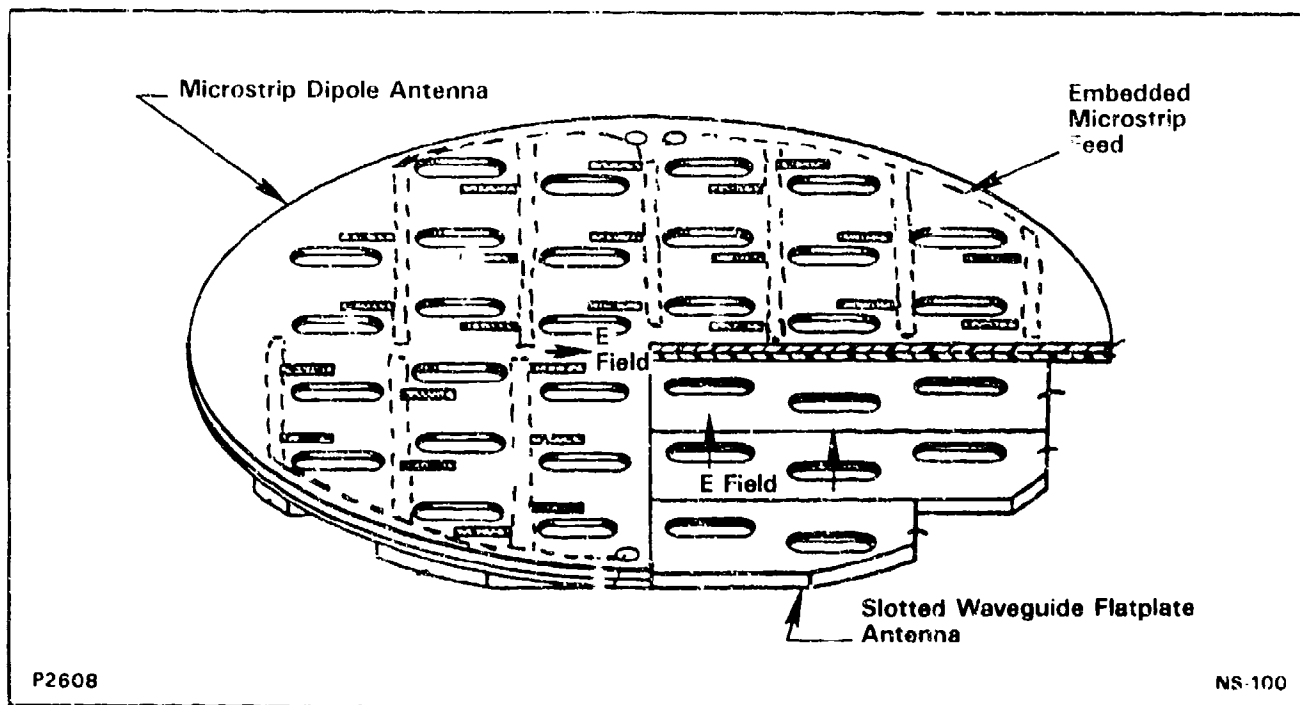


Figure 1. Dual Polarized Radiating Aperture (Microstrip Antenna Cut Away to Show Waveguide Aperture)

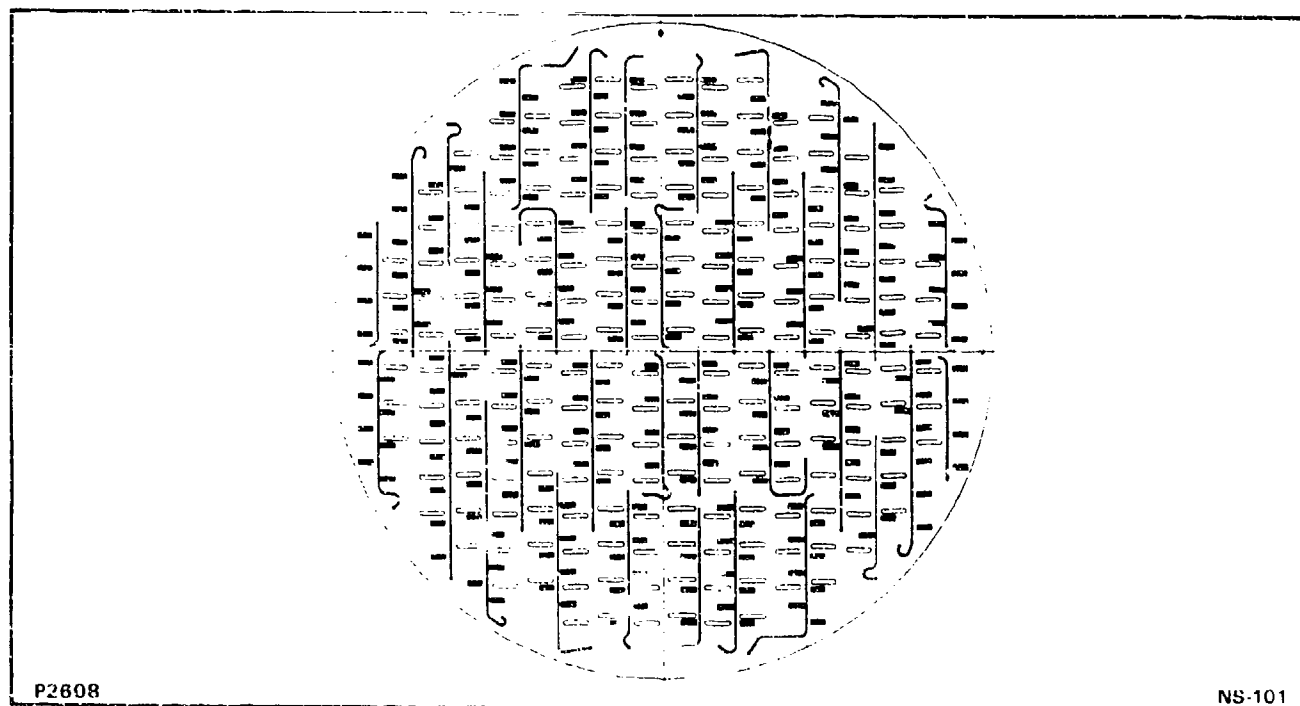


Figure 2 Microstrip Antenna Waveguide Antenna Overlay (13 Wavelength Diameter)

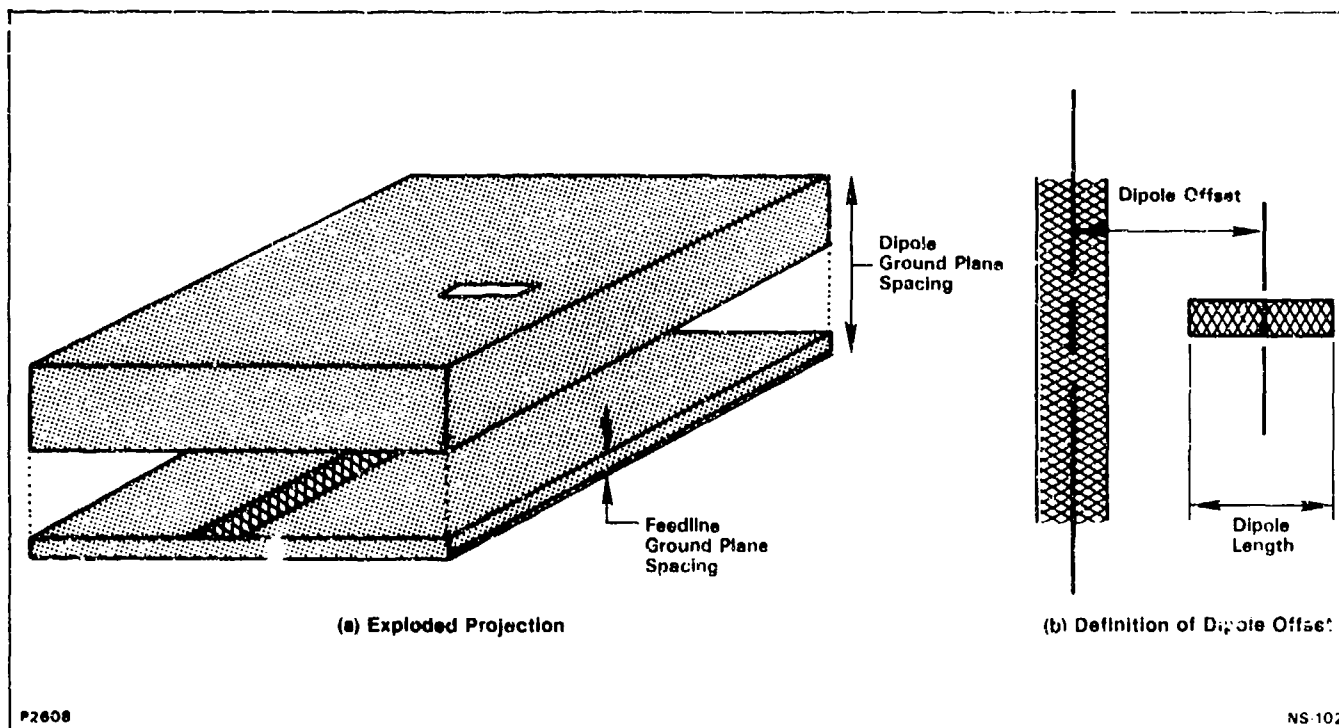


Figure 3. Microstrip Dipole Geometry

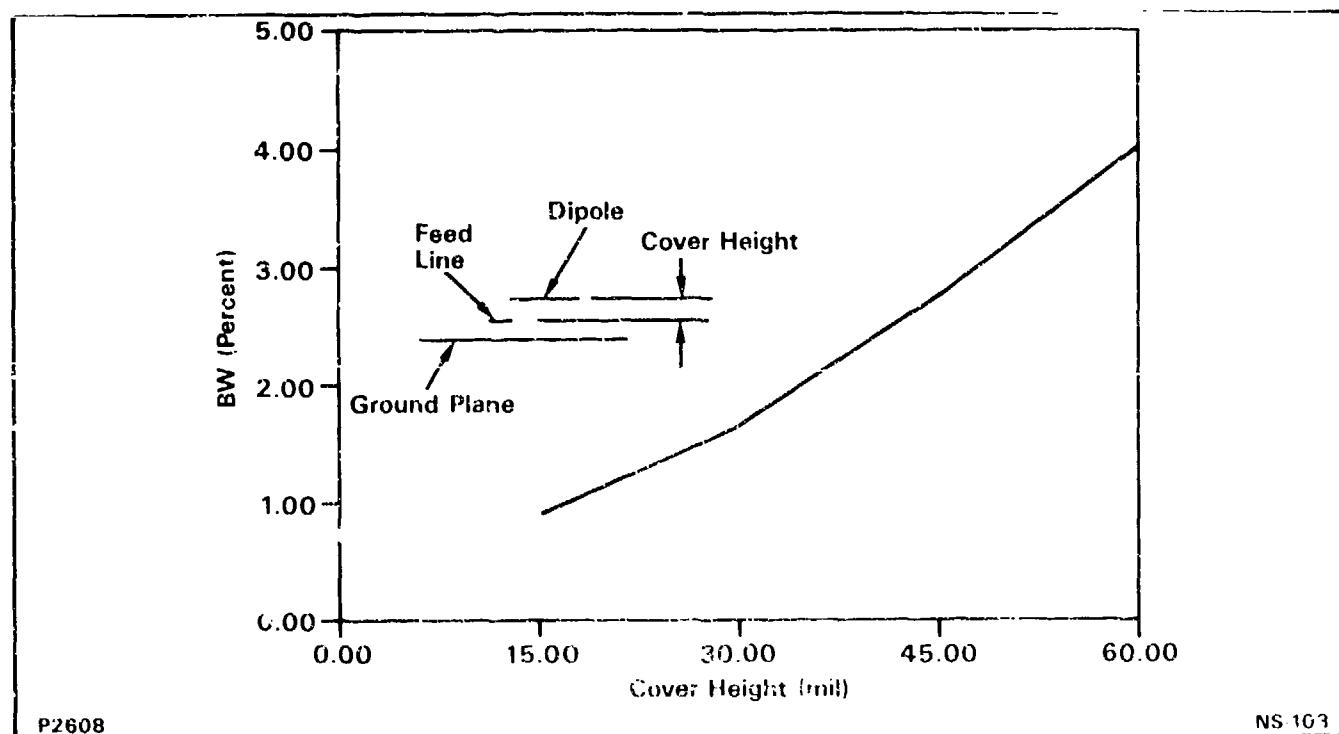
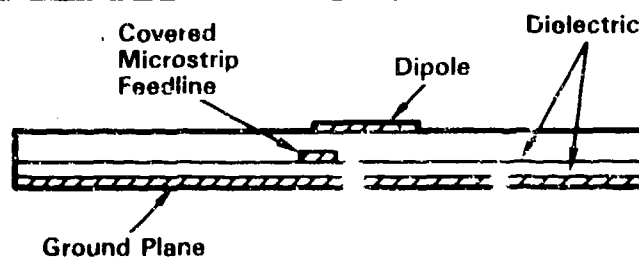
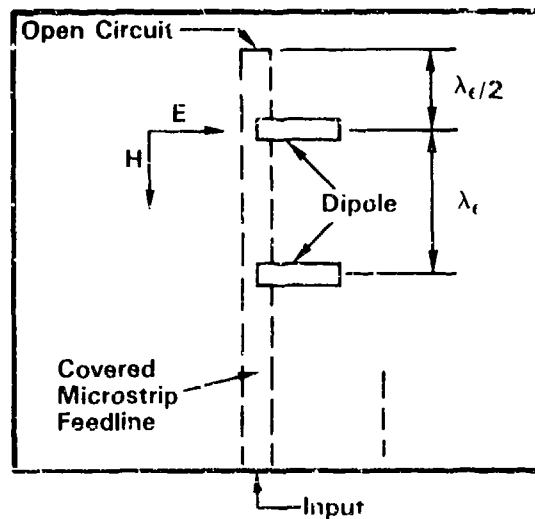


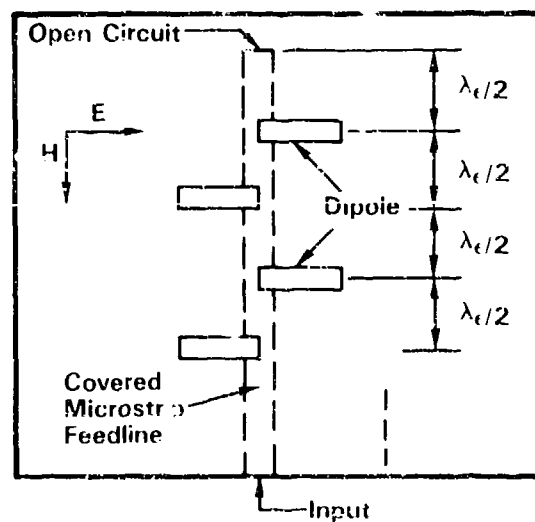
Figure 4. Bandwidth of Microstrip Dipole versus Cover Height of Dielectric ($\epsilon_r = 2.2$)



(a) Microstrip Dipole Concept- Non-Stacked Dipoles, Cross Sectional View



(b) EMC Linear Array- Nonalternating Configuration, Top View



(c) MC Linear Array- Alternating Configuration, Top View

P2608

NS 104

Figure 5 Possible Subarray Configurations

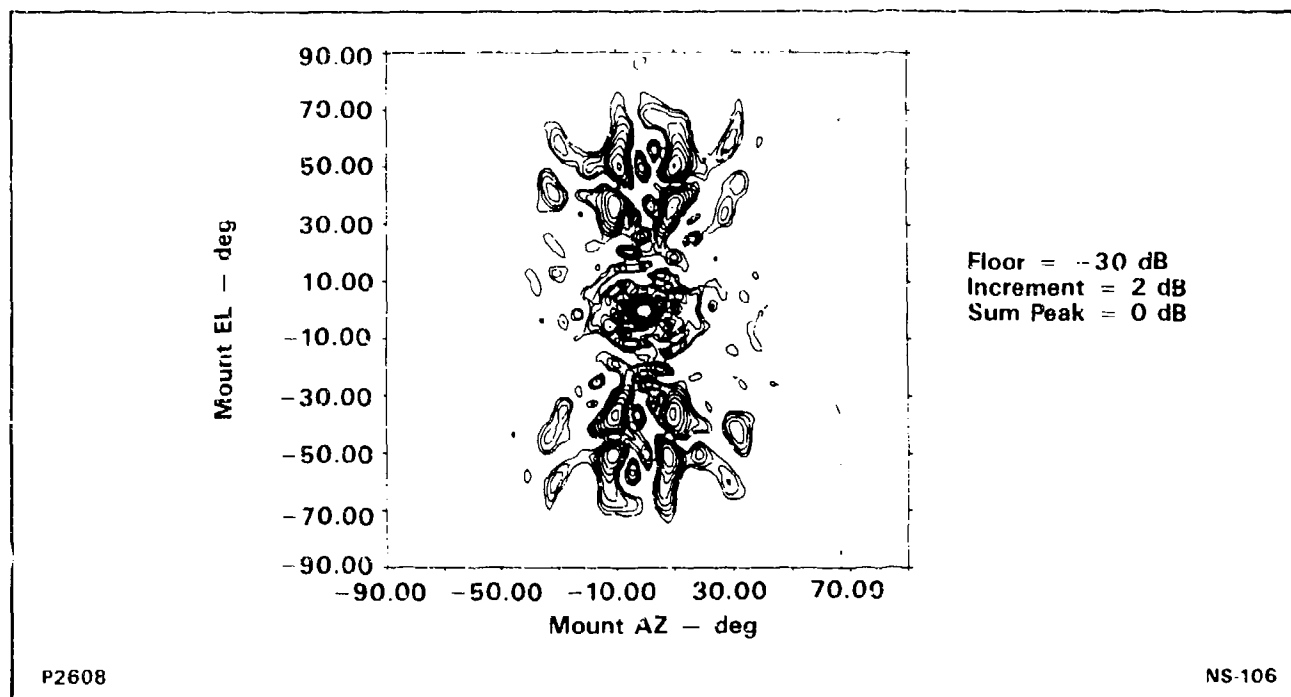


Figure 7. 13 Wavelength Diameter Antenna, Sum Channel Contour (Measured)

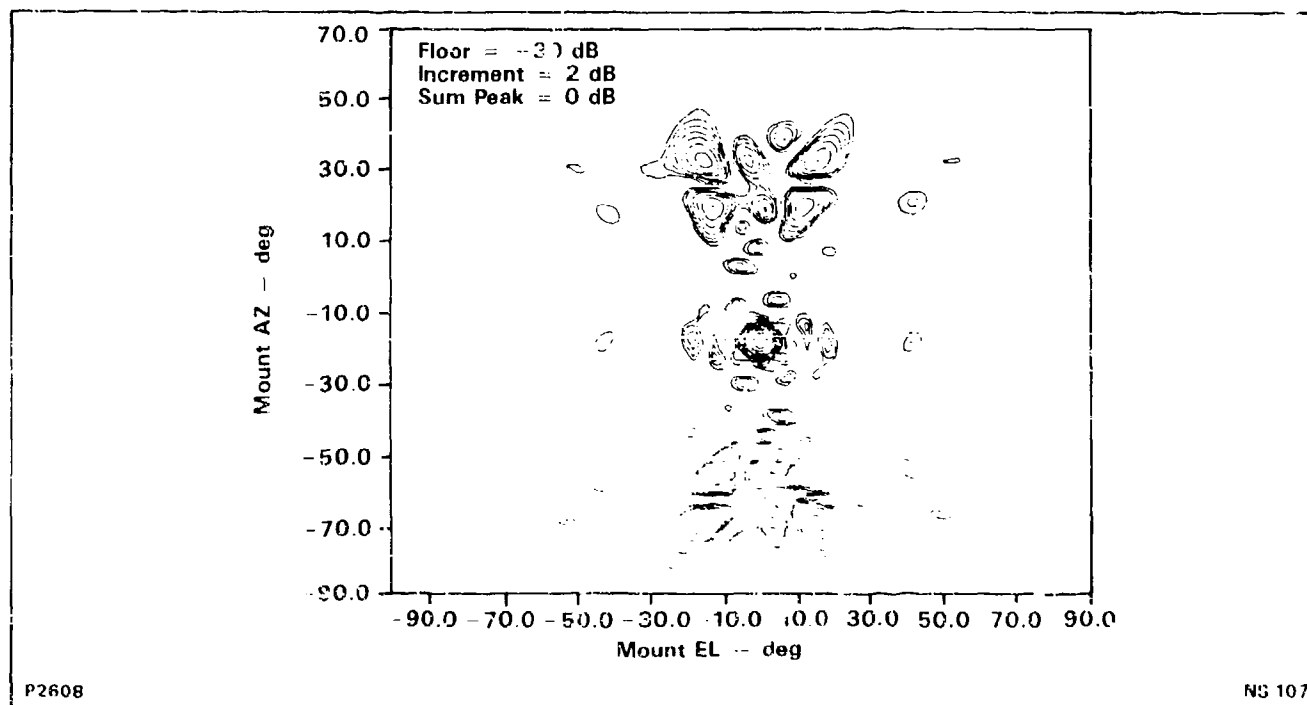
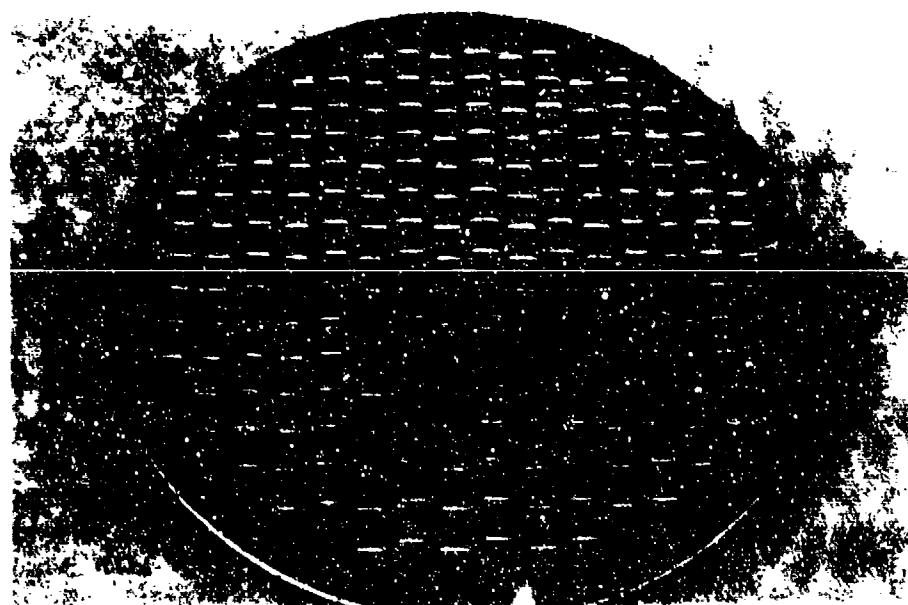
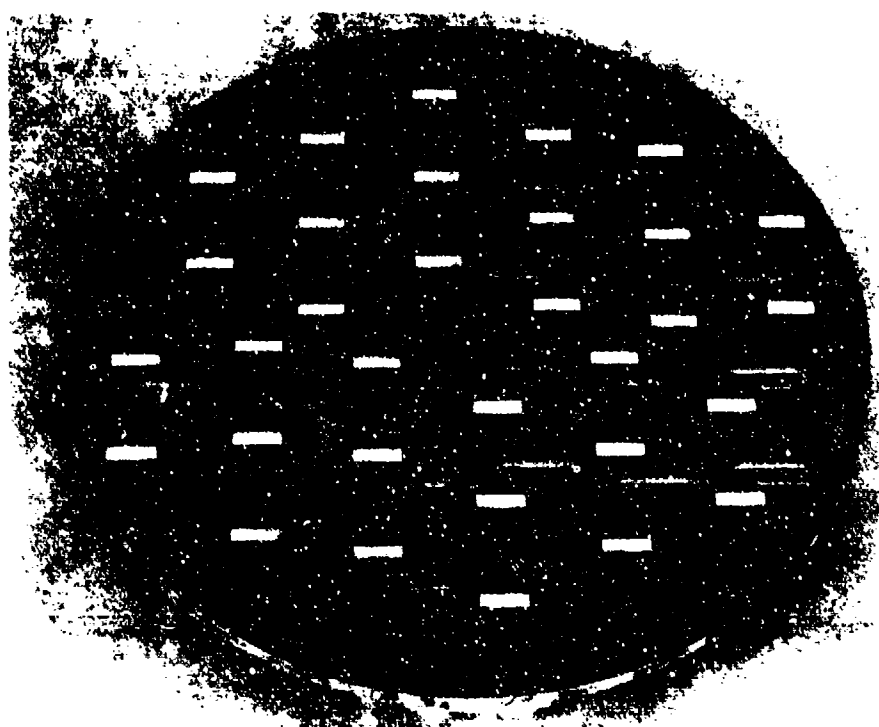


Figure 8. 13 Wavelength Diameter Antenna, Sum Channel Contour (Theoretical)



P2606

NS-108

Figure 9 Two Dual-Polarized Antenna Configurations

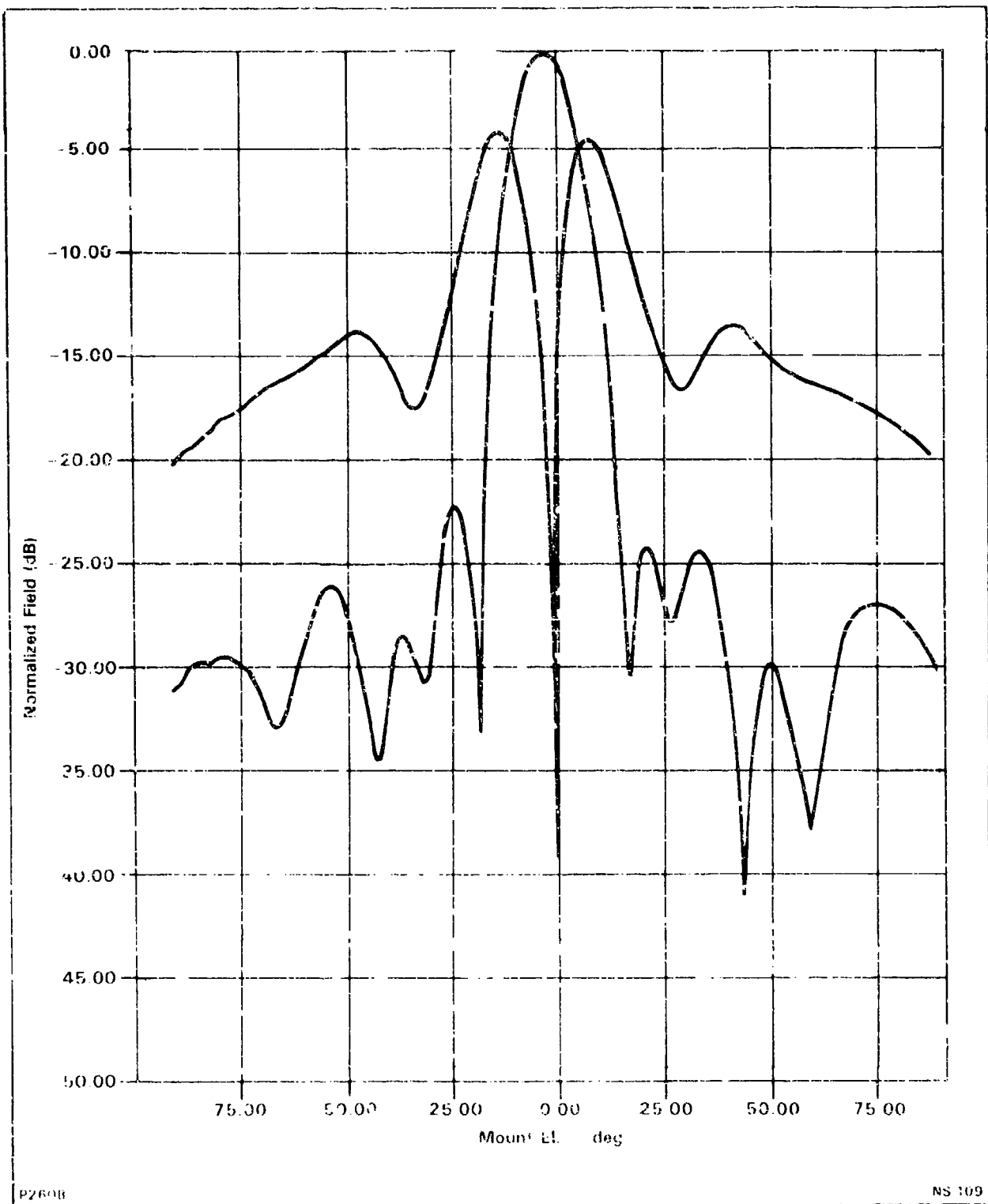


Figure 10. Half-Wave Flatplate Waveguide Array with Microstrip Antenna
Sum and Difference

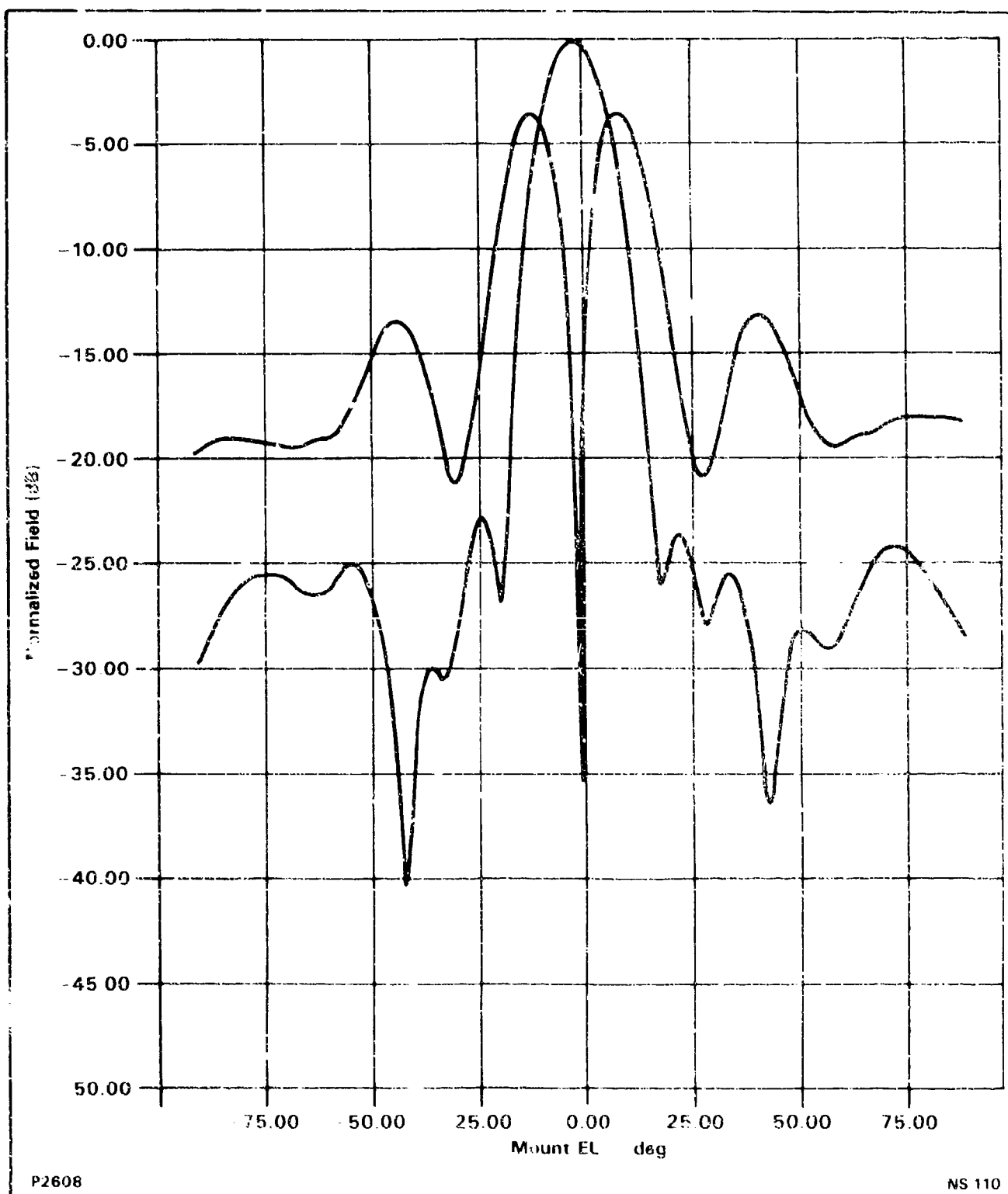
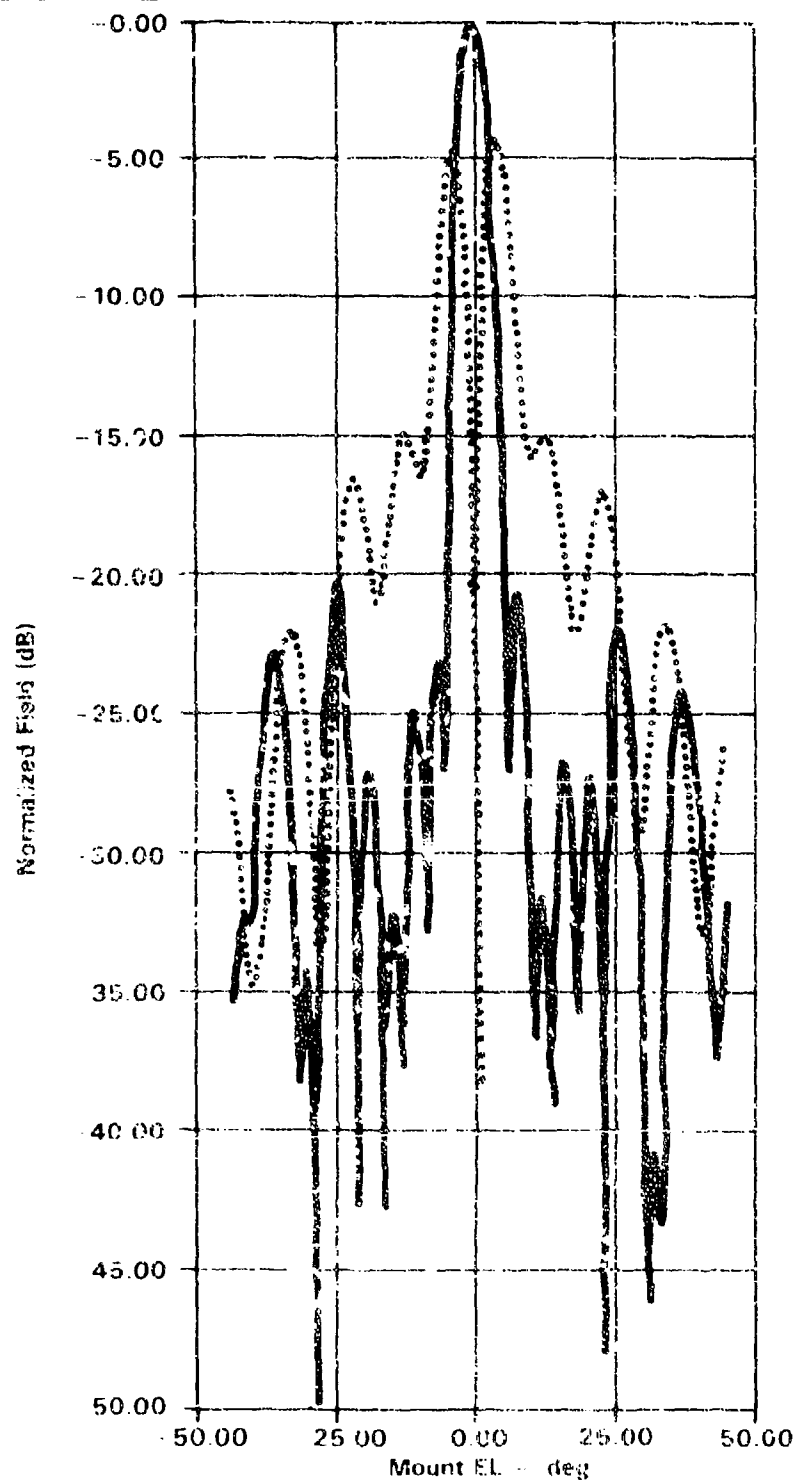


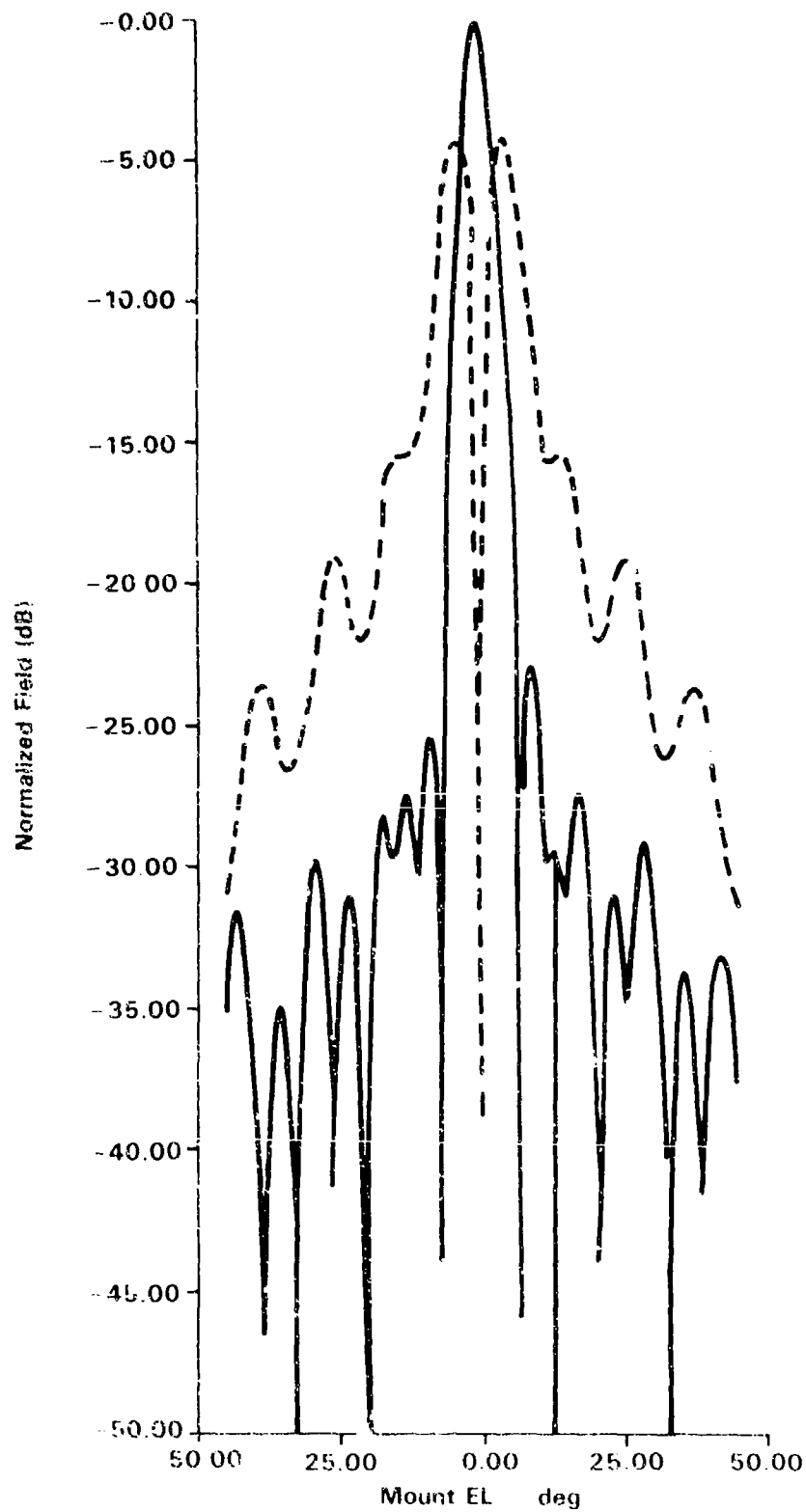
Figure 11. F-Plane Five Wavelength Flatplate Waveguide Antenna with Microstrip Antenna Sum and Delta E1



P260B

NS 111

Figure 12. 13 Wavelength Diameter Microstrip Antenna (Unprofiled). Sum and Delta E1 Channels E-Plane Patterns



P2608

NS 112

Figure 13 13 Wavelength Diameter Microstrip Antenna (Profiled), Sum and Delta Channel Plane Patterns

IMPROVED BANDWIDTH MICROSTRIP ANTENNA ARRAY

Shashi Sanzgiri, Bill Powers and Jim Hart

Texas Instruments Incorporated

Antenna Laboratory

McKinney, Texas

ABSTRACT

A microstrip radiating element design for a 10-percent bandwidth and wide scan angle phased array antenna is described. The radiating element consists of a single probe-fed circular patch on a thick substrate. The element impedance match performance has been characterized both in a waveguide simulator and in a finite array environment. The measured reflection coefficient data as a function of frequency and scan angle have been compared with the analytical data. Also, the array performance with a wide angle impedance matching sheet has been evaluated analytically and experimentally.

1. INTRODUCTION

Recently, printed circuit antenna elements have found widespread use in phased array applications. The main reasons have been low cost, low profile, conformality, light weight, and integrability with monolithic microwave circuit. The system applications using printed circuit arrays have so far been those requiring narrow instantaneous bandwidth (4 to 5 percent) for two-dimensional wide-angle electronic scan or those with wider bandwidth (5 to 10 percent) but limited to either one-dimensional scan with wide field of view or two-dimensional scan with narrow field of view.

This paper addresses the design procedure for a microstrip array antenna intended for airborne radar application. This application required an instantaneous bandwidth of almost 10 percent centered at 9.5 GHz and 60 degrees conical scan sector. The design procedure for such an array involved proper selection of the parameters for the substrate and for the internal and external matching circuits. The array consisted of coaxial probe-fed circular patch antennas with dielectric cover. Both analytical and experimental procedures were used to arrive at the broadband, wide-angle impedance matching techniques used for this array.

This paper is organized into sections that chronologically describe the procedures used for investigating the frequency and scan angle performance of the array. The procedures used are:

- Investigation of blind spots
- Broadbanding of isolated element
- Waveguide simulator tests
- Finite array tests
- Wide angle impedance matching tests.

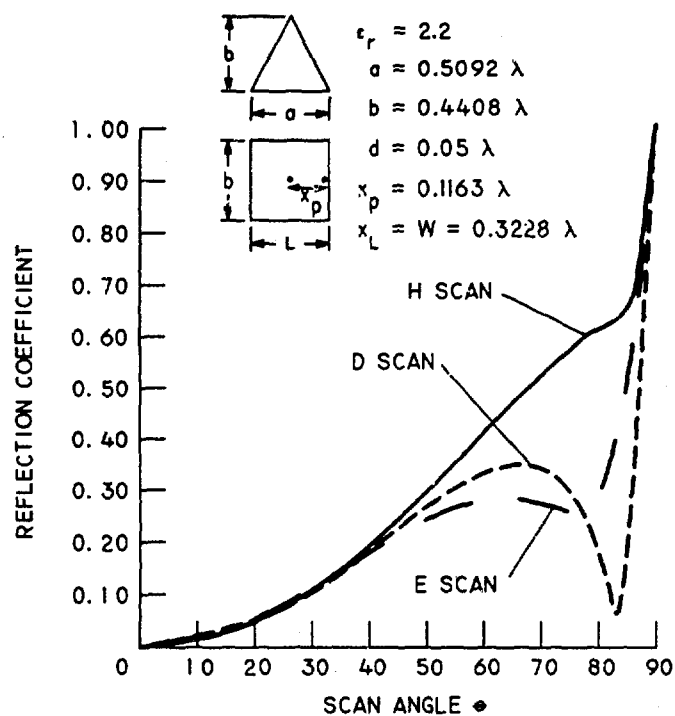
2. INVESTIGATION OF BLIND SPOTS

It is well known that the bandwidth of the microstrip elements can be improved using thick substrates.¹ Thick substrates also support surface and leaky waves, leading to high VSWR conditions at certain scan angles. Previous studies² have indicated that for 0.062-inch-thick substrates with relative dielectric constant of 2.5, the blind spot scan angle lies beyond 60 degrees in the E plane. An investigation was performed for our particular array geometry using an equilateral triangular grid with 0.611 inch side length, 0.062 inch thick substrate, and 2.2 dielectric constant. Analysis using moment method for the calculation of unknown current distributions was performed, using a procedure similar to that given by Pozar.³ In this analysis, the probe is modeled as a filamentary line. For simplicity, the analysis was restricted to rectangular patches.

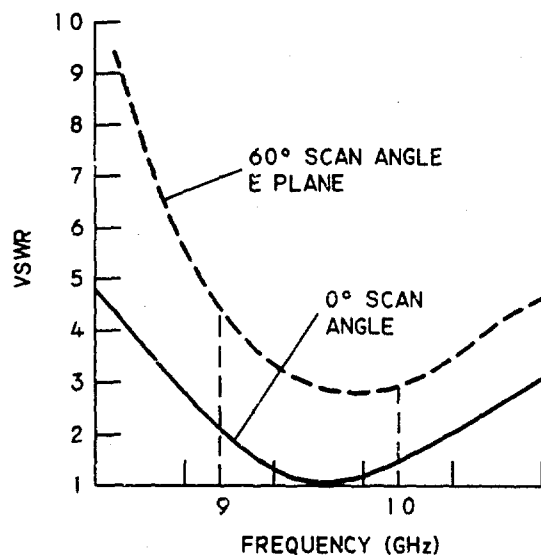
Figure 1(A) shows the reflection coefficient versus scan angle in the E, H, and diagonal planes at center frequency. In the analysis, the array is assumed matched at broadside. Figure 1(B) shows the frequency dependence of the reflection coefficient at 60-degree scan angle in the E plane. The results in Figure 1 show that no blind spot occurs in the 60-degree scan sector over the desired 10-percent bandwidth. The results in Figure 1(B) also show the need for impedance matching at wide scan angles.

3. BROADBANDING OF ISOLATED ELEMENT PERFORMANCE

The broadbanding of the element performance was accomplished using: electrically thick substrate and incorporation of matching network behind the element. The substrate thickness was 0.062 inch (0.05λ at center frequency). The matching circuit consisted of



(A) REFLECTION COEFFICIENT VERSUS SCAN ANGLE AT MID-BAND



(B) VSWR VERSUS FREQUENCY AT 0° AND 60° SCAN ANGLE IN THE E PLANE

C87908001

Figure 1. Infinite Array Analysis Results

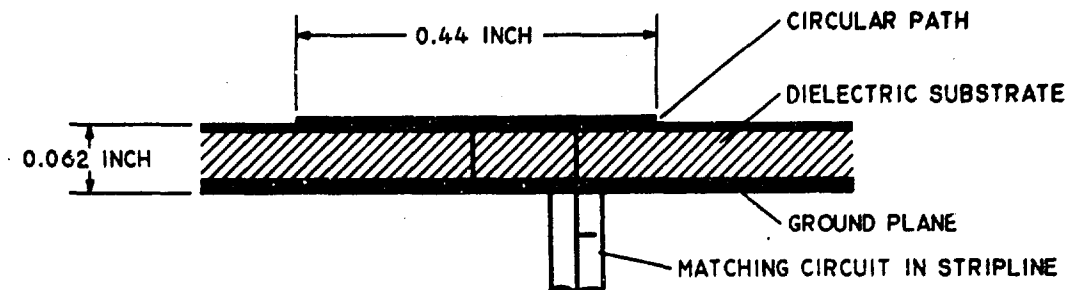
an open circuit stub placed in the feed line below the ground plane. Figure 2(A) shows the radiating element construction with the matching circuit. Both the matching circuit parameters (placement and length of the stub) and the coaxial probe feed location on the patch were optimized to yield a double-tuned response. The matching circuit design procedure is similar to that of an equi-ripple bandpass filter design.⁴ Figure 2(B) shows a comparison of the three microstrip element designs: microstrip element on a thin substrate (0.031 inch thick), microstrip element on a thick substrate (0.062 inch thick), and microstrip element on a thick substrate with the broadband matching circuit. These results show that with a thicker substrate and proper matching, a 2:1 VSWR can be obtained over a bandwidth of 16 percent. Given below are the dimensions of the patch element and the matching circuit that gave the optimum bandwidth:

Circular patch diameter	0.44 inch
Dielectric constant of the substrate	2.2
Substrate thickness	0.062 inch
Distance of the probe from the center	0.065 inch
Probe diameter	0.025 inch
Distance of the stub from the feed	0.381 inch
Length of the stub	0.115 inch

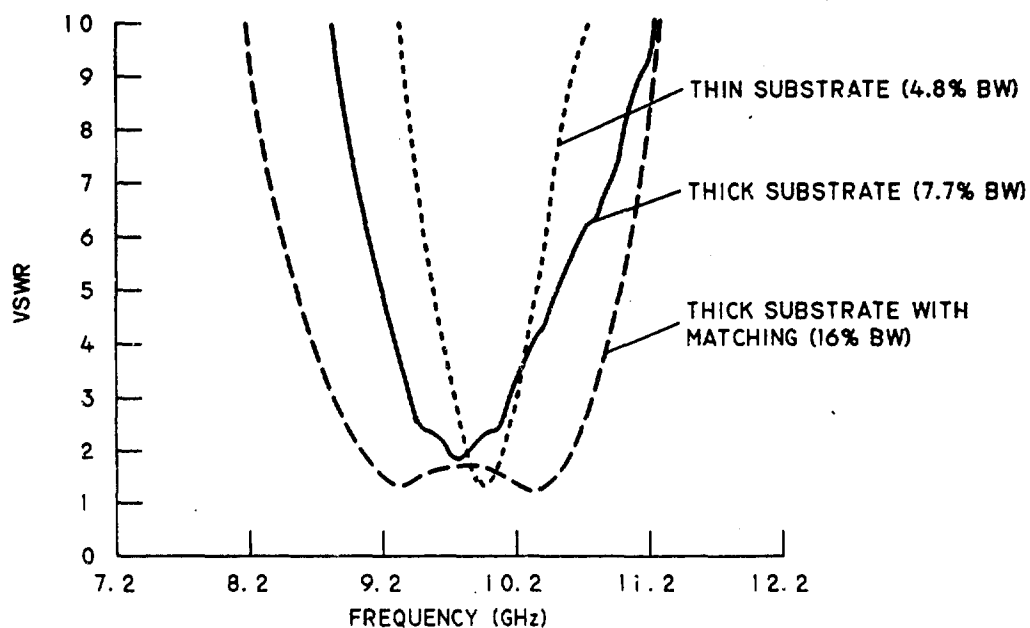
Figure 3 compares the isolated element gains as a function of frequency for the unmatched and matched cases. This figure also shows the cross-polarization levels at broadside.

4. ELEMENT CHARACTERIZATION AND MATCHING IN THE WAVEGUIDE SIMULATOR

It is well known that the element's impedance match changes when the element is immersed in the array environment. To characterize the element impedance in an infinite array environment, a waveguide simulator was fabricated. The dimensions of the simulator were such that it simulated a scan angle of 30 degrees in the H plane. Figure 4 shows the geometry of the subarray or unit cell used for characterizing the element performance in the waveguide simulator. Figure 5 shows the measured VSWR (looking-in measurements) as function of frequency. The matching circuit was the same as used for the



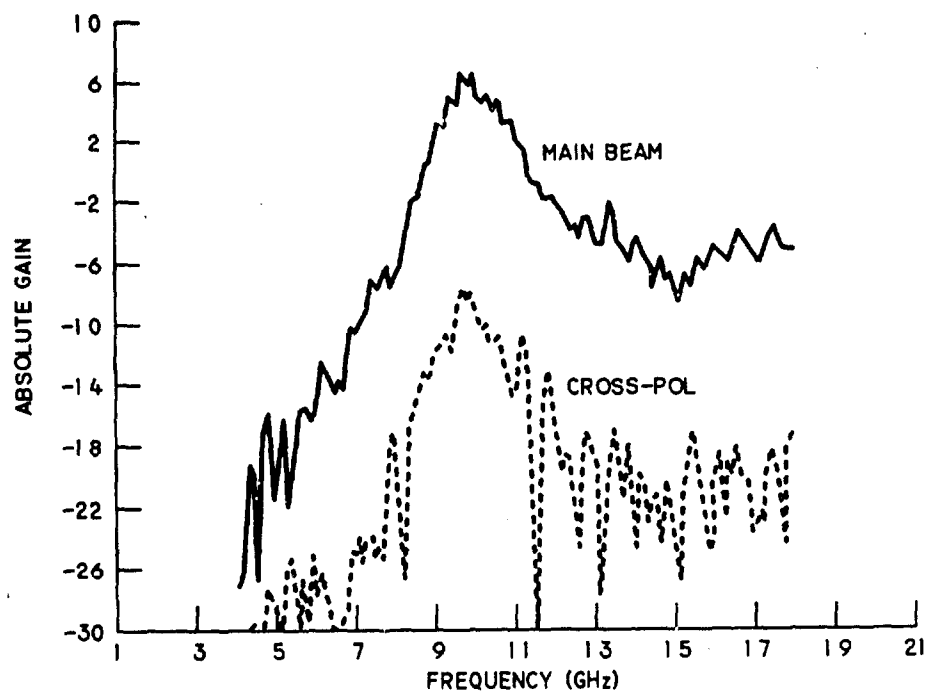
(A) CIRCULAR MICROSTRIP PATCH ANTENNA
WITH MATCHING CIRCUIT



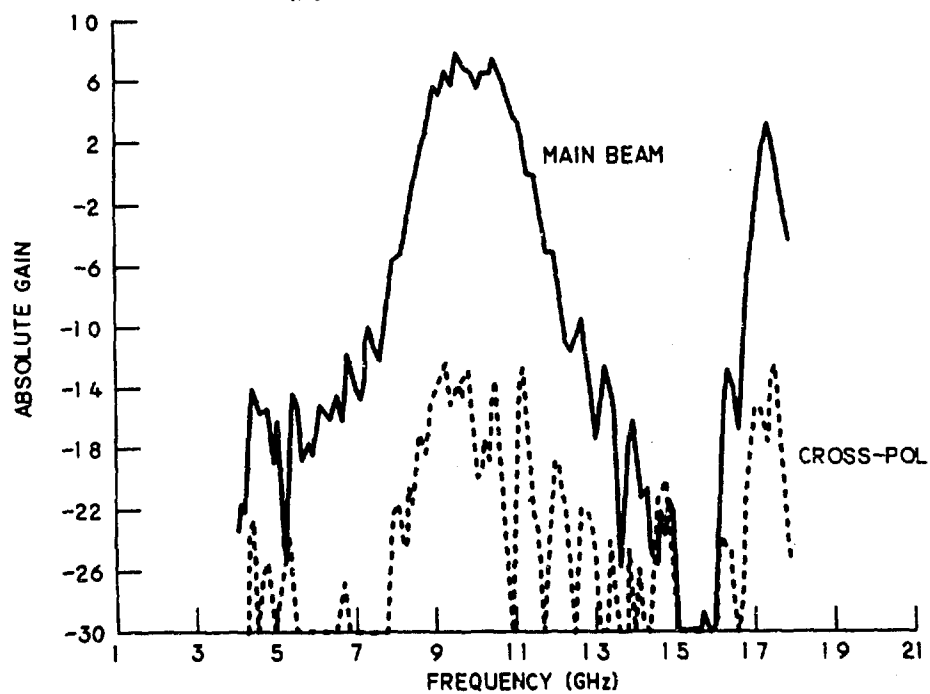
(B) COMPARISON OF THE MEASURED BANDWIDTH PERFORMANCE
OF PATCH ELEMENTS ON THIN AND THICK SUBSTRATES,
WITH AND WITHOUT MATCHING CIRCUITS

C87908002

Figure 2. Isolated Element Construction and Its Performance



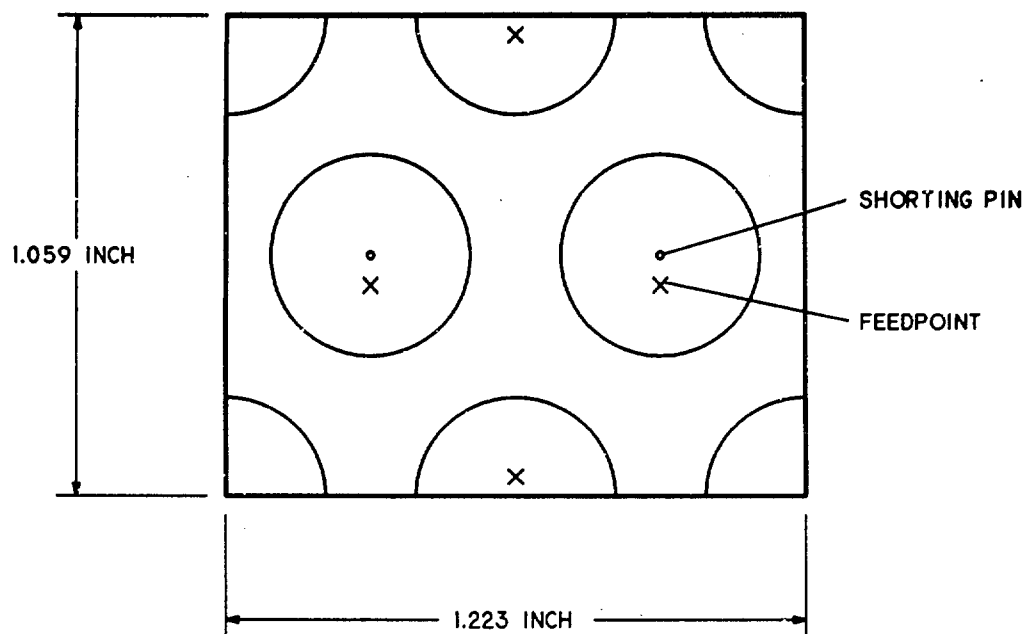
(A) WITHOUT MATCHING CIRCUIT



(B) WITH MATCHING CIRCUIT

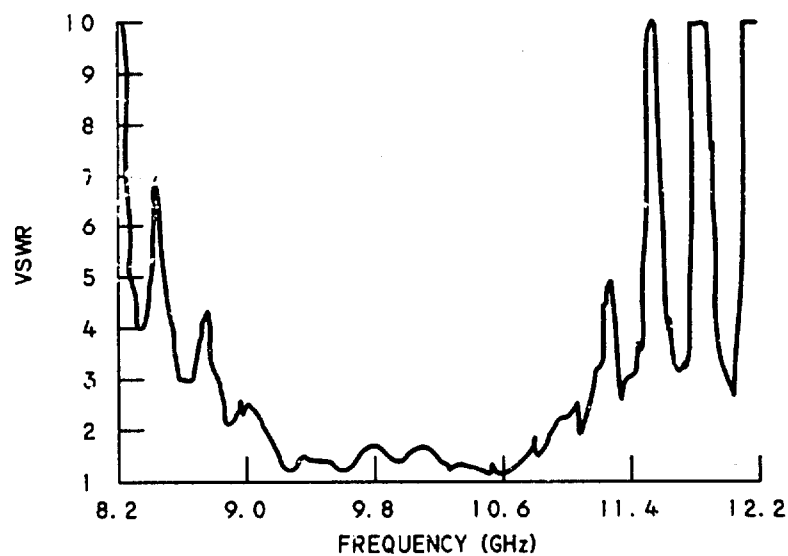
C87908003

**Figure 3. Swept Frequency Gain Measurements on Isolated Subarray
Used for the Waveguide Simulator**



C87908004

Figure 4. Subarray Used for the Waveguide Simulator



C87908005

Figure 5. VSWR Versus Frequency Measured at the Waveguide

isolated element. The results showed that the matching circuit provided a 16-percent (2:1 VSWR) bandwidth performance in the vicinity of 30 degrees in the H plane.

5. ELEMENT CHARACTERIZATION IN THE FINITE ARRAY ENVIRONMENT

The final array performance can best be estimated from the element performance in a finite array environment. The reflection coefficient performance as a function of scan angle and frequency can be estimated from the measured mutual coupling data. The central element patterns also provide an estimate of the scan angle performance of the array.

Figure 6 shows a 108-element array fabricated to evaluate element performance. As shown, each patch is fed by a single coaxial probe. The stripline matching circuit is associated with each element. The elements are spaced on an equilateral triangular grid with a side length of 0.611 inch. The array was fabricated so that the matching circuit could be removed easily from the radiating element if it needed to be modified. The element and matching circuit dimensions were those given in Section 2.



Figure 6. 108 Circular Patch Element Array

Mutual coupling measurements were made between the central element and all other elements in the array. From this mutual coupling data, the reflection coefficient as a function of scan angle and frequency was calculated, using the following expression:

$$\Gamma(\theta, \phi) = \sum_{n=1}^N S_{0n} e^{-j(2\pi/\lambda)(X_n \sin \theta \cos \phi + Y_n \sin \theta \sin \phi)} \quad (1)$$

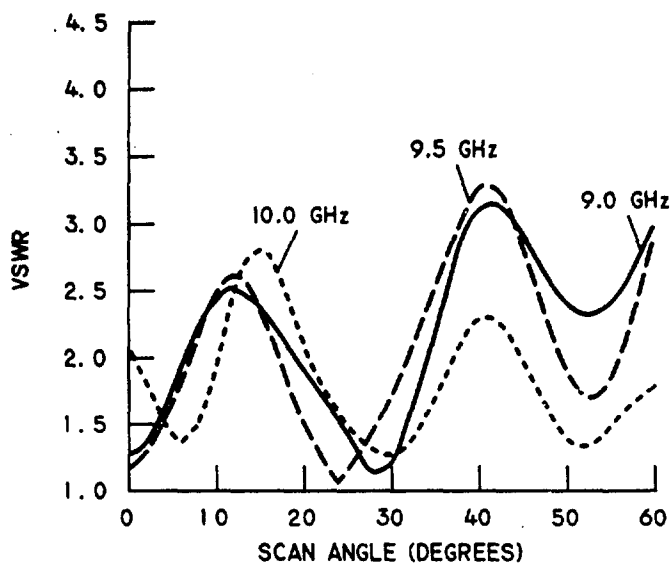
where S_{0n} is the mutual coupling coefficient between the central element and the n th element, and (θ, ϕ) is the scan angle.

Figures 7(A) and (B) show the VSWR as a function of scan angle in the E and H planes respectively and for 9.0, 9.5, and 10.0 GHz. As seen from these results, the VSWR performance both in the E and H planes exceeds 3:1. The scan angle performance in the E plane at wide scan angles was particularly poor, with VSWR exceeding 4:1 at 60 degrees.

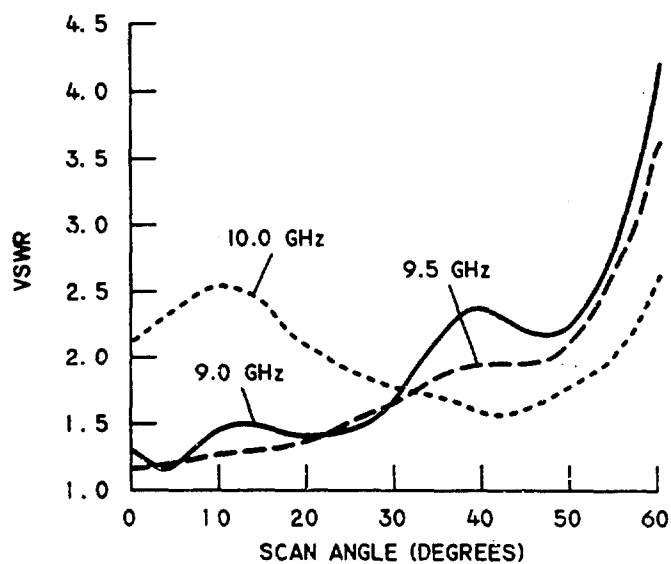
The experimentally obtained VSWR performance was compared with that obtained analytically for the finite element array. A computer program developed by Deshpande and based on the formulation described in Reference 5 was used for this analysis. The program is written for a coaxially fed circular patch antenna array. The center grounding pin and the finite diameter of the probe are not explicitly taken into account in the analysis. The probe effect on the input impedance is, however, taken into account by including a series inductive reactance equal to that of a wire whose diameter and length are the same as that of the probe.

The above mutual coupling analysis program was used to compute the reflection coefficient as a function of scan angle and frequency. The reflection coefficient calculated at the terminal of the feed point was then transformed through the matching circuit to a reference plane at the same location as used in the actual array.

Figure 8 shows the computed VSWR as a function of scan angle in the E plane at 9.0, 9.5, and 10.0 GHz. The VSWR performance from the analytical model shows trends similar to that obtained experimentally. The differences in the actual VSWR values may have been caused by the fact that, in the actual measurements, mutual coupling was measured through the matching circuits while in the analytical model mutual coupling was computed for unmatched radiating elements. The analytical model not explicitly taking into account the grounding pin and the coaxial probe might also have contributed to



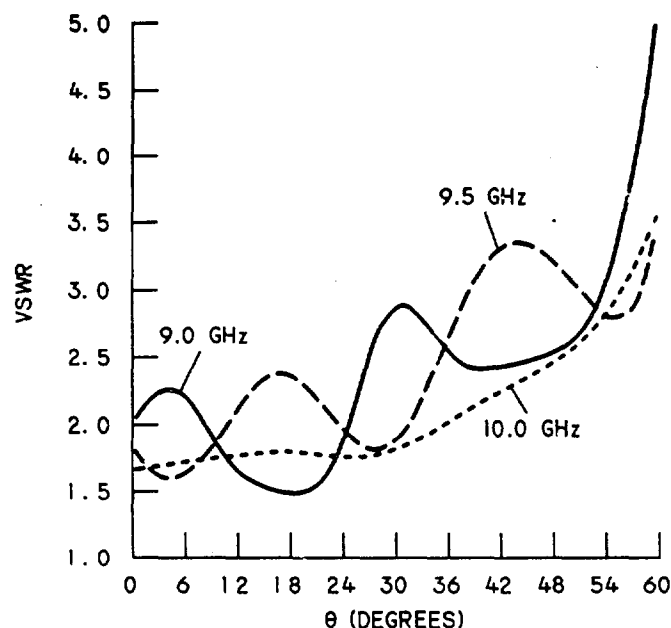
(A) VSWR VERSUS SCAN ANGLE
IN THE H PLANE



(B) VSWR VERSUS SCAN ANGLE
IN THE E PLANE

C87908011

**Figure 7. Computed VSWR Versus Scan Angle From
the Measured Mutual Coupling Data**



C87908007

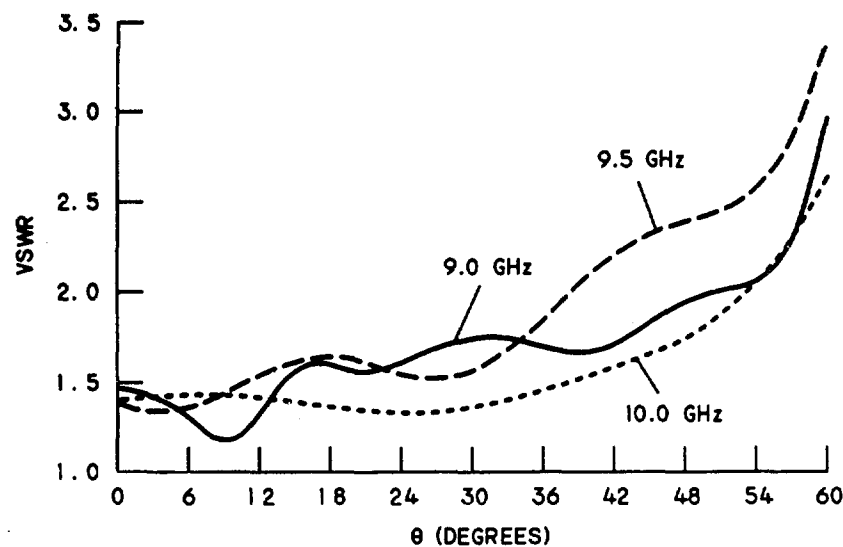
**Figure 8. VSWR Versus Scan Angle in the E Plane
From the Computed Mutual Coupling Data**

the differences. Even with the differences, the similarity in the trends was sufficient to validate the test results.

6. FINITE ARRAY TESTS WITH DIELECTRIC COVER

For waveguide element arrays, mutual coupling analysis tools that include multiple layers of dielectric sheets for wide-angle impedance matching are well developed and are routinely used. For microstrip arrays, such analytical models are still being developed. The analysis developed by Deshpande³ does include a dielectric cover on top of the array. The analysis is, however, restricted to the use of the same dielectric constant for the cover as for the substrate. This analytical procedure was used to determine the thickness of the dielectric cover that gave the best overall VSWR for wide scan angles in the E plane. The optimization process yielded a thickness of 0.01 inch for the dielectric cover.

Figure 9 shows the computed VSWR as a function of scan angle in the E plane at three frequencies. The results show an overall improvement in the VSWR performance in the E plane. A similar improvement was also seen in the H plane.



C87908008

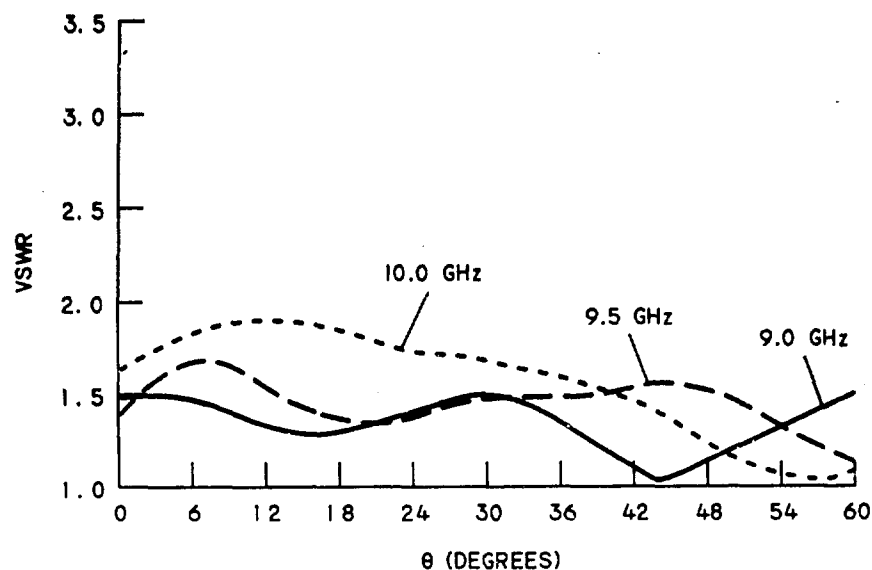
Figure 9. VSWR Versus Scan Angle in the E Plane From the Computed Mutual Coupling Data and With 0.01-Inch-Thick Dielectric Slab ($\epsilon_r = 2.2$)

A 10-mil-thick dielectric sheet with a relative dielectric constant of 2.2 was bonded to the array shown in the Figure 6. Mutual coupling measurements between the center and all other elements were repeated. From this mutual coupling data, the VSWR as a function of scan angle was computed in different planes. The radiating elements had the same matching circuit described in the previous sections. Figure 10 shows the results for the E and H planes. Comparison of these results with those in Figure 7 shows a definite improvement in the impedance matching. Also, the results in Figures 9 and 10 show a good correlation between the analytical and measured results.

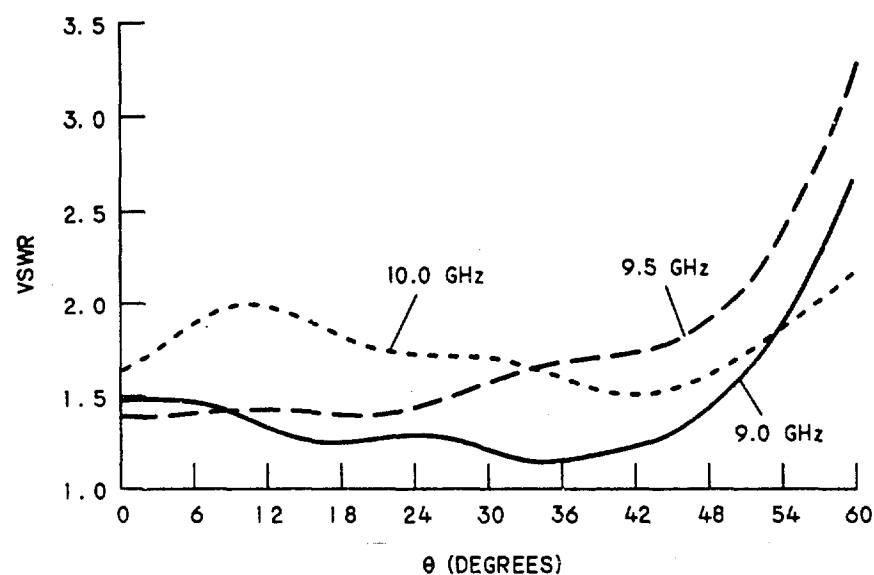
Figure 11 compares the E- and H-plane patterns, with and without the dielectric cover. The broadening of the element pattern as a result of the dielectric cover is seen in both planes, a further validation of improved wide scan angle performance.

7. SUMMARY

Both experimental and analytical results are given to show that the bandwidth performance of array element for wide scan angles can be improved using both internal and external impedance matching schemes. The internal matching consisted of a simple



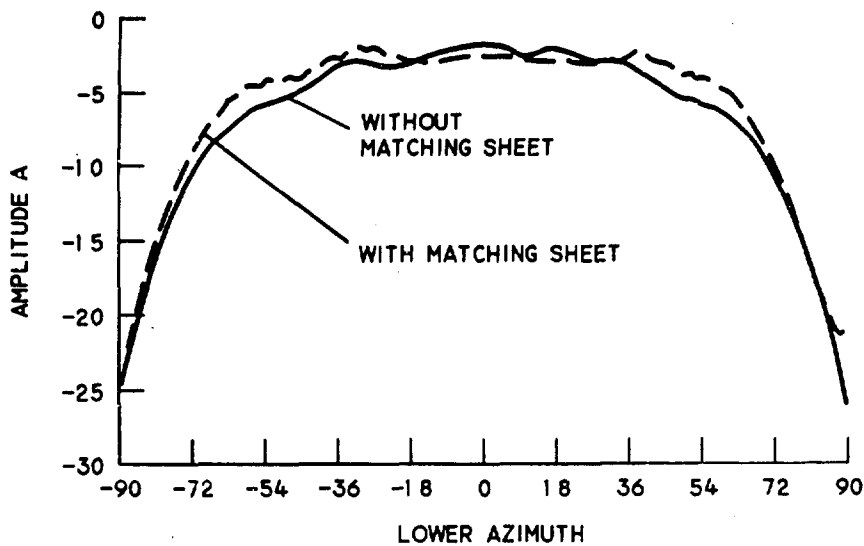
(A) CENTER ELEMENT VSWR VERSUS
SCAN ANGLE IN THE H PLANE



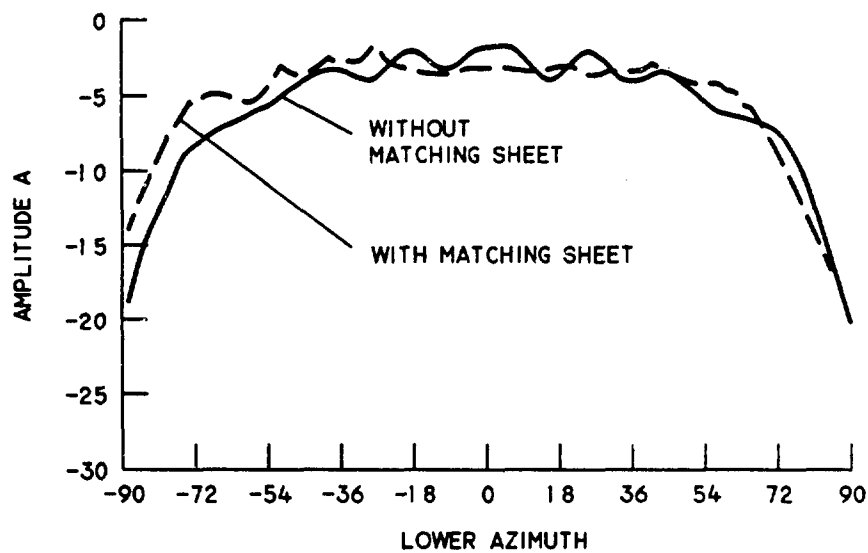
(B) CENTER ELEMENT VSWR VERSUS
SCAN ANGLE IN THE E PLANE

C87908009

**Figure 10. Measured Scan Angle Performance With
Matching Sheet (0.01 Inch Thick, $\epsilon_r = 2.2$)**



(A) H PLANE PATTERNS



(B) E PLANE PATTERNS

C87908010

Figure 11. Comparison of Center Element Patterns With and Without Matching Sheet at Midband

single stub matching and appropriate location of the probe feed. The external impedance matching consisted of a dielectric layer of appropriate thickness. The external matching was restricted to the single dielectric layer with the same dielectric constant as that of the microstrip element substrate. With this dielectric cover, the VSWR of less than 3:1 was achieved over a 10-percent bandwidth and 60 degrees conical scan sector. The analytical model can be extended to include multiple dielectric layers in the future to further optimize the impedance match performance at wide scan angles.

8. ACKNOWLEDGMENTS

The authors acknowledge Dr. M.D. Deshpande for providing a computer program to analyze scan angle performance of the finite array of circular microstrip patches. The authors also acknowledge assistance provided by Dr. Sam Lee in the analysis of an infinite array of rectangular microstrip patches.

9. REFERENCES

1. Bahl, I.J., and P. Bhartia (1980), *Microstrip Antennas*, Artech House.
2. McGrath, D.T., and M. Fitzgerald (1987), *Investigation of surface wave blindness in microstrip phased array antennas*, RADC-TR-87-39, in-house report. ADA189326
3. Pozar, D.M., and D.H. Schaubert (1984), "Analysis of an infinite array of rectangular microstrip patches with idealized probe feeds," *IEEE Trans. Antennas Propag.*, AP-32:1101.
4. Paschen, D.A. (1986), "Practical examples of integral broadband matching of microstrip antenna elements," *Proceedings of the 1986 Antenna Applications Symposium*, Allerton.
5. Deshpande, M.D., and M.C. Bailey (1987), "Analysis of finite phased arrays of circular microstrip patches," *Proceedings of the 1987 Antenna Applications Symposium*, Allerton.



MISSION of Rome Air Development Center

RADC plans and executes research, development, test and selected acquisition programs in support of Command, Control, Communications and Intelligence (C³I) activities. Technical and engineering support within areas of competence is provided to ESD Program Offices (POs) and other ESD elements to perform effective acquisition of C³I systems. The areas of technical competence include communications, command and control, battle management, information processing, surveillance sensors, intelligence data collection and handling, solid state sciences, electromagneticics, and propagation, and electronic maintainability, and compatibility.